



Experimental and numerical analysis of the temporomandibular joint disc behaviour

Lara Kristin Tappert

► To cite this version:

Lara Kristin Tappert. Experimental and numerical analysis of the temporomandibular joint disc behaviour. Biomechanics [physics.med-ph]. Université de Lorraine, 2020. English. NNT : 2020LORR0047 . tel-02940668

HAL Id: tel-02940668

<https://hal.univ-lorraine.fr/tel-02940668>

Submitted on 16 Sep 2020

HAL is a multi-disciplinary open access archive for the deposit and dissemination of scientific research documents, whether they are published or not. The documents may come from teaching and research institutions in France or abroad, or from public or private research centers.

L'archive ouverte pluridisciplinaire **HAL**, est destinée au dépôt et à la diffusion de documents scientifiques de niveau recherche, publiés ou non, émanant des établissements d'enseignement et de recherche français ou étrangers, des laboratoires publics ou privés.



AVERTISSEMENT

Ce document est le fruit d'un long travail approuvé par le jury de soutenance et mis à disposition de l'ensemble de la communauté universitaire élargie.

Il est soumis à la propriété intellectuelle de l'auteur. Ceci implique une obligation de citation et de référencement lors de l'utilisation de ce document.

D'autre part, toute contrefaçon, plagiat, reproduction illicite encourt une poursuite pénale.

Contact : ddoc-theses-contact@univ-lorraine.fr

LIENS

Code de la Propriété Intellectuelle. articles L 122. 4

Code de la Propriété Intellectuelle. articles L 335.2- L 335.10

http://www.cfcopies.com/V2/leg/leg_droi.php

<http://www.culture.gouv.fr/culture/infos-pratiques/droits/protection.htm>

Experimental and numerical analysis of the temporomandibular joint disc behaviour

PhD Thesis

submitted and defended publicly on March 16th 2020
as a partial requirement to qualify for the degree of:

Doctorate in Mechanical Engineering - Material Mechanics
by

Lara Kristin TAPPERT

Composition of the Jury:

Rapporteur:	Nadia	BAHLOULI	Professeur des Universités - Université de Strasbourg
Rapporteur:	Albert	BAARS	Professeur des Universités - Hochschule Bremen
Examineur:	Anne-Sophie	BONNET	Maître de Conférences HDR - Université de Lorraine
Examineur:	Narcisse	ZWETYENGA	Professeur des Universités / Praticien Hospitalier - Dijon Université de Bourgogne / Centre Hospitalier Universitaire Dijon Bourgogne
Thesis Director:	Pawel	LIPINSKI	Professeur émérite - Université de Lorraine
Thesis Co-Director:	Adrien	BALDIT	Maître de Conférences - Université de Lorraine

Für Oma.

Acknowledgement

I wish to express my gratitude to my supervisors Pawel Lipinski and Adrien Baldit for their scientific support, guidance and advice. Thanks to them and their endless patience and motivation throughout these three years I was able to complete this PhD thesis and develop on a personal and professional basis.

Nadia Bahlouli and Albert Baars, I wish to thank them for taking the time to evaluate my manuscript and together with Anne-Sophie Bonnet and Narcisse Zwetyenga for the rich discussion and defence evaluation.

This work would not have been possible without the support and collaboration of many. Therefore, thanks a lot to la Maison Vagner for the supply of my samples. Maude Ferrari and Cedric Laurent I would like to thank for the support to carry out the MRI acquisition. I wish to thank Solsi-Cad for the use of their 3D scanner, especially Sébastien Hatton for his friendly help during the work. My thanks also goes to Gilles Dusfour for his collaboration concerning the digital image correlation. I am also grateful for the histological cuts, which have been prepared by Frédéric Velard. Rodney do Nascimento I would like to thank for his collaboration and many inspiring conversations.

I also got a lot of support from the technicians at ENIM and LEM3, therefore I wish to express my appreciation to Frédéric Schwab, Djamel Meziani and Sébastien Carré. Also together with Emerik Henrion and Patrick Hergalant, I want to say thank you for the cheerful escape during some coffee breaks.

My gratitude goes to my colleagues from the biomechanics group Émilie de Brosse, Cynthia Dreistadt and Rachid Rahouadj for their kindness and support.

I am thankful for my friends and colleagues from LEM3 and ENIM for their friendly welcoming, their kindness and many joyful moments: Pierre, Francis, Nastya, Julien, Mathieu, Chloé, Stéphane, Justine, Baptiste, Zeineb, Komlan, Foli, Ludo, Typhaine, Satya, Manoj, Dasha, Clément, Patricia and many others.

Léonore, Isidore, Erik and Gaiane, thank you for swinging up my life.

I am also happy to receive motivation from all over the world from my first friends in Metz: Andrès, Nia, Kimi, Neringa, Hugues and Lucie.

To Tatti, Joana, Christopher, Philip and Susann I want to say thank you for your friendship and many small and enormous motivation aids.

I wish to express my deepest gratitude to my parents and my brother who always support me, where ever I am and on whom I can always count on.

Beenesh, merci to ti touzour la pou moi!

Contents

Motivation and thesis organisation	1
1 Introduction to the temporomandibular joint and problem definition	3
1.1 The temporomandibular joint and its disorders	4
1.2 The temporomandibular joint disc	5
1.2.1 Biomechanics of the temporomandibular joint disc	9
1.2.2 Biomechanical testing of the temporomandibular joint disc	10
1.2.2.1 Tensile tests	11
1.2.2.2 Compression tests	13
1.3 Objective and strategy	17
2 Analysis of soft material thin layer behaviour through local macro-spherical compression	19
2.1 Introduction	20
2.1.1 Contact mechanics - theoretical background and state of the art . .	21
2.1.2 Problem statement	23
2.2 Material and Methods	25
2.2.1 Finite element model of local spherical compression tests	25
2.2.2 Evaluation of contact radius a	27
2.2.3 Identification of representative strain ϵ^*	28
2.2.4 Curve fitting using the COBYLA method	28
2.3 Results and Discussion	30
2.3.1 Relationships between contact radius a with respect to the measure- ments of indentation depth d and compression tool displacement δ .	30
2.3.2 Relation between indentation depth δ and compression tool dis- placement d	37
2.3.3 Representative stress - strain curves	39
2.3.4 Validation of curve fitting procedure	43
2.3.5 Comparison of hyperelastic laws	45
2.3.6 Density influence on samples behaviour	47
2.4 Conclusion	47
3 Experimental characterisation of the temporomandibular joint disc	49
3.1 Introduction	50
3.1.1 Temporomandibular joint disc samples and animal models	50
3.1.2 Temporomandibular joint disc geometry and thickness	51
3.1.3 Biomechanical characterisation of temporomandibular joint discs . .	51
3.2 Materials & Methods	54
3.2.1 Temporomandibular joint disc sample preparation	54

3.2.2	Acquisition of temporomandibular joint discs external shape and internal microstructure	54
3.2.2.1	3D optical scans of temporomandibular joint disc samples	55
3.2.2.2	3D surface reconstruction of temporomandibular joint discs and printing of condyles	55
3.2.2.3	Magnetic resonance imaging of a temporomandibular joint disc	56
3.2.3	Mechanical tests	56
3.2.3.1	Local spherical compression tests	57
3.2.3.2	Local spherical compression test workbench	60
3.2.3.3	Internal strain analysis	64
3.2.4	Sample thickness calculation	64
3.3	Results and Discussion	66
3.3.1	External shape and internal microstructure of the temporomandibular joint disc	66
3.3.2	Local spherical compression tests	70
3.3.3	Internal strain analysis	84
3.4	Conclusions on experimental results	88
4	Identification of temporomandibular joint disc material parameters through spherical compression tests	91
4.1	Introduction	92
4.2	Material and Methods	94
4.2.1	Representative stress-strain curve construction	94
4.2.2	Hyperelastic material laws used to describe temporomandibular joint disc behaviour	95
4.2.3	Finite element model of local spherical compression test on one temporomandibular joint disc	97
4.3	Results and Discussion	100
4.3.1	Stress-strain curves of local spherical compression tests on temporomandibular joint disc samples	100
4.3.2	Hyperelastic parameter identification	105
4.3.3	Three-dimensional finite element analysis of the temporomandibular joint disc under spherical compression	106
4.3.4	Comparison of experimental and simulated results	109
	Conclusions and Perspectives	111
	A Overview of experimental protocols in literature	123
	B General finite element simulations	127
B.1	Details of finite element simulations	127
B.2	Stress derivation	128
	C Complementary experimental results	129
C.1	Temporomandibular joint disc sample harvesting	129
C.2	3D printed condyles	130
C.3	Magnetic resonance image acquisition	131
C.4	Test machine restrictions	132

C.5	Data base structure	134
C.6	GOM	135
C.7	Experimental force-displacement curves	135
C.8	Average maximal forces per test cycle	140
C.9	Average hysteresis per test cycle	143
C.10	Additional of results internal strain analysis	145
D	Stress-strain curves	149

List of Figures

1.1	Location of the TMJ in the skull with sagittal and frontal view of the articulation, modified from the work of Willard et al. [2011]	4
1.2	(a) Comparison of gross morphology of human and porcine TMJ discs (adapted from Kalpakci et al. [2011]); (b) Example of a porcine TMJ disc indicating anatomical zones and approximate dimensions. Those zones have been defined regarding structural composition variation of the tissue that are related to its biocomposite character. The arrows indicate antero-posterior fibre orientation within the central region.	5
1.3	(a) Second-harmonic generation microscopy images showing collagen fibre distribution within the human TMJ disc [Wright et al., 2016]; (b) Polarized light microscopy images showing collagen fibre distribution within the porcine TMJ disc [Detamore and Athanasiou, 2003b] (400x). Both images highlight the anteroposterior fibre orientation within the central region and the circumferential alignment in the outer disc areas. (c) Scanning electron microscopy image of porcine TMJ disc taken from Juran et al. [2015] , showing that on the superior surface the disc is subdivided in different zones, whereas the inferior side has a more uniform distribution of fibres.	6
1.4	Histology images of transversal cuts: (a) HES (yellow: collagen), (b) Masson's trichrome (blue: collagen) and (c) Safranin O staining (red: GAG) (images obtained through cooperation with the BIOS (Biomatériaux et inflammation en site osseux) laboratory, Université de Reims).	8
1.5	Histology images of sagittal cuts: (a) HES (yellow: collagen), (b) Masson's trichrome (blue: collagen) and (c) Safranin O staining (red: GAG) (images obtained through cooperation with the BIOS laboratory, Université de Reims).	8
1.6	Disc movement while jaw opening, a) during mouth occlusion and b) during mouth opening; the arrows are indicating the condyle's rotation and translation [Athanasiou et al., 2009].	9
1.7	Von Mises stress distribution at the beginning of a clenching process obtained by Mori et al. [2010]	10
1.8	Sketch indicating fibre orientation within tensile test specimen in mediolateral and anteroposterior test direction.	12
1.9	Experimental stress-strain curve from uniaxial tensile test of entire porcine TMJ disc specimen up to failure, in anteroposterior and mediolateral directions with different test velocities obtained by Beatty et al. [2001]	12

1.10	(a) Experimental setup for unconfined compression tests, taken from Allen and Athanasiou [2006] . (b) Stress-strain curve from cyclic unconfined compression tests on porcine TMJ disc specimen obtained by Tanaka et al. [2003b] . A hysteresis between the loading and unloading phase is evident, as well as steady stress-strain state after several cycles indicating viscoelastic characteristics of the specimen.	14
2.1	(a) Schematic representation of the local spherical compression test. H - initial sample thickness, R - spherical compression tool radius, d - compression tool displacement, a - contact radius, δ - indentation depth, g - gravitation, R_δ - radius for indentation depth calculation. (b) Example of force-displacement curves at different displacement levels and an extrapolated equilibrium force (- -) obtained by Lee et al. [2016] conducting local spherical compression tests on articular cartilage of horse stifle joint. The displacement (mm) on the x-axis corresponds to d depicted in Subfigure a.	21
2.2	Axisymmetric finite element model ($h = 2.0$) of an elastic sample placed between a rigid support and a rigid spherical compression tool. The geometry, the mesh and the boundary conditions are shown. The \bullet marks the position of tie-constraint between the compression tool's tip and one node of the mesh. The polygon marks the node used for indentation depth δ calculation and the \cdots line marks the bottom of the sample.	26
2.3	Comparison of dimensionless contact radius a/R as a function of dimensionless indentation depth δ/R obtained through finite element analysis: (a) case of initial thickness ratio from $h = 0.5$ to $h = 2.0$, (b) case of thickness ratios $h = 5.0$ to $h = 100$	31
2.4	Finite element results for $h = 2.0$, shown is the stress distribution and the deformed shape of the sample at a compression tools displacement of $d = 1$ mm. The detachment from the support of the most distal part of the sample can be observed. The maximal compressive stress is -0.96 MPa. Negative stress values are an indication of compressive process of loading.	31
2.5	Fitting of the finite element results of dimensionless contact radius a/R as a function of dimensionless indentation depth δ/R using Equation (2.20) for thickness ratios (a) $h = 0.5$, (b) $h = 1.0$, (c) $h = 5.0$ and corresponding determination coefficients R^2	32
2.6	(a) Shape of the upper and lower surface of the compressed sample for maximal compression tool displacement for three thickness ratios. It becomes clear that with increasing thickness ratio detachment decreases. For a better overview, the samples upper surface is depicted with an offset $y_{coordoffset} = y_{coord} - (H - 0.1)$. (b) For a thickness ratio $h = 2.0$ at a compression tool displacement $d = 0.095$ mm the intermediate part detaches from the support before the distal part detaches.	33
2.7	Comparison of dimensionless contact radius a/R as a function of dimensionless compression tool displacement d/R for (a) samples of different initial thickness ratios h obtained through finite element analysis; (b) Results for thickness ratios $h = 0.5$, $h = 1.0$, and $h = 5.0$, including fitting using Equation (2.21) and associated determination coefficient R^2	34

2.8	(a) Parameter β and (b) parameter m as a function of thickness ratio h ; both with associated curve fitting according to Equation (2.25). The red line marks quasi-linear dependency for thick sample layers.	35
2.9	Dimensionless indentation depth δ/R versus compression tool displacement d/R for thickness ratios (a) $h = 0.5$, (b) $h = 1.0$, (c) $h = 5.0$ with associated curve fitting according to Equation (2.29).	37
2.10	(a) Parameter b_0 as a function of material thickness h with related fitting according to Equation (2.30), (b) parameter b_2 as a function of material thickness h with related fitting according to Equation (2.31).	38
2.11	Compression tool displacement d threshold of detachment as function of sample thickness h with associated linear fitting.	39
2.12	Theoretical stress ($ \sigma_{nH}^n $) for a quasi incompressible neo-Hookean material with $\mu = 0.334$ MPa as a function of strain ϵ and fitted representative stress σ^* as function of representative strain ϵ^* for local spherical compression of a material with thickness ratio (a) $h = 0.5$, (b) $h = 1.0$ and (c) $h = 5.0$. . .	41
2.13	Parameter χ as a function of material thickness ratio h with fitting using Equation (2.32).	42
2.14	Results for a finite element simulation of thickness ratio $h = 0.65$; (a) dimensionless contact radius a/R as function dimensionless compression tool displacement d/R and prediction according to fitting results of Equations (2.26) and (2.27), (b) dimensionless indentation depth δ/R as function dimensionless compression tool displacement d/R and prediction according to fitting results of Equations (2.30) and (2.31), (c) theoretical stress ($ \sigma_{nH}^n $) for an incompressible neo-Hookean material with $\mu = 0.334$ MPa as a function of strain ϵ and fitted representative stress σ^* as function of representative strain ϵ^* for local spherical compression using the parameter χ according to Equation (2.33).	44
2.15	Results of simulation of a sample with thickness ratio $h = 0.75$ and different material laws defined; linear elastic (linE), neo-Hookean (nH), Mooney-Rivlin (MR) and Ogden hyperelastic. Comparison of dimensionless contact radius a/R as a function of dimensionless indentation depth δ/R	45
2.16	Representative stress-strain curves for different material laws applied to the sample of thickness ratio $h = 0.75$, (a) neo-Hookean, (b) Mooney-Rivlin (MR), (c) Ogden, (d) linear elastic (linE).	46
2.17	(a) Dimensionless contact radius a/R as function of dimensionless indentation depth δ/R ; (b) dimensionless contact radius a/R as function of dimensionless compression tool displacement d/R	47
3.1	(a) Photographs of the zero-stress configuration of aorta segments after internal stress release via open angle method from Liu and Fung [1988] . Different sample positions have been analysed, A - anterior, P - posterior, I - inside, O - outside.	53
3.2	(a) Setup for 3D scan using the ATOS-system (GOM, Germany) from Solsi-CAD (Woippy, France), (b) sample in vertical holding system.	55
3.3	Sample positioning and setup for MRI acquisition.	56
3.4	Experimental loading protocol; the number of test cycles depends on the loading frequency (0.01 Hz/0.1 Hz/1 Hz), the related preload is presented in Table 3.1.	57

3.5	(a) Experimental setup for local spherical compression tests, (b) close-up to the TMJ disc sample.	60
3.6	Lateral, central and medial test sites of local spherical compression tests. Shown is the superior view of a left TMJ disc.	61
3.7	Force as a function of displacement for a compression test of the load cell with the calculated load cell stiffness k_m of 18.04 N/mm.	62
3.8	(a) Graphite pattern on TMJ disc sample before hole perforation, (b) site of hole drilling. A \varnothing 8mm specimen was taken from disc's central area. (c) Cylindrical coordinate system used to evaluate results.	64
3.9	Sketch of superoinferior view of hole drilling specimen, with indication of thickness measurement points.	65
3.10	(a) Obtained scans from condyle and disc surfaces as well as thickness measurements between them using GOM Inspect software. (b) Location of measurement points for thickness evaluation on anterior , central and posterior disc area. (c) Thickness measurements using CloudCompare software; for the sample shown the average thickness (\pm STD) is: 2.30 ± 0.53 mm. The grey areas were not included in the thickness measurement.	67
3.11	Measurement of disc curvature estimated by a cylinder.	69
3.12	(a) MRI sagittal cut through middle of the TMJ disc sample. [-] represents sections of thickness measurements and [- -] the transversal plane shown in (b) transversal cut highlighting the inner microstructure of the TMJ disc [Tappert et al., 2018a].	69
3.13	Experimental force - displacement curves obtained from one representative sample at the central test site using different compression tool radii R and loading frequencies f (a)-(e). The first three loading cycles for each test and the last cycle are shown, the latter corresponds to the 5 th , 25 th and 250 th cycle for loading frequencies 0.01 Hz, 0.1 Hz and 1 Hz.	72
3.14	Example of maximal occurring forces per loading cycle over experimental time for one representative TMJ disc sample during local compression tests on samples central site using a sphere with radius 1.75 mm at different loading frequencies f (a) - (c).	73
3.15	Energy loss representing the hysteresis as function of loading cycle for local compression tests of central site of one representative sample using a sphere of radius 1.75 mm at frequencies f (a) - (c).	73
3.16	Average (-) and standard deviation (- - STD) of maximal measured forces as function of experimental time using a compression tool of 1.75 mm radius for different loading frequencies f (a) - (c), (n=18).	75
3.17	Average (n=18) of maximal measured forces as function of experimental time for the three test frequencies f for different compression tool radii R (a)-(c).	76
3.18	Average (-) (\pm standard deviation (- - STD)) of energy loss representing the hysteresis for all spherical compression tests (n=18) using a sphere of radius 1.75 mm at different frequencies f (a) - (c).	77
3.19	Example for relaxation phase at the end of loading cycles at central site of one representative sample using a sphere with radius 1.75 mm at different loading frequencies f (a)-(c), including exponential fitting to determine characteristic relaxation time τ	80

3.20	Average (x) (\pm STD (- -)) relaxation time for spherical compression tests (n=18) using a sphere of radius 1.75 mm at different frequencies f (a)-(c), including exponential fitting to determine characteristic relaxation time τ .	80
3.21	Average of maximum forces (n=6) during first loading phase on the three test sites using a compression tool of radius (a) 0.875 mm, (b) 1.75 mm and (c) 3.0 mm at the three loading frequencies. Error bars indicate the standard deviation.	81
3.22	Force - displacement curves of repeatability tests showing the first and the last loading cycle for the same test on the first and the following day of sample testing, (a) example of a good repeatability (181212_E4 and 181213_E10), (b) example of poor repeatability (181213_E14 and 181214_E19), (c) shifted force-displacement curve from example (b) to highlight influence of initial test conditions. The tests were conducted on sample's central site at 0.1 Hz using the compression tool of 3 mm radius.	83
3.23	Example of the hole drilling specimen from sample 6 (181214) for different time steps of the experiments; 1 min, 30 min and 50 min.	84
3.24	Concept of backward approach to reach internal stress $\sigma^{internal}$ and strain $E^{internal}$.	85
3.25	Example of strain field magnitude obtained on one hole drilling specimen (181130).	86
3.26	(a) Radial E_{rr} and (b) tangential $E_{\theta\theta}$ average strain fields as function of time obtained on one hole drilling specimen (181130), with exponential fitting highlighting characteristic times τ and theoretical <i>in vivo</i> internal strains E^∞ .	87
3.27	(a) Radial E_{rr} and (b) tangential $E_{\theta\theta}$ average strain fields as function of normalised radius.	88
4.1	Finite element model of Creuillot [2016] (adapted), including the mandible, temporal bone, maxilla, temporomandibular joint discs and muscle representation.	92
4.2	Definitions of variables $F_{contact}$ and $d_{contact}$ for stress-strain curve construction.	95
4.3	Example of (a) a post-processed TMJ disc 3D geometry obtained from optical 3D scans and (b) TMJ disc's 3D mesh. The disc is meshed with hexahedral elements, including a bias mesh in the central zone, as shown in the zoom. For the surrounding tissue tetrahedral elements were chosen.	98
4.4	Assembly of 3D simulation including three parts; the spherical compression tool as a rigid body, the TMJ disc sample and the rigid support.	99
4.5	Examples of raw stress-strain ($\sigma^* - \epsilon^*$) data for tests on samples central site using compression tools of radii (a) $R = 3$ mm and (b) $R = 0.875$ mm depicting the noisy beginning of the stress-strain curves caused by the load cell's accuracy.	100
4.6	Stress - strain ($\sigma^* - \epsilon^*$) curves for three exemplary tests on samples central site using compression tools of different radii R (a) - (c), including hyper-elastic fitting using a two-term Ogden model with four fitting parameter μ_1 , α_1 , μ_2 , α_2 and the associated determination coefficient R^2 . (d) depicts the summary of the previous presented stress-strain curves.	101

4.7	Stress - strain ($\sigma^* - \epsilon^*$) curves for three test sites on one sample; (a) central, (b) medial, (c) lateral site using the big compression tool (radius $R = 3$ mm), including hyperelastic fitting using a two-term Ogden model with four fitting parameter $\mu_1, \alpha_1, \mu_2, \alpha_2$ and the associated determination coefficient R^2	103
4.8	Sketch of TMJ disc with enveloping and internal layer and three spherical compression tools (green, red, blue), each affecting a different depth and therefore a different TMJ disc sample layer.	103
4.9	Stress-strain curve from test on samples central site using a compression tool of radius 3 mm and corresponding fitting of neo-Hookean (nH), Mooney-Rivlin (MR), one- and two-term Ogden model. Regarding the coefficient of determination R^2 and the development of the fitting curve, it becomes obvious that the two-term Ogden model suits best to fit experimental results.	106
4.10	(a) Strain field, (b) stress and (c) von Mises stress in the sagittal plane under the compression tool at its maximum displacement into the temporomandibular joint disc.	108
4.11	(a) Contact pressure, (b) contact status highlighting the establishment of contact between the compression tool and the TMJ disc surface and (c) von Mises stress at the tool's maximum displacement on the TMJ discs superior surface.	109
4.12	Reaction force measured on the compression tool as function of its displacement.	110
4.13	(a) Stress-strain curve from two consecutive loading phases of uniaxial tensile test of TMJ disc specimen in anteroposterior test direction. The moduli (E_1, E_2) were identified for the last percent of strain [Tappert et al., 2018b]. (b) Stress-strain curve for first loading phase of a local spherical compression test conducted using a sphere of 3 mm radius with associated modulus E_{load} and hyperelastic two-term ($\alpha_1, \alpha_2, \mu_1, \mu_2$) Ogden model.	113
C.1	Machine's displacement - time curve at a frequency of 0.01 Hz.	132
C.2	Machine's force - time curve at a frequency of 0.01 Hz.	132
C.3	Machine's displacement - time curve at a frequency of 0.01 Hz, detailed view.	133
C.4	Machine's displacement - time curve at a frequency of 0.1 Hz.	133
C.5	Machine's force - time curve at a frequency of 0.1 Hz.	133
C.6	Machine's displacement - time curve at a frequency of 1 Hz.	133
C.7	Machine's force - time curve at a frequency of 1 Hz.	133
C.8	Data base structure of experimental data.	134
C.9	Thickness measurements of three samples using CloudCompare software; the average thicknesses (\pm STD) are the following; (a) 2.32 ± 0.56 mm, (b) 2.43 ± 0.58 mm. The grey areas were not included in the thickness measurement.	135
C.10	Experimental force - displacement curves using a compression tool of 3 mm radius testing the samples central site for different loading frequencies, (a) 0.01 Hz, (b) 0.1 Hz and (c) 1 Hz.	136
C.11	Experimental force - displacement curves using a compression tool of 1.75 mm radius testing the samples central site for different loading frequencies, (a) 0.01 Hz, (b) 0.1 Hz and (c) 1 Hz.	137

C.12	Experimental force - displacement curves using a compression tool of 0.875 mm radius testing the samples central site for different loading frequencies, (a) 0.01 Hz, (b) 0.1 Hz and (c) 1 Hz.	138
C.13	Average (-) and standard deviation (- -) of maximal measured forces as function of experimental time using a compression tool of 3 mm radius for different loading frequencies, (a) 0.01 Hz, (b) 0.1 Hz and (c) 1 Hz, (n=18). .	140
C.14	Average (-) and standard deviation (- -) of maximal measured forces as function of experimental time using a compression tool of 0.875 mm radius for different loading frequencies, (a) 0.01 Hz, (b) 0.1 Hz and (c) 1 Hz, (n=18).	141
C.15	Average (-) (\pm standard deviation (- -)) hysteresis for all spherical compression tests (n=18) using a sphere of radius 3 mm at frequencies (a) 0.01 Hz, (b) 0.1 Hz and (c) 1 Hz.	143
C.16	Average (-) (\pm standard deviation (- -)) hysteresis for all spherical compression tests (n=18) using a sphere of radius 0.875 mm at frequencies (a) 0.01 Hz, (b) 0.1 Hz and (c) 1 Hz.	144
C.17	Strain field magnitude obtained on hole drilling specimen, (a) 181206, (b) 181207, (c) 181213 and (d) 181214.	145
C.18	Radial and tangential average strain fields as function of time obtained on hole drilling specimen (a) 181206 and (b) 181207, with exponential fitting highlighting characteristic times τ and theoretical <i>in vivo</i> internal strains E^∞	146
C.19	Radial and tangential average strain fields as function of time obtained on hole drilling specimen (a) 181213 and (b) 181214, with exponential fitting highlighting characteristic times τ and theoretical <i>in vivo</i> internal strains E^∞	147
D.1	Representative stress-strain curves for local spherical compression test on the discs central site, using a compression tool of 3 mm radius at a frequency of 0.01 Hz and two-term Ogden model fitting.	150
D.2	Representative stress-strain curves for local spherical compression test on the discs lateral site, using a compression tool of 3 mm radius at a frequency of 0.01 Hz and two-term Ogden model fitting.	151
D.3	Representative stress-strain curves for local spherical compression test on the discs medial site, using a compression tool of 3 mm radius at a frequency of 0.01 Hz and two-term Ogden model fitting.	152
D.4	Representative stress-strain curves for local spherical compression test on the discs central site, using a compression tool of 1.75 mm radius at a frequency of 0.01 Hz and two-term Ogden model fitting.	154
D.5	Representative stress-strain curves for local spherical compression test on the discs medial site, using a compression tool of 1.75 mm radius at a frequency of 0.01 Hz and two-term Ogden model fitting.	155
D.6	Representative stress-strain curves for local spherical compression test on the discs lateral site, using a compression tool of 1.75 mm radius at a frequency of 0.01 Hz and two-term Ogden model fitting.	156
D.7	Representative stress-strain curves for local spherical compression test on the discs central site, using a compression tool of 0.875 mm radius at a frequency of 0.01 Hz and two-term Ogden model fitting.	158

D.8 Representative stress-strain curves for local spherical compression test on the discs medial site, using a compression tool of 0.875 mm radius at a frequency of 0.01 Hz and two-term Ogden model fitting. 159

D.9 Representative stress-strain curves for local spherical compression test on the discs lateral site, using a compression tool of 0.875 mm radius at a frequency of 0.01 Hz and two-term Ogden model fitting. 160

List of Tables

2.1	Fitting parameters α and n of dimensionless contact radius a as a function of dimensionless indentation depth δ for all simulated thickness ratios including the corresponding determination coefficient R^2	32
2.2	Fitting results of parameters β and m for curve fitting of dimensionless contact radius a as function of dimensionless compression tool displacement d for all simulated thickness ratios and the corresponding determination coefficient R^2	34
2.3	Resulting constants b_0 and b_1 for fitting of Equation (2.29) to $\delta - d$ curves with associated determination coefficient R^2 for all simulated thickness ratios h	38
2.4	Fitting results of parameter χ for curve fitting of representative stress σ^* as function of representative strain ϵ^* for all simulated thickness ratios and determination coefficient R^2	41
2.5	Summary of material parameter used for different material laws. Section 4.2.2 provides a more detailed description of those models.	45
3.1	Overview of preloads F_{init} for local spherical compression tests, calculated with reference of $F_{init} = 0.0136$ N for a spherical compression tool of 0.875 mm radius.	58
3.2	Overview spherical compression distances for an experimental reference strain of $\epsilon_{exp} = 20\%$ compared also to representative strain ϵ^* and fitting parameter χ according to Chapter 2.	59
3.3	Overview of sample dimensions used during local spherical compression tests (mean \pm standard deviation). Further information regarding the samples are given in the Appendix Table C.1.	61
3.4	Measured thicknesses in the three anatomical regions: anterior, central, posterior from the optical scan depicted in Figure 3.10.a.	66
3.5	Comparison of results from thickness measurements using GOM Inspect and CloudCompare software. Presented are average values (\pm STD) in mm.	68
3.6	Thickness measurement summary of samples used in local spherical compression tests using a micrometre and compression tool (results in mm).	68
3.7	Summary of the dimensions [mm] (mean of three measurements) of the specimen.	85
4.1	Summary of undertaken displacement of compression tools as from the first detection of a force and the first loading phase. Presented are the average values calculated from results presented in the Appendix D (Tables D.1 - D.3, D.4 - D.6, D.7 - D.9).	104

4.2	Average values for two-term Ogden model obtained through fitting to stress-strain curves from test of discs central site using different compression tools.	106
A.1	Max stresses in TMJ disc finite element simulations.	123
A.2	Overview of tensile test conditions used in literature.	124
A.3	Literature overview cyclic compression test on TMJ discs.	125
A.4	Literature overview compression test on TMJ discs.	126
B.1	Overview simulations thickness study, which were carried out using two different Young's moduli (therefore two wallclock times).	127
C.1	Overview sample origin for spherical compression tests.	129
C.2	Overview sample origin for different experiments.	130
C.3	Dimensional data of printed testing cubes.	130
C.4	Imaging parameters for sagittal, transverse and frontal plane acquisition (MSME - multi-slide multi-echo).	131
C.5	Imaging parameters for 3D acquisition.	131
D.1	Results for two-term Ogden fitting for local spherical compression tests on samples central site at 0.01 Hz using a compression tool of size 3 mm. . . .	149
D.2	Results for two-term Ogden fitting for local spherical compression tests on samples lateral site at 0.01 Hz using a compression tool of size 3 mm. . . .	149
D.3	Results for two-term Ogden fitting for local spherical compression tests on samples medial site at 0.01 Hz using a compression tool of size 3 mm. . . .	149
D.4	Results for two-term Ogden fitting for local spherical compression tests on samples central site at 0.01 Hz using a compression tool of size 1.75 mm. . .	153
D.5	Results for two-term Ogden fitting for local spherical compression tests on samples medial site at 0.01 Hz using a compression tool of size 1.75 mm. .	153
D.6	Results for two-term Ogden fitting for local spherical compression tests on samples lateral site at 0.01 Hz using a compression tool of size 1.75 mm. .	153
D.7	Results for two-term Ogden fitting for local spherical compression tests on samples central site at 0.01 Hz using a compression tool of size 0.875 mm. .	157
D.8	Results for two-term Ogden fitting for local spherical compression tests on samples medial site at 0.01 Hz using a compression tool of size 0.875 mm. .	157
D.9	Results for two-term Ogden fitting for local spherical compression tests on samples lateral site at 0.01 Hz using a compression tool of size 0.875 mm. .	157

Motivation and thesis organisation

Eating, drinking, talking - all these activities require the motion of the mandible - the lower jaw - which can be realised, among other joint's elements, thanks to the temporomandibular joint (TMJ). In contrast to other joints of the human body, the two TMJs work in parallel being connected via the mandible. The temporomandibular joint disc is a crucial part of this joint. This fibrocartilagenous tissue ensures congruency between the fossa and the mandible's condyle while moving between these bony structures and distributing forces. In this way, the TMJ disc enhances a smooth jaw movement.

Various pathologies can affect the temporomandibular joint with a non-negligible prevalence which include joint, muscle and disc disorders, leading to pain and masticatory dysfunction. Disc disorders can severely constrain patients well being. In order to find solutions that can substitute the TMJ disc as a treatment for disc disorders, it is necessary to understand and describe the TMJ disc's biomechanical behaviour.

However, characterisation of soft biological tissues is not straightforward, mainly due to their micro-structure similar to composite materials. Indeed, the TMJ disc's biochemical composition consists of different cell types and an extracellular matrix with the latter playing a role in its non-linear, viscous and anisotropic behaviour. Since the TMJ's movement is complex, the TMJ disc undergoes various types of stress states such as tension, compression or shear.

One of the goals of this dissertation is to create and enrich a database providing mechanical behaviour of the disc. To reach this aim, disc samples have to be tested under the most possible physiological conditions, including a physiological positioning of the sample as well as leaving the TMJ disc sample in its integrity. This is of great importance since the TMJ disc is the site of internal stresses due to fibre orientation on the one hand and connection to surrounding joint tissues, as the capsule, on the other hand. Releasing these internal stresses by cutting specimen, for instance for tensile or unconfined compression tests, might strongly affect experimental results. For these reasons, an experimental characterisation through local spherical compression was favoured in this work. However, use of local spherical compression tests on the TMJ disc raises several difficulties: the samples are thin, undergoing large deformation while showing non-linear behaviour.

The manuscript is organised as follows. Chapter 1 summarises basic knowledge concerning the TMJ and it's disc including anatomy and physiology.

Most analytical models of local spherical compression and spherical indentation do not consider a finite sample thickness. That is why an analytical approach of local spherical compression for thin layers is considered in Chapter 2.

With knowledge of the disc's physiology and theory of local spherical compression of thin layers, sample characterisation through local spherical compression can be carried out. For obvious ethical reasons, the *in vivo* study of the disc's behaviour is difficult to conceive. Before using rare healthy human samples, an experimental procedure should be designed that ensures first consistent results and sound techniques. For these reasons,

porcine samples were used in this study. Local spherical compression experiments allow testing an entire and intact TMJ disc on different sites. The experimental setup includes a testing chamber filled with physiological solution and a 3D printed condyle on which the samples can be placed in a natural position. The TMJ disc shows furthermore a complex geometry, being relatively thin in the central part and thicker on the outer regions. This leads to the necessity to study the disc geometry as well, in order to accurately analyse experimental results to obtain the relevant stress-strain curves. Chapter 3 is dedicated to this task.

Combining results from Chapters 2 and 3, the stress-strain curves are finally constructed in Chapter 4. Fitting hyperelastic laws to these curves for material parameter identification and three-dimensional finite element simulations of local spherical compression tests on a TMJ disc sample are further results elaborated in this Chapter. To reach the objective of this study, namely to characterise experimentally and numerically the TMJ disc behaviour, experimental and model results (obtained using the finite element method) are compared.

Finally, the main findings of this study are summarised and the way forward for future research is given.

Chapter 1

Introduction to the temporomandibular joint and problem definition

Contents

1.1	The temporomandibular joint and its disorders	4
1.2	The temporomandibular joint disc	5
1.2.1	Biomechanics of the temporomandibular joint disc	9
1.2.2	Biomechanical testing of the temporomandibular joint disc . . .	10
1.2.2.1	Tensile tests	11
1.2.2.2	Compression tests	13
1.3	Objective and strategy	17

1.1 The temporomandibular joint and its disorders

Essential daily activities such as speaking, eating and drinking would not be possible without the temporomandibular joint (TMJ). The TMJ allows complex mandibular motions, while it is also damping the mechanical loads. Its location within the skull and its anatomy are presented in Figure 1.1 from the work of [Willard et al. \[2011\]](#). The bones associated with the TMJ are the condyle of the mandible and two zones of the temporal bone; the glenoid fossa and the articular eminence. The surfaces of the bones are covered with fibrocartilage [[Stanković et al., 2013](#); [Willard et al., 2011](#)]. Furthermore, the temporomandibular joint disc, another fibrocartilage is positioned between the temporal bone and the condyle. The whole complex is surrounded by a capsule, a connective tissue, forming a synovial joint.

The degrees of motion provided by the TMJ are complex, as they include translatory and rotational movements [[Fernandez et al., 2011](#)]. Smooth movements of the mandible with respect to the skull are ensured by the temporomandibular joint disc. When the condyle is moving, the TMJ disc slides between the two articular surfaces, providing a congruency between them and acting as lubricator, in addition to the synovial fluid [[Chen and Xu, 1994](#)]. The contours of the fossa, the articular eminence and the surrounding ligaments constrain the TMJ disc displacement [[Chen and Xu, 1994](#)]. However, malfunction of one or several joint components can severely affect patients well-being.

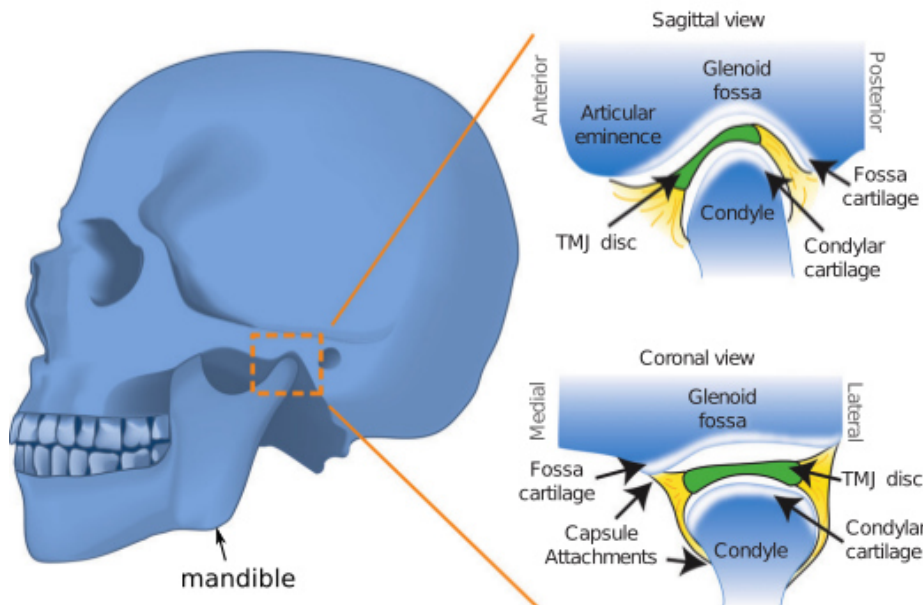


Figure 1.1 – Location of the TMJ in the skull with sagittal and frontal view of the articulation, modified from the work of [Willard et al. \[2011\]](#).

Pathologies that can affect the TMJ include osteoarthritis, rheumatoid arthritis, benign and malignant tumours, wear of cartilage and muscle fatigue due to clenching [[Willard et al., 2011](#)]. TMJ disc displacement is another pathology commonly affecting the TMJ. It is manifested through temporary or permanent dislocation of the TMJ disc in relation to the condyle, often associated with an anterior positioning of the disc [[Detamore and Athanasiou, 2003a](#)]. Bruxism, the clenching of teeth, can furthermore lead to wear not only of the teeth but also of the TMJ disc. With a prevalence between 5–20% [[NIH, 2017](#), [Gray and Al-Ani 2011](#)], TMJ disorders concern an important part of the population. To

compare with, in Europe the prevalence of diabetes was around 7.3% [WHO, 2016] in 2014. Therefore, the investigation of this joint is paramount for maxillofacial therapies. Since the TMJ disc plays a major role in the joint's function, especially in load distribution within the joint, it appears as a crucial element to understand joint physiology and pathologies leading to provision of therapies for patients and advanced computer models to support medical research. In order to achieve this, further understanding of the TMJ disc is needed.

1.2 The temporomandibular joint disc

The temporomandibular joint disc has a sophisticated shape (see Figure 1.2) since it needs to be conform with the bony structures associated with the TMJ. Moreover, it is a mobile part of the joint attached to surrounding tissue and the joint's capsule. It serves as a stress-distributor and absorber that is why its function is highly related to its shape. As a living structure, the TMJ disc consists of different cell types and an extracellular matrix (ECM), which support its function. This section presents therefore the disc's morphology, its biochemical composition and biomechanical behaviour.

The temporomandibular joint disc from external shape to function

Figure 1.2.a depicts the gross morphology of human and porcine TMJ discs, which resemble in overall shape and dimensions. However, one can observe that human TMJ discs are slightly smaller than porcine ones. The human TMJ disc measures approximately 19 mm in mediolateral direction and 13 mm in anteroposterior direction [Detamore and Athanasiou, 2003b; Willard et al., 2011]. The mean dimensions of porcine discs are presented in Figure 1.2.b. Furthermore, Figure 1.2.b presents indication of the TMJ disc anatomical zones in transversal plane. In anteroposterior direction three zones are defined: the anterior and posterior bands with the intermediate zone between [Willard et al., 2011]. The intermediate zone in turn can be subdivided in mediolateral direction in medial, central and lateral regions [Willard et al., 2011]. Due to the oval biconcave shape [Detamore and Athanasiou, 2003a], those zones are not uniform in thickness; varying between 1 to 4 mm in humans, with the intermediate zone being the thinnest area [Detamore and Athanasiou, 2003a].

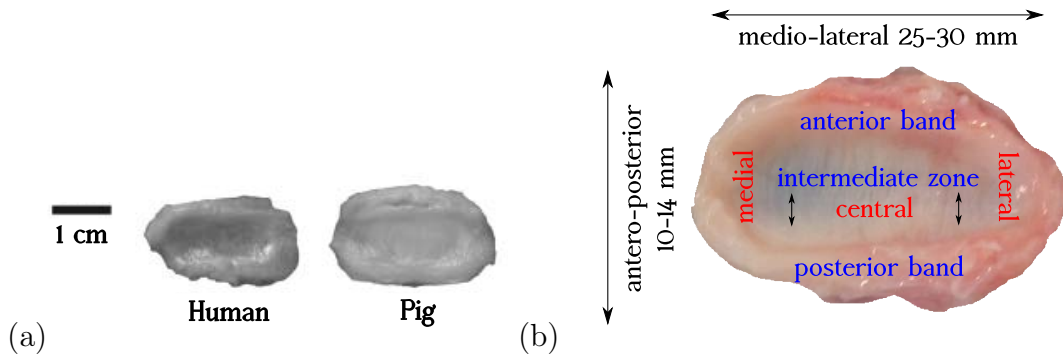


Figure 1.2 – (a) Comparison of gross morphology of human and porcine TMJ discs (adapted from Kalpakci et al. [2011]); (b) Example of a porcine TMJ disc indicating anatomical zones and approximate dimensions. Those zones have been defined regarding structural composition variation of the tissue that are related to its biocomposite character. The arrows indicate anteroposterior fibre orientation within the central region.

The arrows in the central zone in Figure 1.2.b illustrate the anteroposterior orientation of the collagen fibres while concentric orientation has been observed in the outer ring [Detamore and Athanasiou, 2003b]. Therefore, the TMJ disc's tissue can be considered as a composite like material.

The temporomandibular joint disc - a biocomposite

Due to its function as a stress absorber, the TMJ disc is neither innervated nor vascularised. Nutrient supply is therefore realised by the joint's interstitial fluid and thanks to the biphasic disc's composition (solid and fluid phases) with 66 – 80% of water content [Detamore and Athanasiou, 2003a; Kuo et al., 2010]. The extracellular matrix is the solid phase, mainly composed of collagen fibres type I. This organised structure of fibre runs anteroposteriorly in the intermediate zone (see Figure 1.2.b) and is circumferentially aligned in the periphery [Detamore and Athanasiou, 2003b; Fazaeli et al., 2016; Mills et al., 1994; Wright et al., 2016]. The fibre distribution is depicted in microscopy images in Figure 1.3, which also highlights the similarities in collagen distribution between human and porcine TMJ discs.

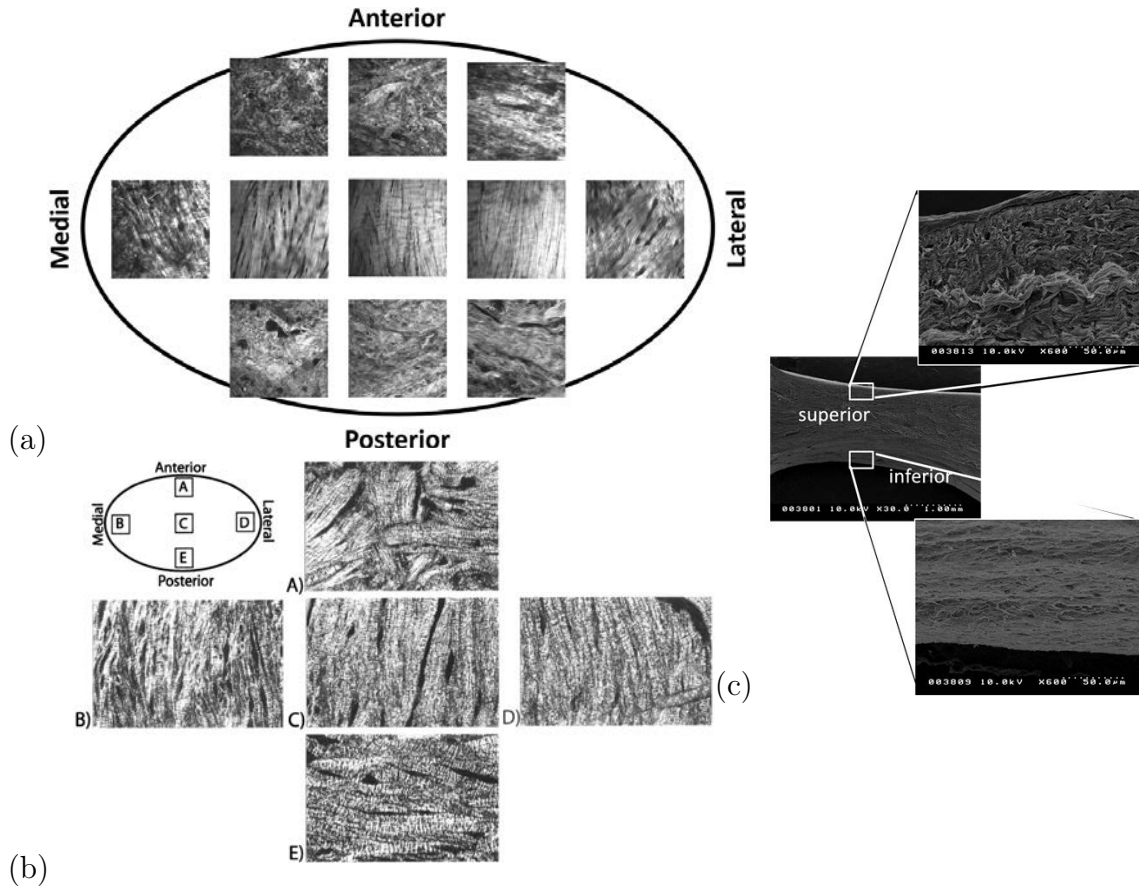


Figure 1.3 – (a) Second-harmonic generation microscopy images showing collagen fibre distribution within the human TMJ disc [Wright et al., 2016]; (b) Polarized light microscopy images showing collagen fibre distribution within the porcine TMJ disc [Detamore and Athanasiou, 2003b] (400x). Both images highlight the anteroposterior fibre orientation within the central region and the circumferential alignment in the outer disc areas. (c) Scanning electron microscopy image of porcine TMJ disc taken from Juran et al. [2015], showing that on the superior surface the disc is subdivided in different zones, whereas the inferior side has a more uniform distribution of fibres.

In superoinferior direction, a distinct thin layer can be observed close to both surfaces. It is described as containing perpendicular orientated collagen fibres in human [Minarelli et al., 1997] and randomly orientated thin fibrils in mice [Chandrasekaran et al., 2017]. In pigs, Juran et al. [2015] found a structural difference between the superior surface, which occurs to have several segments of layers of collagen fibres in contrast to the inferior surface, which is more uniform (Figure 1.3.c).

Another component of the extracellular matrix are proteoglycans. These glycoproteins consist of a core protein with glycosaminoglycan (GAG) chains [Detamore and Athanasiou, 2003a]. GAGs are polysaccharide chains that contain at least one negatively charged side group [Almarza and Athanasiou, 2004; Willard et al., 2011], leading to hydrophilic properties of these molecules. GAG content is about 0.5 – 3.2% of the TMJ disc’s dry weight, depending on the disc’s region. The collagen content varies between 68 – 80% of the dry weight [Almarza et al., 2006; Fazaeli et al., 2016; Kuo et al., 2010]. Whereas no difference was found on superior and inferior surface, the posterior band has significantly less GAG content than the intermediate zone and the anterior band. Also, the medial area was found to have a significantly higher GAG concentration than the central and lateral areas [Almarza et al., 2006]. In anteroposterior direction, the intermediate zone has significantly greater concentration of collagen than the anterior and posterior bands, in mediolateral direction the central area has significantly higher collagen concentration than lateral area [Almarza et al., 2006]. Kuo et al. [2010] could not find a significant difference of total collagen and GAG content per disc region.

GAG and collagen distribution in histological specimen of transversal cuts of half a TMJ disc are shown in Figure 1.4 and sagittal cuts in Figure 1.5. The haematoxylin eosin saffron (HES) staining shows in yellow the distribution of collagen fibres (mainly type I, Figure 1.4.a), while the Masson’s trichrome staining shows collagen in blue (Figure 1.4.b). Stainings of Figure 1.4.a and 1.4.b depict that the central and lateral zones of the shown layer have a high concentration of collagen fibres. The anterior and posterior bands contain more proteoglycans. These latter are red stained with Safranin O that depicts also occasional occurrence of glycosaminoglycans within the disc’s central zone (Figure 1.4.c).

In the sagittal cuts from Figure 1.5, the heterogeneity in the disc’s component distribution through its thickness can be observed. Furthermore, in superoinferior direction, different zones can be distinguished; two zones close to the superior and inferior surfaces with an approximate thickness of 0.5 mm enveloping an inner zone. These two zones can clearly be detected by the stains, indicating a difference in tissue component density.

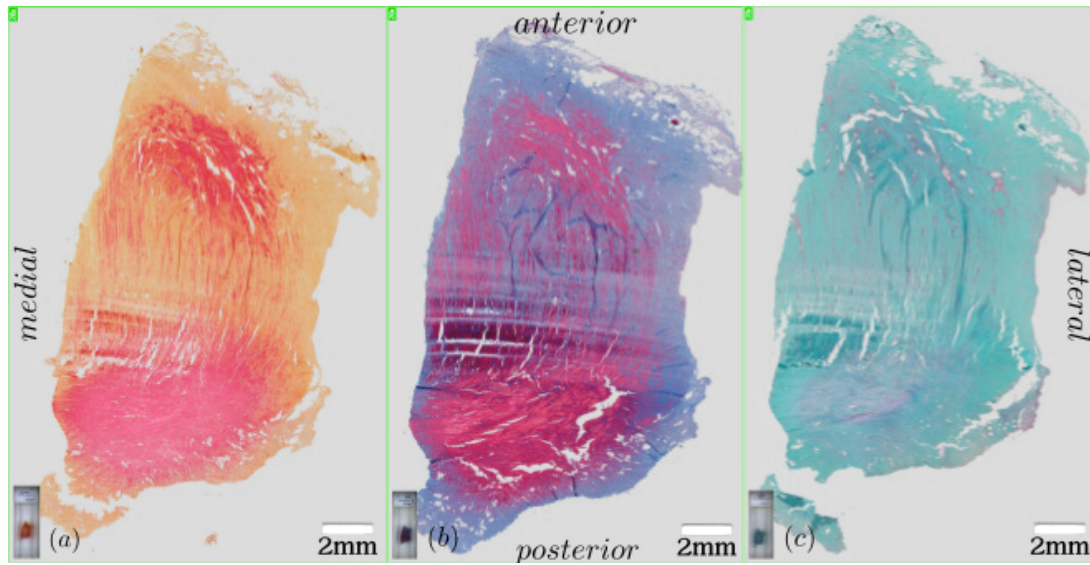


Figure 1.4 – Histology images of transversal cuts: (a) HES (yellow: collagen), (b) Masson's trichrome (blue: collagen) and (c) Safranin O staining (red: GAG) (images obtained through cooperation with the BIOS (Biomatériaux et inflammation en site osseux) laboratory, Université de Reims).

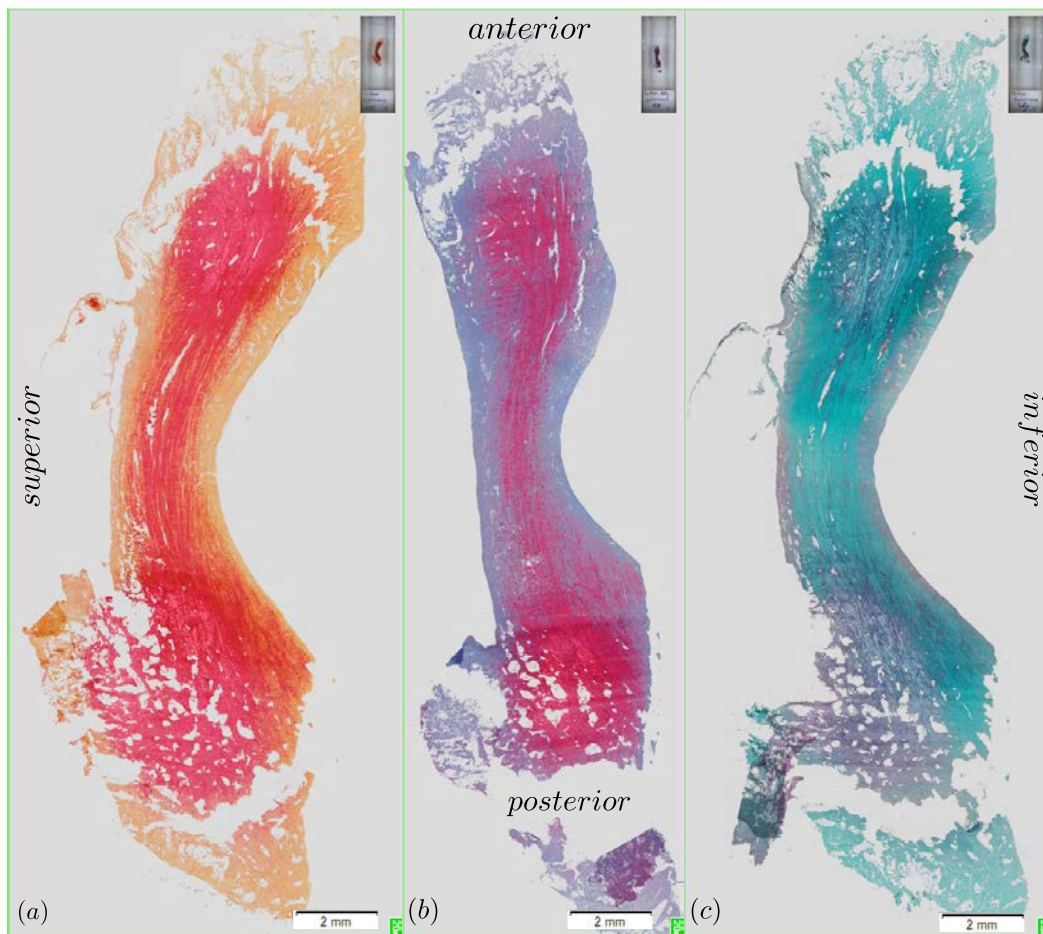


Figure 1.5 – Histology images of sagittal cuts: (a) HES (yellow: collagen), (b) Masson's trichrome (blue: collagen) and (c) Safranin O staining (red: GAG) (images obtained through cooperation with the BIOS laboratory, Université de Reims).

The composition of the TMJ disc's ECM is functional regarding the biomechanical loadings the TMJ is exposed to. In fact, collagen fibres and their alignment play an important role in TMJ disc's tensile properties [Willard et al., 2011], while GAGs influence the tissues compressive behaviour [Tanaka and van Eijden, 2003]. The histological images presented above as well as the conclusions of the work of Willard et al. [2011] and Tanaka and van Eijden [2003] lead to the hypothesis that the TMJ discs are macro-heterogeneous structures from the mechanical point of view, which has an influence on the disc's biomechanics.

1.2.1 Biomechanics of the temporomandibular joint disc

As mentioned in Section 1.2, the TMJ disc provides a congruency between the bones associated with the joint. In motion, the condyle conducts a rotational and translational movement, sliding from the glenoid fossa to the articular eminence (see Figure 1.6), moving together with the disc. The superior and inferior parts of the disc undergo different types of motion, while on the superior side predominately translation occurs, rotation is the major movement on the inferior space [Kim et al., 2003]. On the TMJ disc, this physiological motion causes three types of mechanical loading that occur during daily activities: compression, tension and shear [Hylander, 1979; Tanaka and van Eijden, 2003]. They can be static, for instance during clenching, or dynamic while chewing. Not only the motion of the TMJ disc can induce stresses to the tissue, similar to other biological structures internal strains and stresses occur within the TMJ disc as a result of the morphology and anatomy [Nelson, 2014; Tappert et al., 2018b].

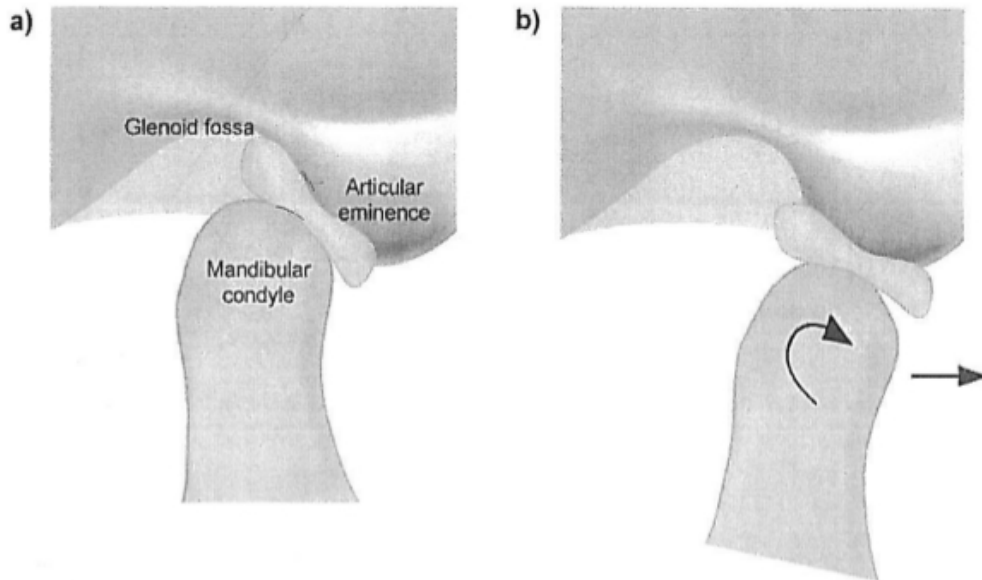


Figure 1.6 – Disc movement while jaw opening, a) during mouth occlusion and b) during mouth opening; the arrows are indicating the condyle's rotation and translation [Athanasiou et al., 2009].

Providing congruency is not the only purpose of the TMJ disc. It is crucial for load distribution and stress absorption during joint loading [Beek et al., 2001; Nickel and McLachlan, 1994; Tanaka et al., 1999]. Forces acting on the condyle were measured in *in vitro* studies reaching up to 210 N while different muscle forces were simulated

[Throckmorton and Dechow, 1994]. Using instrumented prosthesis, bite forces up to 35 N in baboons were determined [Hohl and Tucek, 1982]. Forces occurring in the mandible and the condyle can be measured, for example through strain gauges [Hylander, 1979]. *In vivo*, those measurements demand complicated protocols and ethical approval. On the disc, those measurements are even more difficult to conceive, due to its soft and hydrated nature. For this reason, simulations are carried out in order to estimate loads and resulting stresses on the TMJ disc, as depicted in Figure 1.7. Stresses occurring on the TMJ disc during jaw opening and closing, mastication and clenching vary between 0.9-13 MPa and were accessed through finite element analysis [Alvarez Areiza, 2014; Creuillot, 2016; Hattori-Hara et al., 2014; Hirose et al., 2006; Jaisson et al., 2012; Mori et al., 2010; Savoldelli et al., 2012], see Appendix A.1.

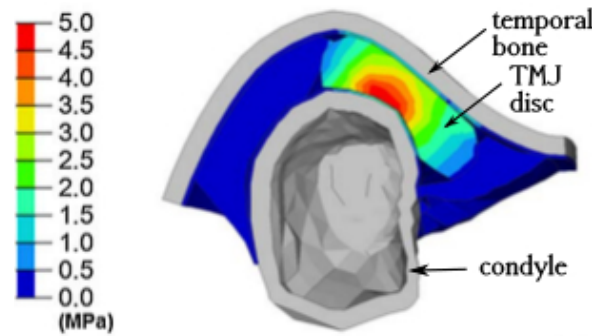


Figure 1.7 – Von Mises stress distribution at the beginning of a clenching process obtained by Mori et al. [2010].

However, for finite element simulations material laws need to be defined in order to accurately describe the TMJ disc behaviour. To achieve this, the disc can be studied *ex vivo* to investigate its mechanical constitutive relationships.

1.2.2 Biomechanical testing of the temporomandibular joint disc

As other biomaterials, the temporomandibular joint disc can be investigated using tensile or compression tests. The main idea of material testing remains the same as for engineering materials, however, experimental setup and protocol should be adapted to biological samples.

Since tests *ex vivo* change the physiological environment of biological samples, it is desirable to provide physiological testing conditions as far as possible. This includes a test environment in which the disc is exposed to a physiological solution at around 37°C to mimic physiological condition of synovial fluid and body temperature [Detamore and Athanasiou, 2003a]. Since experiments on human tissue require higher ethical standards compared to tests on animal ones, frequently experiments are conducted on porcine, bovine or ovine samples.

Test protocols for biological samples commonly include a preconditioning phase, which is generally not examined [Allen and Athanasiou, 2006; Barrientos et al., 2016; Calvo-Gallego et al., 2017; Commisso et al., 2016; Detamore and Athanasiou, 2003b; Fazaeli et al., 2016; Kuo et al., 2010; Gutman et al., 2018; Kalpakci et al., 2011; Matuska et al., 2016; Tanaka et al., 1999, 2003a,b; Wright et al., 2016]. This preconditioning consists of cyclic loading and unloading phases and serves the creation of equal loading history for each sample.

Depending on which tissue behaviour is intended to be studied, different mechanical tests can be conducted. The simplest analysis is based on the linear elastic theory, however, the disc cannot be accurately described using a linear model. Its biochemical composition (see Section 1.2), especially the high amount of water induces a viscous behaviour (Figure 1.10.b). Protocols analysing viscous material behaviour include cyclic (successive loading and unloading phases), creep and relaxation tests for both tensile and compression tests [Allen and Athanasiou, 2006; Barrientos et al., 2016; Comisso et al., 2016; Fernandez et al., 2011; Koolstra et al., 2007; Tanaka et al., 1999, 2003b].

Due to fibre orientation, the distribution of GAG and internal stresses within the TMJ disc, different methods to obtain test samples were established. Either the entire disc sample is tested [Angelo et al., 2016; Barrientos et al., 2016; Beatty et al., 2001; Beek et al., 2001; Fazaeli et al., 2016; Tappert et al., 2017], or tensile and compressive specimen are cut out of the disc [Detamore and Athanasiou, 2003b; Fernandez et al., 2011; Lumpkins and McFetridge, 2009; Matuska et al., 2016; Tanaka et al., 1999, 2003b; Tappert et al., 2018b]. The former method allows characterisation of the TMJ disc without releasing internal stresses, the latter - especially for tensile tests, leads to the analysis of its anisotropic behaviour.

During compression tests of entire TMJ disc samples, the whole sample can be compressed and evaluated on a global scale [Barrientos et al., 2016], since the complete sample is solicited. In contrast, during local compression tests on different sites of the sample, the analysis can be conducted at a local scale [Beek et al., 2001; Fazaeli et al., 2016; Tappert et al., 2017].

In the following, tensile and compression tests carried out on TMJ disc samples and specimen are presented.

1.2.2.1 Tensile tests

During tensile tests, the tissue sample is generally pulled in uniaxial direction, though biaxial tests are also possible (e.g. [Arroyave G. et al., 2015]).

Anisotropy

The TMJ disc contains fibres which are not orientated in the same direction. Therefore, during uniaxial tensile tests, samples from different anatomical directions and TMJ disc regions are required. In this way, the disc's anisotropic biomechanical behaviour can be studied. Figure 1.8 depicts fibre orientation from specimen of different orientations. Tensile test specimen can be obtained by cutting tissue's specimen out of the intact disc sample or by pulling the complete disc. During the latter, the entire disc samples are fixed with grips so that either mediolateral or anteroposterior direction can be tested [Angelo et al., 2016; Beatty et al., 2001]; else strip like specimen are obtained as depicted in Figure 1.8 [Detamore and Athanasiou, 2003b; Matuska et al., 2016].

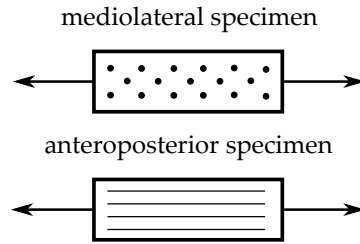


Figure 1.8 – Sketch indicating fibre orientation within tensile test specimen in mediolateral and anteroposterior test direction.

Results obtained from those tests are force-displacement curves from which stress-strain curves are built enabling the identification of mechanical properties such as Young’s modulus, Poisson’s ratio, ultimate tensile strength as well as toughness [Athanasίου et al., 2009].

Typical stress-strain curves obtained from uniaxial tensile tests show a toe region at the beginning of the test and an almost linear region in which the stress increases quasi proportionally to the strain (see Figure 1.9). For fibrous tissues, the toe region is assumed to be the region in which fibres are not completely aligned and loaded, while this is the case in the linear region [Fung, 1993]. From those type of test results, the elastic modulus can be obtained, concerning a linear elastic material model.

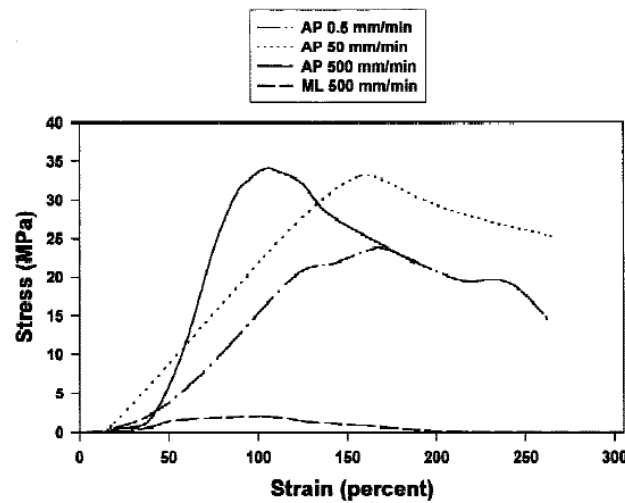


Figure 1.9 – Experimental stress-strain curve from uniaxial tensile test of entire porcine TMJ disc specimen up to failure, in anteroposterior and mediolateral directions with different test velocities obtained by Beatty et al. [2001].

Tensile tests studies on whole TMJ disc specimen found contradictory results regarding properties related to fibre orientation. Beatty et al. [2001] (Figure 1.9) stated the Young’s modulus varying between 2-5 MPa in mediolateral direction and Angelo et al. [2016] obtained an average value of 9.4 MPa. In anteroposterior direction, the Young’s modulus found by Beatty et al. [2001] is higher (25-75 MPa) than in mediolateral direction and higher than the values reported by Angelo et al. [2016] (3.97 MPa in average), who concluded that moduli are lower in anteroposterior direction.

Although studies investigating tensile properties using stripe like samples provide qualitatively different results, they show quantitatively that the tensile properties are region depended. Both Detamore and Athanasίου [2003b] and Matuska et al. [2016] found the

TMJ disc intermediate zone to have the highest tensile properties when tested in antero-posterior direction, [Detamore and Athanasiou \[2003b\]](#) stated 28.6 MPa and [Matuska et al. \[2016\]](#) around 130 MPa. This correlates with the collagen fibres alignment being parallel in anteroposterior direction in the intermediate zone. Tensile properties in mediolateral direction are found also to be region dependent with Young's modulus of around 0.98 MPa in the intermediate zone and 31.8 MPa in the posterior band [[Detamore and Athanasiou, 2003b](#)].

Viscoelasticity

Viscoelastic characterisation of the TMJ disc using tensile tests has been conducted in creep and relaxation tests by [[Tanaka et al., 2002](#)] and [[Gutman et al., 2018](#)].

Incremental stress relaxation tests conducted by [Detamore and Athanasiou \[2003b\]](#) and [Wright et al. \[2016\]](#) revealed typical relaxation of porcine and human tensile specimen. Another viscoelastic characteristic is the strain-rate dependency, which was shown by [Beatty et al. \[2001\]](#). As can be deduced from the tensile tests in anteroposterior direction presented in Figure 1.9, the stress increases faster with increasing strain rate. In dynamic tensile tests [Snider et al. \[2008\]](#) could demonstrate increase of storage and loss moduli with increasing test frequency.

Tensile studies revealed a region dependency of viscoelastic properties as well. [Tanaka et al. \[2002\]](#) conclude that the peripheral regions show a higher tensile stiffness than the central one. In contrast to [Detamore and Athanasiou \[2003b\]](#), who reported higher stiffness of specimen from central and medial region tested in anteroposterior direction. [Gutman et al. \[2018\]](#) found highest tensile moduli in central region and anterior band (around 5 MPa - 6 MPa).

The tensile tests show a high diversity of results, proving that testing soft biological tissues implicates several difficulties such as specimen preparation and fixation. Furthermore, experimental protocols vary in several conditions such as specimen size, test temperature, specimen hydration, preconditioning, strain rates and applied preload. A summary of these conditions is presented in Appendix A.2. It can be concluded that tensile properties are region dependent and anisotropic, however a clear trend cannot be determined by previously discussed findings.

1.2.2.2 Compression tests

Compression tests are divided into different types. During unconfined compression tests the specimen is allowed to expand freely on its lateral side (see Figure 1.10.a), while during confined compression the specimen is constrained laterally. The latter allows therefore also a poro-mechanical characterisation [[Athanasiou et al., 2009](#); [Kuo et al., 2010](#)].

During the classical indentation tests, a force is applied on the sample using a small indenter, leaving an imprint on the sample. This approach is frequently used in hardness tests. Local compression tests also use small tools, compressing the sample locally and leaving or not, a plastic deformation on the sample.

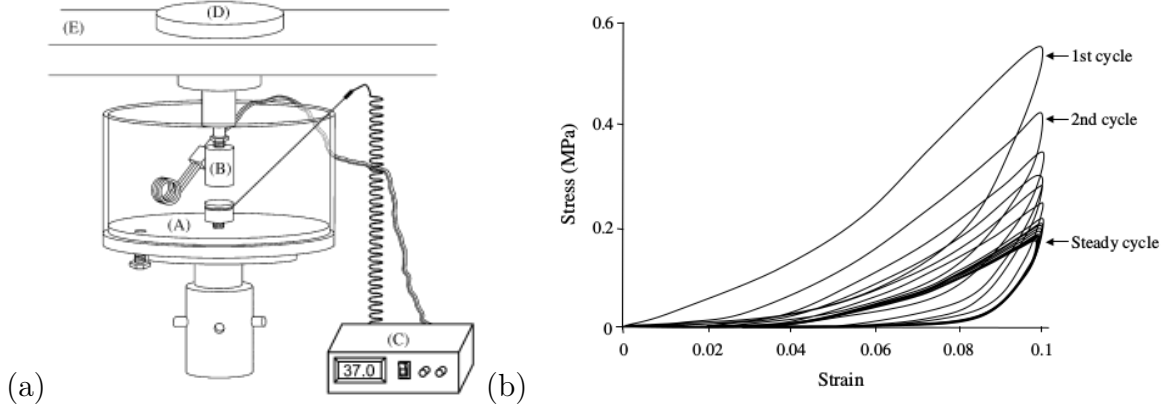


Figure 1.10 – (a) Experimental setup for unconfined compression tests, taken from [Allen and Athanasiou \[2006\]](#). (b) Stress-strain curve from cyclic unconfined compression tests on porcine TMJ disc specimen obtained by [Tanaka et al. \[2003b\]](#). A hysteresis between the loading and unloading phase is evident, as well as steady stress-strain state after several cycles indicating viscoelastic characteristics of the specimen.

It is known that the biochemical composition plays a role in the tissue's behaviour and that the distribution of GAG is not homogeneous throughout the TMJ disc (see Section 1.2). Therefore, the TMJ disc's compressive properties should be examined on various sample sites.

Different studies of confined and unconfined compression have been carried out, including dynamic compressive loading [[Tanaka et al., 2003b](#); [Fernández et al., 2013](#); [Lumpkins and McFetridge, 2009](#)], relaxation tests [[Tanaka et al., 1999](#); [Commisso et al., 2016](#); [Lamela et al., 2011](#)], creep [[Fernandez et al., 2011](#); [Lamela et al., 2011](#)] and strain-rate dependency tests by [Tanaka et al. \[2003a\]](#). Those experiments highlighted the fact that the behaviour of the TMJ disc tissue can vary through loading velocity and loading cycles, location and compression tool used. Moreover, they testify that the discs viscosity results from a coupling between fluid and solid phases.

Viscoelastic behaviour

Similar to tensile test, the viscoelastic characteristics of the TMJ discs can be revealed by different experimental protocols. To highlight the strain-rate sensitivity, [Fernández et al. \[2013\]](#) investigated the dynamic compressive properties of porcine TMJ discs applying sinusoidal compressive strain at different frequencies (0.01-10 Hz). From the obtained results the compressive storage modulus E' , the compressive loss modulus E'' and the loss tangent $\tan \delta$ were determined. E' and E'' increased with increasing frequency through all tested regions. The mean values for E' varied between 20 and 70 kPa depending on region and frequency. The loss tangent $\tan \delta$ decreased for small frequencies and increased for higher frequencies.

The dynamic compression tests revealed a difference between the compressive modulus of the first loading cycles (E_{init}) and during accommodation (E_{SS}), E_{init} being higher than E_{SS} , for all disc regions. This is due to decrease of maximum stress with increasing number of loading cycles as depicted in Figure 1.10.b. Furthermore, this latter highlights a hysteresis between the loading and unloading phase, which decreases with consecutive test cycles. This characteristic was observed on cyclic tests of human TMJ discs by [Beek et al. \[2001\]](#) as well.

[Tanaka et al. \[2003b\]](#) and [Lumpkins and McFetridge \[2009\]](#) also found higher moduli

with increasing testing frequency. However, absolute values of compressive moduli differ between the studies, as can be deduced by cyclic compression tests conducted by [Fazaeli et al. \[2016\]](#), [Lumpkins and McFetridge \[2009\]](#) and [Tanaka et al. \[2003b\]](#). All conducted tests at 1 Hz and 10% strain, however E_{init} in the study of [Fazaeli et al. \[2016\]](#) was lower (0.05-0.15 MPa) than values from [Lumpkins and McFetridge \[2009\]](#) and [Tanaka et al. \[2003b\]](#); ranging between 1.8 MPa and 8 MPa, respectively (Appendix A.3).

Stress relaxation and creep are further viscoelastic characteristics which have been shown among others by [Fazaeli et al. \[2016\]](#), [Lamela et al. \[2011\]](#) and [Tanaka et al. \[1999\]](#).

To sum up, the discs compressive properties increase with increasing loading frequency and decrease with increasing number of loading cycles, pointing out viscoelastic behaviour which could be demonstrated by stress relaxation and creep test as well.

Location sensitivity

[Lumpkins and McFetridge \[2009\]](#) found E_{init} of medial region around 0.5 MPa and lateral 2.3 MPa. [Tanaka et al. \[2003a\]](#) tested only specimen from the central region, announcing E_{init} values between 2 and 10 MPa, depending on testing frequency and applied strain. In [Fernández et al. \[2013\]](#) study, highest values were found in posterior band and lowest in the lateral region. Similarly, highest values for E'' were found in the posterior band (10 – 20 kPa) and lowest values in the lateral region (5 – 10 kPa). [Fazaeli et al. \[2016\]](#) announced E_{init} values in the range from 0.05 to 0.13 MPa, depending on disc testing site with the lateral zone showing the lowest and the medial zone the highest values, which is contradictory to results obtained through unconfined compression by [Lumpkins and McFetridge \[2009\]](#). [Beek et al. \[2001\]](#) found the intermediate zone experienced highest stresses compared to other regions. From results of [Fazaeli et al. \[2016\]](#) and [Lamela et al. \[2011\]](#), it can be deduced that relaxation and creep behaviour is region dependent. However, due to different test regions selected, the comparison between these two studies is not straightforward. Nonetheless, both studies found highest relaxation modulus in the lateral region.

It becomes clear from these results that the TMJ disc shows a sensitivity to tested sample sites, but it is not straightforward to draw conclusions on the region with the highest or lowest properties.

Compression tools

Local compression tests, using cylindrical compression tools, have been conducted on ovine [[Angelo et al., 2016](#)], porcine [[Fazaeli et al., 2016](#)] and human TMJ discs [[Beek et al., 2001](#)], leading to compressive moduli in a range between 0.05 and 446 MPa. To overcome the problem of testing only one sample site during local compression, [Barrientos et al. \[2016\]](#) developed a compression system consisting out of metal condyle and fossa, compressing a complete TMJ sample between those tools. Like [Fernández et al. \[2013\]](#), [Barrientos et al. \[2016\]](#) investigated the dynamic compressive properties of porcine TMJ disc. However, the main difference between the two studies is the sample size. Nonetheless, the results obtained for E' and E'' show the same trend, with [Barrientos et al. \[2016\]](#) results being in the range of results from posterior band studied by [Fernández et al. \[2013\]](#). Results for the loss tangent $\tan \delta$ agree only quantitatively, since [Barrientos et al. \[2016\]](#) obtained values ranging between 1.16 – 1.60, which are higher than those observed by [Fernández et al. \[2013\]](#) (0.2 – 0.3). Nanoindentation studies on the TMJ disc resulted in compressive moduli between 0.064-4.2 MPa [[Chandrasekaran et al., 2017](#); [Juran et al., 2015](#); [Yuya et al., 2010](#)]. Finally, it appears that local spherical compression using a

macro-sphere as the compression tool has not been widely used for TMJ disc characterisation.

Biphasic behaviour

In the biphasic theory, the viscoelastic material behaviour is described as the result of the flow of a fluid phase through pores of a solid phase [Mow et al., 1984]. To highlight the coupling between the fluid phase, the TMJ disc's water content, and the solid extracellular matrix, confined compression tests have been conducted by Kuo et al. [2010], studying on five different TMJ disc sites, the creep and cyclic tissue behaviour. They found the highest aggregate moduli in the central and lateral regions (≈ 74 MPa) and highest hydraulic permeability in anterior and posterior bands ($\approx 8 \times 10^{-15} \text{ m}^4/\text{Ns}$).

Conclusion

Experimental findings from compression test vary in their results, stating compressive moduli in the range of kPa to MPa [Commisso et al., 2016; Fernandez et al., 2011; Fernández et al., 2013; Lamela et al., 2011; Lumpkins and McFetridge, 2009; Tanaka et al., 1999, 2003a,b]. As well as for tensile tests, protocols for compression test vary in test conditions and origin of samples (Appendix A.3 and A.4).

1.3 Objective and strategy

The temporomandibular joint is one of the most used joints of the human body and as presented in Section 1.1 can be associated with different pathologies. Being a crucial part of the TMJ, the TMJ disc needs to be studied in order to propose therapies for patients but also to feed cranio-fascial models that simulate various conditions and scenarios. Therefore, the objective of this thesis is the characterisation of the TMJ disc to serve the prediction of the TMJ functioning.

The literature review points out that the disc has a complex biconcave structure that is difficult to capture through conventional dimension measurements such as rulers or callipers. For this reason, firstly, the sample's geometry is characterised using 3D optical scans and magnetic resonance imaging (Chapter 3).

The mechanical behaviour of the TMJ disc is known to be non-linear, viscous and chemo-sensitive through its biphasic composition. Many approaches have already been used to characterise those behaviours independently or partially coupled. However, the studies vary widely in their experimental conditions and obtained results. For instance, they obtained compressive moduli ranging in their order of magnitude. Furthermore, it has not been studied if cutting test specimen from intact TMJ disc samples does influence test results. [Commisso et al. \[2016\]](#) raised the question of the presence of prestresses within the TMJ disc. However, up to now, no analysis of internal stresses within the TMJ disc has been conducted. Therefore, it is one aim of this thesis to study the internal stress state of TMJ disc samples using the well-known "hole drilling" method, adapted to biological samples. Spherical compression tests are the chosen method to characterise the biomechanical behaviour of TMJ disc samples, since they allow conducting local tests on different zones of the intact TMJ disc, without the disadvantage of peak stresses at the edges of the compression tool [[Lee et al., 2016](#)]. In this way, a combination of a high number of measures on one sample is possible, reducing uncertainties, for instance due to inter-sample discrepancies (Chapter 3).

From these biomechanical *ex vivo* studies, constitutive laws can be deduced to describe the TMJ disc. This step is realised introducing a general approach to analyse results from local spherical compression tests of samples with finite thickness (Chapter 2). This general approach is necessary to be developed since for macro-spherical compression of samples with finite thickness and non-linear material behaviour undergoing large deformation, tools to obtain stress-strain relations are not available in literature.

To achieve the objectives, namely characterising the TMJ disc and predict TMJ behaviour, a large database is built up based on the results from the spherical compression tests, which give a solid base for constitutive law fitting. The constitutive relationships are then used in finite element simulations of the TMJ disc (Chapter 4). Thanks to the optical 3D scans a realistic geometry and mesh can be realised, leading to more accurate models of the TMJ disc and hence will serve to feed cranio-facial models. The internal stress analysis will give further insight in the TMJ disc physiological state and help to draw conclusions on appropriate test conditions.

Chapter 2

Analysis of soft material thin layer behaviour through local macro-spherical compression

Contents

2.1	Introduction	20
2.1.1	Contact mechanics - theoretical background and state of the art	21
2.1.2	Problem statement	23
2.2	Material and Methods	25
2.2.1	Finite element model of local spherical compression tests	25
2.2.2	Evaluation of contact radius a	27
2.2.3	Identification of representative strain ϵ^*	28
2.2.4	Curve fitting using the COBYLA method	28
2.3	Results and Discussion	30
2.3.1	Relationships between contact radius a with respect to the measurements of indentation depth d and compression tool displacement δ	30
2.3.2	Relation between indentation depth δ and compression tool displacement d	37
2.3.3	Representative stress - strain curves	39
2.3.4	Validation of curve fitting procedure	43
2.3.5	Comparison of hyperelastic laws	45
2.3.6	Density influence on samples behaviour	47
2.4	Conclusion	47

Generally, soft biological tissues undergo large deformation and show non-linear mechanical behaviour. During compressive experiments the displacement of the compression tool and the resulting forces are most often recorded. However, to analyse experimental results a relationship between the indentation depth and the contact radius between the compression tool and the sample needs to be established. Work that has already been conducted in this field of research is presented in Section 2.1. However, finite thicknesses of the samples are not considered in most studies. Therefore an approach to analyse local spherical compression experiments of samples with finite thickness is described in Section 2.2, followed with the presentation of results obtained through finite element simulations (Section 2.3).

2.1 Introduction

Mechanical testing of biological samples allows obtaining information that support the prediction of the samples behaviour, feeding numerical models and contributing to the research and development of substitutive materials. However, in order to do so, it is necessary to precisely describe the samples' constitutive law. Recently, spherical indentation tests have been widely used to achieve this goal at different scales.

Nanoindentation tests on biological samples are realised using anatomic force microscopes (AFM). However, this method evaluates material properties very locally. For instance, [Yuya et al. \[2010\]](#) used an indenter tip of $50\text{ }\mu\text{m}$ to carry out experiments on the TMJ disc, for which the mean collagen diameter is stated around $18 \pm 9\text{ }\mu\text{m}$ (mean \pm STD) [[Detamore et al., 2005](#)].

Macroindentation allows the use of more large-scale samples and tools. During macroscopic standard confined or unconfined compression tests, the sample often has to be cut in a specific geometry adapted to the experimental bench. In the case of biological samples, one advantage of macroindentation tests is that the sample can remain intact thus allowing internal fluid flow during testing and therefore a more physiologic testing condition [[Lu and Mow, 2008](#); [Lee et al., 2016](#)].

As the structure and the behaviour of biological samples are not permanently affected during nano- or macroindentation tests, these kind of tests will henceforth be called *local spherical compression* instead of indentation test, which usually relates to plastic strain in classical mechanical investigations.

Biological tissues can undergo large reversible deformation and show non-linear behaviour. It appears that the linear elastic constitutive law is not adapted to model their behaviour. The hyperelastic constitutive relationships, taking into considerations non-linear elastic response of the tissues, are better suited to this purpose [[Zhang et al., 2014](#); [Dagro and Ramesh, 2019](#)].

In this study, local spherical compression of a hyperelastic material of finite diameter and various finite thicknesses is investigated. The objective was to develop a tool, based on an inverse method using analytical definitions confirmed by finite element simulations that allows obtaining soft material properties from experimental force F - compression tool displacement d curves (Figure 2.1.b). A schematic description of a contact between a spherical compression tool and a deformed sample is shown in Figure 2.1.a. To deduce such a constitutive law from experimental data of local spherical compression based the work of [Hertz \[1882\]](#), indentation contact radius a and depth δ are required. However, obtaining these information experimentally is not straightforward.

In silico local spherical compression experiments using finite element method were

carried out to enable evaluation of contact radius a and relation between indentation depth δ and the displacement of compression tool d for non-bonded samples placed on a rigid substrate. Contact mechanics theories lead to obtain the stress-strain curve from the force-displacement curve. As the studied case lies within the limit of those theories an analytical correction had to be introduced.

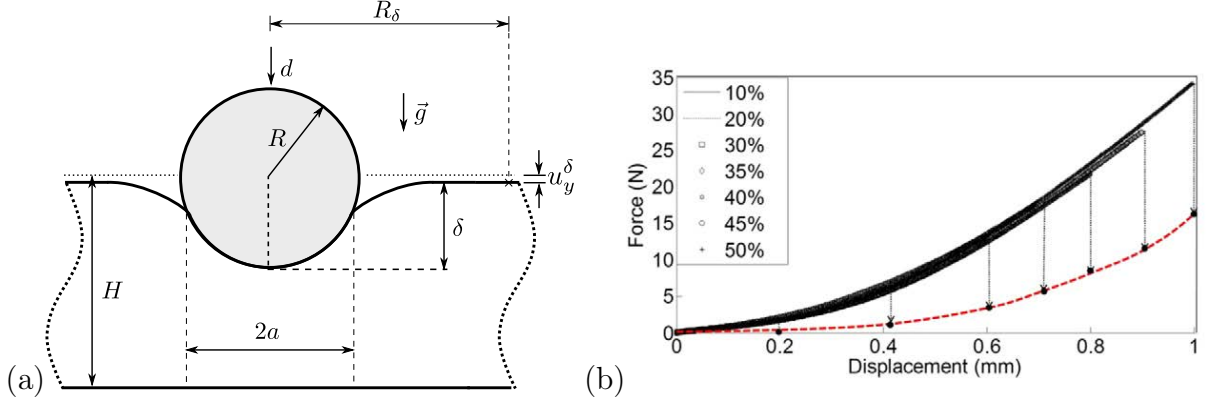


Figure 2.1 – (a) Schematic representation of the local spherical compression test. H - initial sample thickness, R - spherical compression tool radius, d - compression tool displacement, a - contact radius, δ - indentation depth, g - gravitation, R_δ - radius for indentation depth calculation. (b) Example of force-displacement curves at different displacement levels and an extrapolated equilibrium force (---) obtained by Lee et al. [2016] conducting local spherical compression tests on articular cartilage of horse stifle joint. The displacement (mm) on the x-axis corresponds to d depicted in Subfigure a.

2.1.1 Contact mechanics - theoretical background and state of the art

The contact mechanics of a linear elastic half-space indented by a spherical tool are based on the work by Hertz [1882], who defined the resulting force F as a function of the material Young's modulus E , Poisson's ratio ν , indentation depth δ and indenter's radius R :

$$F = \frac{4}{3} E \frac{R^{0.5} \delta^{1.5}}{(1 - \nu^2)}. \quad (2.1)$$

The Hertzian theory is based on the following assumptions [Hertz, 1882; Johnson, 1985; Lin and Horkay, 2008]; the surfaces are continuous and non-conforming, the compressed solid is an infinite elastic and linear half-space, the contact surfaces are frictionless and non-adhesive. The developed stress field is within elastic limit and generates small strains. This last condition is satisfied when $a \ll R$.

Under these hypotheses, one of the principal results of the Hertz' theory is that the contact surface (case of the spherical compression tool and plane) increases proportionally to the indentation depth:

$$a^2 = R\delta. \quad (2.2)$$

Using this result, the indentation force can be expressed as below:

$$F = \frac{4}{3} \frac{Ea\delta}{(1 - \nu^2)}. \quad (2.3)$$

The major restriction of this theory is the assumption of small elastic strain (or $a \ll R$). Using Equation (2.2) this inequality can be reformulated as $\delta \ll R$ or in other words that the indentation depth is small compared to the radius of the compression tool. The second very limiting hypothesis is the assumption of the infinite thickness of the indented body. These restrictions cause a problem during testing of many biological soft tissues, since samples are usually small in size, undergo large deformation and are non-linear concerning their mechanical behaviour.

Since the Hertzian contact law does not hold for thin samples, [Dimitriadis et al. \[2002\]](#) made an attempt to adjust the Hertzian solution for linear elastic compressible and incompressible thin layers, distinguishing bonded and non-bonded indentation configurations. For even thinner samples [Chadwick \[2002\]](#) developed another correction. But their approaches took into consideration only linear elastic materials. However, most biological tissues do not follow linear elastic deformation and are rather described by hyperelastic laws.

For various hyperelastic models, [Lin et al. \[2009\]](#) developed a relationship between the indentation depth and force, the contact radius and representative stress σ^* and strain ϵ^* . The usual definition of the representative Cauchy stress under spherical compression is given below:

$$\sigma^* = \frac{F}{\pi a^2}. \quad (2.4)$$

Concerning representative strain various definitions were used in literature, since the strain under spherical compression is not uniform as this is the case in a uniaxial compression test. The one proposed by [Tabor \[1948\]](#) was adopted in the work of [Lin et al. \[2009\]](#):

$$\epsilon^* = 0.2 \frac{a}{R}. \quad (2.5)$$

Introducing these two definitions to Equation (2.1) yields:

$$\frac{\sigma^*}{\epsilon^*} = \frac{20E}{3\pi(1-\nu^2)}, \quad (2.6)$$

showing that this ratio is function of the material constants E and ν . They also modified the Hertzian relationship linking the indentation depth and contact radius:

$$a = R^{x-\delta y} \delta^z, \quad (2.7)$$

where x , y and z are three fitting parameters.

The limit of this study is the hypothesis of infinite sample thickness, which might be wrong for biological samples, which are often low in thickness. This is also the limitation for studies conducted by [Liu et al. \[2010\]](#); [Zhang et al. \[2014\]](#); [Zhang and Yang \[2017\]](#) and [Dai et al. \[2019\]](#).

Although, [Wu et al. \[2016\]](#) examined the validity of Hertz theory for a large deformation case, their study covers only linear elastic material constitutive law.

Another attempt to obtain spherical compression stress-strain curves has been conducted by [Zhang et al. \[2018\]](#). As [Lin et al. \[2009\]](#), they considered half-spaces of hyperelastic material properties and based the calculation of representative stress and strain adding correction factors ψ and χ such as:

$$\epsilon^* = \frac{4}{3\pi} \frac{\delta^{0.5}}{R} \psi(\delta/R), \quad (2.8)$$

$$\sigma^* = \frac{F}{\pi a^2 \chi(a/r)}. \quad (2.9)$$

However, during macro local spherical compression tests the ratio of sample thickness and compression tool radius $h = \frac{H}{R}$ can be in such a range that the sample needs to be considered as a finite elastic body. Up to date no study is known to consider finite thickness layers of hyperelastic material which are not bonded to the substrate. This Chapter addresses the question of how to solve this problem.

2.1.2 Problem statement

The stress and strain fields generated during local compression tests are non-homogeneous making constitutive law identification difficult. The non-linear effects such as large strains, material non-linearity and contact management, make this approach hard to solve analytically and very time consuming using numerical methods. The inverse method, combining test modelling and optimisation algorithms, can be applied to this end.

Lin et al. [2009] proposed such an approach. They analysed physical aspects of the spherical indentation problem in connection with the Hertz solution for elastic half-spaces. Below, the main conclusions of their work are summarised.

The Hertzian relationship linking the indentation depth δ and the indentation force F through the material properties (E , ν) and the compression tool radius R (Equation (2.1)) can be combined with Equation (2.2), to obtain the equivalent expression of the indentation force, function of the radius of projected contact surface a^2 :

$$F = \frac{4Ea^3}{3(1-\nu^2)R}. \quad (2.10)$$

Numerous authors working on the indentation problem [Tabor, 1948; Briscoe et al., 1998; Fischer-Cripps and Lawn, 1996], elaborated models for various classes of materials based on the correlation between the uniaxial compression test and spherical indentation. By dividing Equation (2.10) by the area of projected contact surface we obtain:

$$\frac{F}{\pi a^2} = \frac{4E}{3\pi(1-\nu^2)} \frac{a}{R}. \quad (2.11)$$

The left-hand side of this expression represents the mean indentation stress (pressure) and is noted σ^* . By comparison with the uniaxial Hook's law for linear elastic materials ($\sigma = E\epsilon$), the right hand side of Equation (2.11) is proportional to some equivalent indentation strain noted ϵ^* . Various definitions of this strain were used, for instance Tabor [1951] and Lin et al. [2009] used Equation (2.5) and Lin et al. [2007]; Briscoe et al. [1998]; Fischer-Cripps and Lawn [1996]; Iwashita et al. [2001] used the following relation:

$$\epsilon^* = \frac{a}{R}. \quad (2.12)$$

These two definitions differ only by a prefactor 0.2 or 1. Essential in both formulae is the ratio $\frac{a}{R}$ representing purely geometric definition of this indentation strain. In the case of Tabor's definition (see Equation (2.5)), Equation (2.11) can now be rewritten as:

$$\sigma^* = \frac{20E}{3\pi(1-\nu^2)}\epsilon^*. \quad (2.13)$$

As stated by [Lin et al. \[2009\]](#), replacing the Hook's law by the non-Hookean uniaxial stress-strain relations, the Hertzian contact theory can be extended to more complex non-Hertzian cases of contact. In this way, in their publication, the authors have extended the Hertz approach to the case of hyperelastic materials. Their results, being derived from the Hertz theory elaborated for semi-infinite bodies, cannot be directly applied in the case of thin non-bonded samples, as this is the case for many biological tissues. However, we suppose, as many other authors (see Section 2.1) that the approach proposed by [Lin et al. \[2009\]](#) remains valid in the case of such a configuration.

The measurement of the contact radius is another difficulty. Therefore, Equation (2.7) was proposed by [Lin et al. \[2009\]](#). They introduced this relation to correct the Hertzian definition predicting the value of $a = R$ for $\delta = R$ which was not validated experimentally. However, it seems that their proposition does not correct this problem. Indeed, supposing that R is equal to a unit (one) and taking $\delta = R$, Equation (2.7) leads to:

$$a = 1^{x-\delta y} 1^z = 1 = R, \quad (2.14)$$

which is exactly the same results as those proposed by Hertz.

Furthermore, the approach by [Lin et al. \[2009\]](#) is based on the definition of representative strain following the work of [Tabor \[1948\]](#), who determined the proportionality factor 0.2 for elastic-plastic deformation of materials. Since biological soft tissues such as the TMJ disc are known to serve as stress absorber, they are supposed to undergo large deformation without plastic straining.

This Chapter is dedicated to the development of a methodology of identification of the hyperelastic material parameters based on the approach initiated by [Lin et al. \[2009\]](#) using finite element simulations, taking into concern thin, non-bonded hyperelastic layers.

2.2 Material and Methods

2.2.1 Finite element model of local spherical compression tests

Assembly and material parameters

An axisymmetric 2D finite element model was created using commercial software Abaqus (version 6.13, Dassault Systemes, France). Since material properties of the compression tool are assumed to be high compared to those of compressed material, the tool was simulated as an analytical rigid sphere. Also, the support on which the soft material lies on was supposed to be rigid in comparison with that material. The compressed material was simulated as deformable, isotropic, homogenous neo-Hookean hyperelastic solid. Neo-Hookean hyperelasticity is commonly used for first models of biological soft tissues [Zhang et al., 2014]. The two material constants are shear (μ_0) and bulk moduli (K_0) (see Equation (2.17)):

$$\mu_0 = \frac{E_0}{2(1 + \nu)}, \quad (2.15)$$

$$K_0 = \frac{E_0}{3(1 - 2\nu)}. \quad (2.16)$$

Simulations were performed using $\mu_0 = 0.334$ MPa and $K_0 = 166.667$ MPa, corresponding to $E = 1$ MPa and $\nu = 0.499$, as in Zhang et al. [2014]. It was demonstrated that choice of material constants does not influence the dimensionless contact radius $\frac{a}{R}$, see for instance Wu et al. [2016] and Zhang and Yang [2017]. To take into consideration the sample weight, a material density was attributed to the compressed material. The value of $\rho = 1000$ kg/m³ was chosen. This value seems to be representative of biological soft tissues, which generally contain a high amount of water.

To study the influence of the layer thickness, several simulations were carried out for various sample thicknesses. Ratios of thickness and compression tool radius $h = H/R$ considered in this study were 0.5, 0.75, 1.0, 1.5, 2.0, 5.0, 10, 20, 30, 40, 50 and 100. The sample diameter was fixed to $D = 16R$. According to Saint Venant principle, it seems to be sufficiently large compared to the contact radius a avoiding influence of the sample's free lateral edge. The geometry of the sample, spherical compression tool and supporting substrate are shown in Figure 2.2 for the case of $h = 2.0$.

To validate the approach presented in the following, an additional simulation with $h = 0.65$ was conducted. This simulation also served to determine the influence of gravity on the behaviour of low thickness samples, since two models were simulated: with and without taking into account density.

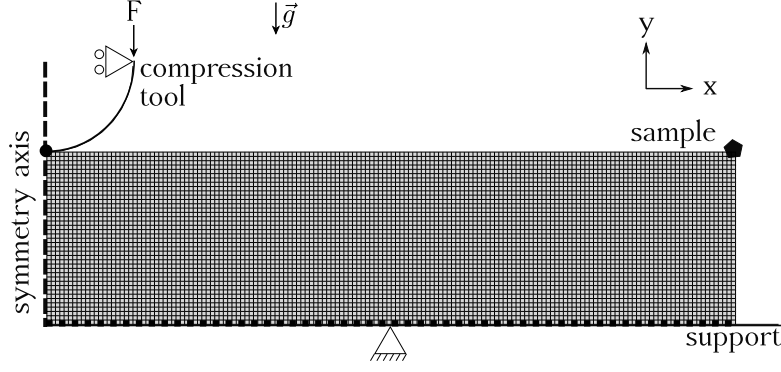


Figure 2.2 – Axisymmetric finite element model ($h = 2.0$) of an elastic sample placed between a rigid support and a rigid spherical compression tool. The geometry, the mesh and the boundary conditions are shown. The \bullet marks the position of tie-constraint between the compression tool's tip and one node of the mesh. The polygon marks the node used for indentation depth δ calculation and the \cdots line marks the bottom of the sample.

Mesh

The sample was meshed using axisymmetric four-node elements of type CAX4RH. For different simulations the number of nodes varied between 3,381-322,161 with a characteristic element size of $0.05R$. Since the zone of contact of our model contains the same number of elements than in the study of [Lin et al. \[2009\]](#) no mesh convergence study was carried out as it has already been done. Further information concerning the meshes for different simulations is provided in Appendix B.1.

Boundary conditions

Boundary conditions are depicted in Figure 2.2. A frictionless surface-to-surface contact was considered between the sample and the compression tool as well as the sample and the support. The sphere and the supporting plane were regarded as masters, while the sample's surfaces were considered as slaves. The support is supposed motionless; the compression tool movement was blocked in radial direction. The upper surface of the sample was stress-free outside the contact zone. To solve the contact problem the penalty method was used. That implies that the contact force is proportional to penetration depth. Separation of modelled bodies after contact was allowed.

Constitutive law

In Abaqus the strain energy potential of compressible neo-Hookean hyperelastic materials [[Rivlin, 1948](#)] is defined as:

$$\Psi = \frac{\mu_0}{2}(\bar{I}_1 - 3) + \frac{K_0}{2}(J^{el} - 1)^2 \quad (2.17)$$

where Ψ is the strain energy density function, \bar{I}_1 first invariant of deviatoric strain, J^{el} Jacobian describing the volume changes, μ_0 and K_0 initial shear and bulk moduli as mentioned before.

Steps

The simulation was carried out in the domain of large strains through two consecutive steps. During the former one, gravity was applied to the model, the bottom tip of the

compression tool was attached to the node of the sample which is lying on the axis of symmetry using a tied constraint. In this way, the compression tool followed the sample's compression caused by its own weight. In the second step, the spherical compression tool compressed the sample, while gravitational load was still applied. The maximum tool's displacement was $d = R$ for samples with $h > 5$. For samples with a small thickness ratio ($h < 5$) compression could obviously not be carried out at the same scale, therefore for those samples spherical compression was carried out up to $d/H = 0.5$, compressing half of their height.

2.2.2 Evaluation of contact radius a

The finite element simulations give access to information, such as the contact radius a and the indentation depth δ , that cannot easily be obtained during experimental local spherical compression tests.

The indentation depth δ was estimated as a difference between the compression tool's displacement d and the displacement u_y^δ of nodes of finite element models situated on the circle of radius R_δ (see Figures 2.1.a and 2.2), for instance:

$$\delta = d - u_y^\delta. \quad (2.18)$$

In this work the value $R_\delta = 8R$ was chosen. The contact between the tool and the sample was assumed to be established when the contact pressure reached at least 1% of the order of magnitude of the samples Young's modulus, which in this case is 0.01 MPa. Using the field output of contact pressure the contact radius was evaluated as a position between two nodes of the edge of last element in contact with the tool using the following interpolation equation:

$$a = \frac{(0.01 - p_1) \cdot (x_2 - x_1)}{p_2 - p_1} + x_1 \quad (2.19)$$

where, x_1 and x_2 are the nodal positions between which the minimal contact pressure of 0.01 MPa was reached and p_1 and p_2 correspond to the contact pressures at nodal position x_1 and x_2 , respectively.

In order to establish the relationship between a and δ these values were evaluated for all time increments of tool displacement d and all simulations corresponding to various sample thicknesses h . Two methods were envisaged to settle this relation. The first one corresponds to the generalisation of the Hertz expression (Equation (2.2)) by using the relation below:

$$\frac{a(t, h)}{R} = \alpha(h) \left(\frac{\delta(t, h)}{R} \right)^{n(h)} \quad (2.20)$$

where α and n are parameters depending on the thickness of the compressed material layer. Obviously, this expression turns to Hertz relationship for $\alpha = 1$ and $n = 0.5$.

The second approach consists in determination of the relationship between the tool displacement d and contact radius a . A similar function to (2.20) is applied to fit the numerical results:

$$\frac{a(t, h)}{R} = \beta(h) \left(\frac{d(t)}{R} \right)^{m(h)}. \quad (2.21)$$

As the indentation strain ϵ^* is given by the ratio $\frac{a}{\delta}$, a function defining the relation between d and δ was built for this second approach.

To determine the factors α , β and the powers n and m , the results from the finite element simulations were used. The curves of contact radius versus indentation depth and versus tool displacement were plotted for all simulated thickness ratios from the range of $0.5 \leq h \leq 100$ and the Equations (2.20) and (2.21) have been fitted to the numerical results. The fitting method used is described in Section 2.2.4. The values obtained for β and m were plotted as a function of sample thickness h . To determine a relationship between the parameters β and m and the thickness ratio h polynomial functions were fitted to the data points. Furthermore, the relationship between the indentation depth δ and the indenter's displacement d was exploited and a parabolic function was fitted to these results.

2.2.3 Identification of representative strain ϵ^*

Generalising [Tabor \[1948, 1951\]](#) and [Lin et al. \[2007, 2009\]](#) definitions (Equations (2.5) and (2.12)), the representative strain is supposed to be proportional to the ratio $\frac{a}{R}$:

$$\epsilon^* = \chi(h) \frac{a}{R} \quad (2.22)$$

with the proportionality factor $\chi(h)$ depending on the sample thickness ratio h as an improvement regarding to the before mentioned definitions. The factor $\chi(h)$ is deduced from the comparison of the uniaxial compression stress-stretch curve of the constitutive law used in simulations and the numerical force-displacement curves transformed to the σ^* function (Equation (2.4)) of λ^* plots, where λ^* is the representative stretch measure (Equation (2.23)). The value of proportionality factor $\chi(h)$ is deduced by fitting $\sigma^* - \lambda^*$ plots to the $\sigma - \lambda$ curves. As, by convention, σ^* and ϵ^* are represented as positive quantities, regardless the fact that indentation is essentially a compressive process, attention must be paid when building these plots. In this case, the representative stretch is determined using the following relation to comply with the convention:

$$\lambda^* = 1 - \epsilon^* \quad \text{with} \quad \epsilon^* > 0. \quad (2.23)$$

For convenience of comparison, the absolute value of stress $|\sigma|$ is plotted in function of ϵ^* .

As for relations $\left(\frac{a}{R}\right) = f\left(\frac{\delta}{R}\right)$ and $\left(\frac{\delta}{R}\right) = f\left(\frac{d}{R}\right)$, the fitting of obtained values of χ will allow obtaining the definition of representative strain ϵ^* in function of material layer thickness.

For comparison with the analytical neo-Hookean incompressible ($J = 1$) material model (Equation 2.17) under uniaxial load, we use the definition of nominal stress (σ_{nH}^n) following the approach of [Lin et al. \[2009\]](#):

$$\sigma_{nH}^n = \mu_0 \left(\lambda - \frac{1}{\lambda^2} \right). \quad (2.24)$$

The derivation from Equation (2.17) to Equation (2.24) is developed in Appendix B.2.

2.2.4 Curve fitting using the COBYLA method

To obtain parameter for curve fitting, throughout this work, the Constrained Optimisation BY Linear Approximation (COBYLA) method implemented in the SciPy Python library

(version 2.7.12) has been used. The optimisation script minimises least square error of experimental data and objective function, whereas the COBYLA method seeks to find the parameter of the objective function. Applying COBYLA, multiple constraints can be used. In this case, the constraints have been normalised so that parameters can more easily be determined if their absolute values differ by their range of magnitude.

2.3 Results and Discussion

This section presents results of *in silico* finite element simulations of local spherical compression tests. The aim is to obtain representative stress-strain curves from local spherical compression tests. To do so, the relationship between the contact radius a and the indentation depth δ is evaluated. Furthermore, the prefactor χ defining the representative strain ϵ^* defined by Equation (2.22) is determined. Since the experimental measurement of indentation depth is difficult to achieve, especially in the case of soft biological tissues tested under physiological conditions, the relation between this depth and the displacement of the rigid spherical compression tool is also assessed. In the last section of this Chapter, the validation of the method of identifying hyperelastic constitutive law parameters is presented.

2.3.1 Relationships between contact radius a with respect to the measurements of indentation depth d and compression tool displacement δ

Twelve simulations were completed with various sample thickness ratios ranging from $h = 0.5$ to $h = 100$. Figure 2.3 depicts the dimensionless contact radius a/R as a function of the dimensionless indentation depth δ/R for all geometries simulated. Two types of resulting graphs can be distinguished. Actually, while points for thickness ratios $h \geq 2$ are nearly superimposable (see Figure 2.3.b), those of thickness ratios $h < 2$ show clearly two regimes separated by a sharp change of the curve shape as it can be easily observed for the curve of thickness ratio $h = 0.5$ (see Figure 2.3.a). Besides, the extent of the first regime decreases rapidly with increasing sample thickness. Also, the final value of a/R diminishes significantly while the sample thickness decreases. As it can be read in this figure, for $\delta/R = 0.8$ for instance, the value of a/R passes from 0.65 for thickness ratio $h = 0.5$ to 0.82 for $h = 1.5$. To interpret the values for δ/R presented Figure 2.3.a one should remember the definition of the indentation depth δ that is the difference between the vertical displacement of compression tool d and a node on the upper surface of the sample (see Equation (2.18) and Figure 2.1). Since the simulations have been carried out for quasi incompressible materials, high compression on the samples' centre introduces a bending of the sample leading to the detachment of its extremity from the rigid support as can be seen in Figure 2.4. For this reason, the dimensionless indentation depth δ/R can exceed thickness ratio h for samples with small thickness ratio. Samples with a larger thickness ratio have higher bending stiffness and mass counteracting bending effects. Therefore, the detachment observed for small thickness ratio samples does not occur. Figure 2.4 also shows the non-homogeneous stress distribution within the sample at the maximum compression tool displacement.

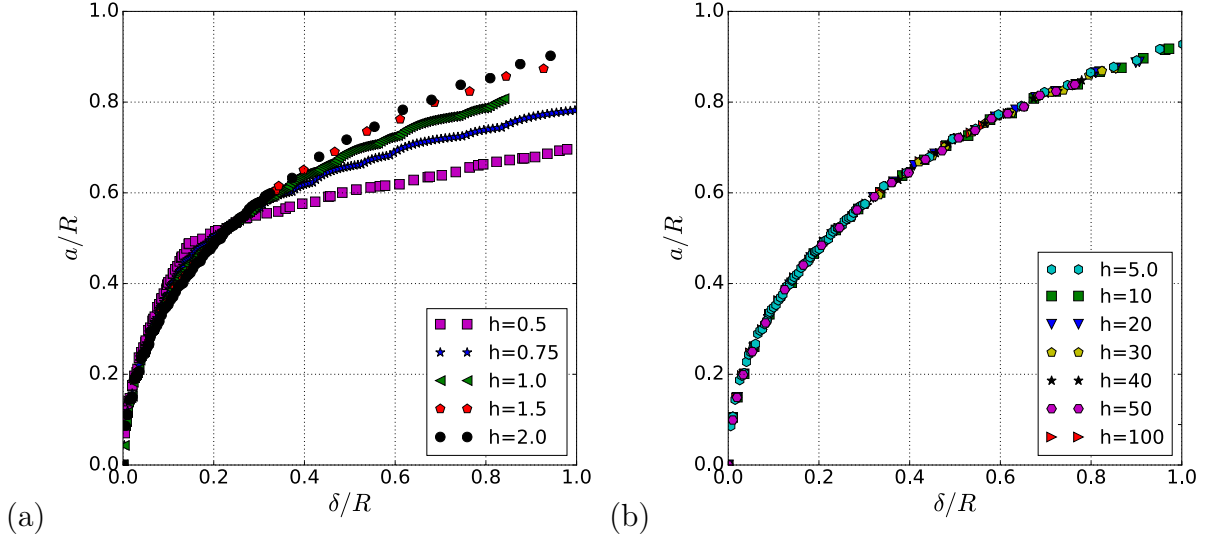


Figure 2.3 – Comparison of dimensionless contact radius a/R as a function of dimensionless indentation depth δ/R obtained through finite element analysis: (a) case of initial thickness ratio from $h = 0.5$ to $h = 2.0$, (b) case of thickness ratios $h = 5.0$ to $h = 100$.

As described in Section 2.2.2, to establish a relation between the contact radius and the indentation depth Equation (2.20) ($\frac{a}{R} = \alpha \left(\frac{\delta}{R}\right)^n$) was fitted to the data presented in Figure 2.3. The evolution of the dimensionless contact radius a/R as a function of the dimensionless indentation depth δ/R confirms the choice of a power function for fitting of these results.

The obtained fitting parameters are gathered in Table 2.1. It can be read from this table that the quality of the fitting reflected by the determination coefficient R^2 , is relatively poor for the first category of the results, i.e. $h < 2.0$. Figure 2.5 shows three examples of fitting for the thickness ratios $h = 0.5/1.0/5.0$. The examples represent the different categories of fitting results, since one ratio lies in the first observed regime ($h = 0.5$) and one in the second regime ($h = 5.0$), while $h = 1.0$ was chosen as intermediate ratio.

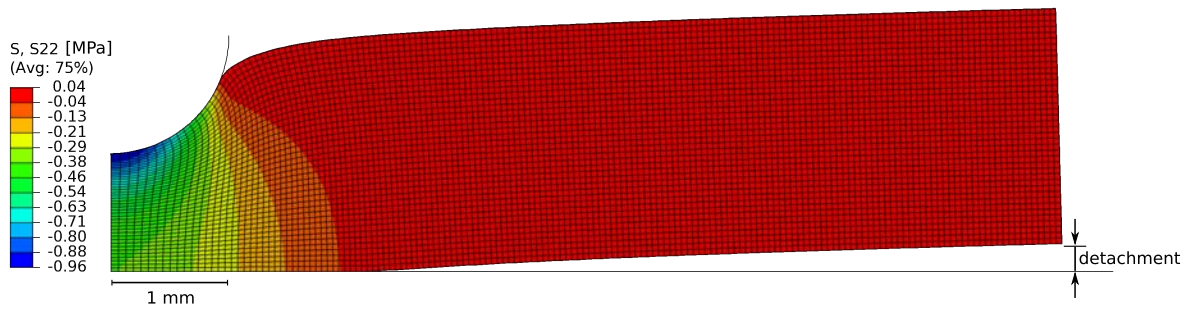


Figure 2.4 – Finite element results for $h = 2.0$, shown is the stress distribution and the deformed shape of the sample at a compression tools displacement of $d = 1$ mm. The detachment from the support of the most distal part of the sample can be observed. The maximal compressive stress is -0.96 MPa. Negative stress values are an indication of compressive process of loading.

Table 2.1 – Fitting parameters α and n of dimensionless contact radius a as a function of dimensionless indentation depth δ for all simulated thickness ratios including the corresponding determination coefficient R^2 .

h	0.5	0.75	1.0	1.5	2.0	5.0	10	20	30	40	50	100
α	0.73	0.80	0.89	0.90	0.93	0.96	0.95	0.95	0.96	0.96	0.96	0.98
n	0.29	0.32	0.38	0.39	0.41	0.44	0.43	0.44	0.44	0.44	0.45	0.44
R^2	0.958	0.983	0.992	0.992	0.995	0.998	0.998	0.998	0.998	0.998	0.998	0.999

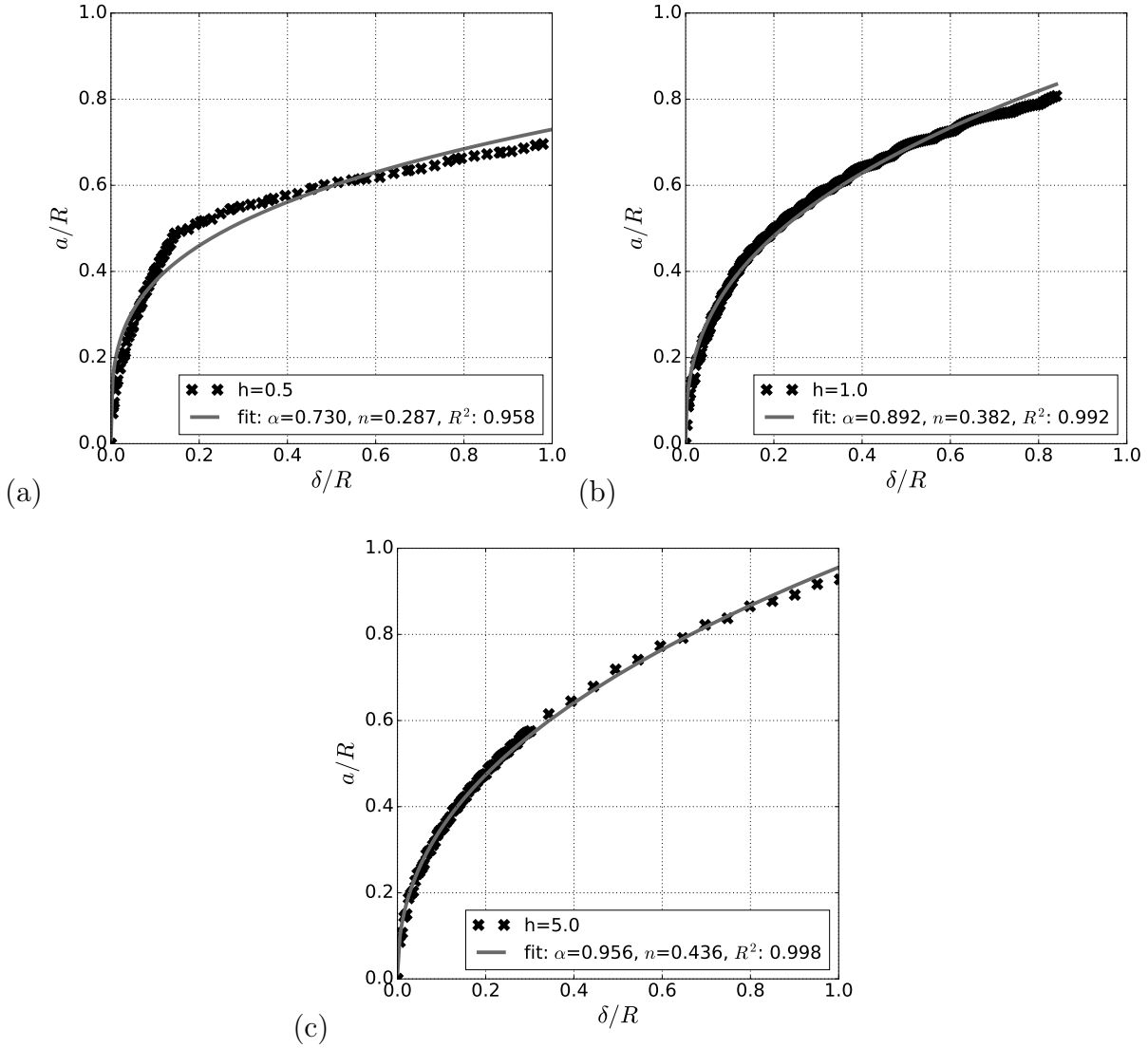


Figure 2.5 – Fitting of the finite element results of dimensionless contact radius a/R as a function of dimensionless indentation depth δ/R using Equation (2.20) for thickness ratios (a) $h = 0.5$, (b) $h = 1.0$, (c) $h = 5.0$ and corresponding determination coefficients R^2 .

It appears from this *in silico* study of the local spherical compression problem that for layers with $h < 2$, the relation in Equation (2.20), but also the Hertzian and [Lin et al. \[2009\]](#) definitions, are not adapted to fit correctly the numerical results. Indeed, the

obtained results are not smooth enough for layers with a small thickness ratio to be fitted by a simple power function.

To understand this particular behaviour, it is useful to observe the deformation process of layers with various thickness ratios. Figure 2.6 helps to draw appropriate conclusions. It depicts the upper and lower surfaces of the compressed samples to highlight the difference of their detachment manner. It becomes apparent from obtained results that for layers with thickness ratio $h > 10$ the sample remains in contact with the support during the whole compression process (see Figure 2.6.a, h10), while samples with thickness ratio $h < 10$ present detachments of the most distal part (see Figure 2.6.a, h2 and h5). Moreover, for samples having a thickness ratio $0.5 < h < 2.0$ the partial loss of contact of their intermediary part, before detachment of the distal part is observed (Figure 2.6.b). It becomes clear from this analysis that the global behaviour of the compressed disc is strongly influenced by the weight of the compressed sample.

Since biological tissues, for instance cartilage samples, can often qualified as thin structures, these observations confirm that the fitting should be improved for low thickness ratios.

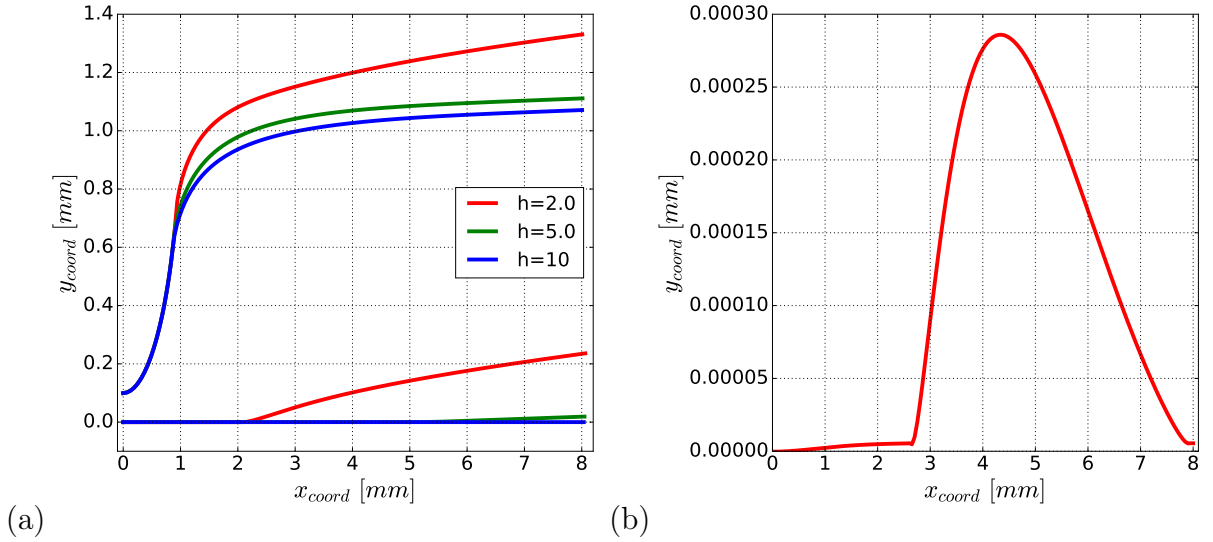


Figure 2.6 – (a) Shape of the upper and lower surface of the compressed sample for maximal compression tool displacement for three thickness ratios. It becomes clear that with increasing thickness ratio detachment decreases. For a better overview, the samples upper surface is depicted with an offset $y_{coordoffset} = y_{coord} - (H - 0.1)$. (b) For a thickness ratio $h = 2.0$ at a compression tool displacement $d = 0.095$ mm the intermediate part detaches from the support before the distal part detaches.

To get around this problem, the second approach of data fitting was applied. The plots of evolution of contact radius as function of compression tool displacement were constructed and are shown in Figure 2.7.a. This time, the increase in contact radius follows a smooth trend for all thickness ratios, however as expected, the maximum value of a/R decreases with increasing thickness ratio. This is due to the increase of the compressed layer stiffness with its decreasing thickness.

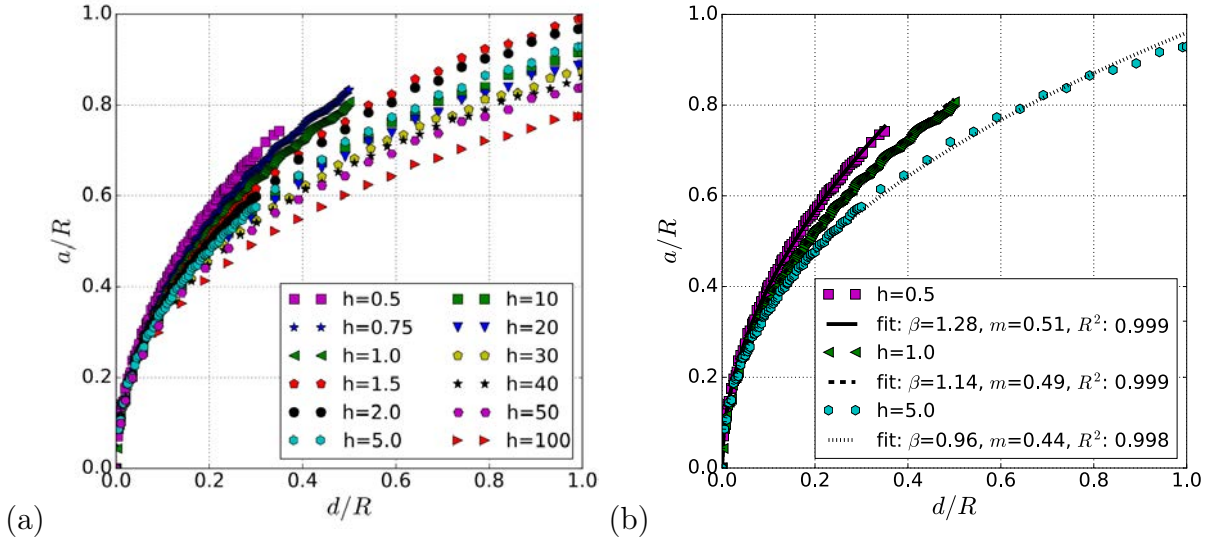


Figure 2.7 – Comparison of dimensionless contact radius a/R as a function of dimensionless compression tool displacement d/R for (a) samples of different initial thickness ratios h obtained through finite element analysis; (b) Results for thickness ratios $h = 0.5$, $h = 1.0$, and $h = 5.0$, including fitting using Equation (2.21) and associated determination coefficient R^2 .

As it can be appreciated in Table 2.2, which is summarising fitting parameters β and m as well as the determination coefficient R^2 for all thickness ratios studied, the relation from Equation (2.21) which, for convenience, is recalled below leads to very accurate fitting of numerical results (for all h $R^2 > 0.997$):

$$\frac{a(t)}{R} = \beta \left(\frac{d(t)}{R} \right)^m.$$

Table 2.2 – Fitting results of parameters β and m for curve fitting of dimensionless contact radius a as function of dimensionless compression tool displacement d for all simulated thickness ratios and the corresponding determination coefficient R^2 .

h	0.5	0.75	1.0	1.5	2.0	5.0	10	20	30	40	50	100
β	1.28	1.18	1.14	1.03	1.01	0.96	0.94	0.91	0.89	0.88	0.86	0.79
m	0.51	0.49	0.49	0.45	0.45	0.44	0.43	0.43	0.42	0.42	0.41	0.40
R^2	0.999	0.999	0.999	0.997	0.997	0.998	0.998	0.998	0.998	0.998	0.998	0.999

Figure 2.7.b shows, for the same thickness ratios as in Figure 2.5, the improvement of curve fitting for the examples $h = 0.5$, $h = 1.0$, and $h = 5.0$.

As it can be deduced from Table 2.2 both parameters β and m strongly depend on dimensionless sample thickness h . Especially, their evolutions are steep for the low values of thickness H considering a constant compression tool radius R or in other words for samples with a small thickness ratio. Figure 2.8, showing β and m as function of h also depicts this evolution.

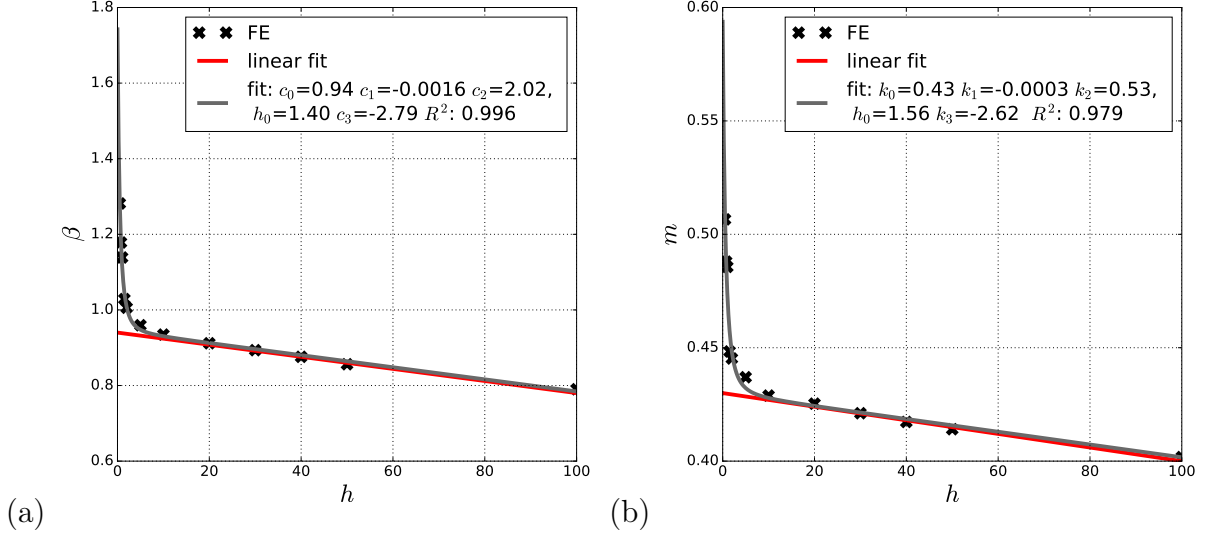


Figure 2.8 – (a) Parameter β and (b) parameter m as a function of thickness ratio h ; both with associated curve fitting according to Equation (2.25). The red line marks quasi-linear dependency for thick sample layers.

As this work is focused on thin layer samples, the linear fitting was not sufficient. To take into account the evolution of β and m for the whole range of thickness ratio h , the data-points have been fitted by a function combining linear and power functions:

$$f(h) = c_0 + c_1 h + c_2 (h + h_0)^{c_3} \quad (2.25)$$

where c_0 , c_1 , c_2 , c_3 and h_0 are the fitting parameters. Figures 2.8.a and 2.8.b illustrate the corresponding best fitting of β and m , which resulted in the following relationships:

$$\beta = 0.94 - 0.0016h + 2.02(h + 1.40)^{-2.79}, \quad (2.26)$$

$$m = 0.43 - 0.0003h + 0.53(h + 1.56)^{-2.62}. \quad (2.27)$$

Remarkable is the fact that for both parameters, their strong evolution for small thickness ratios is described by almost the same power c_3 equal to -2.79 for β and k_3 equal to -2.62 for m . Furthermore, the shift parameter h_0 of the hyperbolic function is close for both fittings, $h_0 = 1.40$ and 1.56 , respectively for β and m . This latter observation suggests the possibility of introducing three types of layers namely "thick", "thin" and "very thin" ones. The thick layers can be defined as those for which the evolution of $\beta(h)$ and $m(h)$ are quasi linear, as represented by the red curves in Figure 2.8. It is due to the fact that for such layers the main part of the indented matter under the compression tool remains insignificantly deformed and consequently the layer stiffness

varies quasi proportionally with its thickness. The threshold separating thick and thin layers can be situated near the thickness ratio:

$$h_T = \frac{H_T}{R} \cong 10. \quad (2.28)$$

Indeed, for thickness ratios greater than 10 the fitting curve of parameter β is practically indistinguishable from the linear approximations drawn in red in Figure 2.8.a. This value corresponds to the limit thickness, mentioned above, indicating samples remaining in contact with the support during the whole compression process.

The evaluation of the second transition point, separating very thin and thin layers, is much more subtle. It is proposed in this work to link this definition with the occurrence of the partial loss of contact between the intermediate part of the sample bottom surface and the compression support as it is illustrated in Figure 2.6.b. As mentioned earlier, this phenomenon appears for thickness ratios within the range $0.5 < h < 2.0$. Samples with $h < 2.0$ will be called very thin while samples within $2 < h < 10$ will be considered as thin. It can be observed in Figure 2.8 that the evolution of the parameters β and m for very thin samples is almost asymptotic. Obviously, the values of these threshold thickness ratios strongly depend on the mechanical properties of the sample and its density. Indeed, the phenomenon of loss of contact of the bottom sample surface results from the competition between the sample stiffness and its weight. This competition can be described by the ratio of the force resulting from elastic deformation represented by the product of Young's modulus and compression tool radius $E_0 R H$ and the samples density in relation to its volume $\rho g L^2 H$. It is proposed to generalise these thresholds values definitions in the following manner:

very thin sample:	$h < 1.25 \times 10^{-4} \frac{E_0 R}{L^2 \rho g}$
thin sample:	$1.25 \times 10^{-4} \frac{E_0 R}{L^2 \rho g} < h < 1.25 \times 10^{-3} \frac{E_0 R}{L^2 \rho g}$
thick sample:	$h > 1.25 \times 10^{-3} \frac{E_0 R}{L^2 \rho g}$

2.3.2 Relation between indentation depth δ and compression tool displacement d

The loss of contact indicated in Section 2.3.1 is also detectable on the curves describing the dependence of the indentation depth δ on the compression tool displacement d . Construction of these curves is important since during experimental local compression tests only the compression tool displacement d is being measured. Figure 2.9 shows three examples of dependency between dimensionless compression tool displacement d/R and indentation depth δ/R . In the first two cases (Figure 2.9.a $h = 0.5$ and Figure 2.9.b $h = 1.0$), two distinct regimes can be distinguished. For small values of compression tool displacement the relation between δ and d is linear, whereas in the case of $h = 0.5$ for $d/R > 0.14$ a non-linear function is required to describe this dependency. In the third case (Figure 2.9.c $h = 5.0$), a unique non-linear relation appears to be sufficient.

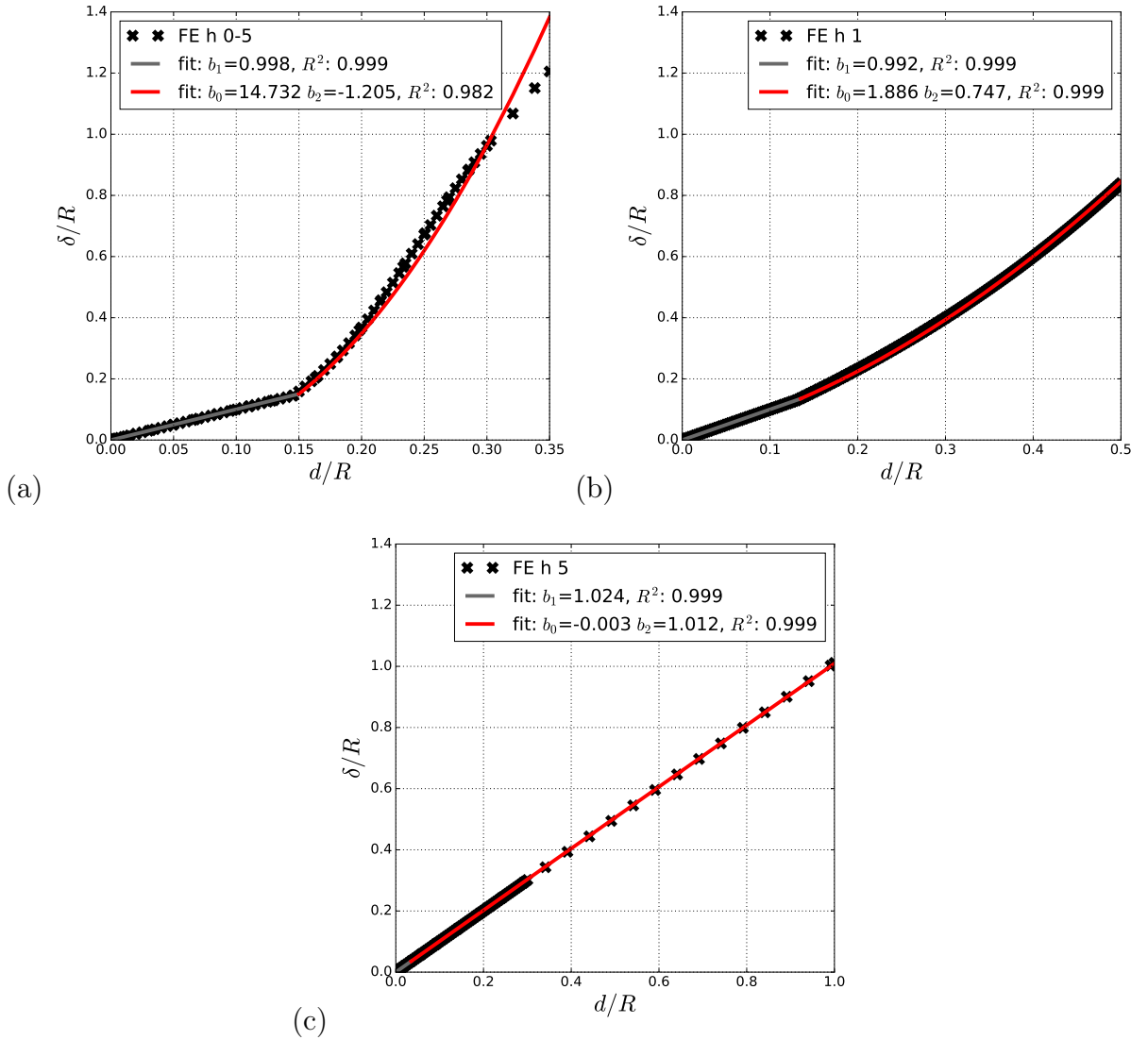


Figure 2.9 – Dimensionless indentation depth δ/R versus compression tool displacement d/R for thickness ratios (a) $h = 0.5$, (b) $h = 1.0$, (c) $h = 5.0$ with associated curve fitting according to Equation (2.29).

Two functions have been used to fit the dimensionless indentation depth δ/R versus

dimensionless compression tool displacement d/R curves using the COBYLA algorithm (Section 2.2.4). To describe the two regimes, the following functions were used:

$$\delta(d) = \begin{cases} b_1 d, & \text{if } d < d_{detach} \\ b_0 d^2 + b_2 d, & \text{if } d > d_{detach} \end{cases} \quad (2.29)$$

with the condition: $b_2 = b_1 - b_0 d_{detach}$.

Examples of this fitting are also presented in Figure 2.9. For all thickness ratios the constants b_0 and b_2 obtained by the fitting are summarised in Table 2.3. One can see that the fitting improves with increasing thickness ratio. For the case of $h = 0.5$ (Figure 2.9.a) the second regime is not completely represented by the fitting, especially for the high values, which can be also noted from the coefficient of determination $R^2 = 0.98$ for the parabolic part. In contrast, for the case $h = 5.0$ (Figure 2.9.c), the fitting describes perfectly the curve obtained through finite element simulation ($R^2 = 1.0$).

Table 2.3 – Resulting constants b_0 and b_1 for fitting of Equation (2.29) to $\delta - d$ curves with associated determination coefficient R^2 for all simulated thickness ratios h .

h	0.5	0.75	1.0	1.5	2.0	5.0	10	20	30	40	50	100
b_0	14.732	4.312	1.886	0.576	0.270	-0.003	-0.014	-0.045	-0.071	-0.089	-0.101	-0.137
b_2	-1.205	0.398	0.747	0.933	0.973	1.012	0.985	0.950	0.919	0.890	0.862	0.754
R^2	0.982	0.9998	0.9999	0.9998	0.9998	0.9999	0.9999	0.9999	0.9999	0.9999	0.9999	0.9997

In order to establish a general relationship between indentation depth δ and compression tool displacement d , the constants b_0 and b_2 were plotted as functions of the thickness ratio h (see Figure 2.10). In these plots the strong evolution of b_0 and b_2 for thin layers is found again, whereas for thick layers their evolution is again linear, supporting the previously evoked differentiation of thick, thin and very thin layers.

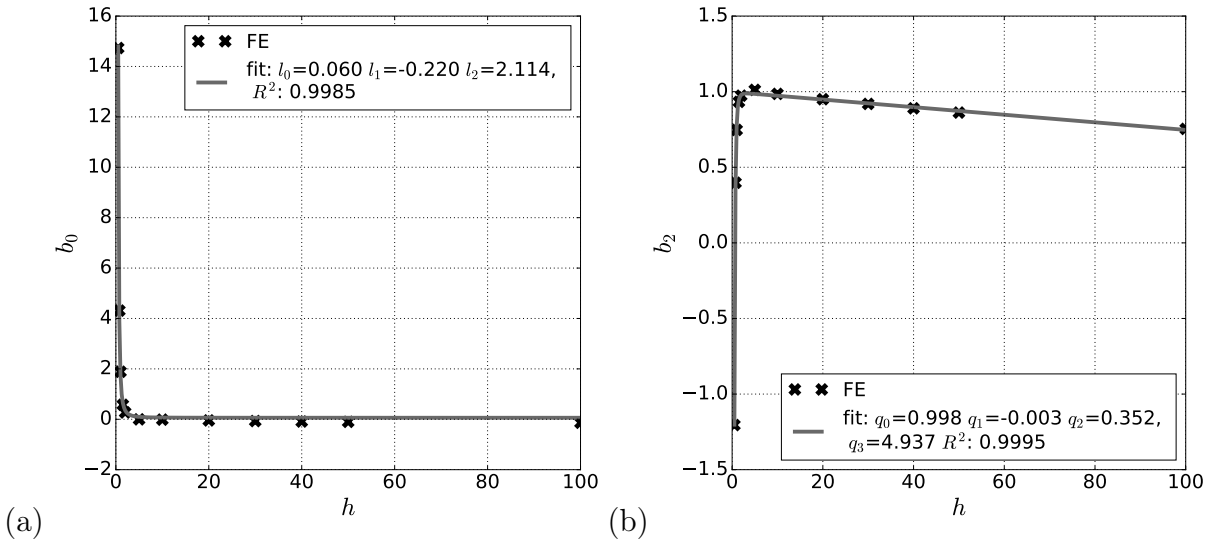


Figure 2.10 – (a) Parameter b_0 as a function of material thickness h with related fitting according to Equation (2.30), (b) parameter b_2 as a function of material thickness h with related fitting according to Equation (2.31).

In the next step, the following functions have been fitted to the constants b_0 and b_2 :

$$b_0 = l_0 + \frac{1}{(h + l_1)^{l_2}}, \quad (2.30)$$

$$b_2 = q_0 + q_1 h - \frac{1}{(h + q_2)^{q_3}}. \quad (2.31)$$

The fitting results are also presented in Figure 2.10. The fitting constants obtained for the fitting of b_0 are: $l_0 = 0.06$, $l_1 = -0.22$ and $l_2 = 2.114$ with a correlation coefficient of $R^2 = 0.9985$. The results of fitting of b_2 are the following: $q_0 = 0.998$, $q_1 = -0.003$, $q_2 = 0.352$ and $q_3 = 4.937$ with a correlation coefficient of $R^2 = 0.9995$. The fitting functions represent a mathematical fitting, therefore fitting constants should not be interpreted physically.

The constant b_1 was found ≈ 1 for all simulations. This means that before the sample detaches, the linear behaviour of the δ - d curves is almost identical, independent of thickness ratio h . The displacement that leads to a sample detachment is shown in Figure 2.11. The detachment of the most distal part occurs earlier with increasing sample thickness ratio. However, the bending effect is less for samples with larger thickness ratios as it can be seen from lower values of δ in for $h = 1$ and $h = 5$ in Figure 2.9.

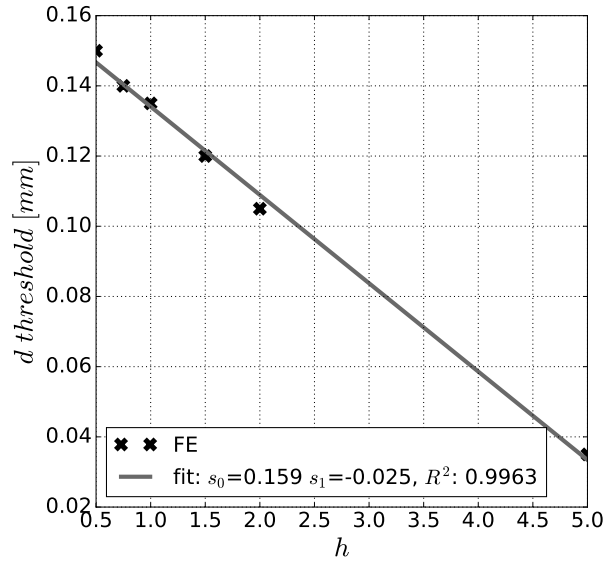


Figure 2.11 – Compression tool displacement d threshold of detachment as function of sample thickness h with associated linear fitting.

2.3.3 Representative stress - strain curves

In order to find the representative strain in the case of local spherical compression test that represents the strain in case of uniaxial loading, the numerical results were fitted to the theoretical stress - strain curves of a quasi incompressible neo-Hookean material. The expressions for stress σ_{nH}^n and strain ϵ for this material according to the convention are evoked in Section 2.2.3. Thanks to the numerical results in term of force F and compression tool displacement d , the representative stress σ^* and strains ϵ^* for local spherical compression tests are recalled here:

$$\sigma^* = \frac{F}{\pi a^2},$$

$$\epsilon^* = \chi \frac{a}{R} \quad \text{with} \quad \frac{a}{R} = \beta \left(\frac{d}{R} \right)^m.$$

Figure 2.12 represents the fitting of representative stress-strain curves to the theoretical neo-Hookean stress-strain curves for material thickness ratios $h = 0.5$, $h = 1.0$ and $h = 5.0$. The fitting is able to represent the corresponding theoretical stress-strain curves, which can be deduced by the values of R^2 . However, for small strains the fitting results do slightly underestimate the stress and overestimate the stress for higher strains. The obtained values for the factor χ are summarised in Table 2.4.

The maximal compressive stress depicted in Figure 2.4 is not covered by the representative stress. The highest values occur directly under the compression tool where compression of the material is the highest. However, values at the end of the simulations depicted in Figure 2.12 of around 0.5 MPa are in the order of magnitude of the average stress.

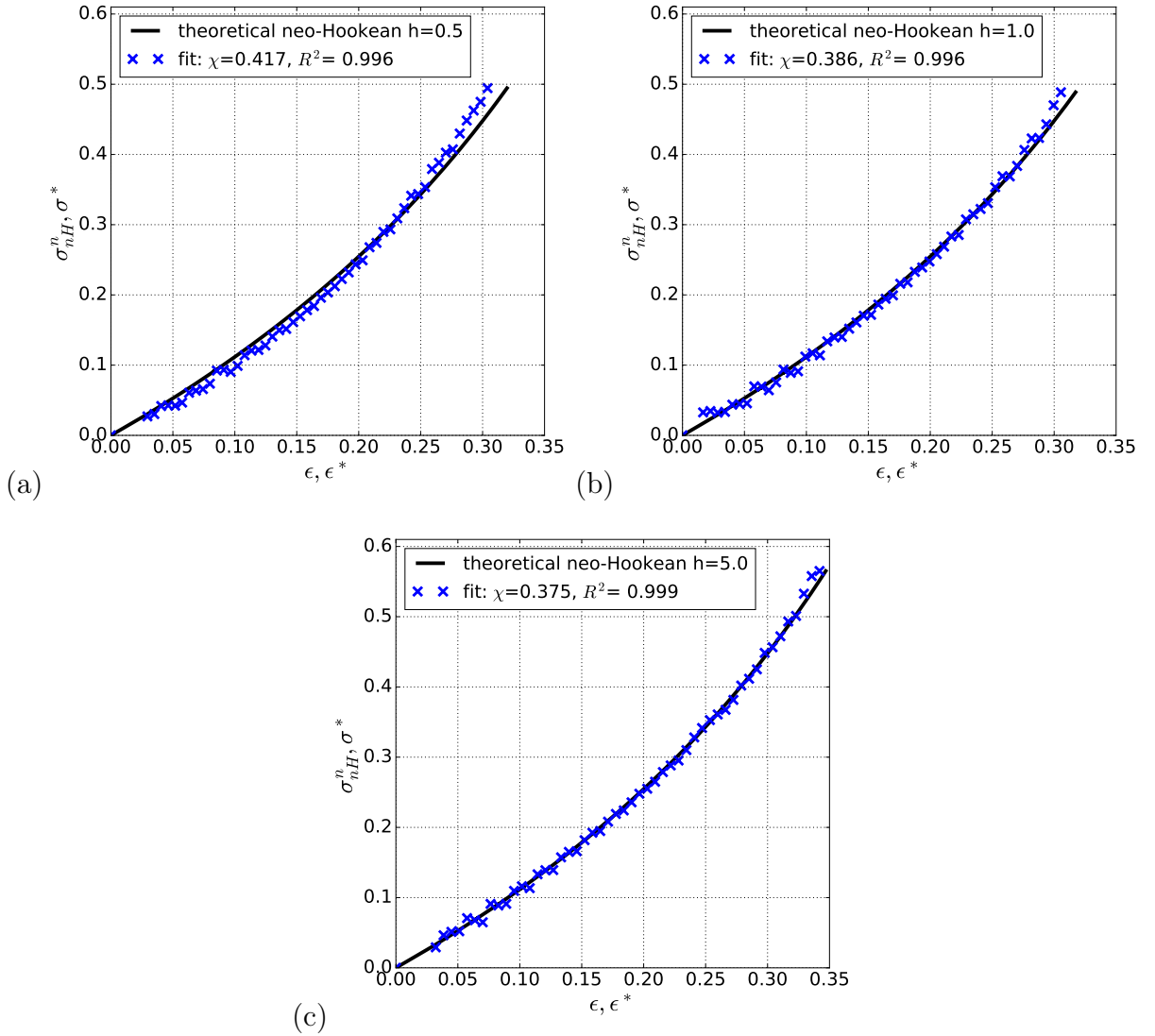


Figure 2.12 – Theoretical stress ($|\sigma^n_{nH}|$) for a quasi incompressible neo-Hookean material with $\mu = 0.334$ MPa as a function of strain ϵ and fitted representative stress σ^* as function of representative strain ϵ^* for local spherical compression of a material with thickness ratio (a) $h = 0.5$, (b) $h = 1.0$ and (c) $h = 5.0$.

Table 2.4 – Fitting results of parameter χ for curve fitting of representative stress σ^* as function of representative strain ϵ^* for all simulated thickness ratios and determination coefficient R^2 .

h	0.5	0.75	1.0	1.5	2.0	5.0	10	20	30	40	50	100
χ	0.42	0.399	0.386	0.386	0.380	0.375	0.376	0.376	0.376	0.374	0.375	0.374
R^2	0.996	0.995	0.996	0.997	0.998	0.998	0.998	0.998	0.998	0.998	0.998	0.999

In order to define a relationship between the factor χ and the material thickness, the results from Table 2.4 have been plotted in Figure 2.13. Table 2.4 and the plot show that for thin material layers the proportionality factor χ declines fast; for $h = 0.5$ the factor χ is respectively 0.417 and for $h = 1.5$ the factor χ is 0.386. For thickness ratios $h > 2$ the factor χ varies between 0.374-0.38.

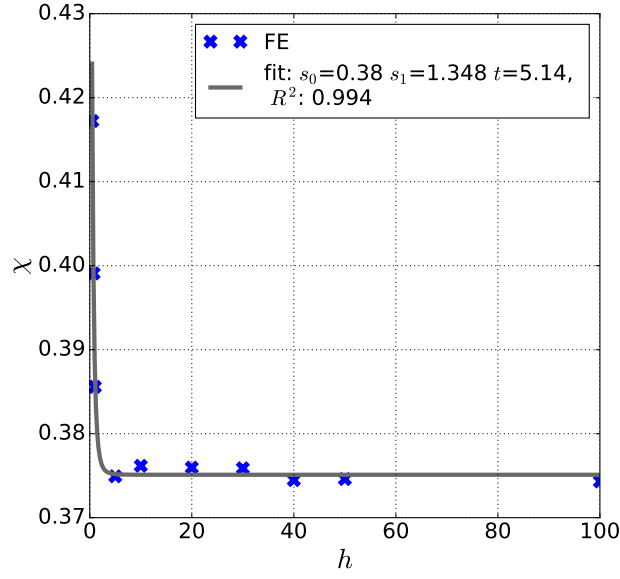


Figure 2.13 – Parameter χ as a function of material thickness ratio h with fitting using Equation (2.32).

The development of the parameter χ as a function of thickness ratio h reminds of that from parameter b_0 presented in Figure 2.10.a. Therefore the same function to fit the results has been chosen:

$$\chi(h) = s_0 + \frac{1}{(h + s_1)^t}. \quad (2.32)$$

The fitting result is presented in Figure 2.13 and resulted in the following equation:

$$\chi(h) = 0.38 + \frac{1}{(h + 1.348)^{5.14}}. \quad (2.33)$$

Using this equation, representative stress - strain curves can be constructed, not only for the presented thicknesses but also for any thickness of thin material layers.

2.3.4 Validation of curve fitting procedure

In order to validate the obtained functions for the fitting parameter couples β / m and b_0 / b_2 , respectively, an additional finite element simulation with a thickness ratio of $h = 0.65$ was carried out, since the focus of this work lies on very thin structures.

Figure 2.14.a presents the dimensionless contact radius a/R as a function of dimensionless compression tool displacement d/R together with the predicted curve following the fitting process described in Section 2.3.1. Using Equations (2.26) and (2.27), the contact radius has been calculated. As it can be observed from Figure 2.14.a, the finite element results superpose well with the predicted curve, permitting to confirm the validity of the proposed fitting, especially in the case of thin layers, with for instance such a ratio $h = 0.65$.

The validation of the relationship of indentation depth δ and compression tool displacement d is carried out in the same manner. Figure 2.14.b depicts the results of the finite element simulation and the predicted curve according to fitting process in Section 2.3.2. The predicted curve underestimates the indentation depth for almost the whole range of sphere displacements, except for the range $0.15 < d/R < 0.23$ where both curves overlap. The validation shows that the fitting procedure can approximately predict the $\delta/R - d/R$ curve, it better describes δ/R for $d/R < 0.25$, though, than for bigger displacements.

Similarly to the two beforehand described validations, the stress-strain curve using the fitting of parameter χ (Section 2.3.3) was plotted in Figure 2.14.c. With a correlation coefficient of $R^2 = 0.9628$, the theoretical stress-strain curve is well described by the fitting value of χ .

However, it is not only of interest to show that the method developed holds for different thickness ratios but also for different material laws. This will be developed in the following section.

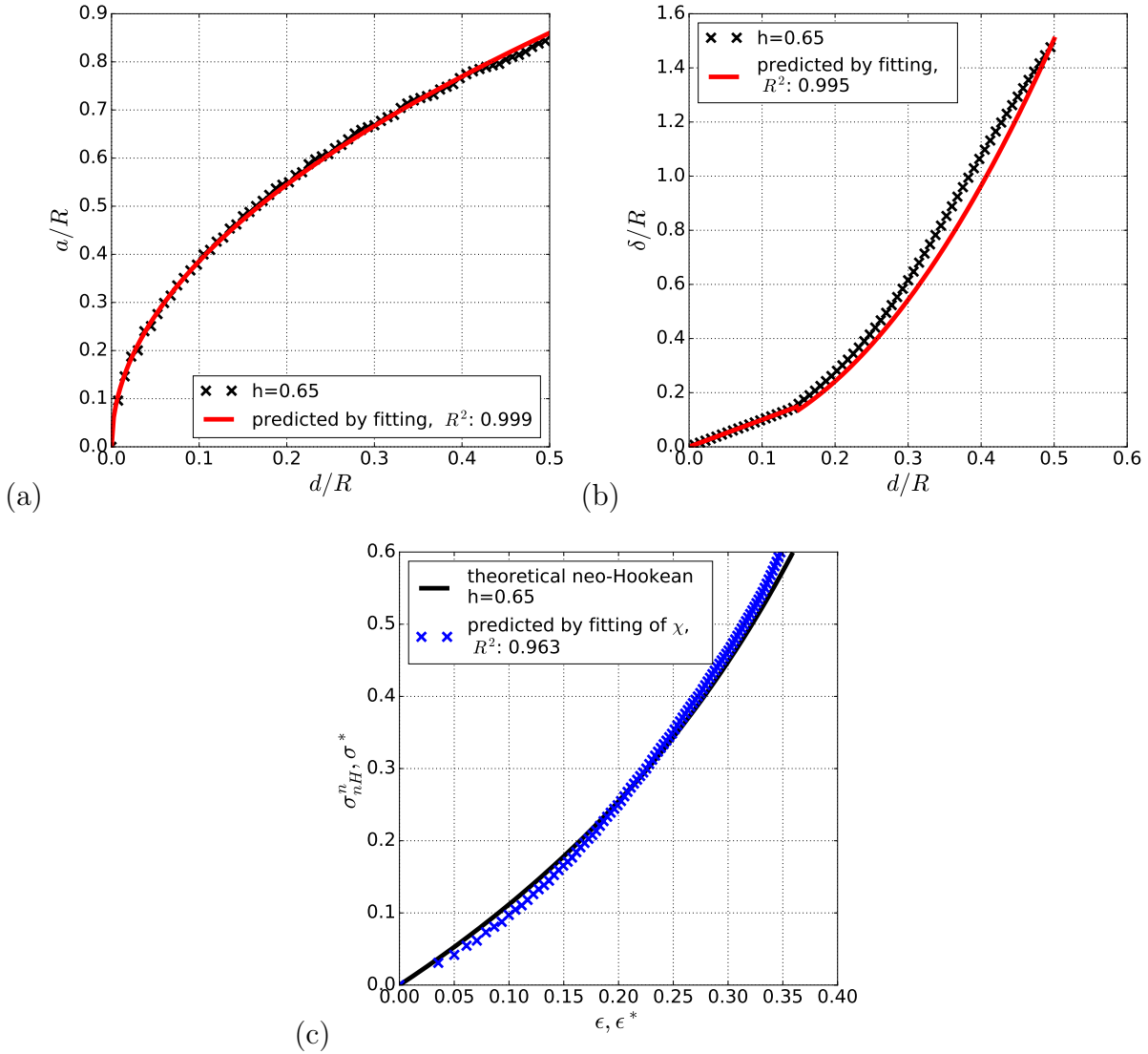


Figure 2.14 – Results for a finite element simulation of thickness ratio $h = 0.65$; (a) dimensionless contact radius a/R as function dimensionless compression tool displacement d/R and prediction according to fitting results of Equations (2.26) and (2.27), (b) dimensionless indentation depth δ/R as function dimensionless compression tool displacement d/R and prediction according to fitting results of Equations (2.30) and (2.31), (c) theoretical stress ($|\sigma_{nH}^n|$) for an incompressible neo-Hookean material with $\mu = 0.334$ MPa as a function of strain ϵ and fitted representative stress σ^* as function of representative strain ϵ^* for local spherical compression using the parameter χ according to Equation (2.33).

2.3.5 Comparison of hyperelastic laws

Verification of independence of the dimensionless contact radius a/R from the constitutive law is provided in Figure 2.15. The results of four simulations, using linear elastic, neo-Hookean, Mooney-Rivlin and Ogden material laws are presented for a sample thickness ratio $h = 0.75$. Further information concerning these hyperelastic laws are provided in Section 4.2.2. It can be seen that the contact radii superpose well for the four different material laws. These results emphasize findings of [Zhang and Yang \[2017\]](#), showing that material non-linearity does not influence the contact geometry. The applied material parameter are summarised in Table 2.5.

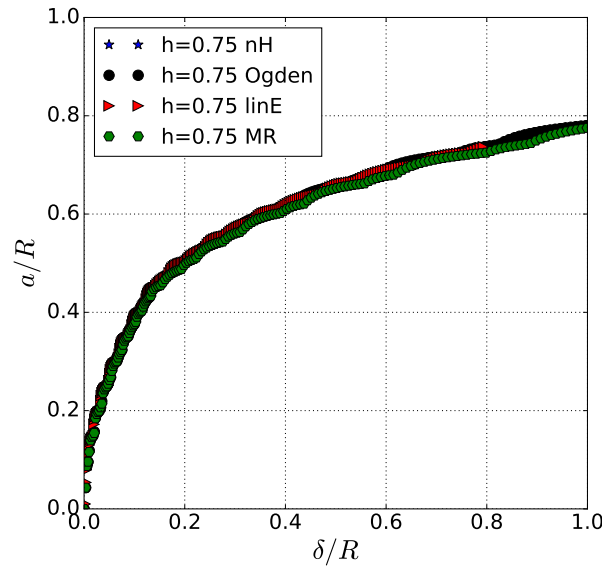


Figure 2.15 – Results of simulation of a sample with thickness ratio $h = 0.75$ and different material laws defined; linear elastic (linE), neo-Hookean (nH), Mooney-Rivlin (MR) and Ogden hyperelastic. Comparison of dimensionless contact radius a/R as a function of dimensionless indentation depth δ/R .

Table 2.5 – Summary of material parameter used for different material laws. Section 4.2.2 provides a more detailed description of those models.

material law	linear elastic	neo-Hookean	Mooney-Rivlin	Ogden
parameter	$E = 1 \text{ MPa}$, $\nu = 0.49$	$c_1 = 0.167 \text{ MPa}$, $D_1 = 0.12$	$c_1 = 0.3 \text{ MPa}$, $c_2 = 0.034 \text{ MPa}$, $D_1 = 0.12$	$\mu_0 = 0.334 \text{ MPa}$, $\alpha = 2.0$, $D_1 = 0.12$

Figure 2.16 compares the fitting for the parameter χ for the different simulations. The parameter χ is almost identical for the neo-Hookean ($\chi = 0.398$), Mooney-Rivlin ($\chi = 0.399$) and Ogden material law ($\chi = 0.398$). The fitting for the linear elastic material is obviously not satisfactory. The results reveal also sensitivity of the method of contact definition, since the stress decreases at the beginning of the simulation and increases as from 3% of strain.

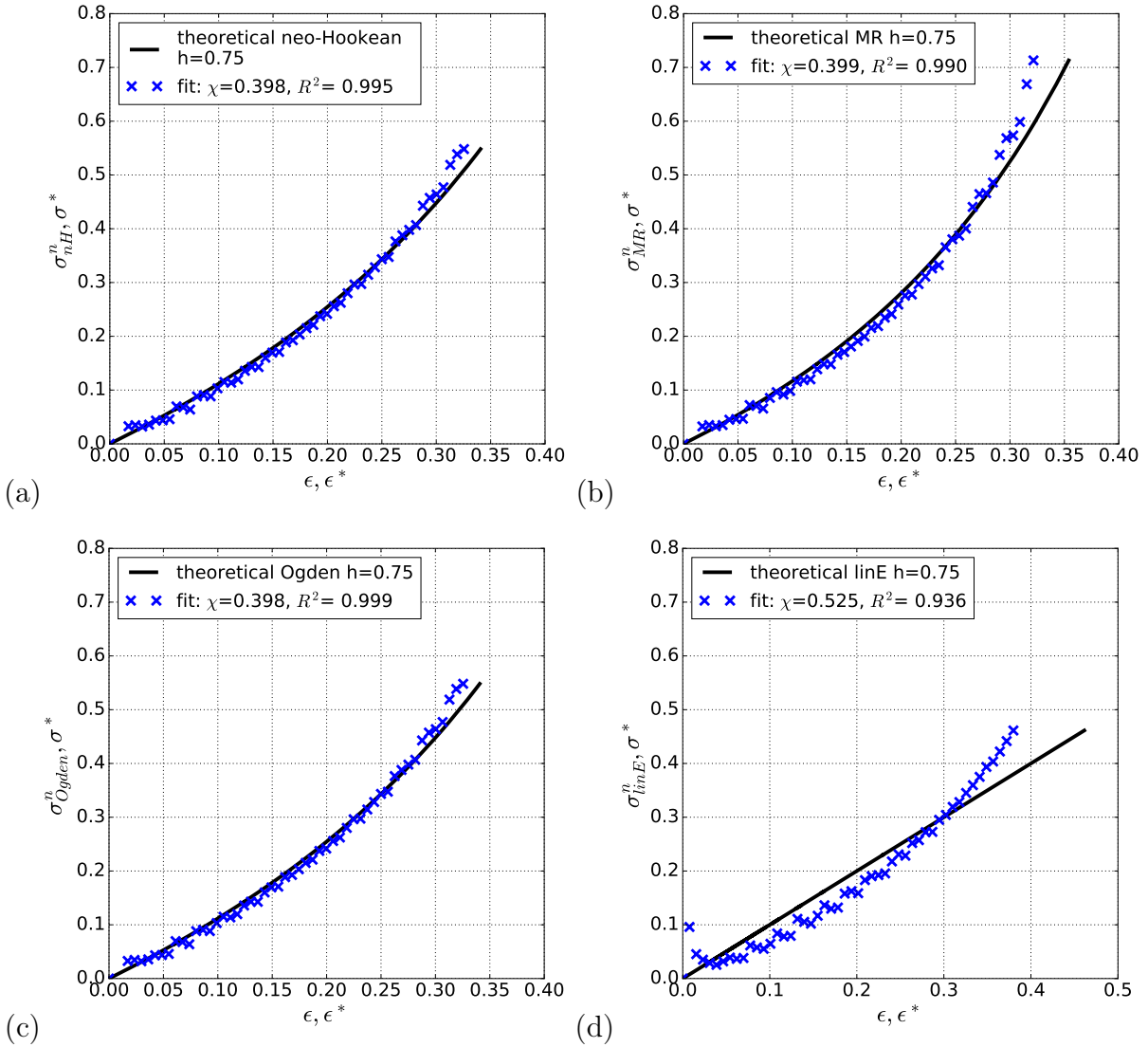


Figure 2.16 – Representative stress-strain curves for different material laws applied to the sample of thickness ratio $h = 0.75$, (a) neo-Hookean, (b) Mooney-Rivlin (MR), (c) Ogden, (d) linear elastic (linE).

As a conclusion, the procedure is valid for all models except the linear elastic approach. As consistent material parameter values were chosen for the models, it is relevant that similar parameter values were obtained through the procedure with $\chi \approx 0.4$. Furthermore, it can be observed that hyperelastic models describe well the compression process up to 30% strain. Even though hyperelastic models have been developed to describe large deformations, their accuracy is often higher for uni-axial tensile loads [Gent, 2012].

2.3.6 Density influence on samples behaviour

Since the simulations have been conducted considering gravitational load, its influence especially on samples with low thickness should be evaluated, in order to analyse detachment and bending behaviour. As can be deduced from Figure 2.17.a for a simulation with a thickness ratio $h = \frac{0.65\text{mm}}{1\text{mm}} = 0.65$, the application of density has a high influence on the samples detachment from the solid support. For the simulation considering density two regimes of the dimensionless contact radius a/R as a function of the dimensionless indentation depth δ/R are present; a linear one ranging from $0 < \delta/R < 0.18$ followed by a parabolic one. This behaviour is linked to the partial detachment of the samples intermediate part followed by the detachment of the distal zones. In contrast, if no density is applied to the sample its distal part loses contact with the support as from the beginning of the simulation. Furthermore, the dimensionless contact radius a/R as a function of the dimensionless compression tool displacement d/R is slightly lower for the sample without applied density (Figure 2.17.b). In summary, the application of density influences low thickness samples behaviour in such a way that samples do not detach in the same manner from the solid support. Which is why for the same compression tool displacement d slightly higher contact radii are obtained, consequently leading to higher forces measured.

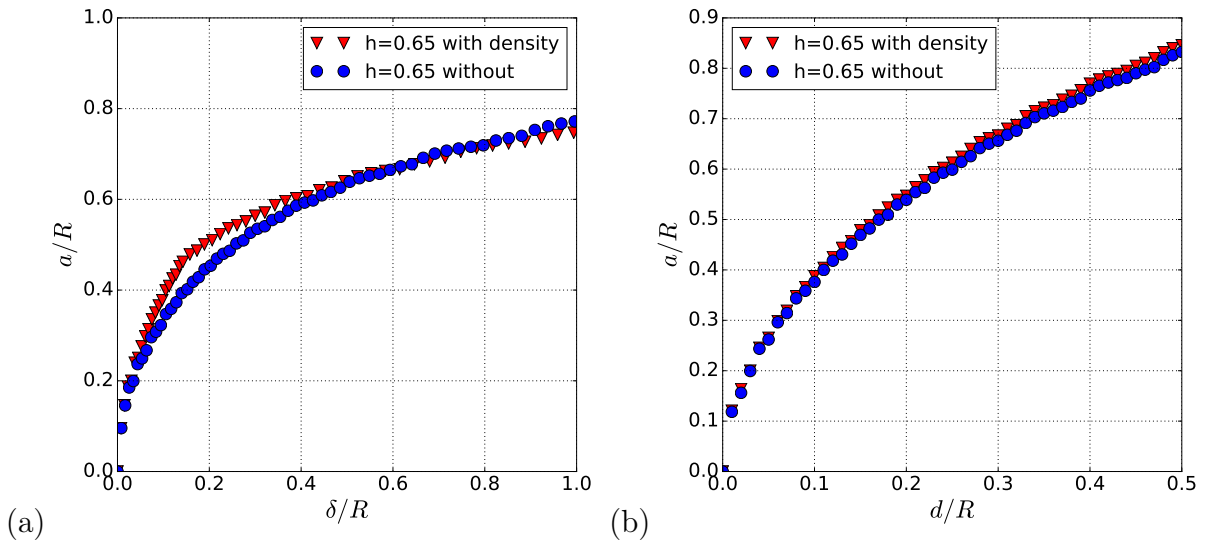


Figure 2.17 – (a) Dimensionless contact radius a/R as function of dimensionless indentation depth δ/R ; (b) dimensionless contact radius a/R as function of dimensionless compression tool displacement d/R .

2.4 Conclusion

In this Chapter a method was developed based on the approach by Lin et al. [2009] in order to find representative strain and stress for local spherical compression tests corresponding to a uniaxial load case. Experimentally, local spherical compression tests permit to test tissue samples in their integrity, cartilage samples can even remain attached to the underlying bone [Lee et al., 2016]. This is of a great advantage, since it allows testing samples in more physiologic conditions. However, spherical compression tests do not generate a uniaxial stress-strain state within the tested matter, leading to non-linear contact

conditions between the compression tool and the sample. Often biological samples are thin in thickness, causing that commonly used contact models, as the Hertz model, are not adapted to analyse results. The here presented method allows investigating contact behaviour and representative stress-strain state of thin samples that are not attached to their support. It should however be reminded that this method has its limitations. The simulated samples are axisymmetric, in contrast, biological samples are rarely of a uniform geometrical shape. Furthermore, the material simulated was considered as isotropic, homogeneous and quasi-incompressible, all characteristics that are usually not fulfilled by biological samples. Further development of the model regarding these aspects could be done in the future to include more characteristics in this analytical approach, but it is not the aim of this work. Nonetheless, this approach is worth giving a first characterisation of such materials that often require an inverse method through finite element simulations to go deeper in mechanical behaviour analysis. In fact, regardless of constitutive laws, parameters' initial values are required for optimisation and the closer to the true value the faster consistent results are obtained, as it will be presented in Chapter 4.

Chapter 3

Experimental characterisation of the temporomandibular joint disc

Contents

3.1	Introduction	50
3.1.1	Temporomandibular joint disc samples and animal models	50
3.1.2	Temporomandibular joint disc geometry and thickness	51
3.1.3	Biomechanical characterisation of temporomandibular joint discs	51
3.2	Materials & Methods	54
3.2.1	Temporomandibular joint disc sample preparation	54
3.2.2	Acquisition of temporomandibular joint discs external shape and internal microstructure	54
3.2.2.1	3D optical scans of temporomandibular joint disc samples	55
3.2.2.2	3D surface reconstruction of temporomandibular joint discs and printing of condyles	55
3.2.2.3	Magnetic resonance imaging of a temporomandibular joint disc	56
3.2.3	Mechanical tests	56
3.2.3.1	Local spherical compression tests	57
3.2.3.2	Local spherical compression test workbench	60
3.2.3.3	Internal strain analysis	64
3.2.4	Sample thickness calculation	64
3.3	Results and Discussion	66
3.3.1	External shape and internal microstructure of the temporomandibular joint disc	66
3.3.2	Local spherical compression tests	70
3.3.3	Internal strain analysis	84
3.4	Conclusions on experimental results	88

This Chapter gives a more detailed overview of local compression tests on the TMJ disc as well as an introduction to internal stresses occurring in biological tissues, techniques to obtain data on sample geometry and the animal models used (Section 3.1). Then, the material and methods concerning the experimental approach used in this study are presented in Section 3.2. The last Section (3.3) of this Chapter is devoted to the presentation of raw experimental results obtained in this work.

3.1 Introduction

As described in Chapter 1, its biochemical composition and structural organisation of collagen fibres make the temporomandibular joint disc a fascinating biocomposite. The non-exhaustive bibliographic study dedicated to the methods of shape characterisations, local compressive mechanical testing and internal stress analysis of the TMJ disc is presented below.

3.1.1 Temporomandibular joint disc samples and animal models

In order to experimentally study the biomechanical characteristics of the TMJ disc, tissue samples are needed. For obvious ethical reasons the *in vivo* study of the disc behaviour is difficult to conceive. Furthermore, obtaining human tissue samples is complicated and includes various formal procedures. Most human tissues studied in literature come from elderly donors, which makes investigation of healthy tissue complicated. Finally, before working on rare human samples, an expertise has to be gained from another model. For these reasons an appropriate animal model needs to be found. Comparative studies of the macroscopic anatomy and biochemical analysis of TMJ discs of human and several animals including pigs, dogs, cats, rabbits, rats, cows, sheep and goats concluded that because of similar anatomy, size of articular structures, disc's shape and omnivorous diet, the pig is the most suitable animal model to compare with humans [Bermejo et al., 1993; Kalpakci et al., 2011].

However, there are differences between human and porcine TMJ discs. Herring et al. [2002] studied pig jaws and found that compared to human they are more supported medially and laterally, nonetheless the gross anatomy is similar to human one's. Differences are found in dimensions that are larger in pigs, where for example condyles measure 21-25 mm in width in pigs and approximately 21 mm in humans [Herring et al., 2002; Valladares Neto et al., 2010]. The TMJ disc dimensions are larger in pigs compared to human [Matuska et al., 2016], what can be seen from Figure 1.2.a.

The most conspicuous difference is found in the morphology of the retrodiscal tissue, which is a fattier tissue for pig [Herring et al., 2002], compared to vascular human retrodiscal tissue [Athanasίου et al., 2009]. Herring et al. [2002] stated that the range of movement between human and pig is similar. Nonetheless, humans usually chew at a frequency of about 0.5-1.3 Hz, in contrast pigs chew faster at approximately 2.0-3.0 Hz [Druzinsky, 1993].

The glucosaminoglycan content between human and porcine samples shows a significant difference with human samples containing more GAG than porcine ones. Also, human tensile properties are higher; in incremental stress relaxation tests, the peak moduli (obtained from linear part of stress-strain curve) vary between approximately 10-55 MPa in human and 5-30 MPa in porcine samples depending on disc region [Kalpakci et al., 2011]. Nonetheless, human and porcine samples remain the most comparable ones according to

several authors [Detamore and Athanasiou, 2003a; Kim et al., 2003]. Kim et al. [2003] assume that direct comparison of mechanical properties of human and porcine TMJ disc is possible.

In spite of the differences presented, porcine TMJ discs have been chosen in this study. According to the method developed in Chapter 2, a peculiar attention has been brought to techniques allowing to measure sample geometry, especially the thickness in superinferior direction.

3.1.2 Temporomandibular joint disc geometry and thickness

As previously described, with its biconcave shape, the TMJ disc provides congruency between the bones of the TMJ, enhancing proper joint movements. In addition, it absorbs mechanical energy and distributes stresses, consequently its shape is highly related to its function. Dimensional measurements of soft biological tissues are not straightforward, in case of the TMJ disc, the curvatures induce thickness measurement difficulties.

While dimensions in mediolateral and anteroposterior directions can be evaluated using a calibrated ruler, thickness measurements are more demanding due to the disc's biconcavity and low thickness. To measure it, different methods were employed, ranging from measurements using optic microscopy [Commisso et al., 2014], needle perforation of the sample [Kim et al., 2003] or measurement of the distance between compression tools between which the sample was positioned [Lumpkins and McFetridge, 2009]. Commonly, the thickness of cylindrical specimens that were obtained from different disc regions were measured [Commisso et al., 2014; Lamela et al., 2011; Lumpkins and McFetridge, 2009]. Kim et al. [2003] conducted needle perforation on whole disc samples. Piercing a needle through their samples, they determined their thickness from the change in force - displacement curves.

Most studies on porcine samples found the central and medial disc region the thinnest parts and the posterior and anterior bands thicker. Thickness values for the disc's central part vary between 0.8 mm [Kim et al., 2003], over 2.14 mm [Commisso et al., 2014] and 2.25 mm [Lumpkins and McFetridge, 2009].

The diversity of the measured dimensions shows how paramount they are to characterise the TMJ disc. They might vary due to inter-species and inter-individual variance, but also on the experimental approach. The knowledge of the sample's dimensions and morphology and especially of this thickness is necessary in the biomechanical characterisation of the TMJ disc. Since one objective of this work is to test the TMJ disc samples in their integrity, non-destructive methods were chosen to characterise the samples dimensions. Especially for thickness measurements different approaches have been realised, a frequently used one, namely sample dimension measurement by the mean of distance calculation between compression tool and sample. In addition, 3D scans and magnetic resonance imaging techniques have been applied to characterise TMJ disc samples.

3.1.3 Biomechanical characterisation of temporomandibular joint discs

As it has been described in Chapter 1, several methods are applied to test biomechanical behaviour of the temporomandibular joint disc. In this study, it is the aim to carry out

characterisation on intact TMJ disc samples, therefore local compression tests are chosen as test method.

Local compression tests

As mentioned previously, local spherical compression tests became a common method to test biological soft tissues. Several advantages are associated with this test type. Since the sample is loaded only locally, it does not need to be prepared in a special way, it is not damaged and it can remain in its full integrity.

The choice of compression tool is important carrying out this kind of tests. Using a cylindrical flat ended compression tool can lead to high stresses on the sample at the edges of the cylinder [Lee et al., 2016].

Nonetheless, this type of test has already been conducted on TMJ disc samples. Actually, Beek et al. [2001] compressed complete human TMJ disc samples on three sites between cylindrical tools of a radius of 1.97 mm, at different frequencies (0.02/0.05/0.1 Hz) at maximum strains between 20 and 40%, obtaining stresses up to 15 MPa in the intermediate zone. Using a cylinder of 2 mm radius, at a frequency of 1 Hz and a strain of 10% Fazaeli et al. [2016] obtained stresses around 1.8 MPa testing porcine TMJ disc samples. Compared to Beek et al. [2001], Fazaeli et al. [2016] tested samples at higher frequencies but at lower compressive strain, which resulted in lower stresses acquired. The different test conditions used complicate proper conclusions on the TMJ discs biomechanical behaviour. To avoid peak stresses that can occur using flat ended compression tools, spherical tools can be used. So far, only nanoindentation has been conducted on the TMJ disc [Chandrasekaran et al., 2017; Juran et al., 2015; Yuya et al., 2010]. Due to the size of the spheres used in nanoindentation, the TMJ disc samples are tested very locally and only the surface layers' response is determined (see Chapter 1, Figure 1.3). For this reason, local spherical compression tests, using macro-spheres, are carried out in this work. Such tests were already used for characterisation of horse articular cartilage [Lee et al., 2016]. They demand a choice of compression tool size adapted to the sample size and shape so that in case of biconcave samples the compression tool does not touch areas that are higher than the tested part. Another important point is to choose the sphere size in a way that not only the surface layers are tested but also the layer detected in the histological cuts in Figure 1.5 (Chapter 1). For this reason, different sizes of spherical tools have been used. The inconvenience of spherical compression tools compared to cylindrical ones is the fact that stress and strain calculation are more complex as it has been presented in Chapter 2.

Internal stresses and strains

In biological structures stresses can occur without exterior forces applied. These stresses are called internal stresses; internal strains are linked to these stresses [Lanir, 2009; Nelson, 2014]. Several experimental methods to determine the internal stresses and strains exist, among others the open angle method, the strip curling method, the hole drilling and ring coring method or strains obtained from dissection [Le Floch et al., 2015; Liu and Fung, 1988; Nelson, 2014; Varner and Taber, 2010]. One example of the open angle method applied to a rat aorta from the work of Liu and Fung [1988] is presented in Figure 3.1.a. It can be observed that aorta specimens deform remarkably after the cut, highlighting that the aorta is not stress-free when it is unloaded.

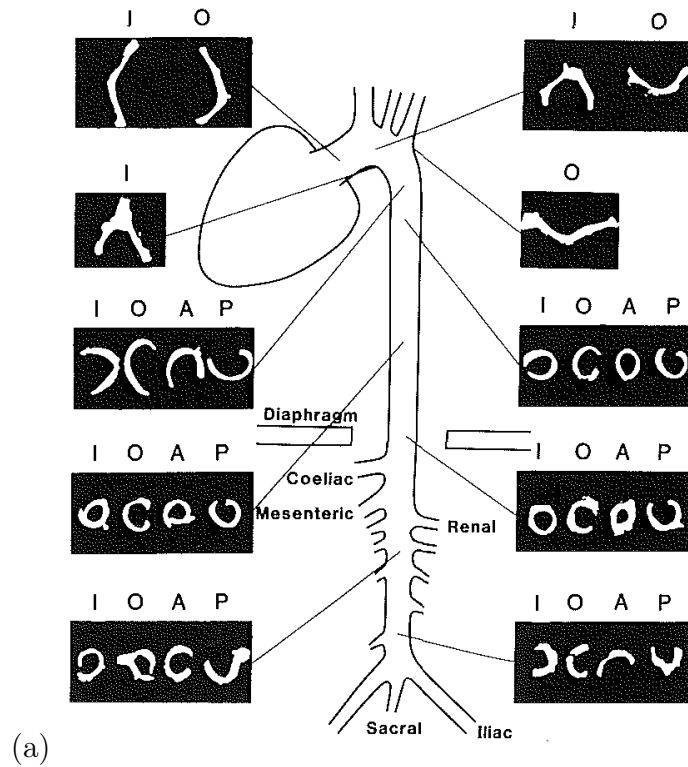


Figure 3.1 – (a) Photographs of the zero-stress configuration of aorta segments after internal stress release via open angle method from [Liu and Fung \[1988\]](#). Different sample positions have been analysed, A - anterior, P - posterior, I - inside, O - outside.

Up to date there is no known study that examines the internal stresses within the TMJ discs. [Commisso et al. \[2016\]](#) indicate the presence of prestresses within specimen obtained using cylindrical tissue punches. This lack of information is certainly due to the complexity to measure internal strains. Furthermore, due to its biochemical composition, including the differently orientated collagen fibres (see Chapter 1, Section 1.2), the TMJ disc is likely to be a site of internal stresses. For this reason, an internal stress analysis based on the hole drilling method was carried out in this work. The advantage of this destructive method is that after the internal strain analysis, the cut specimens can further be used as for instance in confined or unconfined compression tests. The purpose is to gain additional information and to further understand the disc's physiological conditions. The hole drilling method is frequently used for engineering materials (ASTM standard E837), but in this case amended to be used with biological soft tissues. Since on the TMJ disc as a biological sample, strains cannot be measured using strain gauges, the strains occurring on the tissues surface are exploited using image processing, allowing to draw conclusions on the internal stresses.

3.2 Materials & Methods

To characterise biological structures, appropriate experimental methods are needed. It is desirable to maintain the structures in their integrity and set up testing systems that mimic physiological conditions. For a complete understanding of the TMJ discs, the experimental characterisation in this study starts with harvesting of tissue samples and analysing their external shape and internal microstructure via optical scans and magnetic resonance imaging (MRI). The biomechanical characterisation is realised by local spherical compression tests and internal strain analysis. The following section describes the procedures followed and methods used to conduct the study of this important cartilage of the cranio-maxillo-facial area.

3.2.1 Temporomandibular joint disc sample preparation

As mentioned in Section 3.1.1 "Specimen and samples", for this study pigs were chosen as animal model, showing a lot of similarities with human TMJ discs. Pig heads were provided by a local slaughterhouse (la Maison Vagner, Marange Zondrange, France). All obtained samples were from hybrid large white - landrace pietran breeds, their age was around 220 days. Exact age, gender and weight could not be obtained due to complex procedure in the slaughterhouse.

After sacrifice, the heads were stored in a fridge at -4°C until the next day on which the discs were harvested. Knife, scissors and scalpel were used to harvest 13 discs as well as a saw to obtain the condyles. Detailed steps concerning this procedure are described in Appendix C.1, additional information on the samples are given as well. Discs were harvested with some surrounding tissue remaining, to allow fixation of samples without interfering with the disc's tissue, as presented in Figure 1.2.b. Anatomical directions are as well presented in Figure 3.6. The disc's dimensions in anteroposterior and mediolateral direction were documented taking photos including a calibrated ruler which allowed examination of dimensions via image processing software (ImageJ, 1.50d, National Institutes of Health, USA). Afterwards, discs were placed in hermetic containers filled with physiological solution (9 gNaCl/L) before freezing. Discs were kept frozen at -20°C until testing. The left and right condyles were kept in freezer bags and were frozen as well.

Prior testing, samples were thawed at room temperature and kept in physiological solution for at least 30 min before the experiments in order to equilibrate with the environment.

3.2.2 Acquisition of temporomandibular joint discs external shape and internal microstructure

In order to evaluate the disc's biomechanical behaviour, it is crucial to identify its geometry, especially its thickness and the internal microstructure. In most studies the disc was assumed as being flat on the inferior side, neglecting its physiological biconcave shape [Beek et al., 2001; Lumpkins and McFetridge, 2009]. To study the disc's geometry in conditions as close as possible to physiological ones, two different methods were adopted; optical scans and MRI imaging. The latter also allows internal microstructure observation.

3.2.2.1 3D optical scans of temporomandibular joint disc samples

Optical scans allow acquisition of the disc's and condyle's shape. The obtained three-dimensional datasets can be used to measure samples dimensions including thickness (see Section 3.2.4) as well as evaluating sample's biconcavity.

The 3D scans were carried out using an ATOS Compact Scan system (GOM GmbH, Braunschweig, Germany; system specification 5M/SO) in collaboration with Solsi-CAD (Woippy, France) and more precisely Mr Hatton. The system, consisting out of two cameras, a sample area and a PC for image reconstruction, is depicted in Figure 3.2.a.

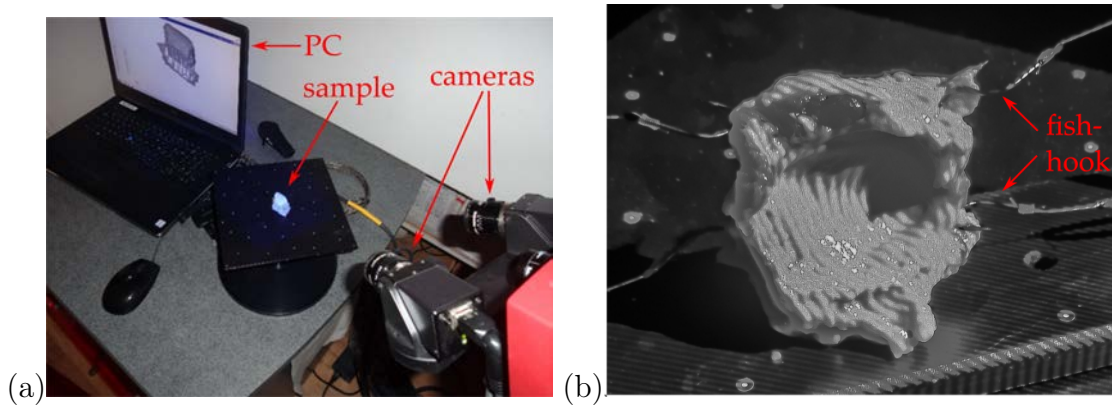


Figure 3.2 – (a) Setup for 3D scan using the ATOS-system (GOM, Germany) from Solsi-CAD (Woippy, France), (b) sample in vertical holding system.

In a first attempt, the disc was scanned placed on a condyle, to create the most physiological condition possible. The condyles were scanned separately as well. In order to obtain the disc's dimensions in superoinferior direction, the samples were placed in a holding system and maintained in position using fish-hooks (see Figure 3.2.b). The method of the sample's thickness evaluation is presented in Section 3.2.4.

3.2.2.2 3D surface reconstruction of temporomandibular joint discs and printing of condyles

Using the GOM Inspect software (GOM Software 2017, Hotfix 1, Rev. 103616, build 2017-08-09), the 3D surfaces of the condyles and the TMJ discs were reconstructed. Post-processing steps included correction of scanning artefacts and closing of mesh gaps.

Condyle models were additionally post-processed using MeshLab (MeshLab, Visual Computing Lab - ISTI - CR; Version 1.3.2_64bit) to combine single scans to average left and right condyle models. These models were printed using a 3D printer (Form 2, Formlabs, Somerville, Massachusetts, USA; Formlabs resin: Standard Black, FLGPBL04). The precision of the 3D printer was calibrated printing cubes of different edge sizes highlighting variation between 0.7-2.2% between the model and the printed sample. Additional information concerning the 3D prints and the calibration are presented in Appendix C.2.

The optical scans do not allow looking inside the highly organised structure of the TMJ disc. Since its microstructure is known to influence its biomechanical behaviour (Section 1.2), observation of the TMJ disc's microstructure might give a further understanding of its function. Magnetic resonance imaging is a common medical tool enabling

to image cartilages and joint tissues through their water content. Therefore, MRI has been conducted to get insight into the TMJ disc.

3.2.2.3 Magnetic resonance imaging of a temporomandibular joint disc

The magnetic resonance imaging system of the Institut Jean Barriol (Université de Lorraine) was used for image acquisition. It consists out of a 14.1 T vertical superconducting magnet Avance III 600 Wide Bore (Bruker, Germany). The micro-imaging probe (MicWB57) was equipped with a 40 mm quadrature resonator.

The sample was positioned inside a tube that was inserted in the probe and then placed into the MRI system. Complete TMJ disc samples fit undamaged in the tube of 31 mm internal diameter and height of 80 mm. The field of vision (FOV) is 25 mm, which allows observing the entire disc sample.

In order to position the disc in the FOV and to further obtain physiological test conditions, the disc was glued using cyanoacrylate (ethyl 2-cyanoacrylate, Loctite Super Glue 3 Power Flex Gel, Henkel) to a 3D printed condyle, which served as a sample holder once assembled with a support. Together with the positioning system the TMJ disc sample was placed inside the tube. Preventing the sample to dry out, physiological solution was added until the sample was completely covered. Figure 3.3 shows a sketch of the experimental setup. During image acquisition, the temperature inside the MRI system was 24 – 25°C and could not be further controlled.

Imaging was carried out in main anatomical planes (sagittal, transverse and frontal), with three images per plane. Parameters of image acquisition can be found in Appendix C.3 (Table C.4 and Table C.5). A full scan was performed over a night to obtain a 3D geometry of the disc.

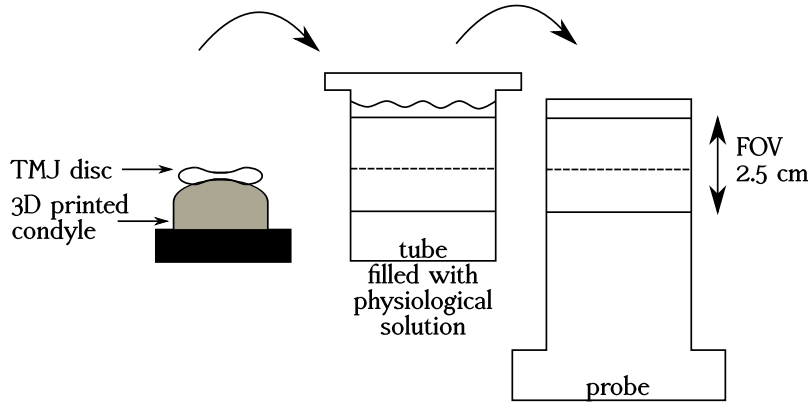


Figure 3.3 – Sample positioning and setup for MRI acquisition.

3.2.3 Mechanical tests

After characterisation of the TMJ discs shape via optical scans and MRI, the biomechanical behaviour was studied in local spherical compression tests and internal strain analysis was carried out.

3.2.3.1 Local spherical compression tests

The range of motion supported by the TMJ is large, from mouth opening and closing to chewing or even teeth clenching. In order to understand the disc's behaviour under various conditions, experiments at different loading and unloading frequencies are carried out. The physiological frequency of human chewing varies between 0.5 Hz-1.3 Hz, the one of pig - our animal model - is higher (2.0 Hz-3.0 Hz) [Druzinsky, 1993]. To cover human physiological ranges, frequencies commonly used are 0.1 Hz - 2.0 Hz [Barrientos et al., 2016; Lumpkins and McFetridge, 2009; Tanaka et al., 2003b]. To take into account static loading that might occur during clenching, quasi-static loading frequencies should be used while higher ones might be more suitable to study the disc's behaviour during joint activity such as eating or talking. For this reason, the frequencies intended to be used in this study to test the samples were 0.01 Hz, 0.1 Hz and 1.0 Hz. However, due to limitations of the testing machine (see Appendix C.4) the following frequencies were really applied: 0.01 Hz, 0.095 Hz and 0.625 Hz.

The loading protocol including a preconditioning phase, search for preload, cyclic loading and a relaxation phase is depicted in Figure 3.4.

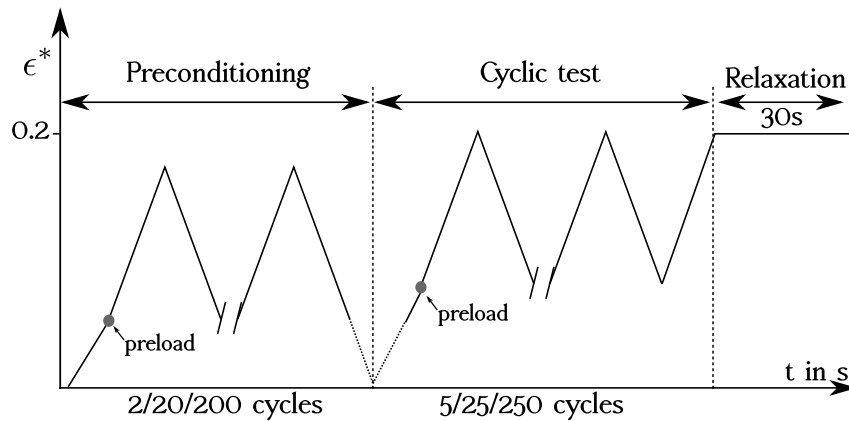


Figure 3.4 – Experimental loading protocol; the number of test cycles depends on the loading frequency (0.01 Hz/0.1 Hz/1 Hz), the related preload is presented in Table 3.1.

It is desirable to obtain comparable sample behaviour for all test frequencies and to keep the time span of load constant. Different number of preconditioning and loading cycles for the three different frequencies were therefore chosen, which are indicated in Figure 3.4.

Furthermore, spherical compression tools of three different radii were used; 3 mm, 1.75 mm and 0.875 mm. The sizes were chosen with regard to the samples biconcave shape so that interaction with the anterior and posterior band are avoided. Additionally, using different compression tool sizes, the zones observed in the histological study (Figure 1.5) can be examined. As indicated in Figure 3.4, the loading protocol includes a preload and loading reaches a certain strain. In order to be able to compare experimental results obtained with the three spherical compression tools, equivalent pre-stress-pre-strain conditions should be applied to the sample. In the following, the approach to calculate equivalent preloads as well as equal final strains is presented.

In order to apply the same prestress to the sample while using different sizes of spherical compression tools, the following equation has to be verified:

$$\sigma_{R1} = \sigma_{R2},$$

with $\sigma_{Rx} = \frac{F}{A} = \frac{F_{Rx}}{\pi a_{Rx}^2}$ the stress for a compression tool of radius R_x and $a_{Rx}^2 = d_{Rx} R_x$, where a_{Rx} is the spherical compression radius, d_{Rx} the spherical compression tool's displacement as defined by Hertzian contact formulation. This equation leads to:

$$F_{R2} = F_{R1} \frac{R_2 d_{R2}}{R_1 d_{R1}}. \quad (3.1)$$

Relation 3.1 gives F_{R2} as a function of two unknowns, namely d_{R2} and d_{R1} . Therefore, admitting the homogeneity of the disc tissue, the following relationship for final equivalent strains can be used:

$$\epsilon_{exp\ R1} = \epsilon_{exp\ R2}. \quad (3.2)$$

Actually, if we consider the spherical compression process as mainly a 1D compression for which we consider the Hooke's law to be valid ($\sigma = E\epsilon$), we can introduce a representative strain measure in correspondence with uniaxial compression (see Chapter 2):

$$\epsilon^* = \chi \frac{a(h)}{R}. \quad (3.3)$$

Since for the preload we are in the domain of small strains, the Hertzian contact is supposed to be valid. So, it can be written:

$$\frac{a_1}{R_1} = \frac{a_2}{R_2}, \quad (3.4)$$

with $a_{Rx}^2 = d_{Rx} R_x$ leading to:

$$d_1 = \frac{R_1 d_2}{R_2}. \quad (3.5)$$

Combining Equation (3.5) with (3.1):

$$F_{R2} = F_{R1} \frac{R_2^2}{R_1^2}. \quad (3.6)$$

Preloads calculated with the acceptable reference load of 0.0136 N for the smallest spherical compression tool are presented in Table 3.1.

Table 3.1 – Overview of preloads F_{init} for local spherical compression tests, calculated with reference of $F_{init} = 0.0136$ N for a spherical compression tool of 0.875 mm radius.

radius R of spherical compression tool [mm]	initial force F_{init} [N]
0.875	$F_{R1} = 0.0136$
1.75	$F_{R2} = 0.0544$
3.00	$F_{R3} = 0.16$

The maximum strain applied to the samples should be in the physiological range of loading and the strains should be comparable for the different compression tool sizes used.

The maximum joint space reduction during clenching is stated to be 5-10% [Kuboki et al., 1999]. For the smallest spherical compression tool, the maximum applied strain should therefore be about 10%, however preliminary tests have shown that this is not sufficient to obtain measurable forces, that is why a maximum strain of $\epsilon_{exp}^* = 20\%$ was chosen.

Applying the same maximum strain for the three spherical compression tools leads to different compression tool displacements d , which are calculated in the following manner:

$$\begin{aligned}\epsilon_{exp\ R1} &= \epsilon_{exp\ R2}, \\ \chi \frac{a_{R1}}{R1} &= \chi \frac{a_{R2}}{R2}.\end{aligned}\tag{3.7}$$

In a first approach we defined χ_{exp} as (see Hertz solution):

$$\chi_{exp} = \frac{4}{3\pi(1 - \nu^2)}\gamma.\tag{3.8}$$

If incompressible materials are considered ($\nu = 0.5$), which is representative for the TMJ disc due to the high amount of water (Section 1.2), it leads to:

$$\chi_{exp} = 0.57\gamma.\tag{3.9}$$

The constant γ was estimated in the first attempt, fitting the following equations to dimensionless contact radius - indentation depth curves (see Chapter 2):

$$\frac{a}{R} = \gamma \left(\frac{\delta}{R} \right)^{0.5}.\tag{3.10}$$

The obtained values for γ , corresponding values for χ , the resulting displacements and velocities as well as representative strain ϵ^* according to results in Chapter 2 are summarised in Table 3.2 for an arbitrary chosen thickness of 2 mm as it cannot be known a priori. Although it is a consistent value according to the literature (Section 1.2).

Table 3.2 – Overview spherical compression distances for an experimental reference strain of $\epsilon_{exp} = 20\%$ compared also to representative strain ϵ^* and fitting parameter χ according to Chapter 2.

spherical compression tool radius R_x [mm]	fitting parameter for contact radius-indentation depth curves γ	fitting parameter for representative strain χ_{exp}	compression tool's displacement d_{Rx} [mm]	compression velocities [mm/s] for 0.01/0.1/1 Hz	χ	ϵ^*
$R_1 = 0.875$	0.91	0.519	$d_{R1} = 0.13$	0.0026/0.026/0.26	0.382	14.7%
$R_2 = 1.75$	1.02	0.581	$d_{R2} = 0.21$	0.0042/0.042/0.42	0.391	13.5%
$R_3 = 3$	1.13	0.644	$d_{R3} = 0.29$	0.0058/0.058/0.58	0.408	12.6%

The experimental reference strain of ϵ_{exp}^* and the representative strain ϵ^* differ due to final determination of factor χ according to Chapter 2, Section 2.3.3 "Representative stress - strain curves", which is also summarised in Table 3.2 for samples of thickness ratio $h = \frac{2mm}{R_x}$.

3.2.3.2 Local spherical compression test workbench

A universal testing machine (Zwicki, Zwick Roell, Ulm, Germany) equipped with a 10 N loadcell (Xforce P, uncertainty class 1 above 0.04 N and 0.5 above 0.2 N) was used for local spherical compression experiments. The samples were tested in an environmental testing chamber filled with physiological solution (9 gNaCl/L) which had a temperature of 37°C at the beginning of each test mimicking body temperature, as recommended by [Detamore and Athanasiou \[2003a\]](#). Solution was heated in a basin outside the environmental testing chamber using a heating immersion circulator. A pump allowed renewing of solution via connecting tubes within the testing chamber before every new test. During experiments, the solution level was chosen to an extend so that samples were half immersed. This is to ensure that the sample is not drying out and to avoid interactions of the compression tool and solution as for instance adhesion or capillary effects might occur. The experimental setup is shown in Figure 3.5.

To further obtain a physiological test position, the disc samples were carefully attached on their surrounding tissue to a 3D printed condyle using cyanoacrylate. The 3D printed condyles served as a sample holder and were obtained like those used in MRI acquisition (see Section 3.2.2.2). Another advantage of this holding system is that the disc's biconcave shape on the inferior sample surface is balanced, so that the superior surface is easier accessible (see Figure 3.5.b) providing the possibility of compression tests normal to the sample's surface. Samples were compressed on three different sites (central, medial, lateral) as illustrated in Figure 3.6. Anterior and posterior sites could not be tested since compression normal to the curved surface could not be ensured. To enable equal distances between compression sites, the environmental chamber is connected to a micrometre positioning stage. The distance between the testing spots, was chosen as 25% of the disc's mediolateral dimension.

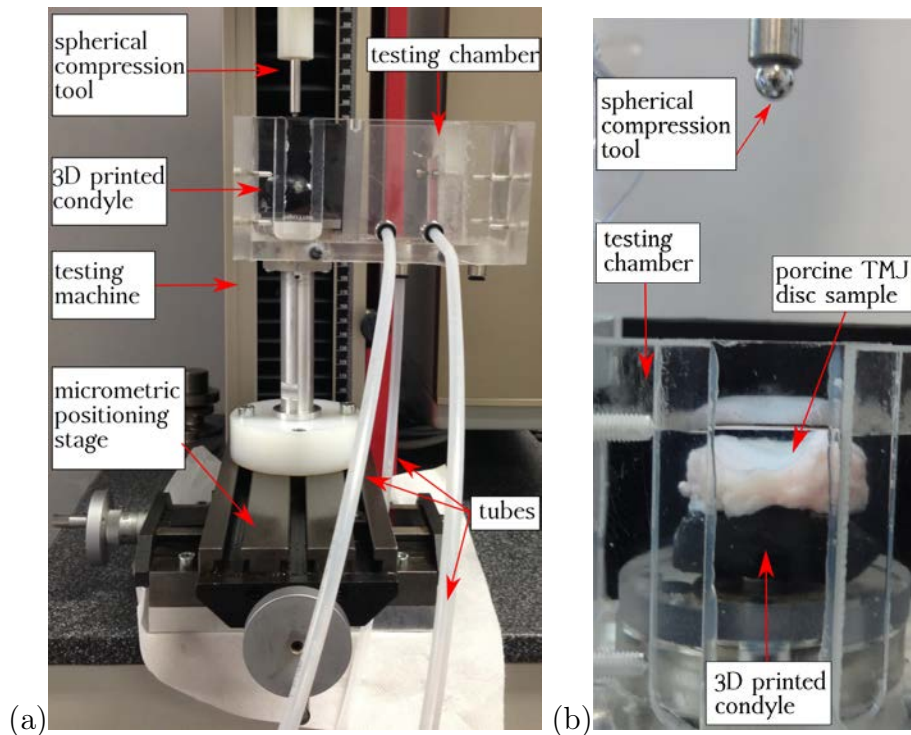


Figure 3.5 – (a) Experimental setup for local spherical compression tests, (b) close-up to the TMJ disc sample.

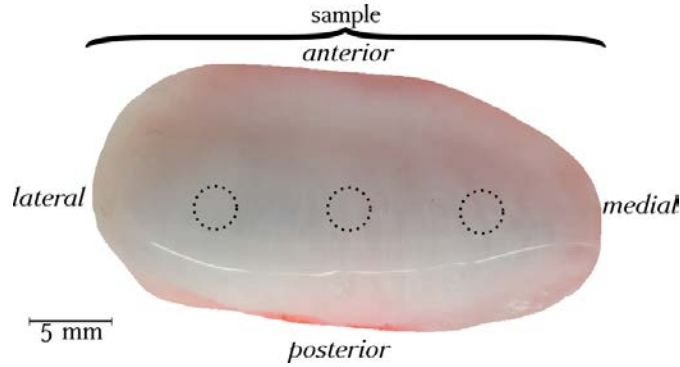


Figure 3.6 – Lateral, central and medial test sites of local spherical compression tests. Shown is the superior view of a left TMJ disc.

To summarise, on each sample 27 tests were done. In all, on three test sites, using three compression tools at the three chosen frequencies. Every test site was examined once per test condition and while other sites were tested, it was allowed to relax and equilibrate to ensure that its loading history does not influence following experimental runs. TMJ disc samples are known to recover after 4-5 minutes [Beek et al., 2001; Tanaka et al., 2003b]. This time was easily respected during experiments, with at least 45 min between tests on the same test site.

Due to the duration of the experiments (in total 14 hours) the tests on one sample were conducted on two consecutive days. The samples were kept overnight in physiological solution and stored in a refrigerator at 4°C. To validate the assumption that these storing conditions do not influence the experimental results, one repetition test was carried out per sample. This repetition was a test on the central zone at 0.1 Hz using the compression tool of 3 mm radius.

In total six samples were tested through the same procedure, three right and three left ones from three donor animals, which were harvested approximately seven month prior experimental characterisation. Calvo-Gallego et al. [2017] showed that long term storage of TMJ disc samples has only small effects on samples viscous behaviour during compressive stress relaxation tests. Therefore, it is assumed that the samples were not affected by storing conditions. An overview of sample dimension is presented in Table 3.3.

Table 3.3 – Overview of sample dimensions used during local spherical compression tests (mean \pm standard deviation). Further information regarding the samples are given in the Appendix Table C.1.

sample no.	side	mediolateral [mm]	anteroposterior [mm]
1	left	30.85 ± 0.16	15.48 ± 0.13
2	right	29.65 ± 0.15	15.62 ± 0.15
3	left	26.39 ± 0.28	13.74 ± 0.41
4	right	27.66 ± 0.54	15.15 ± 0.22
5	left	27.79 ± 0.43	12.54 ± 0.18
6	right	27.64 ± 0.55	14.66 ± 1.09

Machine stiffness

The testing system consists out of the load cell, the compression tool holder, the spherical compression tool, the environmental chamber, the 3D printed condyle, the chamber's

holding system and the micrometre stage (see Figure 3.5). Except for the load cell and the micrometre stage, the parts of the testing system are custom-made. Since the stiffness of all parts is unknown, it needs to be measured in order to avoid distortion and misinterpretation of experimental results. Therefore, the testing system was evaluated under compression up to forces of 1 N to 2 N at a velocity of 0.005 mm/s. Stiffness tests were carried out in consecutive steps, removing one component more from the system after each measurement to identify the stiffness of each of them. The results demonstrate that the load cell is the most flexible part of the testing system with a stiffness of $k_m \approx 18 \text{ N/mm}$. The resulting force - displacement curve of load cell compression is shown in Figure 3.7. These results are important compared to compression tool displacement and therefore leading to a necessary correction of local compression data obtained from TMJ disc sample tests. The correction was performed following the direct technique described by Kalidindi et al. [1997]. The testing system and the sample are considered as two springs in series. The measured force F is defined as the product of total displacement d_t of both springs and stiffness k :

$$F = kd_t. \quad (3.11)$$

The total displacement of the assembly d_t is the sum of the machine displacement d_m and the sample displacement d_s :

$$d_t = d_m + d_s. \quad (3.12)$$

Since the force acting in both springs is the same, this enables to deduce the sample displacement:

$$d_s = d_t - \frac{F}{k_m}, \quad (3.13)$$

with k_m being the machine stiffness.

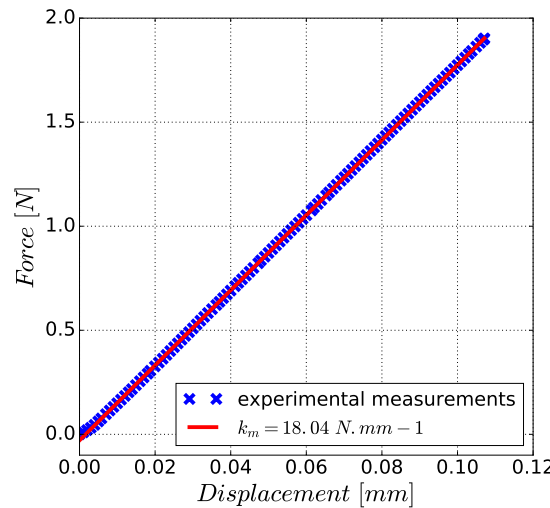


Figure 3.7 – Force as a function of displacement for a compression test of the load cell with the calculated load cell stiffness k_m of 18.04 N/mm.

Since the testing system needed to be dismantled between the testing days, the stiffness of the system was monitored. Therefore, after changing the compression tool, compression

tests on each of the three testing sites without sample has been carried out. They did not show any changes in the system stiffness, therefore it can be assumed that the system stiffness did not further influence the experimental results.

Data processing

Experimental characterisation using local spherical compression led to a high amount of data. In order to handle data processing and analysis, data were organised; the structure of the database is presented in Appendix C.5. The tests are referenced as the following YYMMDD_EXX. Python scripts (version 2.7.12) based on functions from the libraries *Bibliothèque d'Analyse de Mesures Expérimentales (BAME)* [Chapuis, 2011] and *bio2ms* (development by our biomechanical team of the LEM3 laboratory) were used for exploitation.

Different results were plotted to highlight the complex behaviour of the TMJ disc:

Force vs displacement curves allow observation the disc's non-linear and viscous behaviour.

Maximal forces per test cycle vs time highlight the force peaks for each test cycle allowing to study the effect of force accommodation during loading.

Hysteresis per test cycle is calculated as enclosed area between loading and unloading phase in the force - displacement loop via the trapezoidal rule highlighting viscous disc behaviour and commonly interpreted as energy loss.

Force vs time curves during the final relaxation phase present a viscous characteristic of the samples.

3.2.3.3 Internal strain analysis

Since internal strain analysis has not yet been conducted on the TMJ disc, it has been the aim of this work, to examine if they are present in this tissue and to characterise them.

To do so, a graphite pattern was applied on intact disc samples, as depicted in Figure 3.8.a. Afterwards, a perforation of 8 mm is cut of the disc's central zone (see Figure 3.8.b) using a cylindrical cutting tool. Subsequently, the disc sample and the hole drilling specimen were observed using a camera (SONY HDR-CX240E; 1280x720 pixel, frame-rate: 25 fps) for 50 min after perforation. During this period both the disc sample and the hole drilling specimen were immersed in physiological solution.

Two methods were used to investigate specimen behaviour after perforation:

global measurement The hole drilling specimen's dimensions were evaluated directly after cutting (time 1 min) and after 50 min using ImageJ software (ImageJ 1.50d, NIH, USA).

digital image correlation (DIC) In cooperation with the *Laboratoire de Mécanique et Génie Civil* of Montpellier, DIC analysis was carried out to estimate internal strain within the samples [Dusfour, 2018].

The DIC method developed by Dusfour [2018] consists of a backward approach from the relaxed condition ($t = t_{final}$) to reach the initial state and access the internal strain. In addition access to the stress through a constitutive law is possible. For this study, cylindrical coordinates were used and are represented in Figure 3.8.c.

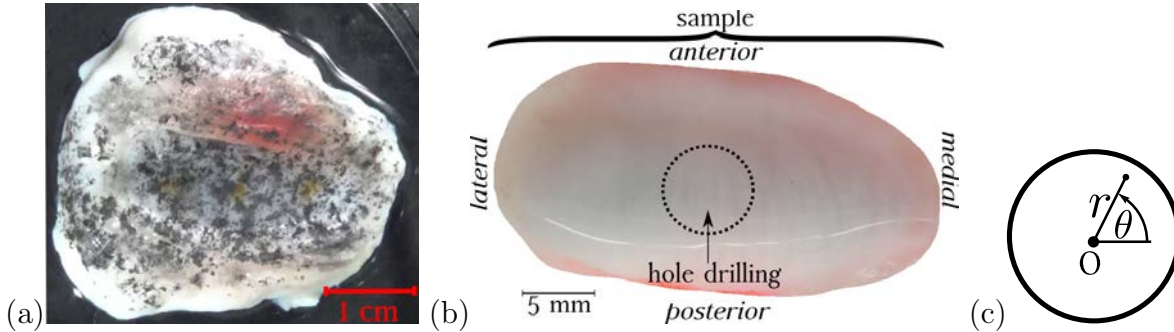


Figure 3.8 – (a) Graphite pattern on TMJ disc sample before hole perforation, (b) site of hole drilling. A \varnothing 8 mm specimen was taken from disc's central area. (c) Cylindrical coordinate system used to evaluate results.

3.2.4 Sample thickness calculation

Data concerning the disc's thickness is crucial in order to interpret experimental results (e.g. stress-strain data) and to simulate properly the disc's behaviour in finite element calculations.

In this study, different methods have been used in order to determine the thickness of TMJ disc samples. The measurements were based on the methods previously described to study the TMJ disc:

3D scans Both types of 3D scans (see Section 3.2.2.1) were used to characterise TMJ disc thickness. The two scans of the first attempt, one containing data of the condyle

only and one containing data of condyle and disc, were post-processed individually and then compared using the software GOM Inspect (GOM Software 2017, Hotfix 1, Rev. 103616, build 2017-08-09). First post-processing steps included correction of scanning artefacts and closing of the mesh gaps. In the second step the creation of perpendicular distances between the two surfaces was realised. Five data rows (one anterior, one posterior, three central) were defined each containing 5-6 distances and evaluated with GOM Inspect on one sample. However, this software does not allow surface evaluation. That is why CloudCompare software (CloudCompare Omnia, Version 2.9.1) was used for evaluation of three vertically scanned samples. A region of interest, containing the disc's central zone, was defined and thickness measurements carried out, using a point-to-surface method.

MRI The three images from the sagittal plane from one TMJ disc sample (see Section 3.2.2.3) served for thickness evaluation of the central zone (superoinferior direction) using imageJ (1.50d). For each of the three images, the thickness was measured on three sites within the central zone (n=9).

Crosshead travel of uniaxial test machine The comparison between the compliance test data (see Section 3.2.3.2) at first contact of the compression tool with the 3D printed condyle and the experimental data permits calculation of sample thickness T_{sample} :

$$T_{sample} = s_{contact} - s_{preload}, \quad (3.14)$$

with $s_{contact}$ crosshead travel in mm during compliance test at moment of contact compression tool - 3D printed condyle and $s_{preload}$ crosshead travel in mm during experiments at moment when preload is reached.

Micrometre The specimen obtained by the hole drilling method were measured using a micrometre (0-25mm, 0.01mm). Due to their relatively large diameter, thickness measurements were obtained at the specimens largest and thinnest part, as can be seen in Figure 3.9.

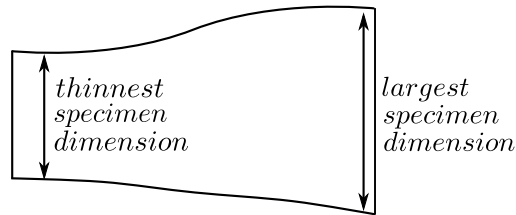


Figure 3.9 – Sketch of superoinferior view of hole drilling specimen, with indication of thickness measurement points.

3.3 Results and Discussion

Compared to the material and method Section, the results and discussion Section presents first the TMJ disc sample dimensions, then results from mechanical tests and finally the internal strain observations.

3.3.1 External shape and internal microstructure of the temporomandibular joint disc

The optical scan generates surfaces of the condyle and the disc as can be seen in Figure 3.10.a. Due to reflections of the humid and whitish tissue the scans contain gaps, however general dimensions can be measured. As depicted in Figure 3.10.a, distance measurements between the superior disc surface and the condyle's surface serve to evaluate disc's thickness. The different anatomical zones were evaluated separately (see Figure 3.10.b). Posterior band was found thicker than anterior band and the central region with an average of 3.24 mm was the thinnest region. The difference in thickness is consistent with previous findings [Athanasίου et al., 2009; Detamore and Athanasίου, 2003a]. Results are summarised in Table 3.4.

Table 3.4 – Measured thicknesses in the three anatomical regions: anterior, central, posterior from the optical scan depicted in Figure 3.10.a.

	anterior	central	posterior
number of measurements	5	18	5
mean [mm]	6.14	3.24	7.43
standard deviation (STD) [mm]	0.26	0.63	0.33

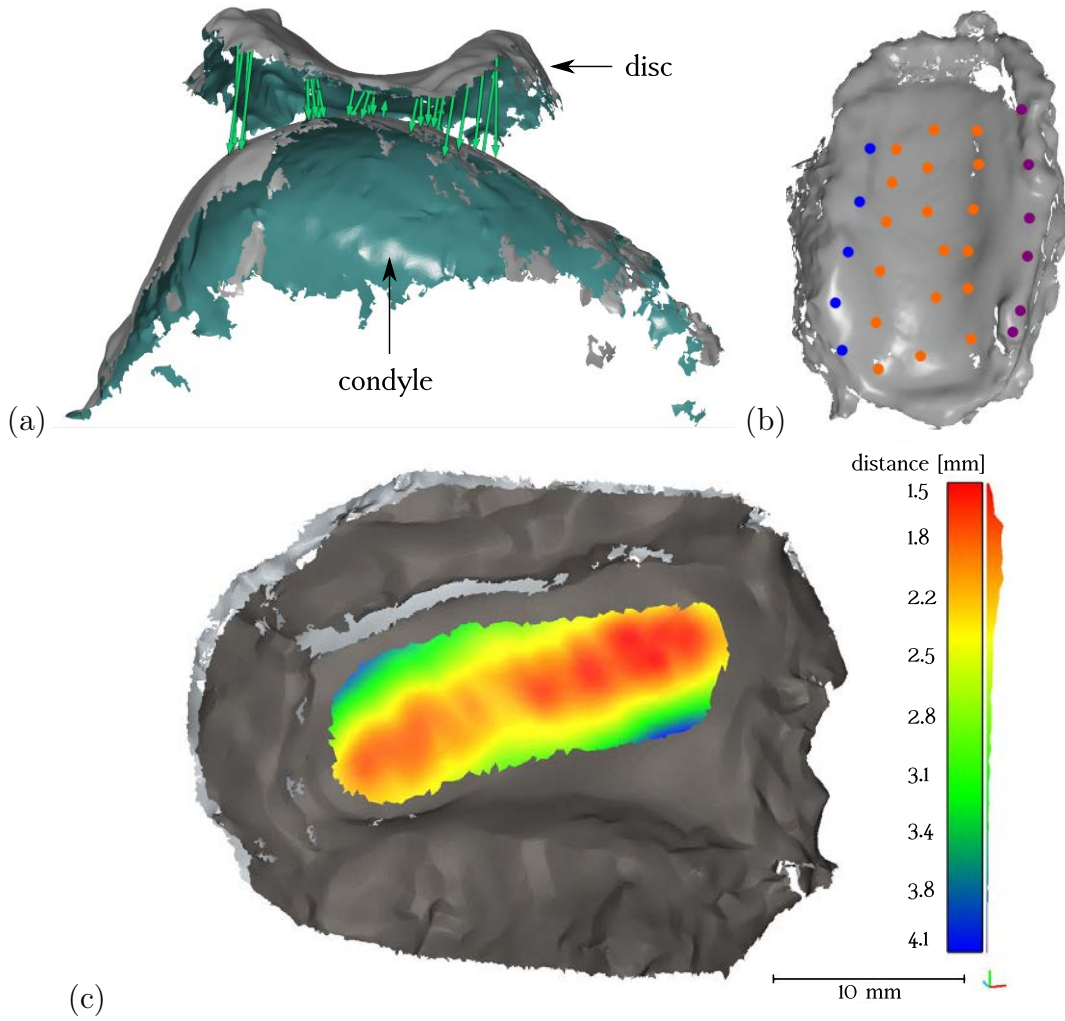


Figure 3.10 – (a) Obtained scans from condyle and disc surfaces as well as thickness measurements between them using GOM Inspect software. (b) Location of measurement points for thickness evaluation on **anterior**, **central** and **posterior** disc area. (c) Thickness measurements using CloudCompare software; for the sample shown the average thickness (\pm STD) is: 2.30 ± 0.53 mm. The grey areas were not included in the thickness measurement.

The measurement technique placing the disc on the condyle has the disadvantage that disc thickness cannot be measured directly but indirectly through distance measurement between disc and condyle. For this reason, the second attempt with the TMJ disc in vertical scanning position has been undertaken.

Figure 3.10.c shows one example from the thickness measurements conducted on the central part of the three samples vertically scanned (for additional results see Appendix C.6). The coloured areas mark the regions included in the measurement zone whereas grey zones were excluded. It can be observed that the thinnest part is the intermediate zone with a dispersion in mediolateral direction. In anteroposterior direction the highest thickness values are found, which reach up to 4.1 mm for the sample shown. The thinnest area is the medial region, with a thickness of 1.5 mm for the same disc. The mean values for the zones measured on all three scanned discs are summarised in Table 3.5. 3D scans were further post-processed in GOM Inspect where nodal distances were used to evaluate disc thickness, as it has been done for samples scanned placed on the condyle

(Figure 3.10.a). Measurements carried out in GOM Inspect vary between 2.04-2.28 mm, surface comparison within CloudCompare resulted in values between 2.30-2.43 mm. In conclusion, those 3D surface measurement procedures allowed to estimate a disc thickness of an average value of 2.26 ± 0.14 mm over three samples.

Table 3.5 – Comparison of results from thickness measurements using GOM Inspect and CloudCompare software. Presented are average values (\pm STD) in mm.

Sample	GomInspect	CloudCompare
1 (left disc)	2.04 ± 0.32 (n=25)	2.30 ± 0.53
2 (right disc)	2.17 ± 0.30 (n=28)	2.32 ± 0.56
3 (left disc)	2.28 ± 0.40 (n=27)	2.43 ± 0.58

On the other hand, thanks to the experimental tests, the thickness of hole drilling specimens was measured using a micrometre and the universal testing machine with two compression tools (with the two radii $r=0.875$ mm and $r=1.75$ mm). Those measures represent thicknesses in disc's central region, as it can be seen in Figure 3.8.b. A summary of all measurements for these specimens is provided in Table 3.6.

Due to the biconcave disc shape the specimens were first measured at their maximum thickness and then at their most central part, when using a micrometre (see Figure 3.9) as presented in columns "maximum sample thickness" and "central part thickness" of Table 3.6. The measurements from the mechanical tests through compression tools of radii 0.875 mm and 1.75 mm are presented in the two last columns of Table 3.6.

The thickest part of the specimen measures around 1 mm more than the most central part. Measurements of the central part via micrometre and compression tool are in the same order of magnitude and slightly higher than measurements realised with GOM Inspect and CloudCompare.

Table 3.6 – Thickness measurement summary of samples used in local spherical compression tests using a micrometre and compression tool (results in mm).

Sample	micrometre		compression tool	
	maximum sample thickness	central part thickness	$r=0.875$ mm	$r=1.75$ mm
1	3.54	2.54	2.89	2.76
2	3.57	2.61	2.79	2.63
3	3.72	2.30	2.25	2.52
4	3.25	2.79	2.80	2.65
5	3.44	2.60	2.12	2.07
6	3.00	2.61	2.02	2.07
average \pm STD	3.42 ± 0.24	2.58 ± 0.15	2.48 ± 0.36	2.41 ± 0.29

The results obtained with the optical 3D scans allowed an estimation of the disc's curvature, which could be evaluated drawing a cylinder as depicted in Figure 3.11. Measurements resulted in diameters of 12 - 13 mm. This confirms the choice of sizes chosen for spherical compression tools, which do not exceed a diameter of 6 mm. In this way, it could be affirmed that the compression tool touches the sample extremities, allowing only measuring in the intermediate zone.

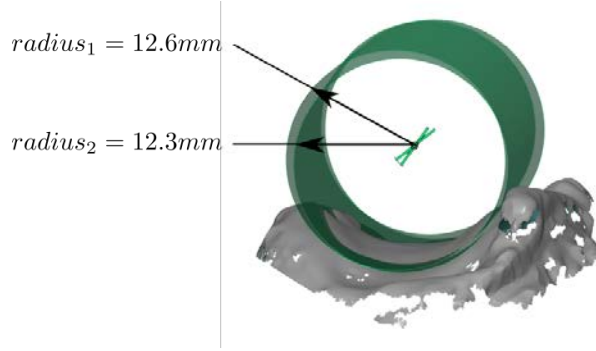


Figure 3.11 – Measurement of disc curvature estimated by a cylinder.

The MRI image of the sagittal cut in Figure 3.12.a shows the concavity of the TMJ disc's surfaces. The image confirms that the central part is the thinnest sample area while thickness increases in direction of the anterior and posterior bands. Thickness measurements of the central zone through three sagittal sections (Image No 58/59/60) resulted in 2.75 ± 0.72 mm (mean \pm STD, n=9). The sample lost contact with the 3D printed support, most probably evoked due to buoyancy forces since the sample holding tube is filled with physiological solution. Nevertheless, it can well be observed that the samples' shape is congruent with the condyles counterpart, indicating the function of shape, namely establishing a good contact between the disc and the condyle.

The red dotted line in Figure 3.12.a indicates position of the transversal cut shown in Figure 3.12.b. The anteroposterior orientated microstructure within the central zone can be appreciated. Towards the outer zones the circumferential alignment becomes apparent. However, exact interpretation concerning the fact that the depicted structure represents the collagen fibres demands deeper analysis. Actually, since MRI induces hydrogen molecule motion which are present in the TMJ disc fluid phase as well, the scans depict the "negative" of the collagen structure. Furthermore, the resolution of the MRI (see Appendix C.3), with $68\text{-}137\text{ }\mu\text{m}/\text{pixel}$ can only visualize fibre bundles.

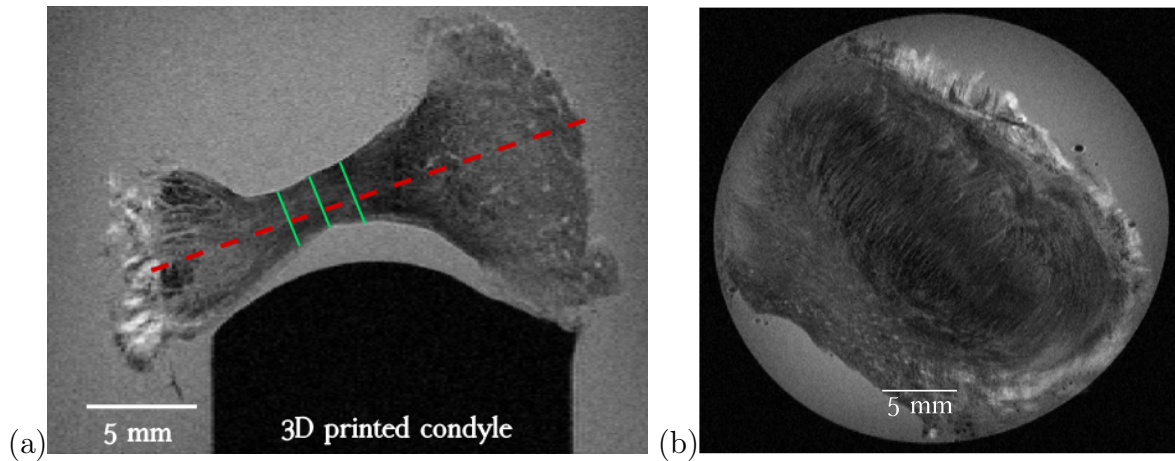


Figure 3.12 – (a) MRI sagittal cut through middle of the TMJ disc sample. [—] represents sections of thickness measurements and [- -] the transversal plane shown in (b) transversal cut highlighting the inner microstructure of the TMJ disc [Tappert et al., 2018a].

In conclusion, the 3D scans allowed acquisition of TMJ disc's and condyle's external shape. In the first attempt of measuring the discs' thickness with the 3D scan technique, it is problematic to determine whether the disc and condyle were in good contact or not.

Therefore, the estimation of the thickness especially in the anterior and posterior areas might contain inaccuracies due to insufficient contact, hence the distance might be over-estimated. In order to prevent inaccuracies due to dehydration of samples, scanning time was kept as short as possible, not exceeding 15 min. The second attempt, the vertical scan allowed direct measurement of disc thickness; two different software were used for evaluation; GOMInspect and CloudCompare. Both techniques found sample 1 the thinnest and sample 3 the thickest one. The difference between the two measurements might occur due to the approach which is measuring single distances with GOMInspect whereas with CloudCompare a whole surface area was analysed. Thickness measurements of the central area obtained through the vertical scan were lower (2.04-2.43 mm) than those obtained through the first attempt (3.24 mm). This might be due to the before mentioned contact uncertainties.

The outcome of measurements of hole drilling specimen thickness lies between 2.41-2.58 mm and of the MRI image evaluation 2.75 mm. The evaluation of the hole drilling specimen enables also to identify a variation in thickness between the thickest and thinnest part of the specimen.

The variation in thickness of about 1 mm is consistent with those evaluated by [Commisso et al. \[2014\]](#) who found an average variation of 0.89 mm for samples with average diameter of 5.43 mm, which are smaller than specimen used in this study (\varnothing 8 mm). Therefore, it seems logical that variation of specimen thickness presented in this study is higher. Compared to thickness measurements presented in the state of the art (Section 3.1.2) the samples in this study are slightly thicker. However, obtained results lie in the order of magnitude of thicknesses (2.0-2.25 mm) previously reported for porcine TMJ disc central part [[Commisso et al., 2014](#); [Lamela et al., 2011](#); [Lumpkins and McFetridge, 2009](#)]. In contrast, [Angelo et al. \[2016\]](#) and [Kim et al. \[2003\]](#) reported lower sample thicknesses. Diverse testing protocols, measurement techniques used and also the origin of samples which were ovine in the study conducted by [Angelo et al. \[2016\]](#), are reasons for discrepancy of the results.

However, the presented results show a consistency through all methods used, leading to the conclusion that the disc's central region has a range of thickness of 2.0 - 2.6 mm. This range is acceptable keeping in mind the natural variability occurring in biologic samples.

Since all the methods presented have different advantages and disadvantages, but determine the same range of sample thickness, the measurements conducted using the compression tools during local spherical compression was applied to all samples. This is the most convenient method since all samples undergo the spherical compression tests and are therefore not exposed to further experiments requiring additional freezing cycles.

3.3.2 Local spherical compression tests

From the experimental test of local spherical compression, the force and displacement data are obtained. For one sample, Figure 3.13 depicts typical experimental results for the three loading frequencies and the three compression tool sizes used. In this figure, the first three loading cycles of each test and the last one are shown. The latter one is the fifth for a loading frequency of 0.01 Hz, the 25th for 0.1 Hz and the 250th for 1 Hz, respectively.

A non-linear behaviour can be observed for all presented tests. This conclusion can be extended to all tests conducted. Two regimes can be distinguished during loading, a first

one in which forces increase slowly and a second one in which the forces increase almost proportionally to increasing displacement.

Independently of test frequency, the maximum forces diminish from cycle to cycle. This phenomenon can for instance be observed in Figures 3.13.a, 3.13.c and 3.13.e. Despite increasing loading frequency, they all show the accommodation behaviour concerning the maximal forces. This behaviour is also independent of compression tool size, as can be deduced by comparison of Figures 3.13.b, 3.13.c and 3.13.d. The figures depict loading at 0.1 Hz, with three compression tools of different radii and it results in higher forces for bigger spheres.

Figures 3.13.a, 3.13.c and 3.13.e show that with increasing loading frequency the maximum force values increase. For instance, during the first loading cycle at a test frequency of 0.01 Hz a maximal force of 0.195 N was recorded (Figure 3.13.a), at 0.1 Hz the maximal force reached 0.283 N (Figure 3.13.c) and at 1 Hz a maximal force of 0.352 N (Figure 3.13.e) was obtained for the same sample at the same test site using a compression tool of radius 1.75 mm.

Since the loading is driven by the displacement of the crosshead of the machine, the displacement of the sample increases in consecutive loading cycles, because of the load cell stiffness correction and the decrease of measured forces. This decrease deduced from Equation 3.13 which defines the relation between tool displacement and machine stiffness.

For a sphere of radius 1.75 mm, the maximum forces throughout the complete experimental time for all three test frequencies are shown in Figure 3.14. As in Figure 3.13, the diminution of the peak forces with increasing test time and therefore with increasing number of test cycles can be seen. Additionally, Figure 3.14 highlights that peak forces do not decline in a linear manner but are tending towards a steady state, independent of the loading frequency.

Another observation made from Figure 3.13 is that after a cycle of loading and unloading the sample does not return into its initial state, due to a decrease of force minima with increasing loading cycles. This can especially be observed for the test at 1 Hz (Figure 3.13.e) and it highlights the softening of the TMJ disc with increasing loading cycles.

The force-displacement curves and the figures depicting the peak forces show that the forces increase with higher loading frequencies. This fact indicates that the TMJ disc behaviour is dependent on loading frequency, underlining the viscosity of this tissue. The increasing in force under higher loading might be a result of solid and fluid phases interaction within the tissue. If the compression frequency is lower, the fluid within the disc has more time to be transferred from more compressed to less compressed areas whereas under higher loading frequency the time shortens, therefore less fluid is displaced and the sample reacts stiffer.

Another expression of the tissue viscosity can be observed in Figure 3.13. It is the hysteresis phenomenon, commonly interpreted as dissipated energy or energy loss [Beek et al., 2001], in cyclic loading. The hysteresis loop is highest for first loading cycle and decreases with ongoing loading cycles, as do the peak forces. The amount of this hysteresis, calculated as the area enclosed between the loading and unloading curves, is shown in Figure 3.15, as an example for one tested sample using a spherical compression tool of radius 1.75 mm. One can observe that at all test frequencies the energy loss decreases rapidly for the first loading cycles tending to some asymptotic value. One can further note that with increasing loading frequency the energy loss increases as well. While during the first loading under a loading frequency of 0.01 Hz a value of 0.011 mJ was obtained, it increases to 0.015 mJ for a loading frequency of 1 Hz for the example shown in Figure 3.15.

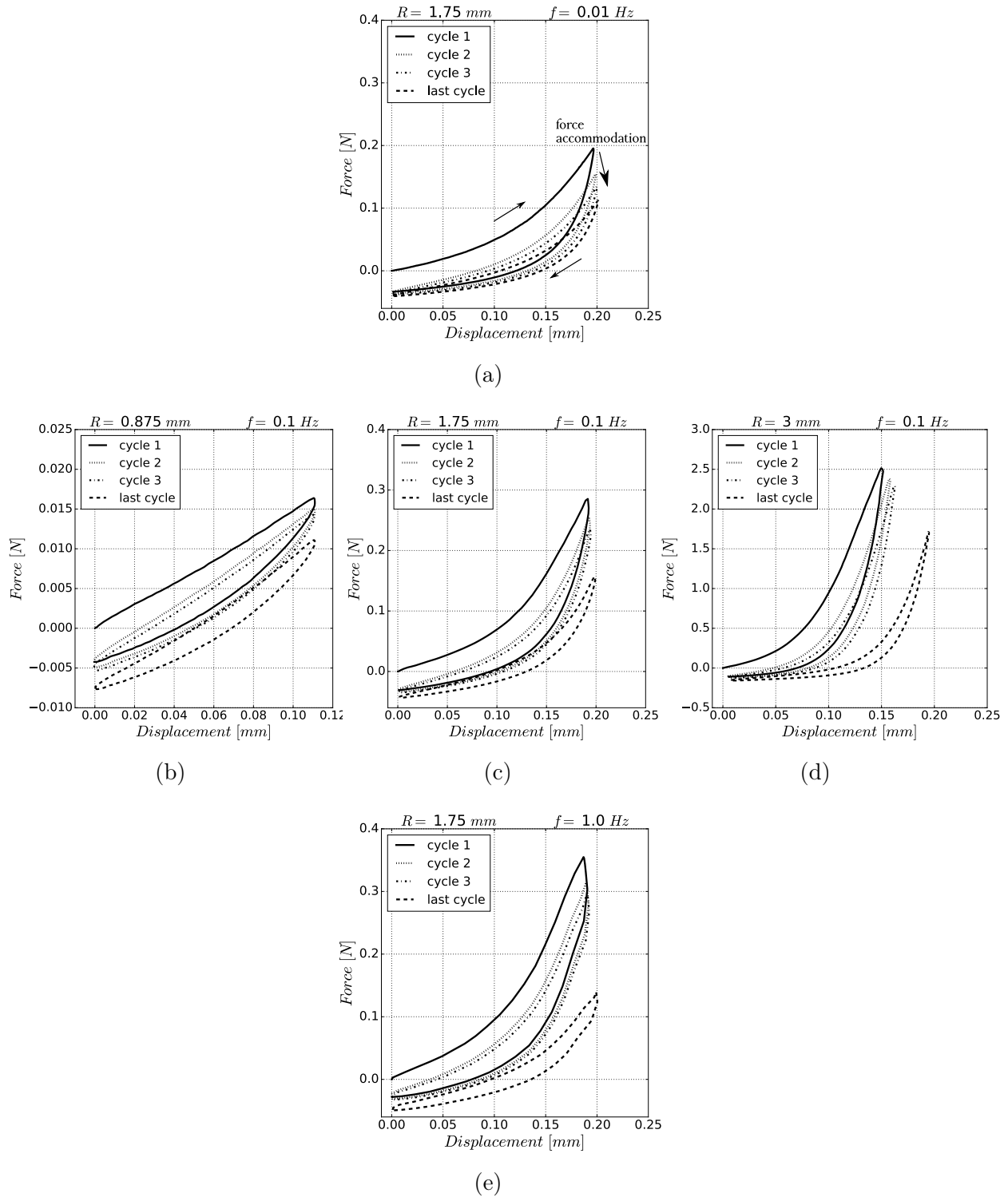


Figure 3.13 – Experimental force - displacement curves obtained from one representative sample at the central test site using different compression tool radii R and loading frequencies f (a)-(e). The first three loading cycles for each test and the last cycle are shown, the latter corresponds to the 5th, 25th and 250th cycle for loading frequencies 0.01 Hz, 0.1 Hz and 1 Hz.

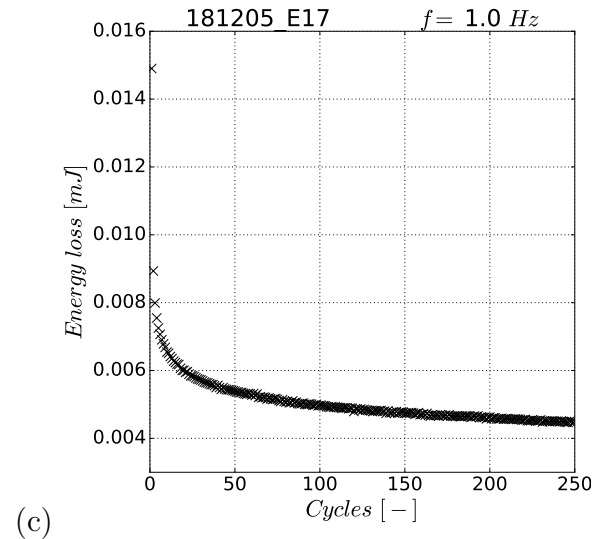
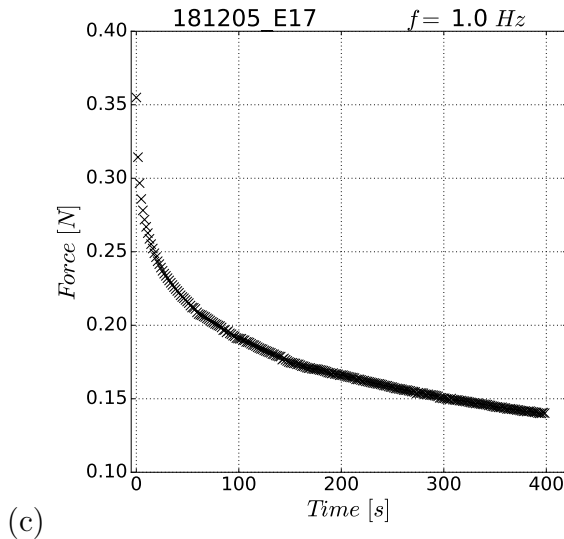
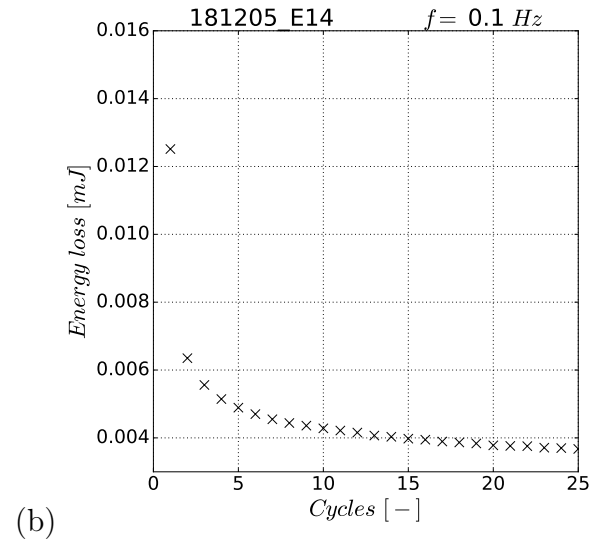
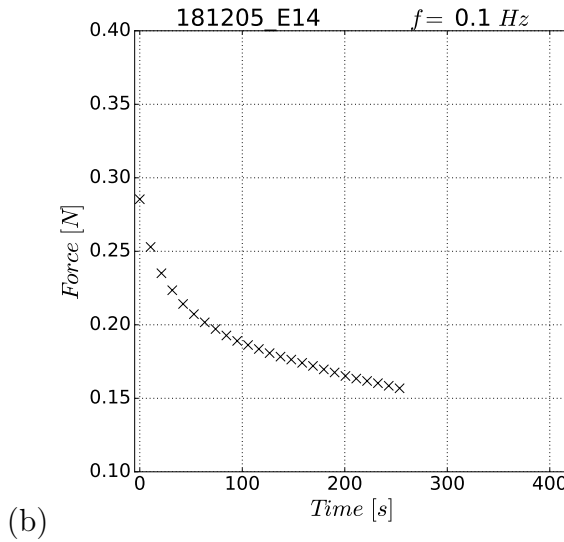
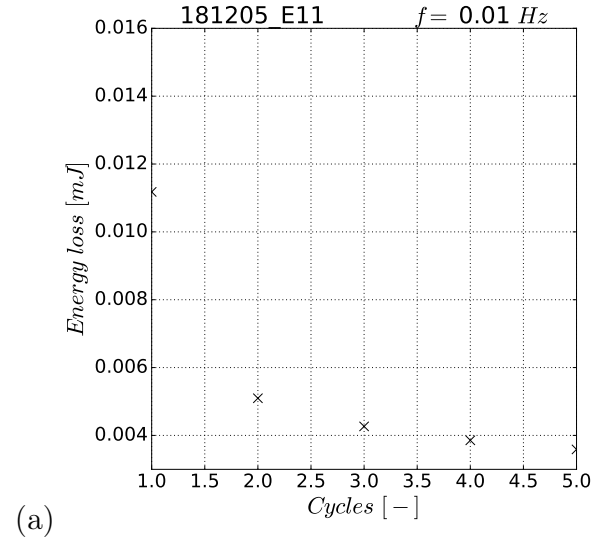
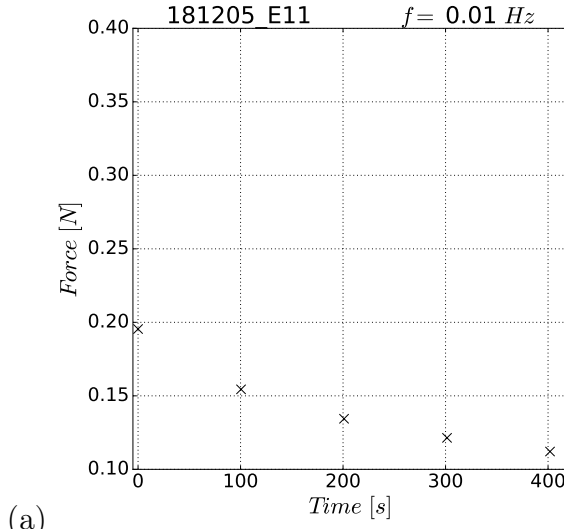


Figure 3.14 – Example of maximal occurring forces per loading cycle over experimental time for one representative TMJ disc sample during local compression tests on samples central site using a sphere with radius 1.75 mm at different loading frequencies f (a) - (c).

Figure 3.15 – Energy loss representing the hysteresis as function of loading cycle for local compression tests of central site of one representative sample using a sphere of radius 1.75 mm at frequencies f (a) - (c).

Figure 3.16 shows for a compression tool of radius 1.75 mm the average maximum force (\pm standard deviation) occurring in each test cycle for the whole experimental time. For the remaining compression tools corresponding graphs can be found in the Appendix C.8 (Figures C.13 and C.14). To obtain these average values, every single test has been interpolated so that average calculation per compression tool size and frequency could be obtained. For all three compression tool sizes, one can observe that test time was not identical for the three test frequencies. This is caused by the displacement-delay of the testing machine especially for high frequencies, further described in Appendix C.4.

Maximum forces show a dependency on loading frequency; with higher loading frequency, the maximum forces per loading cycle increase. The average for a loading frequency of 0.01 Hz ranges between 0.09-0.15 N (Figure 3.16.a), for a frequency of 1.0 Hz the range is between 0.13-0.39 N (Figure 3.16.c).

A decrease of maximum forces can be observed for all samples tested under the same test conditions. The decrease in the measured forces is more prominent during the first loading cycles, leading to an almost constant value after 100 seconds of experimental time. This accommodation effect is independent of loading frequency and compression tool used as can be observed from Figure 3.17. Depicted are the mean values of the peak forces for all three test frequencies for each compression tool used.

Furthermore, at higher loading frequencies, the energy loss increases, as shown in Figure 3.18. The mean values of energy loss (\pm standard deviation) as a function of test cycles for tests using a sphere of radius 1.75 mm are presented. It can be observed that the tests at a higher frequency show a higher mean value of energy loss than those at lower loading frequencies. However, all curves show the same tendency of accommodation and a fast decrease at the first loading cycles. Corresponding curves for experiments using the two other compression tools are presented in the Appendix C.9 (Figures C.15 and C.16).

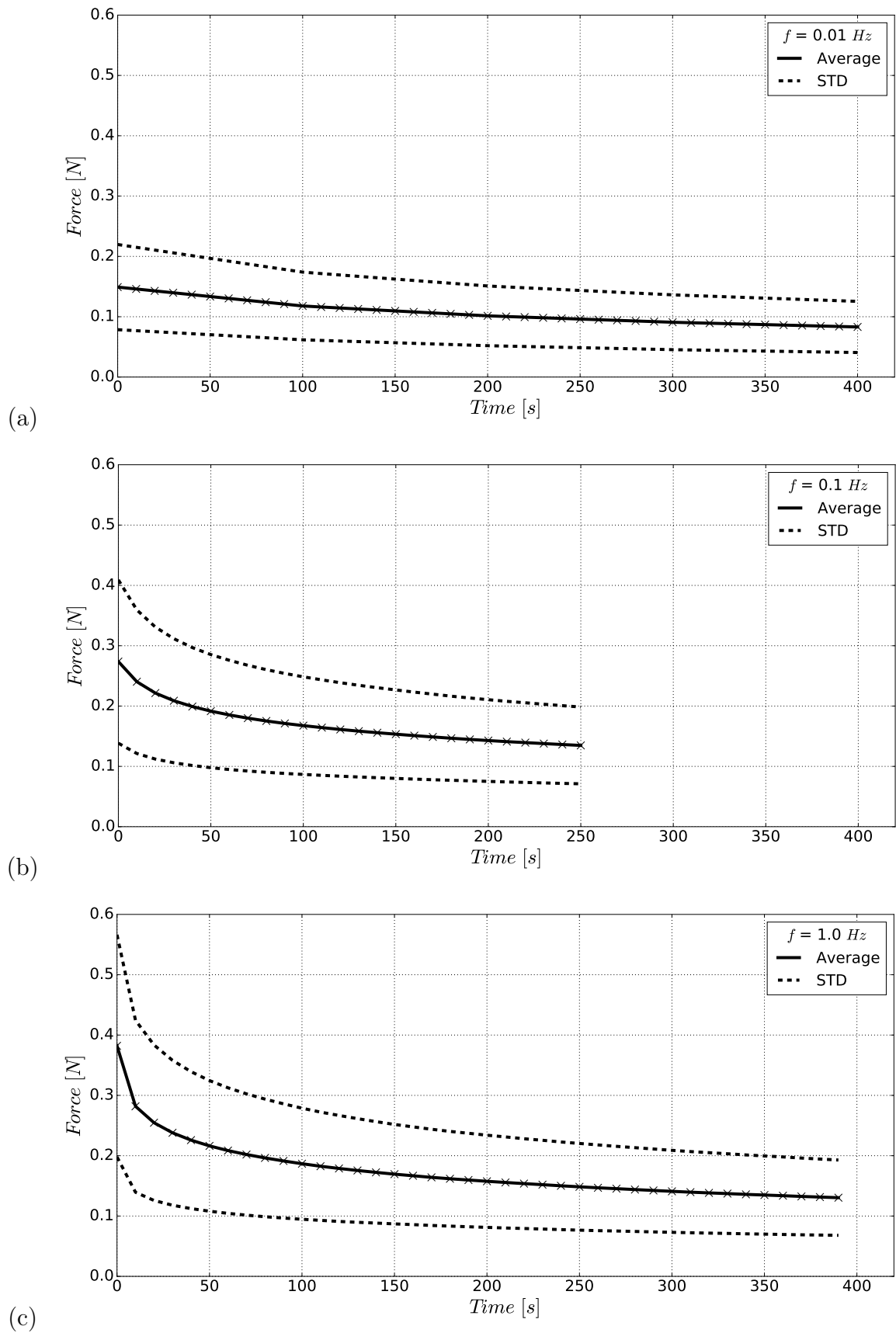


Figure 3.16 – Average (—) and standard deviation (--- STD) of maximal measured forces as function of experimental time using a compression tool of 1.75 mm radius for different loading frequencies f (a) - (c), ($n=18$).

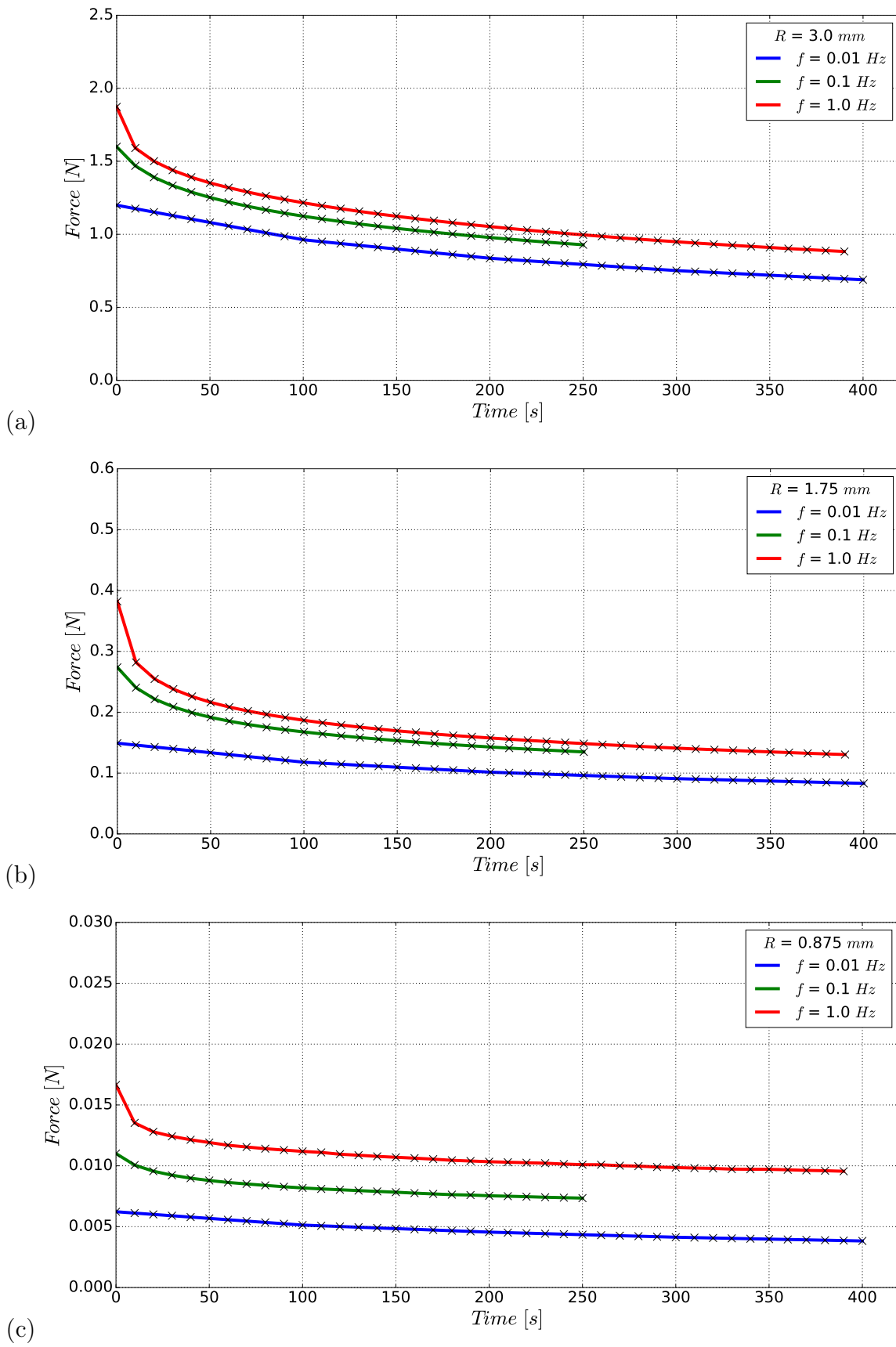


Figure 3.17 – Average (n=18) of maximal measured forces as function of experimental time for the three test frequencies f for different compression tool radii R (a)-(c) .

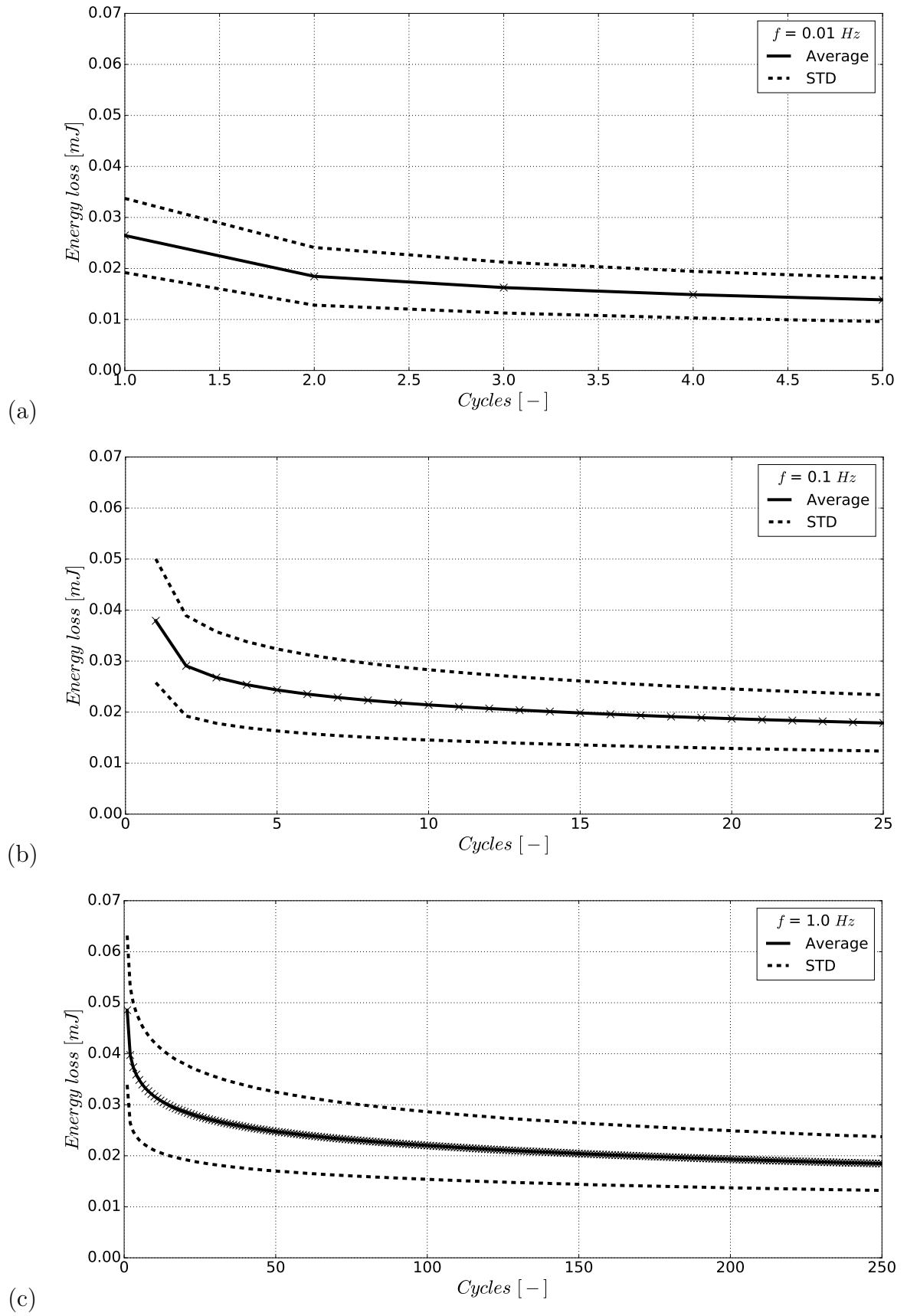


Figure 3.18 – Average (—) (\pm standard deviation (--- STD)) of energy loss representing the hysteresis for all spherical compression tests ($n=18$) using a sphere of radius 1.75 mm at different frequencies f (a) - (c).

The main characteristics found during local spherical compression tests of temporomandibular joint disc samples are: a non-linear behaviour, a hysteresis expressed as energy loss during loading and unloading phases, dependency of sample behaviour on loading frequency, accommodation of force and hysteresis with consecutive test cycles. These observations are common for soft biological tissues [Fung, 1993].

Force accommodation within the TMJ disc under unconfined compression has been observed previously [Beek et al., 2001; Fazaeli et al., 2016; Lumpkins and McFetridge, 2009; Tanaka et al., 2003b]. The characteristic time to obtain a steady state was found ≈ 100 s and was also reported in the work of Beek et al. [2001] and Tanaka et al. [2003b], however in the study conducted by Lumpkins and McFetridge [2009], this state is achieved faster within ≈ 50 s.

These studies present also analysis of hysteresis. The hysteresis is a representation of energy dissipated during a loading-unloading cycle [Athanasίου et al., 2009; Beek et al., 2001; Lumpkins and McFetridge, 2009]. Differences in methods of hysteresis calculation and presentation complicate comparison with the results presented in this study. Beek et al. [2001] observed also an increase of hysteresis with increasing loading frequency. For a compressive strain of $\epsilon = 0.25$ and at a loading frequency of 0.1 Hz, they obtained a mean hysteresis of ≈ 2.5 Nmm for the first loading cycle. Which is higher than the observations presented in this study, as for instance at $\epsilon^* = 0.2$ and 0.1 Hz using a sphere of 1.75 mm radius 0.04 mJ (0.04 Nmm) during the first loading cycle were obtained. The discrepancy might be caused by the order of magnitude of measured forces, which reach up to 70 N in the study of Beek et al. [2001] and are therefore much higher than forces observed during local spherical compression tests. It should be noted that Beek et al. [2001] studied human samples of elderly donors while in this study samples from young pigs were used and that a cylindrical compression tool of radius 1.97 mm was used by Beek et al. [2001]. The stress-strain definition is compulsory to achieve better comparison and it will be the aim of the Chapter 4.

Viscous characteristics of the TMJ discs, as the dependency of TMJ discs behaviour on the loading frequency has as well be shown by previously conducted TMJ disc characterisations [Lumpkins and McFetridge, 2009; Tanaka et al., 2003b].

Relaxation time

The cyclic loading of the TMJ disc samples was followed by a 30 seconds relaxation phase. Figure 3.19 presents three examples of force acquisition during this phase for one sample tested on its central site using a spherical compression tool of radius 1.75 mm at three different frequencies. It can be observed that after cyclic loading the forces decrease when compression tool displacement is kept constant. More precisely, forces decrease faster during the first seconds of the relaxation phase, then the rate of force diminution reduces. It can be noted that at the beginning of the relaxation phase the smallest forces were measured at a loading frequency of 0.01 Hz (0.16 N, Figure 3.19.a). The initial force at a loading frequency of 0.1 Hz is higher (0.21 N, Figure 3.19.b) than at a loading frequency of 1 Hz (0.19 N, Figure 3.19.c). At first sight, this fact seems incoherent, however it most properly derives from the difference of test times due to displacement delay of the testing machine, as previously discussed.

To determine a characteristic relaxation time τ , an exponential function of the form

$$F(t) = F_{init} - F_{\Delta} \left[1 - \exp\left(\frac{-t}{\tau}\right) \right], \quad (3.15)$$

with F_{init} being the force measured at the beginning of the relaxation phase and

$F_{\Delta} = F_{init} - F_{(t=30s)}$ was fitted to the experimental results using the COBYLA method (see Section 2.2.4). The results of this fitting are presented in Figure 3.19, too. The characteristic relaxation time τ decreases with increasing loading frequency. At a loading frequency of 0.01 Hz τ is 10.89 s, at 0.1 Hz $\tau = 6.58$ s and at 1 Hz $\tau = 3.77$ s.

To obtain a more global view of the relaxation process, for each test condition - that includes the same compression tool size and cyclic loading frequency - the force-time curves were interpolated and an average curve calculated. The results for tests using a spherical compression tool of radius 1.75 mm are presented in Figure 3.20. Similar to the examples depicted in Figure 3.19, the average curve follows the same trend with lower characteristic relaxation times for faster loading. In average τ is 10.52 s after a cyclic loading of 0.01 Hz, 6.91 s and 4.21 s after loading of 0.1 Hz and 1 Hz.

Relaxation behaviour of temporomandibular joint disc samples and specimen have been studied by the means of stress relaxation. The general tendencies, such as that a high amount of relaxation occurs within the first seconds of a relaxation test [Barrientos et al., 2016; Fernandez et al., 2011; Lamela et al., 2011; Tanaka et al., 1999] are consistent with the here presented results.

Since the focus of this experimental study was not only on the discs relaxation behaviour, the relaxation phase was kept relatively short (30 s) compared to pure relaxation and creep behaviour studies that commonly last between 100 and 1000 seconds. Therefore, comparison of characteristic relaxation times becomes complicated. It should be noticed that many studies use Kelvin [Tanaka et al., 1999] or General Maxwell models [Fernandez et al., 2011] of several parameters in order to characterise relaxation behaviour and to better fit experimental results.

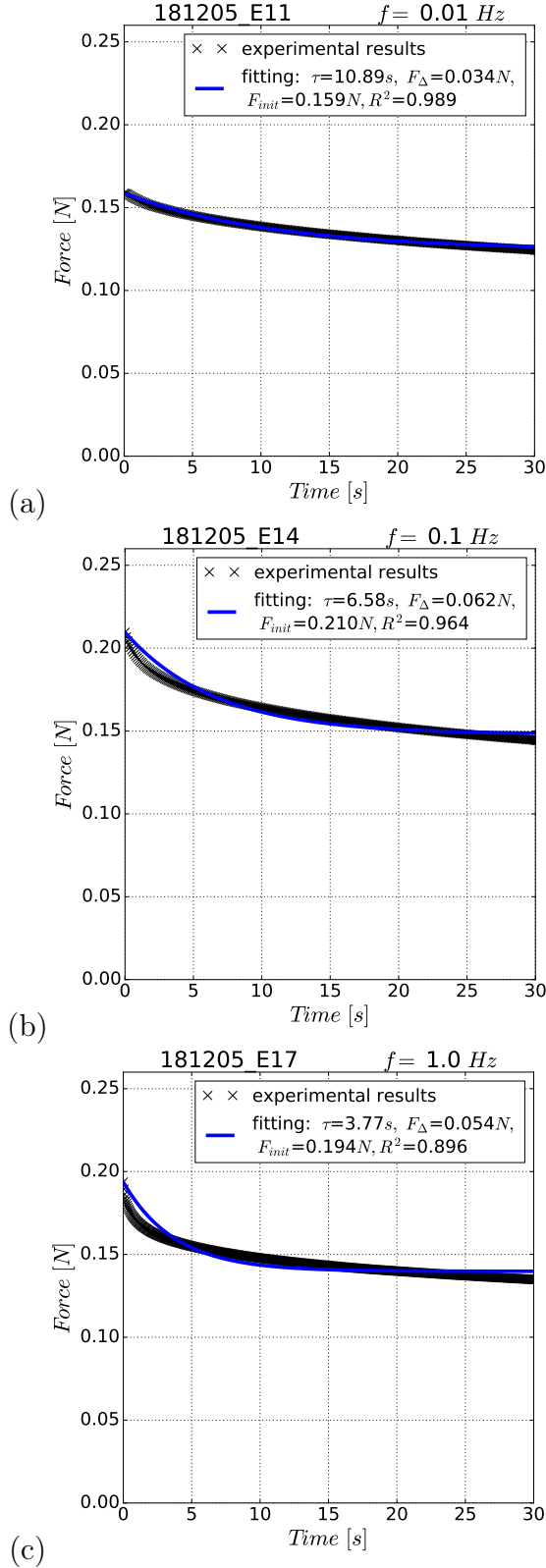


Figure 3.19 – Example for relaxation phase at the end of loading cycles at central site of one representative sample using a sphere with radius 1.75 mm at different loading frequencies f (a)-(c), including exponential fitting to determine characteristic relaxation time τ .

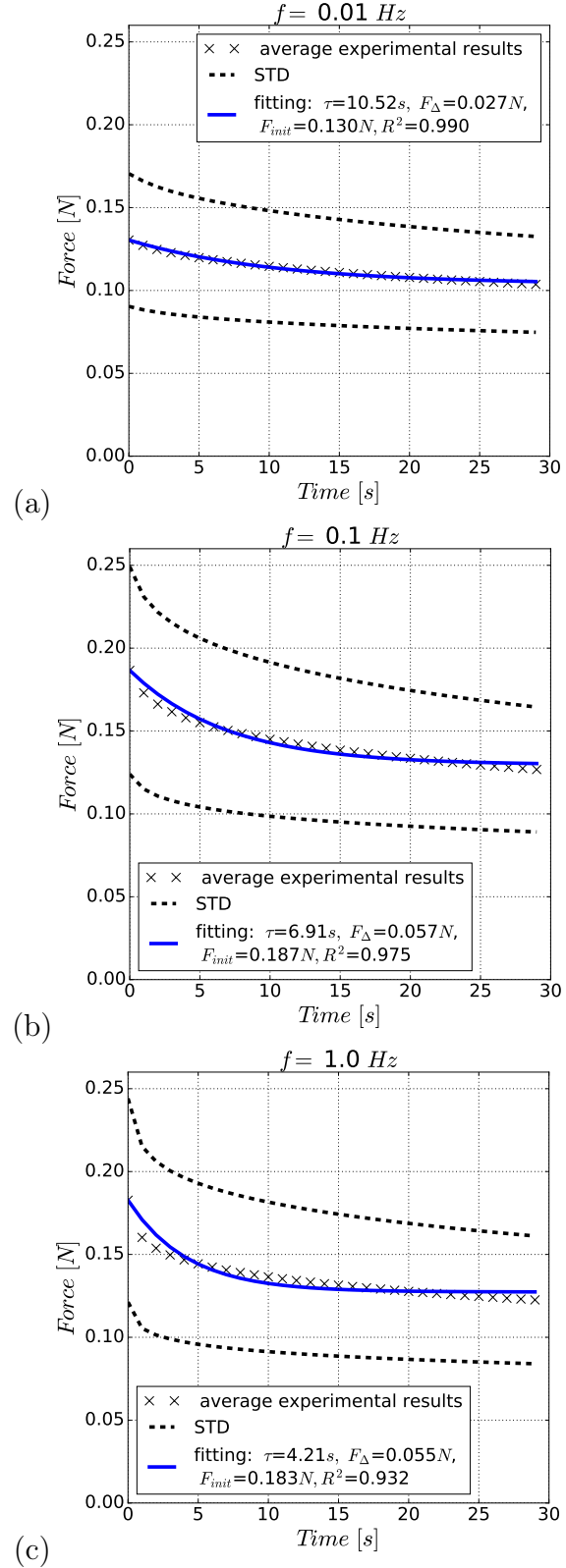


Figure 3.20 – Average (x) (\pm STD (- -)) relaxation time for spherical compression tests ($n=18$) using a sphere of radius 1.75 mm at different frequencies f (a)-(c), including exponential fitting to determine characteristic relaxation time τ .

Comparison of three test sites

In order to compare the three test sites - central, medial and lateral - the maximum forces occurring during the first loading cycle were analysed. The average of these maximal forces for tests under the same test conditions are shown in Figure 3.21. Again, it can be observed that independent of test site, the maximum force during the first loading cycle increases with increasing loading frequency as well as with increasing size of the compression sphere the forces increase.

The test using a compression tool of radius 0.875 mm (Figure 3.21.a) and 1.75 mm (Figure 3.21.b) show for all three loading frequencies the highest forces for the medial test site and the lowest for the lateral site. Figure 3.21.c shows that at all loading frequencies using the biggest compression tool (3 mm radius) results in highest forces found on the central test site, followed by the medial and lateral one.

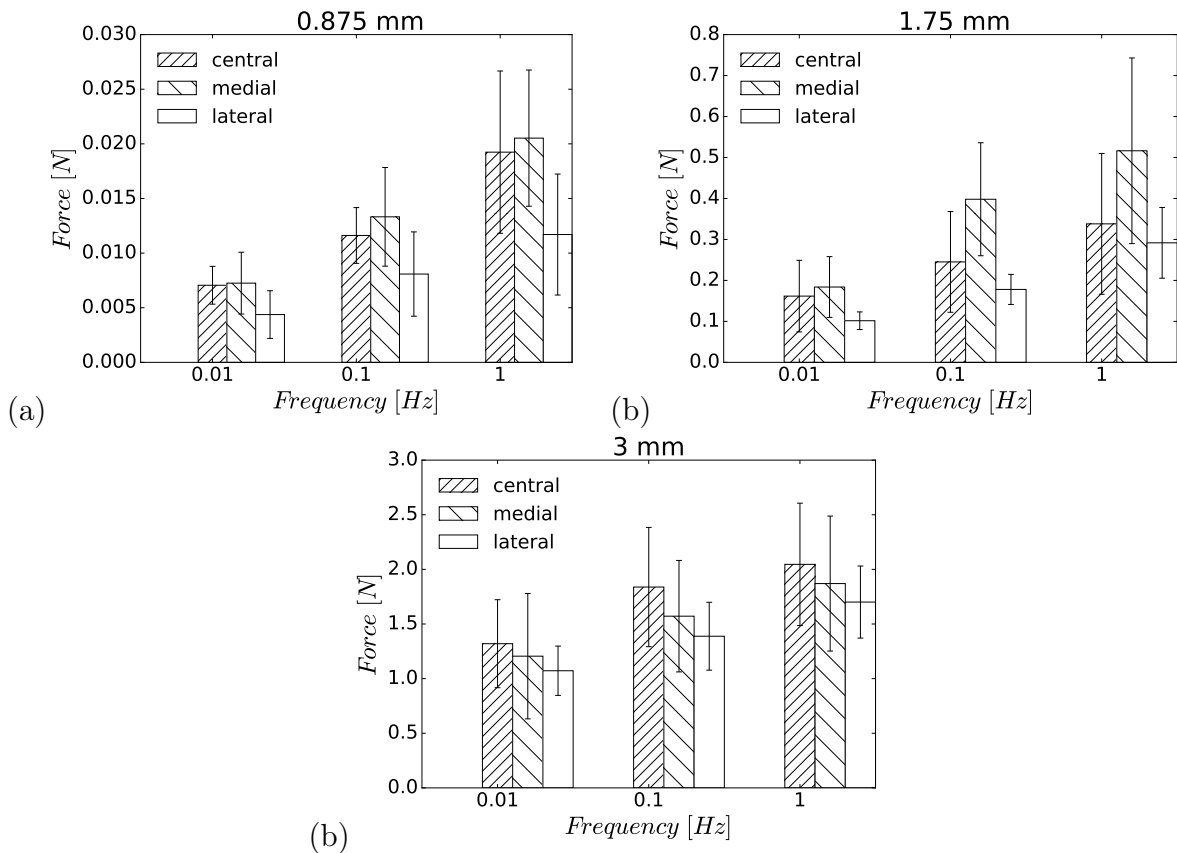


Figure 3.21 – Average of maximum forces ($n=6$) during first loading phase on the three test sites using a compression tool of radius (a) 0.875 mm, (b) 1.75 mm and (c) 3.0 mm at the three loading frequencies. Error bars indicate the standard deviation.

A clear trend for a region showing highest forces and therefore being the stiffest could not be determined. One reason why local spherical compression tests using the biggest compression tool result in highest forces for the central site might be that a larger area is affected by compression and therefore measurements are more likely to be influenced by the samples geometry. The biconcave shape of the TMJ disc samples might result in differences of the local topography, which has minor effects on smaller compression tools.

Since the glycosaminoglycan (GAG) content is known to impact compressive properties [Allen and Athanasiou, 2006], it is worth comparing the results with biochemical

analysis of the TMJ disc. As reported in Chapter 1, Section 1.2 "The temporomandibular joint disc", Kuo et al. [2010] could not find a significant difference of GAG content between different locations within the TMJ disc. In contrast Almarza et al. [2006] report a significant higher GAG content in the medial zone compared to central and lateral TMJ disc parts, whereas Fazaeli et al. [2016] stated the lateral region to have the highest GAG content. These biochemical analysis could not come to a conclusion which region of the disc contains the highest amount of GAG. However, in cylindrical local compression, Fazaeli et al. [2016] found the highest compressive modulus in the medial region, as this was the case in the here presented results for indentation tools of radii 0.875 mm and 1.75 mm.

The presence of GAG within the samples used in this study has only be assessed via histological cuts. Figure 1.4 in Chapter 1 shows the presence of GAG in the Safranin O staining, however this analysis allows only qualitative interpretation. Due to the presence of hydrophilic GAGs, which interact with the interstitial fluid, the fluid flow is affected and the tissue becomes stiffer.

Since the tests have been conducted on two consecutive days with the samples stored over night in the fridge, the results might not only be frequency, site or compression tool size dependent, also the storing could influence experimental outcomes. Therefore, it should be ensured that the storage conditions do not influence the sample and that experiments remain repeatable. For this reason, the repeatability has been tested.

Repeatability of experiments

The test protocol demanded sample testing on two consecutive days, therefore a repeatability test was carried out on the central part of the same sample (see Section 3.2.3.2). This experiment helps to assess the repeatability of initial conditions and the effect of the sample's storage overnight in the fridge. The repeatability tests revealed that the overall sample behaviour remains similar, as it can be seen in Figure 3.22. The non-linear behaviour, accommodation of maximal forces in function of the cycle number and hysteresis phenomenon were observed on the first and second day of experimental analysis.

Figure 3.22 shows examples of the force-displacement curves of the same experiment, carried out on the central part of the same sample during two consecutive days. In three out of five tests almost the same sample behaviour was observed (see Figure 3.22.a). Forces obtained during the second day are slightly higher than during the first day. For instance, during the first loading of day one F_{max} is 1.73 N and 1.81 N during the second day, for the presented example.

For the remaining two tests the maximum forces of the first loading cycle were approximately 1 N higher on the first day (Figure 3.22.b). Indeed, during the first test a maximal force of 1.85 N was recorded while during the second day a force of 1.0 N was measured.

Various factors might be the cause of the difference of the repetition experiment. To be stored, the sample was removed from the 3D printed condyle and re-attached the next day. Even with a great vigilance the sample might have been slightly positioned in a different way. Also, compression might have been conducted not on exactly the same site, resulting in loading of different volume of material and therefore generating different forces. The initial test conditions, more precisely the contact of the compression tool with the sample, is another detail that changes the experimental results. Therefore, the force-displacement curves from the second day have been shifted, in order to study if the definition of contact via the calculated preload holds an influence on the results.

Figure 3.22.c depicts such a shift, highlighting that a comparable slope of force as a function of displacement can be observed, when the offset is changed. This leads to the conclusion, that the definition of initial experimental conditions might have a predominant influence on experimental results, compared to biochemical variation over one night. It can be furthermore concluded that the TMJ disc has viscoelastic characteristics, since the samples behaviour showed a return to the samples initial state.

Taking into consideration that biological samples present a natural variability, it was concluded that local spherical compression tests are reproducible, since the general sample behaviour did not change. However, the repeatability tests underline the importance of initial test conditions, which should be controlled with a high precision.

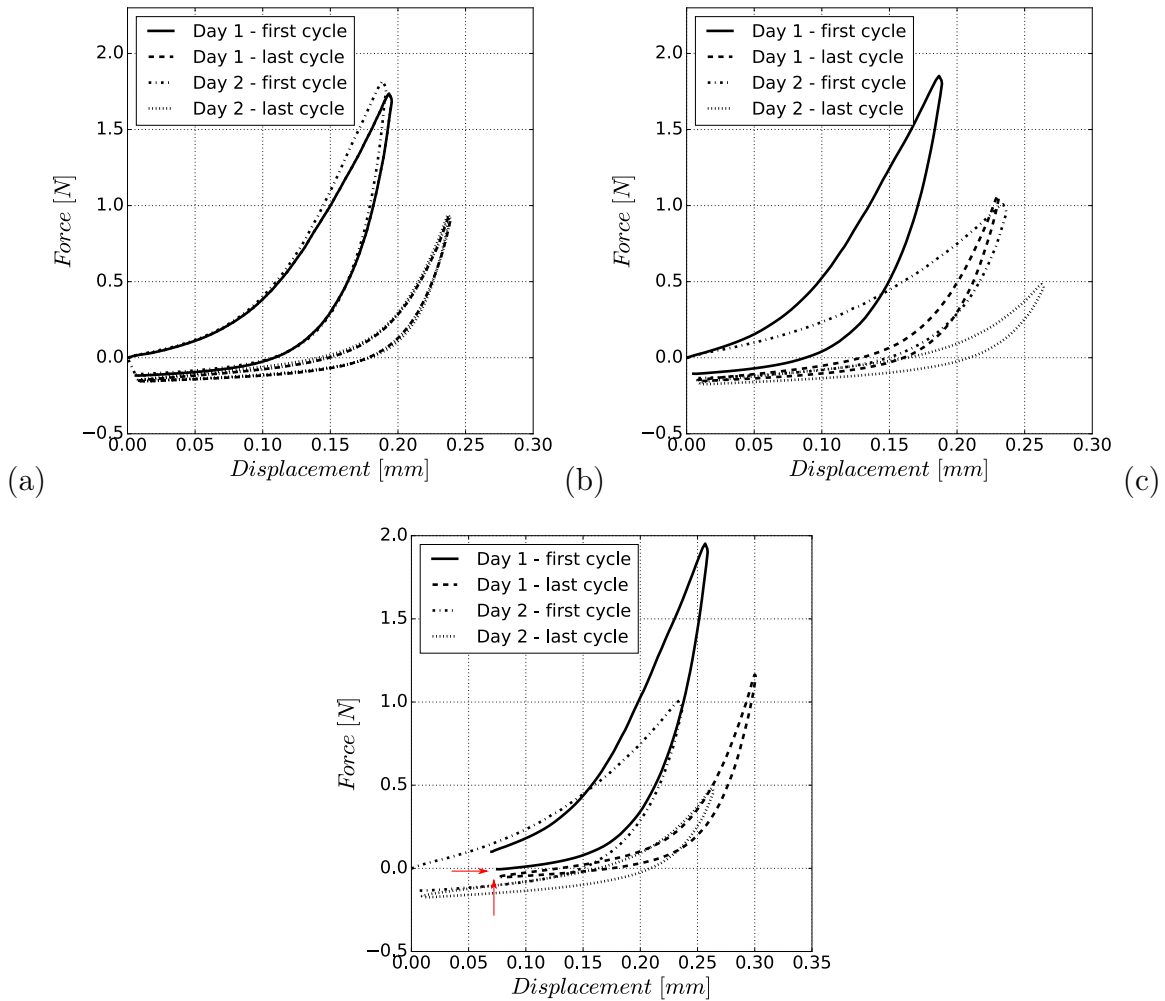


Figure 3.22 – Force - displacement curves of repeatability tests showing the first and the last loading cycle for the same test on the first and the following day of sample testing, (a) example of a good repeatability (181212_E4 and 181213_E10), (b) example of poor repeatability (181213_E14 and 181214_E19), (c) shifted force-displacement curve from example (b) to highlight influence of initial test conditions. The tests were conducted on sample's central site at 0.1 Hz using the compression tool of 3 mm radius.

During the local spherical compression tests, special attention was paid for samples to remain in their integrity. The importance of this experimental condition lies in the internal strains, which are analysed in the following.

3.3.3 Internal strain analysis

It was observed from microscopic studies (Section 1.2) and MRI analysis (Section 3.3.1), that the fibres within the TMJ disc are distributed and aligned differently in the anatomical zones of the disc. To see the influence of this alignment on the mechanical behaviour a cylindrical specimen was cut from the central area of the TMJ disc samples. Figure 3.23 shows an example of one of these specimens. In the main anatomical directions (antero-posterior and mediolateral, see Figure 3.8.b), the evaluation of expansion and contraction of the specimen was done. Table 3.7 summarises the samples' dimensions in mediolateral and anteroposterior directions at different moments of observation. The samples' dimensions in both directions during the first measurement is already higher than the diameter of the tool used to cut the specimen (\varnothing 8 mm), except for sample 2 (181130). The specimen shape in Figure 3.23 is also not completely cylindrical. This indicates that, within the TMJ discs, internal stresses were present. If this was not the case, the sample's form and dimensions would have remained unchanged after hole perforation. Another important point to underline is the fact that relaxation occurs really fast, since specimens were already deformed during the time it takes after cutting to place them in the field of vision of the camera, which takes less than a minute. Expansion was observed for all samples in both studied directions, except for sample 3 (181206), which showed contraction in both directions. The expansion of almost all samples is another indicator that within the TMJ disc a internal stress is present which is released when the specimen is cut; the sample relaxes and highlights internal strain. However, as can be seen from the stretch ratio (Table 3.7), this relaxation is relatively small. The presence of internal stresses is an important result, underlining that testing only specimen extracted from the TMJ sample, as this is the case in many studies [Commisso et al., 2016; Fernandez et al., 2011; Lumpkins and McFetridge, 2009; Matuska et al., 2016; Tanaka et al., 2003b], might result in different outcome due to the internal stress release.

Such internal stresses can have several reasons of existence. It can be another mechanism to support the stresses induced due to joint movements as this is the case for internal stresses in arteries to resist pressures caused by blood flow [Fung, 1993].

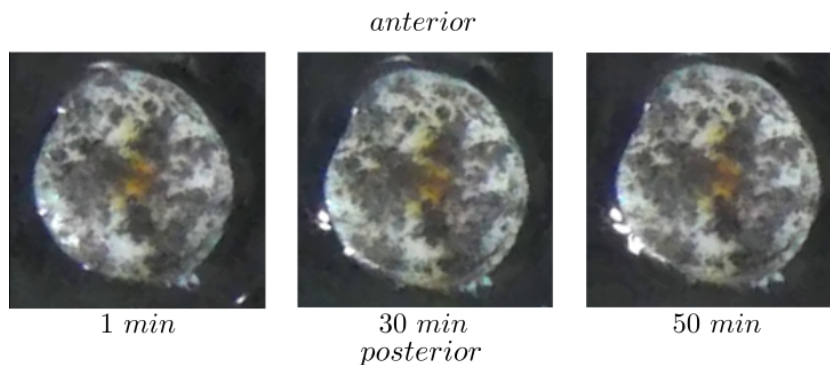
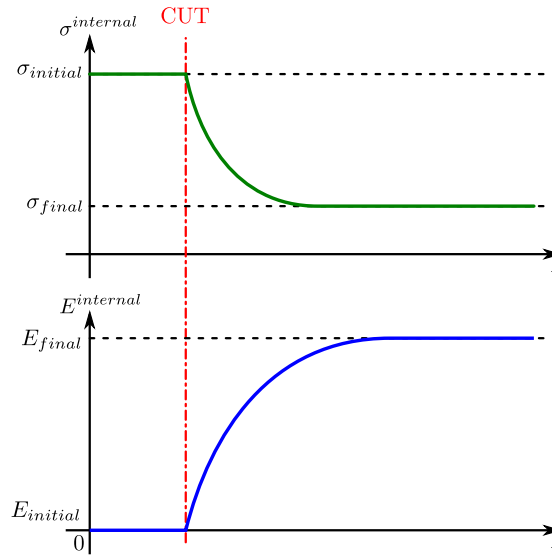


Figure 3.23 – Example of the hole drilling specimen from sample 6 (181214) for different time steps of the experiments; 1 min, 30 min and 50 min.

Table 3.7 – Summary of the dimensions [mm] (mean of three measurements) of the specimen.

specimen	mediolateral 1 min	mediolateral 50 min	mediolateral stretch ratio	antero- posterior 1 min	antero- posterior 50 min	antero- posterior stretch ratio
1: 181129	8.216	8.522	1.037	8.269	8.4	1.016
2: 181130	7.869	7.964	1.026	8.216	8.426	1.037
3: 181206	8.964	8.879	0.991	8.103	8.028	0.991
4: 181207	8.644	9.025	1.044	8.451	8.715	1.032
5: 181213	8.835	9.098	1.030	8.808	9.157	1.040
6: 181214	8.229	8.281	1.006	8.293	8.599	1.037

Those first results highlighted a variation of the outer diameter but required deeper analysis to understand how the internal stresses affect the internal strain observed. For example, it is not known how far the internal stress of the inner structure impacts the behaviour. The image capture allows using sophisticated techniques to extract mechanical data. Therefore, in cooperation with the *Laboratoire de Mécanique et Génie Civil of Montpellier*, digital image correlation (DIC) based on the method developed by [Dusfour \[2018\]](#) was performed. Comparing image to image through a mesh decomposition of the region of interest, the displacement of each element of the mesh is obtained. It allows in the following to calculate the associated strain field, through a backward approach (Section 3.2.3.3). This approach can be illustrated by Figure 3.24.

Figure 3.24 – Concept of backward approach to reach internal stress $\sigma^{internal}$ and strain $E^{internal}$.

The method calculating the internal strain is a "backward" calculation, the strain at the end of the experiment indicates the internal strain the specimen was undergoing in its physiological configuration. Once the internal strains are known, a suitable constitutive law yields to the internal stresses within the tissue.

The final state is hence taken as a reference and the correlation is made up to the initial image allowing to access the initial mechanical state of the tissue, in other word

its in situ conditions before the cutting. DIC analysis gives a lot of information with heterogeneous strain fields as presented in Figure 3.25.

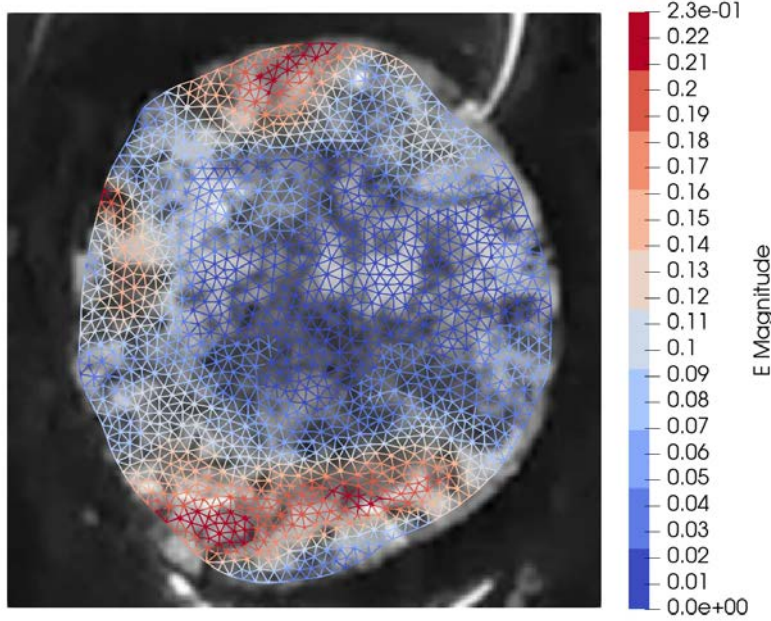


Figure 3.25 – Example of strain field magnitude obtained on one hole drilling specimen (181130).

In total five samples were processed and the final strain field magnitudes are presented in Appendix C.10, Figure C.17. The main conclusions of this type of results were heterogeneities, large strains and radius dependency. Therefore, two axial components have been pursued to assess the characteristic time of internal strain (E) relaxation thanks to an exponential fitting such as

$$E = E^\infty \left[1 - \exp\left(\frac{-t}{\tau}\right) \right] \quad (3.16)$$

with E^∞ theoretical *in vivo* internal strain, t experimental time and τ relaxation time.

On the other hand, the radius dependency of those components has been studied. First of all, cylindrical coordinates (see Figure 3.8) were used to perform the study allowing plotting for the same sample presented above (Figure 3.26).

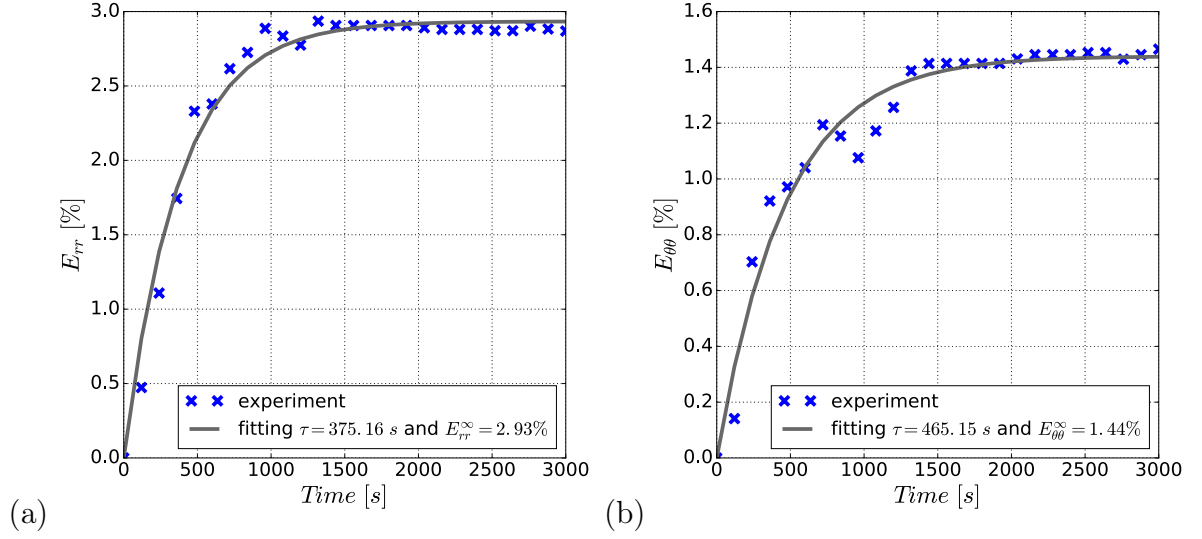


Figure 3.26 – (a) Radial E_{rr} and (b) tangential $E_{\theta\theta}$ average strain fields as function of time obtained on one hole drilling specimen (181130), with exponential fitting highlighting characteristic times τ and theoretical *in vivo* internal strains E^{∞} .

Fitting an exponential function on the average strains as function of time allowed concluding that the average characteristic times ($n=5$) in radial and tangential direction are: $\tau_{rr} = 1006.414 \pm 711.71$ s and $\tau_{\theta\theta} = 812.89 \pm 248.50$ s. All the results are gathered in Appendix C.10, Figures C.18 and C.19 and emphasize the fact that the permanent regime was reached for 2 over 5 samples. This conclusion can be discussed due to the procedure of backward approach. Actually, there is a gap between the extraction of the sample and the beginning of picture capture where the maximum value of the internal stress is released. The exponential fitting would enable assessing these unknown asymptotic values that are in average over five specimens $E_{rr}^{\infty} = 5.30 \pm 2.40\%$ and $E_{\theta\theta}^{\infty} = 5.37 \pm 2.42\%$. It highlights the fact that specimen extraction definitely changes the initial or "close to" *in vivo* condition of the sample. Finally, it has to be noted that strain concentration are located on the surrounding part of the sample where discrepancies can appear due to artefacts of the analysis procedure. That is why, it was crucial to investigate the behaviour along the normalised sample's radius $R_{norm} = \frac{R}{R_{max}}$, with R the sample's radius and R_{max} the maximal value of the sample's radius, as presented in Figure 3.27.

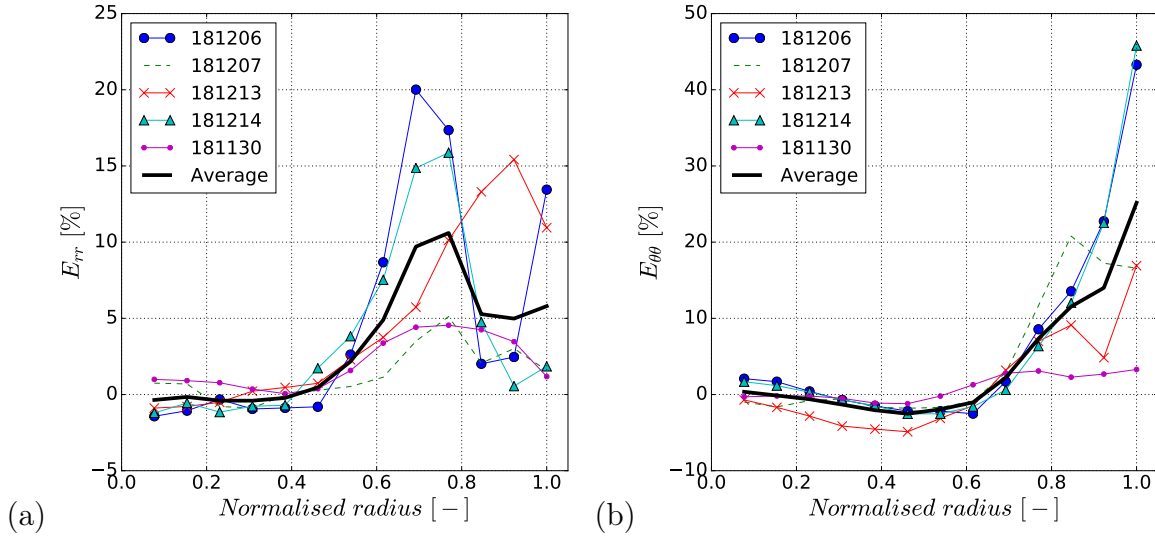


Figure 3.27 – (a) Radial E_{rr} and (b) tangential $E_{\theta\theta}$ average strain fields as function of normalised radius.

It clearly appears a radius dependency of the strain where around 40% of the radial direction is not affected by the internal stress release, while the remaining 60% presents high values compared to the previous average results.

This major result points out the sample sensitivity to harvesting procedure. In fact, for an 8 mm diameter cylindrical sample, an outer ring of 4.8 mm thickness is affected by the internal stresses release and finally a 3.2 mm diameter centre part keeps the same conditions than *in vivo*. Hence, it points out many questions regarding experimental characterisation on samples with diameter lower or equal to 5 mm [Allen and Athanasiou, 2005; Calvo-Gallego et al., 2017; Comisso et al., 2016; Lumpkins and McPetridge, 2009; Tanaka et al., 1999]. Actually, this phenomenon is independent of the sample geometry since it relies on the collagen structure. Therefore, for all TMJ disc samples the affected zone by the internal stress release should be of the same order of magnitude and it questions initial stress state of the extracted tissues. It comforts then the approach of this work, where a peculiar attention was given to keep sample integrity while reproducing its environment to mimic *in vivo* conditions during local spherical compression tests.

3.4 Conclusions on experimental results

The experimental characterisation of biological tissues implies many difficulties. In the case of the temporomandibular joint disc, the samples are sensitive to the test environment. Since the TMJ discs are part of a synovial joint, they are naturally exposed to physiological fluid that is mainly constituted of water. Therefore, it was necessary to provide a humid test environment. The experimental set-up for local spherical compression and hole drilling tests as well as MRI imaging took this into consideration. The TMJ discs fill the gap between the temporal bone and the condyle. For this function their shape is adapted with a biconcavity that can be appreciated on MRI images. Since this shape has a major role, it cannot be neglected during mechanical tests, which is the origin of difficulties for the test setup. For this reason, the 3D printed condyles were used as sample holders. However, one reason for dispersion of results from local spherical com-

pression tests is the establishment of contact between the sample and the compression tool. Furthermore, the repeatability tests revealed a non-negligible sensitivity to initial conditions. This highlights the difficulty that during compressive experiments the loading of an equal volume of sample is not easy to achieve.

Nonetheless, the results obtained through local spherical compression tests bring to light the non-linear and viscous behaviour of the TMJ disc. Non-linearity was shown by the two regimes of the force-displacement curves, while viscosity was highlighted by force accommodation and hysteresis. The viscous effects might be results of the interaction of different biochemical components found in the TMJ disc. As it is made of a fluid phase, which contains mostly water, and a solid phase formed by GAGs and fibres such as collagen, there is interaction of the two phases when the tissue is under loading. Since the fluid can be transported during compression, it creates internal friction. The hydrophilic property of the GAG intervenes in this process as well. During loading it can retard fluid flow while it can have the inverse effect during unloading. Those phenomena have not been assessed in this study even though first attempts were made. The repeatability tests underlined furthermore that the TMJ disc is viscoelastic. After storing the sample for a night in a fridge, experimental results were reproducible, showing that the samples returned into their initial state and that storing condition did not influence their behaviour.

Using the hole drilling method, for the first time the presence of internal stresses within the TMJ disc was demonstrated. These findings underline the importance of testing the samples in their integrity and not specimens cut from different disc regions. Interpreting results obtained from experiments using cut specimen should take into consideration that the internal stresses and strains have been released prior testing. Furthermore, a dependency on the samples radius was found, showing that the centre of the hole drilling specimen was less affected by the release of internal stresses than the outer ring.

Perspective

Even though using the 3D printed condyles as sample holders to compensate the TMJ discs biconcavity, using an experimental protocol including a preconditioning to obtain the most comparable sample state for all tests, the contact between compression tool and sample might not be equal throughout different experiments. To eliminate this uncertainty the experimental set-up could be improved. For instance, it might include the use of a combination of a spherical compression tool with an LED and a CCD camera for contact determination [Dai et al., 2019], or techniques identifying the contact area based on a fluorescent layer [Johnson et al., 2018] or talc coating [Barrientos et al., 2016].

The orientation of collagen fibres in the intermediate zone is mainly anteroposterior. The dominant orientation causes an anisotropic behaviour which is difficult to characterise through local spherical compression tests. Such behaviour is commonly studied in tensile tests [Angelo et al., 2016; Beatty et al., 2001; Detamore and Athanasiou, 2003b; Matuska et al., 2016]. Preliminary results have been obtained [Tappert et al., 2018b] but they were not relevant enough compared to the literature to pursue during this work period. Moreover, chemo-sensitivity test has also been tried to highlight the effect of GAGs within the structure. The coupling with the force measurement was not clear enough to continue but comforts the literature regarding the fact that GAG amount in porcine discs seems to be lower than in human ones. Therefore, other experiments will have to be carried out to manage a characterisation of those negatively charged elements within the collagen

structure.

The results obtained from local spherical compression tests cannot be directly transferred to stress-strain diagrams since they cannot be directly calculated from the experimental measurements. For instance, the contact radius was not measurable with the here presented experimental method. The link between the results obtained in Chapter 2 concerning representative stress-strain analysis and the experimental ones will be made in the following Chapter.

Chapter 4

Identification of temporomandibular joint disc material parameters through spherical compression tests

Contents

4.1	Introduction	92
4.2	Material and Methods	94
4.2.1	Representative stress-strain curve construction	94
4.2.2	Hyperelastic material laws used to describe temporomandibular joint disc behaviour	95
4.2.3	Finite element model of local spherical compression test on one temporomandibular joint disc	97
4.3	Results and Discussion	100
4.3.1	Stress-strain curves of local spherical compression tests on temporomandibular joint disc samples	100
4.3.2	Hyperelastic parameter identification	105
4.3.3	Three-dimensional finite element analysis of the temporomandibular joint disc under spherical compression	106
4.3.4	Comparison of experimental and simulated results	109

4.1 Introduction

The aim of this study is to choose a constitutive law that is able to describe accurately the behaviour of the temporomandibular joint disc. Such information will be used to feed finite element simulations of the TMJ disc, the TMJ or even more complex models including the skull. Figure 4.1 from the work of [Creuillot \[2016\]](#) shows such a model developed by our biomechanical research team of the LEM3 laboratory. The limitations of that work regarding the TMJ were first of all that the TMJ disc's geometry was estimated from tomographic studies of the skull, filling the space between the temporal bone and the condyle. Furthermore, no experimental tests on the TMJ had been carried out and the constitutive law parameters were obtained fitting a hyperelastic Marlow model to the experimental results of [Beek et al. \[2003\]](#).

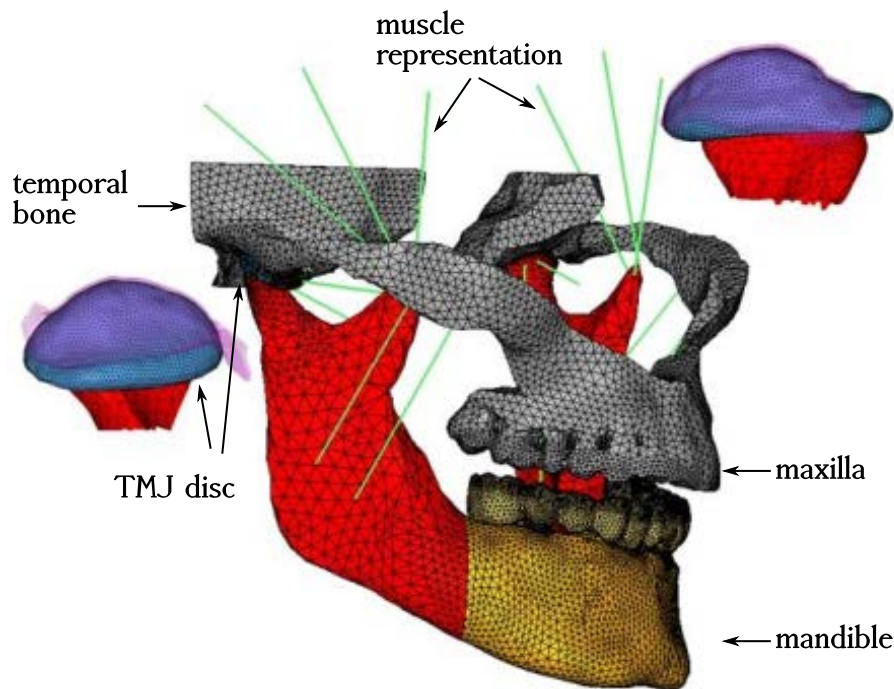


Figure 4.1 – Finite element model of [Creuillot \[2016\]](#) (adapted), including the mandible, temporal bone, maxilla, temporomandibular joint discs and muscle representation.

In order to remove these two limitations, a method has been developed on pig samples to acquire the geometry of the TMJ disc (Chapter 3, Section 3.2.2.1). The optical 3D scans proved to be a rapid method to obtain geometrical sample data. Due to a fast experimental procedure, sample's exposure time to air is short, so that TMJ disc samples are not damaged using this non-invasive method. The quality of this technique will allow improving models of human TMJ implementing accurate disc geometries. On the other hand, to obtain constitutive law parameters, a method to analyse local spherical compression tests based on finite element simulations has been developed in Chapter 2. This method takes into concern the finite size of the TMJ disc as well as the experimental setup, which includes the samples position on a support, in contrast to the assumption that the sample is bonded to the surface (e.g [Lin et al., 2009](#); [Zhang and Yang, 2017](#)). Chapter 3 presents results of local spherical compression tests on porcine temporomandibular joint disc samples, including study of influence of loading frequency, compression site and compression tool size.

In this Chapter the force - displacement data experimentally obtained are processed to deduce stress-strain curves in order to identify parameters of various hyperelastic constitutive laws that can be used to describe the behaviour of the TMJ disc's tissue in a first step. Hyperelastic laws are developed to take into concern large strain elasticity, as this is the case for many soft biological tissues. For this reason, those models were chosen to fit the experimental data. The obtained parameters are used to simulate the local spherical compression tests on the temporomandibular joint disc in three-dimensional finite element analysis. The results of the simulation are compared to the experimental data to validate the obtained parameter and by extension the workflow propose in this work aiming to characterise the biomechanical behaviour of the TMJ disc.

4.2 Material and Methods

The aim of the work reported in this Chapter is to obtain representative stress-strain curves from the experimental force-displacement data in order to deduce constitutive coefficients describing the TMJ disc. In a first step, this Section presents the construction of representative stress-strain curves, followed by the presentation of hyperelastic law fitting. Finally, the application of obtained constitutive relation in a three-dimensional finite element simulation is demonstrated.

4.2.1 Representative stress-strain curve construction

In Chapter 3 the acquisition of force-displacement data from local spherical compression is described and results are presented. To these data the method developed in Chapter 2 is applied.

Since the model developed in Chapter 2 considers only one loading phase, the experimental representative stress-strain relationships were consequently only constructed for this phase. The loading protocol of the samples should be remembered, consisting out of a preconditioning phase followed by a return to zero, a search for a preload and the subsequent test cycles (see Figure 3.4). This protocol has been established because experimental characterisation of the temporomandibular joint disc causes several experimental difficulties due to its complex shape and nature as a soft biological tissue.

During local spherical compression, the most challenging problem is the definition of contact between the compression tool and the sample. In the experimental investigation this problem was solved by defining an initial force from which the compression tool was considered to be in contact with the sample (see Section 3.2.3.1). The displacement corresponding to this defined preload was taken as an offset for the displacement d , respectively. For the presentation of the force-displacement curves (see Figure 3.13), the preload and the corresponding displacement d have been used as offsets. However, the preload charges the sample inducing both pre-strain and pre-stress in the matter that complicates the construction of stress-strain curves from experimental force - displacement data. Furthermore, regarding the calculation of the representative stress and strain, we observe that the compression tool's displacement d influences strongly resulting strains and stresses since d intervenes in the calculation of the contact radius a which is used to calculate the representative stress and strain.

If the same offset would be applied for stress-strain curves, namely the force and displacement of the preload defined in Chapter 3, the contact radius will be set as zero, although experimentally the compression tool is already in contact with the sample, leading to an overestimation of the representative stress.

For this reason, the steps executed to obtain representative stress-strain curves from local spherical compression test were the following:

- During the "search for preload", the instant of contact between the compression tool and the sample is determined as the moment from which the force increases constantly. Two variables were therefore added per sample and named $F_{contact}$ and $d_{contact}$ (see Figure 4.2).
- $F_{contact}$ and $d_{contact}$ were used for an offset and corresponding representative stress-strain curves were calculated.

- Due to the load cell limit, representative stress-strain curves contain a noisy beginning, which was eliminated before plotting.

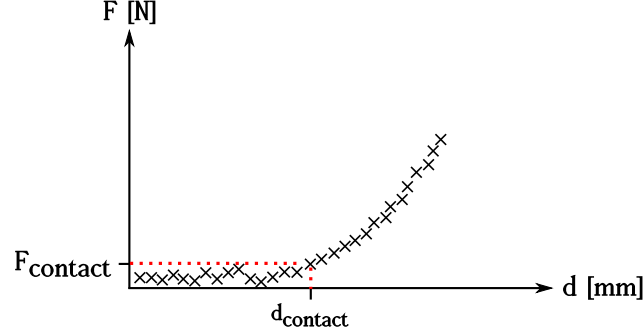


Figure 4.2 – Definitions of variables $F_{contact}$ and $d_{contact}$ for stress-strain curve construction.

Another point that complicates the construction of stress-strain curves is the fact that in the experimental protocol different velocities have been used during the phase in search of the preload and the following cyclic loading phase. While during the cyclic loading phase the velocities applied correspond to the three loading frequencies, the velocity during the search for preload was always the lowest velocity used during the tests (corresponding to the loading velocity of the test at 0.01 Hz), in order to detect the preload accurately. Since in Chapter 3 the viscoelastic behaviour of the TMJ disc samples was shown, it is known that the loading rate strongly affects the tissues behaviour. For this reason, stress-strain curves were only exploited for the results from the experiments at a loading frequency of 0.01 Hz. Hyperelastic material laws are fitted to these curves, in order to receive constitutive relationships describing the TMJ disc.

4.2.2 Hyperelastic material laws used to describe temporomandibular joint disc behaviour

In a first step, hyperelastic models were chosen to simulate the TMJ disc due to their regular application for biological soft tissues. The hyperelastic laws tested to describe the TMJ disc behaviour were neo-Hookean, Mooney-Rivlin and Ogden strain energy potentials. The neo-Hookean model is the simplest hyperelastic law and has already been used to simulate the TMJ disc [Savoldelli et al., 2012]. Since neo-Hookean hyperelasticity is a special case of the Mooney-Rivlin model, this law has been used as well. In addition, the Ogden approach was shown to fit well spherical indentation results within the Hertz regime [Lin et al., 2009].

Neo-Hookean form

In Abaqus [Abaqus, 2013] the strain energy potential Ψ of a compressible neo-Hookean [Rivlin, 1948] hyperelastic material is defined as:

$$\Psi = C_1(\bar{I}_1 - 3) + \frac{1}{D_1}(J^{el} - 1)^2 \quad (4.1)$$

where \bar{I}_1 is the first deviatoric strain invariant, J^{el} elastic volume ratio, $C_1 = \frac{\mu_0}{2}$ and $D_1 = \frac{K_0}{2}$ material parameters that are linked to the initial shear (μ_0) and bulk moduli (K_0) (Chapter 2, Section 2.2.1). Regarding incompressible neo-Hookean materials, the

elastic volume ratio is 1 and consequently the second term of Equation 4.1 becomes nil. Due to the high amount of water within the TMJ disc, this assumption is legitimized.

In a uniaxial loading case, the principal Cauchy stress can be written as (see Appendix B.2):

$$\sigma_I = 2C_1 \left(\lambda^2 - \frac{1}{\lambda} \right) = \mu_0 \left(\lambda^2 - \frac{1}{\lambda} \right) \quad (4.2)$$

with λ the stretch in loading direction. The nominal stress can be written as:

$$\sigma_{nominal} = 2C_1 \left(\lambda - \frac{1}{\lambda^2} \right) = \mu_0 \left(\lambda - \frac{1}{\lambda^2} \right) \quad (4.3)$$

Mooney-Rivlin form

A compressible Mooney-Rivlin [Mooney, 1940] hyperelastic material is defined in Abaqus by the potential:

$$\Psi = C_1(\bar{I}_1 - 3) + C_2(\bar{I}_2 - 3) + \frac{1}{D_1}(J^{el} - 1)^2 \quad (4.4)$$

where \bar{I}_1 and \bar{I}_2 are first and second deviatoric strain invariant, C_1 , C_2 and D_1 temperature-dependent material parameters linked to initial shear (μ_0) and bulk moduli (K_0):

$$\mu_0 = 2(C_1 + C_2) \quad (4.5)$$

$$K_0 = \frac{2}{D_1} \quad (4.6)$$

For an incompressible Mooney-Rivlin material the principal stretches are:

$$\lambda_1 = \lambda; \lambda_2 = \lambda_3 = \frac{1}{\sqrt{\lambda}}$$

and the principal Cauchy stress can be written as:

$$\sigma_I = \left(2C_1 + \frac{2C_2}{\lambda} \right) \left(\lambda^2 - \frac{1}{\lambda} \right) = 2C_1 \left(\lambda^2 - \frac{1}{\lambda} \right) + 2C_2 \left(\lambda - \frac{1}{\lambda^2} \right) \quad (4.7)$$

the nominal stress becomes:

$$\sigma_{nominal} = 2C_1 \left(\lambda - \frac{1}{\lambda^2} \right) + 2C_2 \left(1 - \frac{1}{\lambda^3} \right) \quad (4.8)$$

Ogden form

In Abaqus the strain energy potential of an Ogden type [Ogden, 1972] hyperelastic material is defined as:

$$\Psi = \sum_{i=1}^N \frac{2\mu_i}{\alpha_i^2} (\bar{\lambda}_1^{\alpha_i} + \bar{\lambda}_2^{\alpha_i} + \bar{\lambda}_3^{\alpha_i} - 3) + \sum_{i=1}^N \frac{1}{D_1} (J^{el} - 1)^{2i} \quad (4.9)$$

where $\bar{\lambda}_i$ are the deviatoric principal stretches $\bar{\lambda}_i = J^{-\frac{1}{3}} \lambda_i$; λ_i are the principal stretches, μ_i , α_i and D_i are 3N temperature-dependent material parameters. For the Ogden model the initial shear modulus and bulk modulus are defined as:

$$\mu_0 = \sum_{i=1}^N \mu_i \quad (4.10)$$

$$K_0 = \frac{2}{D_1} \quad (4.11)$$

The maximal principal Cauchy stress σ_I can be written as:

$$\sigma_I = \sum_{p=1}^N \frac{2\mu_p}{\alpha_p} \left[\lambda^{\alpha_p} - \left(\frac{1}{\sqrt{\lambda}} \right)^{\alpha_p} \right] \quad (4.12)$$

In the case of $N = 1$ the above equation becomes:

$$\sigma_I = \frac{2\mu_1}{\alpha_1} \left[\lambda^{\alpha_1} - \left(\frac{1}{\sqrt{\lambda}} \right)^{\alpha_1} \right]$$

and the nominal stress becomes:

$$\sigma_{nominal} = \frac{1}{\lambda} \left\{ \frac{2\mu_1}{\alpha_1} \left[\lambda^{\alpha_1} - \left(\frac{1}{\sqrt{\lambda}} \right)^{\alpha_1} \right] \right\}$$

For a two-term Ogden model the nominal stress has the following form:

$$\sigma_{nominal} = \frac{1}{\lambda} \left\{ \frac{2\mu_1}{\alpha_1} \left[\lambda^{\alpha_1} - \left(\frac{1}{\sqrt{\lambda}} \right)^{\alpha_1} \right] \right\} + \frac{1}{\lambda} \left\{ \frac{2\mu_2}{\alpha_2} \left[\lambda^{\alpha_2} - \left(\frac{1}{\sqrt{\lambda}} \right)^{\alpha_2} \right] \right\}$$

As in Chapter 2, these theoretical stresses have been fitted to the experimental results. The same method as described in Section 2.2.4 has been applied to perform the parameters' identification. The objective function and the fitting parameters have been changed to the corresponding nominal stress of the hyperelastic law. The obtained material parameter were used in finite element simulations of the local spherical compression tests of the TMJ disc.

4.2.3 Finite element model of local spherical compression test on one temporomandibular joint disc

In many finite element simulations of the TMJ, the disc geometry is obtained by filling geometrically the gap between the condyle and the temporal bone [Creuillot, 2016; Hattori-Hara et al., 2014; Hirose et al., 2006; Mori et al., 2010]. In Chapter 3 the optical scan of TMJ discs has been described. These scans do not only serve for disc dimension measurements, the obtained datasets were transferred to meshes to be used in finite element simulations. The post-processing of the scan data included several steps.

GOM Inspect Using the GOM Inspect software (GOM Software 2017, Hotfix 1, Rev. 103616, build 2017-08-09), holes in the scans were filled and irregularities smoothed. From this software stereolithography files were exported.

Catia Using the Digitized Shape Editor from Catia (Dassault Systems, V5r2015), the surface is reconstructed from the stereolithography file and exported as .stp file. This reconstruction is shown in Figure 4.3.a.

HyperMesh Within HyperMesh (Altair HyperWorks, Version 13) the surface-based geometry was partitioned and meshed, the mesh is presented in Figure 4.3.b.

The TMJ disc's geometry surface was divided in two parts, a central part of the geometry and an outer region which includes the anterior and posterior band and the surrounding tissue that has been scanned. The central part was meshed using hexahedral elements including a bias factor of the mesh size (see detail in Figure 4.3.b). The bias allows optimizing the element size with small elements (average size 0.1 mm) under the compression tool and bigger elements (maximum size 0.35 mm) in the remaining central part. For the outer part, which has a more complicated shape, a tetrahedral mesh was preferred. The obtained mesh consists out of 78584 nodes (52224 linear hexahedral (C3D8R), 12 linear wedge (C3D6) and 115179 linear tetrahedral (C3D4) elements).

The mesh's partition permits optimisation of calculation time and precision. While the zone of contact is meshed with a refined hexahedral mesh, the TMJ disc parts, which are not within the zone of contact between the compression tool and the support, are meshed with tetrahedral elements. A calculation using this mesh required the use of the cluster provided by the LEM3 laboratory, using one node and eight processors.

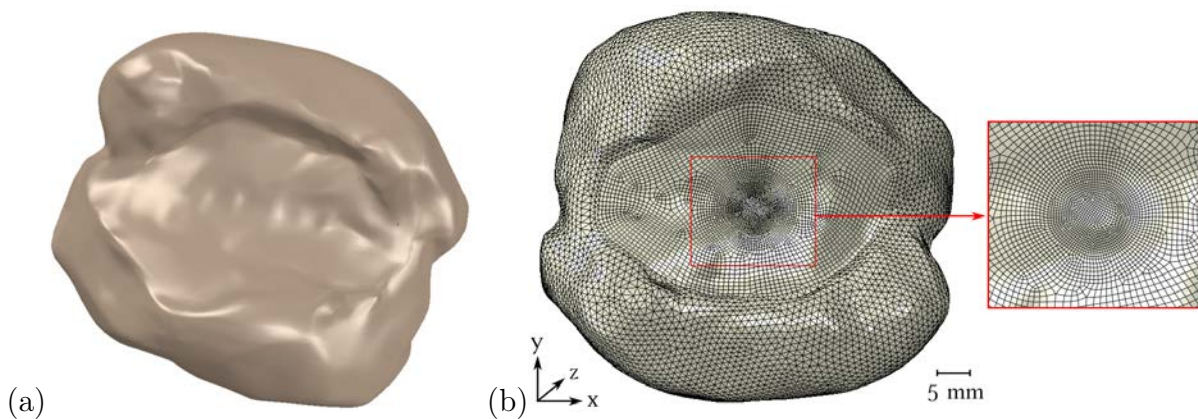


Figure 4.3 – Example of (a) a post-processed TMJ disc 3D geometry obtained from optical 3D scans and (b) TMJ disc's 3D mesh. The disc is meshed with hexahedral elements, including a bias mesh in the central zone, as shown in the zoom. For the surrounding tissue tetrahedral elements were chosen.

In order to reproduce the experimental setup, the model included three parts; the TMJ disc, the compression tool of radius 3 mm and the support (Figure 4.4). In contrast to the experiment, the support was not represented by a condyle geometry. Instead, the inferior surface of the TMJ disc has been duplicated in HyperMesh and meshed, using a coarser mesh than for the TMJ disc. This surface served as the disc support in order to avoid calculation instabilities of the contact between the disc and its support. Since the surface, as well as the compression tool were assumed to be much stiffer than the TMJ disc, they were considered as rigid bodies, with the compression tool being an analytical rigid body. The positioning of the TMJ disc with respect to the compression tool has been selected in such a way that the compression tool got in contact with the TMJ disc under a right angle and that contact occurred in the refined mesh region. The TMJ disc was considered as a hyperelastic material, the material parameters applied were those obtained through fitting of the stress-strain curves and are presented in Section 4.3.2.

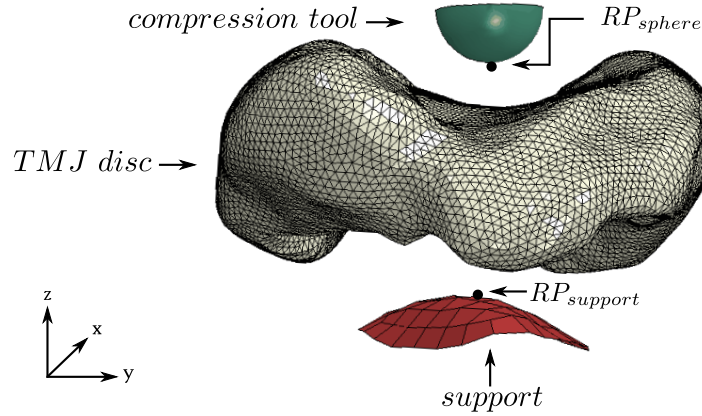


Figure 4.4 – Assembly of 3D simulation including three parts; the spherical compression tool as a rigid body, the TMJ disc sample and the rigid support.

The compression tool and the supporting surface were regarded as masters and the superior and inferior TMJ disc surfaces as slaves. The surface-to-surface contact formulation was used, including friction. To stabilise the simulation, a high friction coefficient of 0.4 between the support and the TMJ disc was chosen. On the second contact surface, between the TMJ disc and the compression tool, a friction coefficient of 0.005 was applied. A lower friction coefficient describes better the physiological conditions including synovial fluid, respectively the experimental condition in which physiological solution was present.

The simulations were carried out in two consecutive steps in the domain of large strains. During the first step gravity is applied and over-closures between the TMJ disc and the master surfaces are allowed to be removed. In this way, it was ensured to obtain a contact between the parts in the following step. In the second step, the compression tool is moved in order to compress the sample.

Boundary conditions

In the first step, during the application of gravity, the compression tool and the supporting surface are completely fixed ($RP_{\text{sphere}}: U_x = U_y = U_z = 0$, $RP_{\text{surface}}: U_x = U_y = U_z = 0$). The disc nodes are free to move in vertical direction ($U_x = U_y = 0$).

The second step simulates the first loading of the TMJ disc, therefore a displacement of 0.5 mm is applied to the compression tool ($RP_{\text{sphere}}: U_x = U_y = 0$), taking into account the actual displacement undergone of the sample during the experiment. In this step, all disc nodes can be displacement in all degrees of freedom, the compression tool is fixed in two directions ($RP_{\text{sphere}}: U_x = U_y = 0$) the surface is completely fixed ($RP_{\text{surface}}: U_x = U_y = U_z = 0$).

Force-displacement curves

To compare numerical and experimental results, the reaction force and displacement of the compression tool (RP_{sphere}) were evaluated.

4.3 Results and Discussion

This section presents the stress-strain curves from local spherical compression tests, the hyperelastic fitting using different material models and finite element simulations of local spherical compression tests on one TMJ disc sample.

4.3.1 Stress-strain curves of local spherical compression tests on temporomandibular joint disc samples

As described in Section 4.2.1, the raw stress-strain curves show a beginning containing noise, which is exemplary shown in Figure 4.5 for a big (Figure 4.5.a) and a small compression tool (Figure 4.5.b). The noise is a result of the load cell accuracy, which lies in the range of low forces measured (see Section 3.2.3.2). Henceforth, the following stress-strain curve figures are presented after resolving this noise.

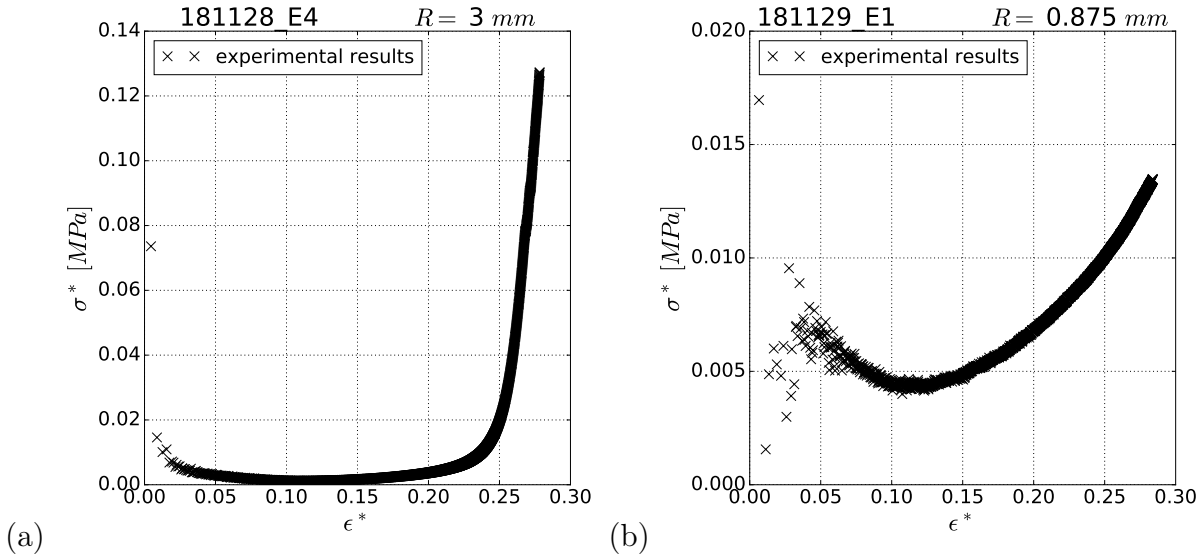


Figure 4.5 – Examples of raw stress-strain ($\sigma^* - \epsilon^*$) data for tests on samples central site using compression tools of radii (a) $R = 3 \text{ mm}$ and (b) $R = 0.875 \text{ mm}$ depicting the noisy beginning of the stress-strain curves caused by the load cell's accuracy.

Figure 4.6 illustrates three typical examples for stress-strain curves obtained during the preloading and first loading phase of local spherical compression tests on samples' central site using the three different compression tools (for further results see Appendix D). Several characteristics can be deduced from these results.

A long "toe" region up to 22% strain is present for tests using the big (radius 3 mm, Figure 4.6.a) and the medium size compression tool (radius 1.75 mm, Figure 4.6.b). This toe region is followed by an almost linear region in which the stress increases rapidly.

The strains applied to the samples using the three compression tools vary between 27-31% for the examples shown in Figure 4.6. The highest strain was obtained using the smallest compression tool (radius 0.875 mm, Figure 4.6.c) and the lowest using the biggest one (radius 3 mm, Figure 4.6.a).

Regarding the obtained stresses, this relationship reverses. The highest stress value up to 0.13 MPa occurs for the test using the big compression tool, whereas during the test using the small one, stresses up to 0.013 MPa were detected. For the case of the medium

size compression tool, the maximum stress reached was 0.075 MPa.

Figure 4.7 compares stress-strain curves from spherical compression on the central, medial and lateral sites of one sample (using the big compression tool). The general characteristics of the stress-strain curves, including the toe region, the rapid increase in stress and differences in the applied strain are found on all sites. In the examples presented, the highest stress occurs during the test on the samples medial site (Figure 4.7.b) with up to 0.18 MPa, the lowest on the samples lateral site (0.12 MPa, Figure 4.7.c). In general, no trend could be observed regarding differences in results on the three test sites, as can be observed from additional results presented in Appendix D. The fitting curves shown in Figures 4.6 and 4.7 will be subject of Section 4.3.2.

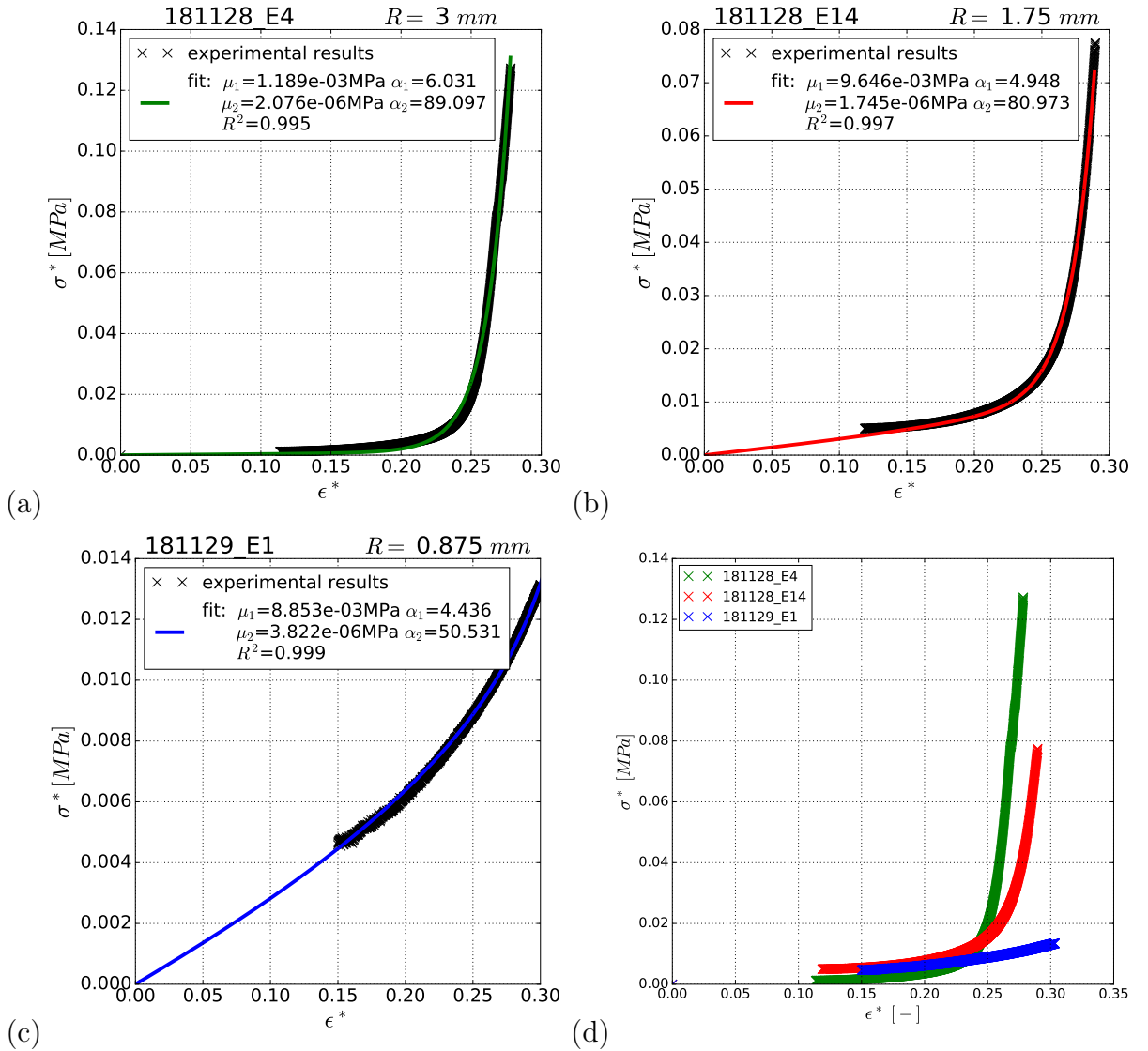


Figure 4.6 – Stress - strain ($\sigma^* - \epsilon^*$) curves for three exemplary tests on samples central site using compression tools of different radii R (a) - (c), including hyperelastic fitting using a two-term Ogden model with four fitting parameter μ_1 , α_1 , μ_2 , α_2 and the associated determination coefficient R^2 . (d) depicts the summary of the previous presented stress-strain curves.

Although during the cyclic test phase the same displacement was applied to all samples tested with the same compression tool, the strains differ slightly (Figure 4.7). Regarding tests using different sizes of compression tools (Figure 4.6), the obtained strains are between 27-31%. There are two main causes for this behaviour. First, the stress-strain curves are constructed for the "search of preload" and first loading phase. Experimentally, displacement of the compression tool during the "search of preload" phase depends on the moment of contact, which was for example defined at a detected force of 0.16 N for the big compression tool (see Table 3.1). The displacement undergone by the compression tool until detection of contact can therefore vary for each test. Second, due to the correction of load cell stiffness (see Chapter 2, Section 3.2.3.2), displacement applied to the sample depends also on forces measured. In order to avoid the influence of this second point, the machine's loading protocol should directly take into consideration the load cell stiffness in future experiments.

The measured forces in turn do influence the maximum stresses. For tests using the same size of compression tool, the stress values lie in the same range of magnitude (Figure 4.7). The dispersion of values might be a result of inter-individual variance and establishment of contact between the sample and the compression tool. Comparison of the results using the three different compression tool sizes (Figure 4.6) however results in different absolute values. At a first sight, this result is surprising, but the TMJ disc, although often considered as a macro-homogeneous material to simplify models, is a complex and heterogeneous structure. And here lies the reason why the stress-strain states differ. Using the small compression tool, the first enveloping layer was mainly tested, while using bigger compression tools, deeper layers were investigated. This is also the reason, why Figure 4.6.c actually only shows one distinct region and not the toe and the following almost linear region, what can be deduced from Figure 4.6.d.

Figure 4.8 describes this hypothesis and shows a disc sketch with the layers detected in histological cuts (see Figure 1.5). Figure 4.8 and results from Figure 4.6 highlight that the disc has a macro-heterogeneous structure.

To verify this hypothesis, not only the strains were investigated but also the actual undergone displacement of the compression tools, which are summarized in Table 4.1. First, it can be noted that the displacement of the compression tool during the preload and first loading phase differs for the three compression tools used. The largest displacements were undergone by the biggest sphere, the smallest by the smallest one. This is related to the experimental test conditions, which specify higher preload and higher compression tool displacement for the bigger sphere (Tables 3.1 and 3.2). Using the big compression tool, which radius is bigger than the thickness of the external envelop, it could be admitted that the behaviour of the internal part of the disc is mainly characterised. Indeed, using the compression tool of radius 3 mm, the average displacements reached up to 1.16 mm (Table 4.1) on the lateral site, which means that these tests allowed characterisation of deeper TMJ disc layers. Using the smallest compression tool, the radius of which is comparable with the envelop thickness, the reaction of this envelop is mainly tested according to the histological cuts in Figure 1.5. It is confirmed by the average displacement recorded between 0.412 mm (medial) to 0.622 mm (lateral). The compression tool of radius 1.75 mm underwent in average a displacement of 0.80 mm for tests on the samples central site. The impact of the three different compression tool radii on the TMJ disc confirms the idea of sample layers deformation depicted in Figure 4.8.

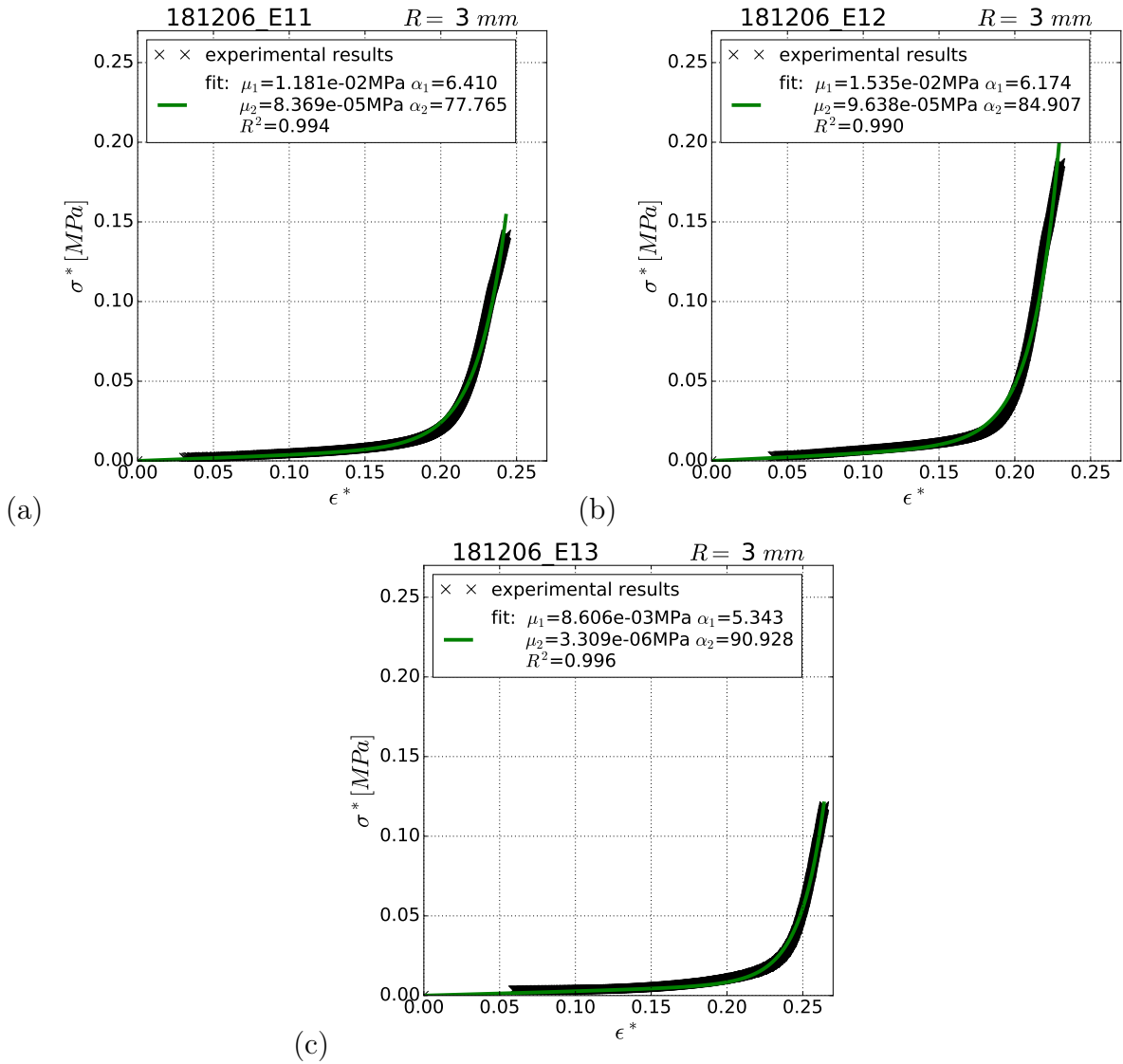


Figure 4.7 – Stress - strain ($\sigma^* - \epsilon^*$) curves for three test sites on one sample; (a) central, (b) medial, (c) lateral site using the big compression tool (radius $R = 3 \text{ mm}$), including hyperelastic fitting using a two-term Ogden model with four fitting parameter μ_1 , α_1 , μ_2 , α_2 and the associated determination coefficient R^2 .

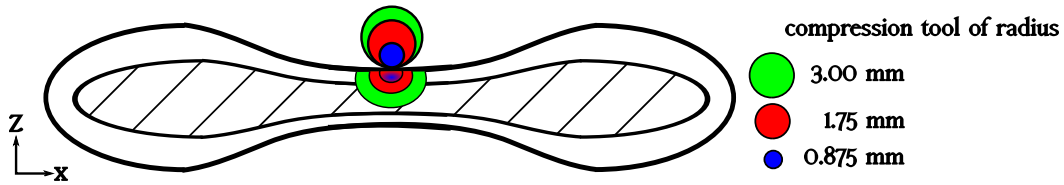


Figure 4.8 – Sketch of TMJ disc with enveloping and internal layer and three spherical compression tools (green, red, blue), each affecting a different depth and therefore a different TMJ disc sample layer.

Since the obtained stress-strain curves are very different, it proves the macro- heterogeneous structure of the TMJ disc. It appears that the external envelop of the disc is very soft compared to the inner layer. Remembering that the disc tissue is constituted of various biochemical components such as the fibres with preferential orientations, it can be concluded that the TMJ disc is a micro- and macro-heterogeneous structure similar to, for instance, skeletal bones, with its cortical and trabecular structure.

Regarding the displacements of the compression tools, it can further be noted that the smallest standard deviations occur for the displacements affected on samples central site, highest on samples lateral site, independent of compression tool size. This relies most probably on the samples' geometry and the way the compression tool touches the sample. During experiments, care was taken that the contact of the sample and the tool was affected on the sphere's tip, however, it is possible that for some tests the compression tool did touch the sample more on its side. Nonetheless, the compression tool sizes were chosen in accordance with the estimated sample curvatures which were around 12 mm (see Figure 3.11) and are therefore bigger than the biggest sphere used.

Table 4.1 – Summary of undertaken displacement of compression tools as from the first detection of a force and the first loading phase. Presented are the average values calculated from results presented in the Appendix D (Tables D.1 - D.3, D.4 - D.6, D.7 - D.9).

test site	average (\pm STD) d_{max} [mm] of com- pression tool of radius 0.875 mm	average (\pm STD) d_{max} [mm] of com- pression tool of radius 1.75 mm	average (\pm STD) d_{max} [mm] of com- pression tool of radius 3.00 mm
central	0.427 ± 0.046	0.80 ± 0.126	0.86 ± 0.093
medial	0.412 ± 0.076	0.78 ± 0.205	0.94 ± 0.30
lateral	0.622 ± 0.288	1.03 ± 0.186	1.16 ± 0.35

From stress-strain curves, compressive moduli can be calculated as the tangent modulus of the final part of the loading phase. The obtained results show that using bigger compression tools and respectively testing deeper sample layers results not only in higher stresses, but also in higher compressive moduli. For the small compression tool, the compressive modulus was calculated for two tests (181129_E1 and 181206_E1), resulting in 0.112 MPa and 0.160 MPa. For the big compression tool, a compressive modulus of 5.74 MPa (181128_E4) and for the compression tool with the radius 3.5 mm a modulus of 3.86 MPa was obtained (181128_E14).

These findings highlight that every part of the TMJ disc structure has special characteristics that support the function of the TMJ. The disc is not only a stress absorber and distributor, but it also provides congruency between the bones. With the first enveloping layer being softer than the inner one, the disc is able to adjust its shape to the bony structures, while the inner layer's role is to resist to the external forces applied.

In cylindrical local compression tests on complete human TMJ discs, [Beek et al. \[2001\]](#) obtained a compressive modulus (secant modulus calculated for first load) of around 16 MPa applying a strain of 32%. The strain applied is in the range of strains applied in this study, however, the applied preload and method of detection of contact are unknown. [Beek et al. \[2001\]](#) and [Fazaeli et al. \[2016\]](#) used cylindrical compression tools of radii 2.00 mm to test complete TMJ discs, however, [Fazaeli et al. \[2016\]](#) applied a strain of

10% to their porcine samples after applying a tare load of 0.02 N and a preconditioning. They obtained instantaneous moduli in the range of 0.05 - 0.13 MPa, which are lower than those obtained by [Beek et al. \[2001\]](#) and in the range of the results using the small compression tool. This fact might result from the lower strains applied, it can be expected that applying higher strains would lead to higher moduli. Results from [Beek et al. \[2001\]](#) lie in the order of magnitude of the moduli obtained from the tests using the big and the medium size compression tool and are therefore comparable and in agreement with here presented results.

The stress-strain curves presented in this section highlight that the preconditioning and definition of preload are important experimental parameters. If the preload is chosen in a way that a compression tool - no matter its geometry - already enters remarkably in the samples first layer, this needs to be considered evaluating the experimental results. For this reason, it is important to communicate those experimental conditions in order to be able to compare studies among each other. As already mentioned before, the moment of contact and choice of velocity to reach the preload caused problems constructing the stress-strain curves. For this reason, only experimental results from loading frequency of 0.01 Hz were evaluated. With the propositions made in Section 3.4, the experimental protocol could be improved in order to overcome these difficulties.

With regard to nanoindentation studies, it should be considered that even thinner layers of the TMJ disc can be distinguished and tested. From their nanoindentation tests [Chandrasekaran et al. \[2017\]](#) and [Yuya et al. \[2010\]](#) obtained compressive moduli of 81 kPa and 65-487 kPa, using indentation depth of $1.5\ \mu\text{m}$ and $3\ \mu\text{m}$. The compressive moduli obtained using the small compression tool (0.112 MPa and 0.160 MPa) lie in the high range of results obtained by [Yuya et al. \[2010\]](#), even though indentation depth varies. Since nanoindenters are very small in size, they create very focussed deformation and therefore high pressures. This can be observed also in results obtained by [Juran et al. \[2015\]](#), who obtained compressive moduli up to 4.2 MPa for indentation depth of around $6\ \mu\text{m}$.

In summary, the stress-strain curves highlight the heterogeneity of the TMJ disc which was accessed using compression tools of different radii. These curves serve to deduce constitutive law coefficients describing the TMJ disc.

4.3.2 Hyperelastic parameter identification

Neo-Hookean, Mooney-Rivlin and one- and two-term Ogden hyperelastic models were used to fit the experimental results. From Figure 4.9 it can be seen that the two-term Ogden model is best to fit the experimental curve. The neo-Hookean model with one and the Mooney-Rivlin model with two fitting parameters are not able to satisfactory describe the two zones of the stress-strain curve. For the example shown (181128_E4), both Ogden models achieve a high coefficient of determination. However, regarding the complete set of results, better fittings were obtained using the two-term Ogden model. For this reason, only this solution is presented in the Figures 4.6 and 4.7. The model is able to accurately describe the stress-strain curves obtained from experimental data during the first loading phase as can be seen from the determination coefficients R^2 , which are higher than 0.99 for all presented examples. It demonstrates that the samples behaviour during the loading phase can be described by a hyperelastic material model.

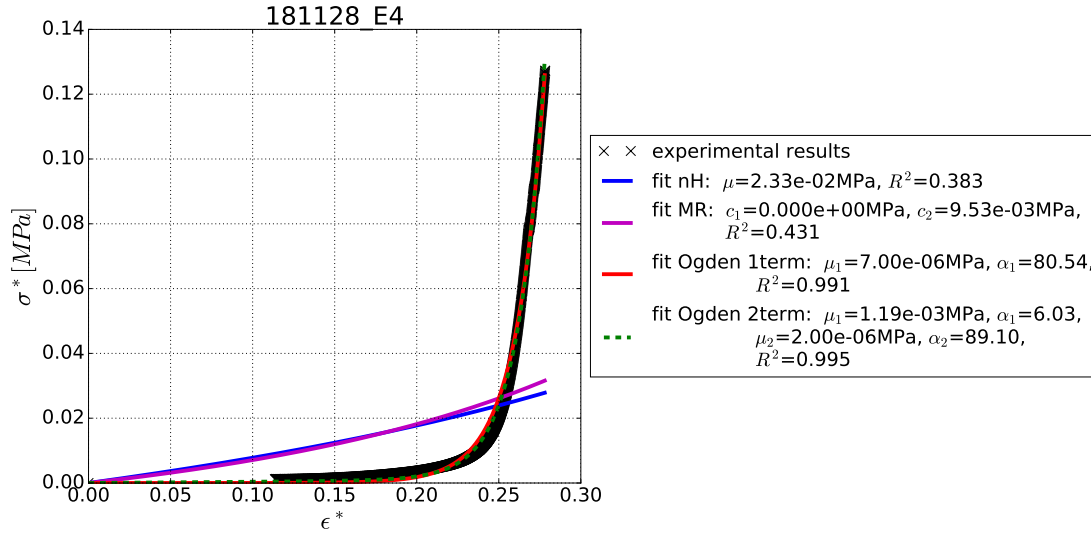


Figure 4.9 – Stress-strain curve from test on samples central site using a compression tool of radius 3mm and corresponding fitting of neo-Hookean (nH), Mooney-Rivlin (MR), one- and two-term Ogden model. Regarding the coefficient of determination R^2 and the development of the fitting curve, it becomes obvious that the two-term Ogden model suits best to fit experimental results.

A summary of obtained model parameter for tests on samples central site is provided in Table 4.2, further results are provided in the Appendix D (Tables D.1 - D.3, D.4 - D.6, D.7 - D.9.) It can be observed from the examples presented in Figure 4.6 and Table 4.2 that independently of the compression tool used the obtained parameters lie in the same order of magnitude. However, parameter α_2 decreases with decreasing compression tool size. Figure 4.7 shows that values for μ_1 and μ_2 range in the order of $1e-2$ to $1e-3$ and $1e-5$ to $1e-6$, respectively.

Table 4.2 – Average values for two-term Ogden model obtained through fitting to stress-strain curves from test of discs central site using different compression tools.

compression tool radius [mm]	μ_1 [MPa]	α_1	μ_2 [MPa]	α_2
3.00	$6.56e-3$	6.55	$3.24e-5$	84.9
1.75	$8.58e-3$	4.44	$2.89e-5$	58.9
0.875	$9.79e-3$	6.21	$6.09e-5$	16.0

The fitting of the experimental stress-strain curves using the hyperelastic two-term Ogden model resulted in different material parameters, most prominent α_2 , depending on compression tool used. Taking this into account, the parameter will be used in finite element models of the TMJ disc.

4.3.3 Three-dimensional finite element analysis of the temporo-mandibular joint disc under spherical compression

The results from the previous Chapters and Sections led to a three-dimensional finite element simulation of local spherical compression on one TMJ disc sample.

Figure 4.10.a presents the strain occurring in the sagittal plane under the compression tool's tip. Maximal compressive strains are 28% and the zone undergoing strains does not show a symmetry, which results from the samples geometry. Furthermore, the strain field shows that not only samples volume under the zone of contact is deformed but also volume which is not under the compression tool. The stresses existing within the TMJ disc sample are depicted in Figures 4.10.b and 4.10.c. The highest stress in the plane of compression is 7.4 MPa, the highest von Mises stress is 1.5 MPa. The highest stress occurring in the zone of contact is 10.1 MPa (Figure 4.11.a). This high stress is a result of the very localised contact zone (Figure 4.11.b). The figure depicts as well that the established contact between the compression tool and the TMJ disc surface is not an ideally circular one.

Compared to the experimental stress calculation for the simulated case (Figure 4.6.a, $\sigma_{max}^* = 0.14$ MPa) the maximum compressive stress in the simulation is one magnitude higher (7.4 MPa). The difference derives from stress measure, which is a stress representing a uniaxial loading case in the case of Figure 4.6.a.

The von Mises distribution resembles to the distribution obtained by [Mori et al. \[2010\]](#) (Figure 1.7), where the highest stress occurred at the zone of contact between the condyle and the TMJ disc. [[Mori et al., 2010](#)]

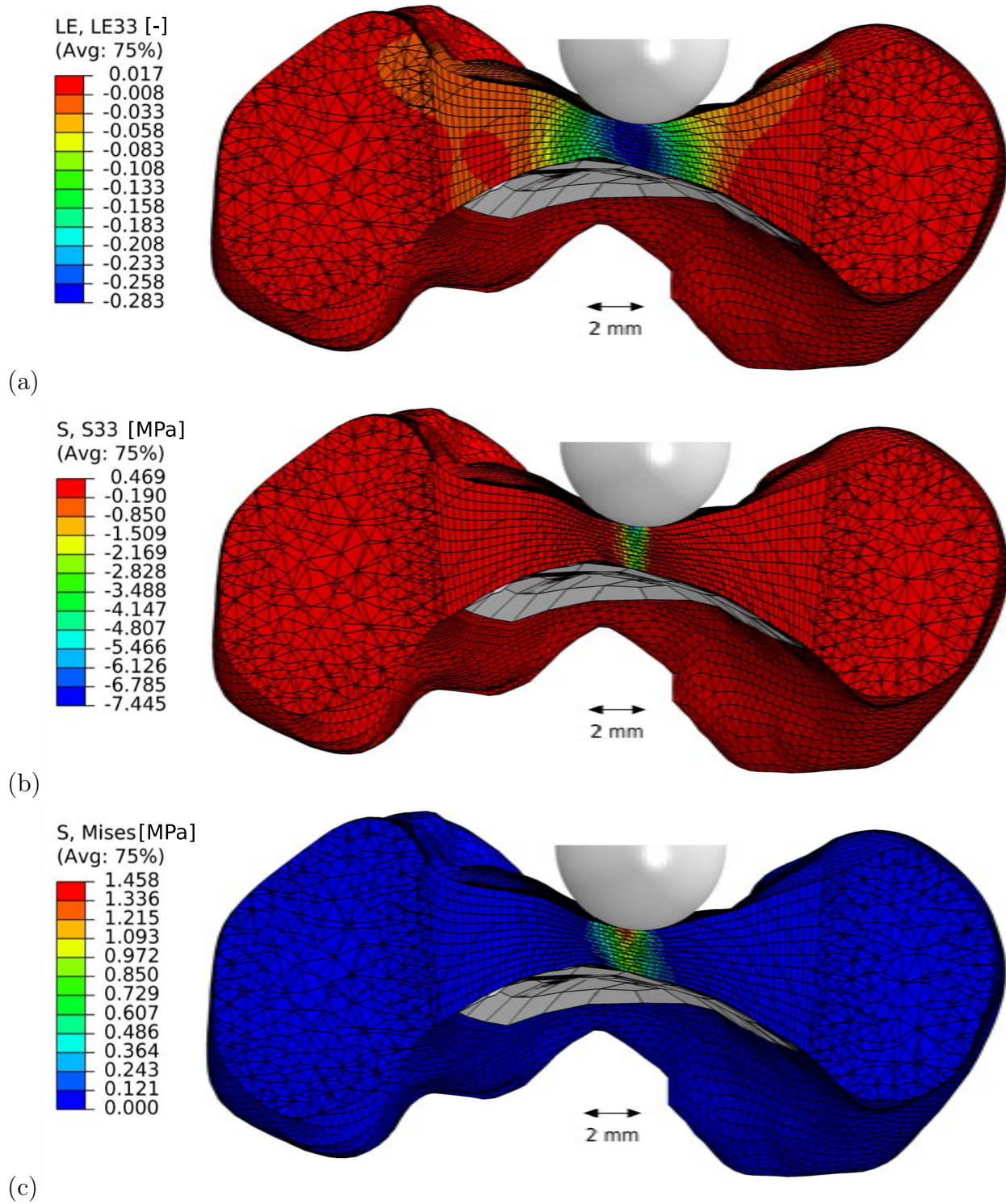


Figure 4.10 – (a) Strain field, (b) stress and (c) von Mises stress in the sagittal plane under the compression tool at its maximum displacement into the temporomandibular joint disc.

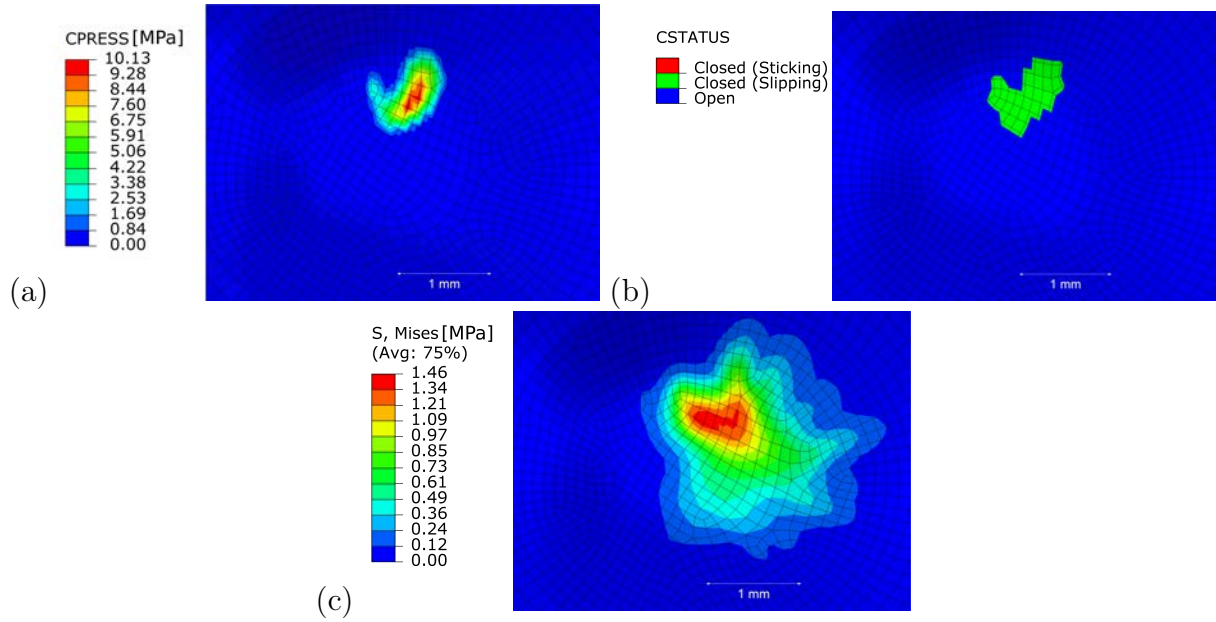


Figure 4.11 – (a) Contact pressure, (b) contact status highlighting the establishment of contact between the compression tool and the TMJ disc surface and (c) von Mises stress at the tool's maximum displacement on the TMJ discs superior surface.

4.3.4 Comparison of experimental and simulated results

In order to compare the finite element model results with the experimental ones, the force-displacement curves for both, simulation and experiments are plotted in Figure 4.12. The simulation was carried out with a compression tool of 3.00 mm radius on the discs central part and therefore the results are compared to the corresponding experiments. As can be seen from Figure 4.12.b, it was possible to represent the general material behaviour using the finite element simulation. The most distinct difference however is the "toe" region, which is shorter in the simulation compared to the experiments. This underlines the experimental difficulty of contact establishment between the sample and the compression tool. In the simulation, the compression tool was positioned in a way that its tip was in a minimal contact with the TMJ disc mesh at the beginning of the simulation to avoid convergence problems. Furthermore, the simulation is not taking into consideration the two different layers, which influence the length of the toe region, since the first layer was found softer than the inner layer. The simulation underlines that in spite of simplifications such as a plane support and an axisymmetric sample, using the approach developed in Chapter 2 and its application to experimental force-displacement data, consistent hyperelastic material coefficients can be obtained.

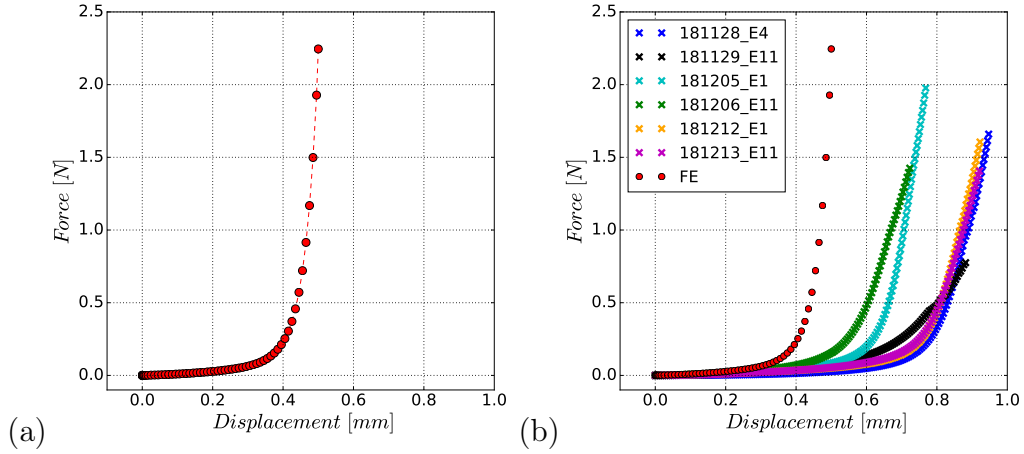


Figure 4.12 – Reaction force measured on the compression tool as function of its displacement.

However, it should be kept in mind that several differences exist between the simulation and the experimental setup, as there are no physiological solution and no 3D printed condyle in the simulation. Furthermore, only the first loading phase was analysed. These results can be seen as a first step. Future analysis should include viscous effects on the complete loading cycle.

Conclusions and Perspectives

The temporomandibular joint disc plays a crucial role in the jaw joint's activities and consequently causes severe problems in the event of injuries and diseases. In order to comprehend, prevent or cure those pathologies and to build up numerical models, it is necessary to understand and describe the TMJ disc. The goal of this study was therefore the experimental and numerical characterisation of the temporomandibular joint disc tissue to serve the aim of the prediction of the TMJ functioning.

In a first step, the TMJ disc geometry was analysed. The 3D optical scans of the TMJ disc samples allowed thickness measurements but most importantly, reconstruction of the geometry leading to the realisation of a mesh for finite element analysis. This method opens the advantage to feed numerical models with accurate TMJ disc geometries in contrast to often used methods in which the space between the bony structures of the joint is filled by the disc (e.g. [Hattori-Hara et al., 2014](#)).

The internal stress analysis, based on digital image correlation, was the first study of this kind conducted on TMJ disc samples. The presence of internal strain /stresses was revealed and was shown to influence the specimen's periphery as presented in Section 3.3.3.

These results question previously reported experimental protocols, where the effect of cutting specimen out of a TMJ disc sample are not taken into consideration.

However, in the experimental setup presented in this work special care was taken to provide test conditions adapted to soft biological tissues. Therefore, the experimental protocol presented in Chapter 3 took into consideration several physiological conditions, such as sample positioning on a 3D printed condyle, a testing chamber allowing experiments in a tempered environment and testing of the sample in its integrity during spherical compression tests.

One main achievement of the experimental characterisation of the TMJ disc (Chapter 3) was the development of a rich experimental database, resulting from 162 cyclic local spherical compression measurements on porcine TMJ discs. These tests highlighted the non-linear and viscoelastic behaviour of this fibrocartilage. Differences in the force-displacement behaviour concerning the three test sites - central, medial and lateral - could not be determined.

Another aim formulated was the characterisation of the TMJ disc to be able to predict the TMJ behaviour. To do so, a constitutive law has to be deduced from the experimental force-displacement curves.

With the advantage of testing intact samples during local spherical compression tests comes the disadvantage of construction of stress-strain curves. Unlike during cylindrical compression, the surface area, and therefore the contact radius of the spherical compression tool in contact with the sample changes during loading and unloading phases. The actual contact radius between the compression tool and the tested sample is not mea-

surable by simple means, but necessary for stress and strain calculations. Therefore, a method based on finite element models to determine the contact radius was developed and presented in Chapter 2. This method allows construction of stress-strain curves for local spherical compression tests of samples of finite thickness. The general approach takes into consideration hyperelastic samples that can partially detach from their support, as it might happen experimentally, in contrast to many studies presented in literature where samples are bonded to the support. The influence of the samples' own weight was found to affect low thickness samples' compressive behaviour, since their distal part clearly detaches from the support. The method is a first step to analyse macro-spherical compression tests of samples with finite thickness and may be applied not only to the TMJ disc but to any hyperelastic material with equal geometrical limitations.

Using this approach, the experimental force-displacement curves of the first loading phase were transformed into stress-strain curves and were presented in Chapter 4. Comparison of the stress-strain curves obtained using compression tools of three different sizes revealed the disc's macro-heterogeneity. More precisely, the TMJ disc consists of two substructures, which have different biomechanical behaviours, with the inner core being stiffer than its external envelop. Evaluating histological cuts in superoinferior direction, these layers were well observed. Furthermore, fitting of hyperelastic material laws to these curves gave the first constitutive parameters that were fed into finite element models simulating the local spherical compression tests. It was possible to numerically reproduce force-displacement curves comparable to those obtained experimentally.

The results give the possibility of wide applications, including an inverse method, for which the approach in Chapter 2 could serve as a basis to acquire an initial collection of parameters. Inverse method can be used to later obtain parameters for more complicated material models.

Due to the complex experimental protocol only the first loading phase was taken into consideration for the stress-strain analysis. In order to implement viscoelastic material properties, cyclic loading should be included to further develop the appropriate identification approach. Even more complicated constitutive relationships such as poroelastic or porohyperelastic laws could be considered to translate the biphasic composition of the TMJ disc tissue. It is well established that the biochemical environment around tissue changes the mechanical properties of the latter as it has been highlighted through our recent work [do Nascimento et al., 2020].

A limitation of our experimental approach is that it does not allow characterisation of TMJ discs anisotropy. Tensile tests allow to point out the anisotropy. A preliminary study on TMJ disc samples in anteroposterior direction was done [Tappert et al., 2018b]. Figure 4.13.a resumes the obtained results. This latter one shows the first and consecutive second loading phases with identification of the modulus for the final one percent of strain. Similarly to the local spherical compression test (Figure 4.13.b), two regions (the toe and quasi linear parts) of the stress-strain curve were observed.

The maximum stresses measured in the tensile test are higher than those occurring during spherical compression using the biggest compression tool. Consequently, they are also higher compared to results obtained using the two remaining smaller tools. However, the maximum stress in the tensile test occurred at a lower strain. In fact, the transition point between the toe region and the quasi linear part of the stress-curve is situated at around 5% in the tensile test shown, compared to 24% for the compression test. For the compressive test shown (Figure 4.13.b), identification of the modulus during the loading

phase has been conducted, which is about 5.74 MPa. It is much lower than the moduli obtained during the tensile test (9 MPa, Figure 4.13.a). This highlights that the softer enveloping substructure affects less the samples' stress-strain curve in anteroposterior tensile test.

Tensile tests are essential when more extreme movements of the TMJ are analysed, since during wide opening of the mouth the disc movement covers a greater distance and tensile forces exerted by the retrodiscal tissue will bring the TMJ disc back into its resting position. During limited mouth movements, compressive loads on the TMJ disc are more relevant, that is why this study started with compressive experiments. Moreover, the focus in this study lied in the biomechanical characterisation of intact samples, for this reason no additional tensile tests were conducted, but they are an important step to further describe the TMJ disc's biomechanical behaviour.

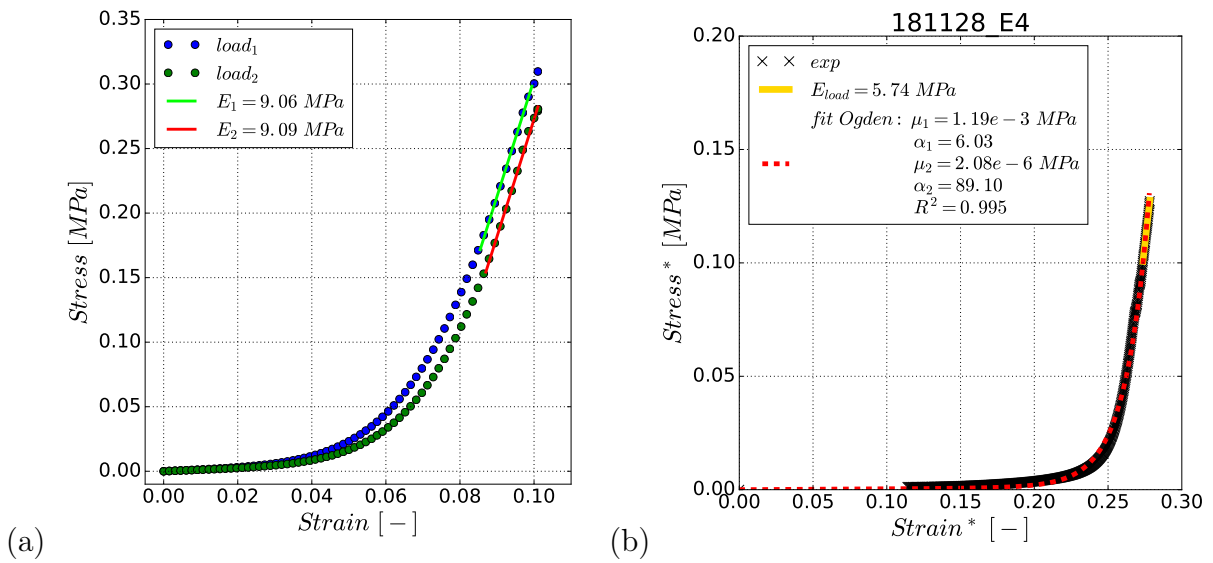


Figure 4.13 – (a) Stress-strain curve from two consecutive loading phases of uniaxial tensile test of TMJ disc specimen in anteroposterior test direction. The moduli (E_1 , E_2) were identified for the last percent of strain [Tappert et al., 2018b]. (b) Stress-strain curve for first loading phase of a local spherical compression test conducted using a sphere of 3 mm radius with associated modulus E_{load} and hyperelastic two-term (α_1 , α_2 , μ_1, μ_2) Ogden model.

Nonetheless, not only the fibre orientation, but also the GAGs are known to influence cartilage behaviour. During first tensile and local spherical compression tests, osmotic pressure effects were investigated changing the saline solution to hyper- and hypotonic states. The results were not relevant enough to pursue with the current design of the workbench. A more appropriate experimental setup to characterise change in fluid flow within the samples or specimen might be a confined compression test. In fact, the specimen obtained after the internal strain analysis have been stored to be used for such experiments.

Tensile and confined compression tests will add additional information to the database to better understand the TMJ disc behaviour and its influence on pathologies. Furthermore, the finite element models can be enriched by more realistic constitutive laws. Adding further partitions to the TMJ disc mesh, taking into consideration the heterogeneity defined by the two zones observed in the histological cuts and in local spherical

compression tests will further lead to more accurate finite element models. Depending on the research problem, the improvements on the FEM model can be adapted. Since in this study, compression test were conducted normal to the main fibre orientation, the hypothesis of a homogeneous material was justified. Before adding fibres to the model, leading to a heterogeneous composition and supporting the study of the discs micro-mechanics, anisotropic characteristics could be considered.

This study and the corresponding results led to the participation of two international conferences [[Tappert et al., 2018a,b](#)] and one francophone conference with a publication of the latter one in the conference proceedings [[Tappert et al., 2017](#)]. The cooperation with Dr do Nascimento from University of São Paulo contributed to one publication [[do Nascimento et al., 2020](#)].

Bibliography

- Abaqus [2013], ‘Abaqus Analysis User’s Guide’, Abaqus 6.13 .
- Allen, K. D. and Athanasiou, K. A. [2005], ‘A surface–regional and freeze–thaw characterization of the porcine temporomandibular joint disc’, Annals of Biomedical Engineering **33**(7), 951–962.
- Allen, K. D. and Athanasiou, K. A. [2006], ‘Viscoelastic characterization of the porcine temporomandibular joint disc under unconfined compression’, Journal of Biomechanics **39**(2), 312 – 322.
- Almarza, A., Bean, A., Baggett, L. and Athanasiou, K. [2006], ‘Biochemical analysis of the porcine temporomandibular joint disc’, British Journal of Oral and Maxillofacial Surgery **44**(2), 124 – 128.
- Almarza, A. J. and Athanasiou, K. A. [2004], ‘Design characteristics for the tissue engineering of cartilaginous tissues’, Annals of Biomedical Engineering **32**(1), 2–17.
- Alvarez Areiza, D. [2014], ‘Réflexions sur la reconstruction prothétique de l’Articulation Temporo- Mandibulaire (ATM) à travers une étude biomécanique comparative entre sujets asymptomatique et pathologique’, PhD thesis, Université de Lorraine .
- Angelo, D., Morouço, P., Alves, N., Viana, T., Santos, F., González, R., Monje, F., Macias, D., Carrapiço, B., Sousa, R., Cavaco-Gonçalves, S., Salvado, F., Peleteiro, C. and Pinho, M. [2016], ‘Choosing sheep (ovis aries) as animal model for temporomandibular joint research: Morphological, histological and biomechanical characterization of the joint disc’, Morphologie **100**(331), 223 – 233.
- Arroyave G., A., Lima, R., Martins, P., Ramião, N. and Jorge, R. [2015], ‘Methodology for mechanical characterization of soft biological tissues: Arteries’, Procedia Engineering **110**, 74 – 81. 4th International Conference on Tissue Engineering, ICTE2015, An ECCOMAS Thematic Conference.
- Athanasiou, K. A., Almarza, A. J., Detamore, M. S. and Kalpakci, K. N. [2009], ‘Tissue engineering of temporomandibular joint cartilage’, Synthesis Lectures on Tissue Engineering **1**(1), 1–122.
- Barrientos, E., Pelayo, F., Tanaka, E., Lamela-Rey, M. J. and Fernández-Canteli, A. [2016], ‘Dynamic and stress relaxation properties of the whole porcine temporomandibular joint disc under compression’, Journal of the Mechanical Behavior of Biomedical Materials **57**, 109 – 115.

- Beatty, M. W., Bruno, M. J., Iwasaki, L. R. and Nickel, J. C. [2001], ‘Strain rate dependent orthotropic properties of pristine and impulsively loaded porcine temporomandibular joint disk’, Journal of Biomedical Materials Research **57**(1), 25–34.
- Beek, M., Aarnts, M., Koolstra, J., Feilzer, A. and Van Eijden, T. [2001], ‘Dynamic properties of the human temporomandibular joint disc’, Journal of Dental Research **80**(3), 876–880.
- Beek, M., Koolstra, J. and van Eijden, T. [2003], ‘Human temporomandibular joint disc cartilage as a poroelastic material’, Clinical Biomechanics **18**(1), 69 – 76.
- Bermejo, A., González, O. and González, J. [1993], ‘The pig as an animal model for experimentation on the temporomandibular articular complex’, Oral Surgery, Oral Medicine, Oral Pathology **75**(1), 18 – 23.
- Briscoe, B. J., Fiori, L. and Pelillo, E. [1998], ‘Nano-indentation of polymeric surfaces’, Journal of Physics D: Applied Physics **31**(19), 2395–2405.
- Calvo-Gallego, J. L., Commisso, M. S., Domínguez, J., Tanaka, E. and Martínez-Reina, J. [2017], ‘Effect of freezing storage time on the elastic and viscous properties of the porcine tmj disc’, Journal of the Mechanical Behavior of Biomedical Materials **71**(Supplement C), 314 – 319.
- Chadwick, R. S. [2002], ‘Axisymmetric indentation of a thin incompressible elastic layer’, SIAM Journal on Applied Mathematics **62**(5), 1520–1530.
- Chandrasekaran, P., Doyran, B., Li, Q., Han, B., Bechtold, T. E., Koyama, E., Lu, X. L. and Han, L. [2017], ‘Biomechanical properties of murine tmj articular disc and condyle cartilage via afm-nanoindentation’, Journal of Biomechanics **60**(Supplement C), 134 – 141.
- Chapuis, J. [2011], ‘Une approche pour l’optimisation des opérations de soudage à l’arc’, PhD thesis, Université de Montpellier 2, I2S .
- Chen, J. and Xu, L. [1994], ‘A finite element analysis of the human temporomandibular joint’, Journal of Biomechanical Engineering **116**(4), 401–407.
- Commisso, M., Calvo-Gallego, J., Mayo, J., Tanaka, E. and Martínez-Reina, J. [2016], ‘Quasi-linear viscoelastic model of the articular disc of the temporomandibular joint’, Experimental Mechanics **56**(7), 1169–1177.
- Commisso, M. S., Martínez-Reina, J., Mayo, J., Domínguez, J. and Tanaka, E. [2014], ‘Effect of non-uniform thickness of samples in stress relaxation tests under unconfined compression of samples of articular discs’, Journal of Biomechanics **47**(6), 1526 – 1530.
- Creuillot, V. [2016], ‘Etude de l’impact d’une prothèse dentaire implanto-portée sur le comportement des articulations temporo-mandibulaires et de l’os péri-implantaire’, PhD thesis, Université de Lorraine .
- Dagro, A. M. and Ramesh, K. T. [2019], ‘Nonlinear contact mechanics for the indentation of hyperelastic cylindrical bodies’, Mechanics of Soft Materials **1**(1), 7.

- Dai, A., Wang, S., Zhou, L., Wei, H., Wang, Z. and He, W. [2019], ‘In vivo mechanical characterization of human facial skin combining curved surface imaging and indentation techniques’, Skin Research and Technology **25**(2), 142–149.
- del Palomar, A. P. and Doblaré, M. [2006], ‘Finite element analysis of the temporomandibular joint during lateral excursions of the mandible’, Journal of Biomechanics **39**(12), 2153 – 2163.
- Detamore, M. S. and Athanasiou, K. A. [2003a], ‘Motivation, characterization, and strategy for tissue engineering the temporomandibular joint disc’, Tissue engineering **9**(6), 1065–1087.
- Detamore, M. S. and Athanasiou, K. A. [2003b], ‘Tensile properties of the porcine temporomandibular joint disc’, Journal of Biomechanical Engineering **125**(4), 558–565.
- Detamore, M. S., Orfanos, J. G., Almarza, A. J., French, M. M., Wong, M. E. and Athanasiou, K. A. [2005], ‘Quantitative analysis and comparative regional investigation of the extracellular matrix of the porcine temporomandibular joint disc’, Matrix Biology **24**(1), 45 – 57.
- Dimitriadis, E. K., Horkay, F., Maresca, J., Kachar, B. and Chadwick, R. S. [2002], ‘Determination of elastic moduli of thin layers of soft material using the atomic force microscope’, Biophysical Journal **82**(5), 2798 – 2810.
- do Nascimento, R. M., Baldit, A., Kokanyan, N., Tappert, L. K., Lipinski, P., Hernandez, A. C. and Rahouadj, R. [2020], ‘Mechanical-chemical coupling in temporomandibular joint disc’, Materialia **9**, 100549.
- Druzinsky, R. E. [1993], ‘The time allometry of mammalian chewing movements: Chewing frequency scales with body mass in mammals’, Journal of Theoretical Biology **160**(4), 427 – 440.
- Dusfour, G. [2018], ‘Contribution à l’étude de la croissance du disque intervertébral et de cartilage de synthèse’, PhD thesis, Université de Montpellier, LMGC .
- Fazaeli, S., Ghazanfari, S., Everts, V., Smit, T. and Koolstra, J. [2016], ‘The contribution of collagen fibers to the mechanical compressive properties of the temporomandibular joint disc’, Osteoarthritis and Cartilage **24**(7), 1292 – 1301.
- Fernandez, P., Lamela Rey, M. J. and Fernández Canteli, A. [2011], ‘Viscoelastic characterisation of the temporomandibular joint disc in bovines’, Strain **47**(2), 188–193.
- Fernández, P., Lamela, M. J., Ramos, A., Fernández-Canteli, A. and Tanaka, E. [2013], ‘The region-dependent dynamic properties of porcine temporomandibular joint disc under unconfined compression’, Journal of Biomechanics **46**(4), 845 – 848.
- Fischer-Cripps, A. and Lawn, B. [1996], ‘Indentation stress-strain curves for “quasi-ductile” ceramics’, Acta Materialia **44**(2), 519 – 527.
- Fung, Y. [1993], Biomechanics: Mechanical Properties of Living Tissues, Springer New York.

- Gent, A. [2012], Engineering with Rubber: How to Design Rubber Components, Carl Hanser Verlag GmbH & Company KG.
- Gray, D. R. J. and Al-Ani, D. M. Z. [2011], Temporomandibular Disorders: A problem based approach, John Wiley and Sons, Ltd., pp. 1–5.
- Gutman, S., Kim, D., Tarafder, S., Velez, S., Jeong, J. and Lee, C. H. [2018], ‘Regionally variant collagen alignment correlates with viscoelastic properties of the disc of the human temporomandibular joint’, Archives of Oral Biology **86**, 1 – 6.
- Hattori-Hara, E., Mitsui, S. N., Mori, H., Arafurue, K., Kawaoka, T., Ueda, K., Yasue, A., Kuroda, S., Koolstra, J. H. and Tanaka, E. [2014], ‘The influence of unilateral disc displacement on stress in the contralateral joint with a normally positioned disc in a human temporomandibular joint: An analytic approach using the finite element method’, Journal of Cranio-Maxillofacial Surgery **42**(8), 2018 – 2024.
- Herring, S. W., Decker, J. D., Liu, Z.-J. and Ma, T. [2002], ‘Temporomandibular joint in miniature pigs: Anatomy, cell replication, and relation to loading’, The Anatomical Record **266**(3), 152–166.
- Hertz, H. [1882], ‘Über die Berührung fester elastischer Körper’, Journal für reine und angewandte Mathematik **92**, 156–171.
- Hirose, M., Tanaka, E., Tanaka, M., Fujita, R., Kuroda, Y., Yamano, E., Van Eijden, T. M. G. J. and Tanne, K. [2006], ‘Three-dimensional finite-element model of the human temporomandibular joint disc during prolonged clenching’, European Journal of Oral Sciences **114**(5), 441–448.
- Hohl, T. H. and Tucek, W. H. [1982], ‘Measurement of condylar loading forces by instrumented prosthesis in the baboon’, Journal of Maxillofacial Surgery **10**, 1 – 7.
- Hylander, W. L. [1979], ‘An experimental analysis of temporomandibular joint reaction force in macaques’, American Journal of Physical Anthropology **51**(3), 433–456.
- Iwashita, N., Swain, M. V., Field, J. S., Ohta, N. and Bitoh, S. [2001], ‘Elasto-plastic deformation of glass-like carbons heat-treated at different temperatures’, Carbon **39**(10), 1525 – 1532.
- Jaisson, M., Lestriez, P., Taiar, R. and Debray, K. [2012], ‘Finite element modeling of tmj joint disc behavior’, International Orthodontics **10**(1), 66 – 84.
- Johnson, A. W., Moghaddam, A. O., Wei, J., Dunn, A. and Kim, J. [2018], An indentation-based approach to determine the elastic constants of tendon. Oral presentation, World Congress of Biomechanics, Dublin.
- Johnson, K. [1985], Contact Mechanics, Cambridge University Press.
- Juran, C. M., Dolwick, M. F. and McFetridge, P. S. [2015], ‘Mechanobiological assessment of tmj disc surfaces: Nanoindentation and transmission electron microscopy’, Journal of oral & maxillofacial research **6**(4).
- Kalidindi, S. R., Abusafieh, A. and El-Danaf, E. [1997], ‘Accurate characterization of machine compliance for simple compression testing’, Experimental Mechanics **37**(2), 210–215.

- Kalpakci, K., Willard, V., Wong, M. and Athanasiou, K. [2011], ‘An interspecies comparison of the temporomandibular joint disc’, Journal of dental research **90**(2), 193–198.
- Kim, K.-W., Wong, M. E., Helfrick, J. F., Thomas, J. B. and Athanasiou, K. A. [2003], ‘Biomechanical tissue characterization of the superior joint space of the porcine temporomandibular joint’, Annals of Biomedical Engineering **31**(8), 924–930.
- Koolstra, J., Tanaka, E. and Eijden, T. V. [2007], ‘Viscoelastic material model for the temporomandibular joint disc derived from dynamic shear tests or strain-relaxation tests’, Journal of Biomechanics **40**(10), 2330 – 2334.
- Kuboki, T., Takenami, Y., Orsini, M. G., Maekawa, K., Yamashita, A., Azuma, Y. and Clark, G. T. [1999], ‘Effect of occlusal appliances and clenching on the internally deranged tmj space.’, Journal of Orofacial Pain **13**(1), 38 – 48.
- Kuo, J., Zhang, L., Bacro, T. and Yao, H. [2010], ‘The region-dependent biphasic viscoelastic properties of human temporomandibular joint discs under confined compression’, Journal of Biomechanics **43**(7), 1316 – 1321.
- Lamela, M. J., Pelayo, F., Ramos, A., Fernández-Canteli, A. and Tanaka, E. [2013], ‘Dynamic compressive properties of articular cartilages in the porcine temporomandibular joint’, Journal of the Mechanical Behavior of Biomedical Materials **23**, 62 – 70.
- Lamela, M., Prado, Y., Fernández, P., Fernández-Canteli, A. and Tanaka, E. [2011], ‘Non-linear viscoelastic model for behaviour characterization of temporomandibular joint discs’, Experimental mechanics **51**(8), 1435–1440.
- Lanir, Y. [2009], ‘Mechanisms of Residual Stress in Soft Tissues’, Journal of Biomechanical Engineering **131**(4).
- Le Floch, S., Ambard, D., Baldit, A., Kouyoumdjian, P., Canadas, P. and Cherblanc, F. [2015], ‘Residual stress in pig intervertebral discs’, Proceedings of European Society of Biomechanics (21st Congress of European Society of Biomechanics, Jul 2015, Prague, Czech Republic).
- Lee, H., Campbell, W. D., Canning, M. E., Theis, K. M., Ennis, H. Y., Jackson, R. L., Wright, J. C. and Hanson, R. R. [2016], ‘Correlation between signalment and the biphasic hyperelastic mechanical properties of equine articular cartilage’, Biotribology **7**, 31 – 37.
- Lin, D. C. and Horkay, F. [2008], ‘Nanomechanics of polymer gels and biological tissues: A critical review of analytical approaches in the hertzian regime and beyond’, Soft Matter **4**, 669–682.
- Lin, D. C., Shreiber, D. I., Dimitriadis, E. K. and Horkay, F. [2009], ‘Spherical indentation of soft matter beyond the hertzian regime: numerical and experimental validation of hyperelastic models’, Biomechanics and Modeling in Mechanobiology **8**(5), 345.
- Lin, D., Dimitriadis, E. and Horkay, F. [2007], ‘Elasticity of rubber-like materials measured by afm nanoindentation’, Express Polym Lett **1**(9), 576–584.

- Liu, D., Zhang, Z. and Sun, L. [2010], ‘Nonlinear elastic load–displacement relation for spherical indentation on rubberlike materials’, Journal of Materials Research **25**(11), 2197–2202.
- Liu, S. Q. and Fung, Y. C. [1988], ‘Zero-Stress States of Arteries’, Journal of Biomechanical Engineering **110**(1), 82–84.
- Lu, X. L. and Mow, V. C. [2008], ‘Biomechanics of articular cartilage and determination of material properties’, Medicine & Science in Sports & Exercise **40**(2), 193–199.
- Lumpkins, S. B. and McFetridge, P. S. [2009], ‘Regional variations in the viscoelastic compressive properties of the temporomandibular joint disc and implications toward tissue engineering’, Journal of Biomedical Materials Research Part A **90A**(3), 784–791.
- Matuska, A. M., Muller, S., Dolwick, M. and McFetridge, P. S. [2016], ‘Biomechanical and biochemical outcomes of porcine temporomandibular joint disc deformation’, Archives of Oral Biology **64**, 72 – 79.
- Mills, D. K., Fiandaca, D. J. and Scapino, R. P. [1994], ‘Morphologic, microscopic, and immunohistochemical investigations into the function of the primate tmj disc.’, Journal of orofacial pain **8**(2).
- Minarelli, A. M., Del Santo, M. and Liberti, E. A. [1997], ‘The structure of the human temporomandibular joint disc: a scanning electron microscopy study’, Journal of orofacial pain **11**(2), 95–100.
- Mooney, M. [1940], ‘A theory of large elastic deformation’, Journal of applied physics **11**(9), 582–592.
- Mori, H., Horiuchi, S., Nishimura, S., Nikawa, H., Murayama, T., Ueda, K., Ogawa, D., Kuroda, S., Kawano, F., Naito, H., Tanaka, M., Koolstra, J. H. and Tanaka, E. [2010], ‘Three-dimensional finite element analysis of cartilaginous tissues in human temporomandibular joint during prolonged clenching’, Archives of Oral Biology **55**(11), 879 – 886.
- Mow, V. C., Holmes, M. H. and Lai, W. M. [1984], ‘Fluid transport and mechanical properties of articular cartilage: A review’, Journal of Biomechanics **17**(5), 377 – 394.
- National Institutes of Health (NIH) [2017], ‘Prevalence of TMJD and its signs and symptoms’. - National Institute of Dental and Craniofacial Research (NIDCR), assessed 25.06.2017.
URL: <https://www.nidcr.nih.gov/DataStatistics/FindDataByTopic/FacialPain/PrevalenceTMJD.htm>
- Nelson, D. [2014], ‘Experimental methods for determining residual stresses and strains in various biological structures’, Experimental Mechanics **54**(4), 695–708.
- Nickel, J. and McLachlan, K. [1994], ‘In vitro measurement of the stress-distribution properties of the pig temporomandibular joint disc’, Archives of Oral Biology **39**(5), 439 – 448.

- Ogden, R. W. [1972], ‘Large deformation isotropic elasticity—on the correlation of theory and experiment for incompressible rubberlike solids’, Proceedings of the Royal Society of London. A. Mathematical and Physical Sciences **326**(1567), 565–584.
- Rivlin, R. S. [1948], ‘Large elastic deformations of isotropic materials. I. Fundamental concepts’, Philosophical Transactions of the Royal Society of London. Series A, Mathematical and Physical Sciences **240**(822), 459–490.
- Savoldelli, C., Bouchard, P.-O., Loudad, R., Baque, P. and Tillier, Y. [2012], ‘Stress distribution in the temporo-mandibular joint discs during jaw closing: a high-resolution three-dimensional finite-element model analysis’, Surgical and Radiologic Anatomy **34**(5), 405–413.
- Snider, G., Lomakin, J., Singh, M., Gehrke, S. and Detamore, M. [2008], ‘Regional dynamic tensile properties of the tmj disc’, Journal of Dental Research **87**(11), 1053–1057.
- Stanković, S., Vlajković, S., Bošković, M., Radenković, G., Antić, V. and Jevremović, D. [2013], ‘Morphological and biomechanical features of the temporomandibular joint disc: An overview of recent findings’, Archives of Oral Biology **58**(10), 1475 – 1482.
- Tabor, D. [1948], ‘A simple theory of static and dynamic hardness’, Proceedings of the Royal Society of London A: Mathematical, Physical and Engineering Sciences **192**(1029), 247–274.
- Tabor, D. [1951], The hardness of metals., Monographs on the physics and chemistry of materials, Clarendon Press.
- Tanaka, E., del Pozo, R., Tanaka, M., Aoyama, J., Hanaoka, K., Nakajima, A., Inuzuka, S. and Tanne, K. [2003a], ‘Strain-rate effect on the biomechanical response of bovine temporomandibular joint disk under compression’, Journal of Biomedical Materials Research Part A **67A**(3), 761–765.
- Tanaka, E., Kikuzaki, M., Hanaoka, K., Tanaka, M., Sasaki, A., Kawai, N., Ishino, Y., Takeuchi, M. and Tanne, K. [2003b], ‘Dynamic compressive properties of porcine temporomandibular joint disc’, European Journal of Oral Sciences **111**(5), 434–439.
- Tanaka, E., Tanaka, M., Aoyama, J., Watanabe, M., Hattori, Y., Asai, D., Iwabe, T., Sasaki, A., Sugiyama, M. and Tanne, K. [2002], ‘Viscoelastic properties and residual strain in a tensile creep test on bovine temporomandibular articular discs’, Archives of Oral Biology **47**(2), 139 – 146.
- Tanaka, E., Tanaka, M., Miyawaki, Y. and Tanne, K. [1999], ‘Viscoelastic properties of canine temporomandibular joint disc in compressive load-relaxation’, Archives of Oral Biology **44**(12), 1021 – 1026.
- Tanaka, E. and van Eijden, T. [2003], ‘Biomechanical behavior of the temporomandibular joint disc’, Critical Reviews in Oral Biology & Medicine **14**(2), 138–150.
- Tanne, K., Tanaka, E. and Sakuda, M. [1991], ‘The elastic modulus of the temporo-mandibular joint disc from adult dogs’, Journal of Dental Research **70**(12), 1545–1548.

- Tappert, L., Baldit, A., Laurent, C., Ferrari, M. and Lipinski, P. [2018a], ‘Acquisition of accurate temporomandibular joint disc external shape and internal microstructure’. Poster presentation, 8th World Congress of Biomechanics (July 2018), Dublin, Ireland.
- Tappert, L., Baldit, A., Rahouadj, R. and Lipinski, P. [2017], ‘Local elastic properties characterization of the temporo-mandibular joint disc through macro-indentation’, Computer Methods in Biomechanics and Biomedical Engineering **20**(sup1), 201–202.
- Tappert, L. K., Baldit, A., do Nascimento, R. M., Lipinski, P. and Rahouadj, R. [2018b], ‘Mechanical characterisation of the temporomandibular joint disc through local compression and traction’. Oral communication, BSSM’s International Conference on Advances in Experimental Mechanics (29.-31.08.2018), Southampton, Great Britain.
- Throckmorton, G. S. and Dechow, P. C. [1994], ‘In vitro strain measurements in the condylar process of the human mandible’, Archives of Oral Biology **39**(10), 853 – 867.
- Valladares Neto, J., Estrela, C., Bueno, M. R., Guedes, O. A., Porto, O. C. L. and Pécora, J. D. [2010], ‘Mandibular condyle dimensional changes in subjects from 3 to 20 years of age using Cone-Beam Computed Tomography: A preliminary study’, Dental Press Journal of Orthodontics **15**, 172 – 181.
- Varner, V. D. and Taber, L. A. [2010], On measuring stress distributions in epithelia, in K. Garikipati and E. M. Arruda, eds, ‘IUTAM Symposium on Cellular, Molecular and Tissue Mechanics’, Springer Netherlands, Dordrecht, pp. 45–54.
- Willard, V. P., Zhang, L. and Athanasiou, K. A. [2011], Tissue engineering of the temporomandibular joint, Vol. 5, Elsevier, pp. 221–235.
- World Health Organization (WHO) [2016], ‘Global report on diabetes’.
- Wright, G. J., Coombs, M. C., Hepfer, R. G., Damon, B. J., Bacro, T. H., Lecholop, M. K., Slate, E. H. and Yao, H. [2016], ‘Tensile biomechanical properties of human temporomandibular joint disc: Effects of direction, region and sex’, Journal of Biomechanics **49**(16), 3762 – 3769.
- Wu, C.-E., Lin, K.-H. and Juang, J.-Y. [2016], ‘Hertzian load–displacement relation holds for spherical indentation on soft elastic solids undergoing large deformations’, Tribology International **97**, 71 – 76.
- Yuya, P. A., Amborn, E. K., Beatty, M. W. and Turner, J. A. [2010], ‘Evaluating anisotropic properties in the porcine temporomandibular joint disc using nanoindentation’, Annals of Biomedical Engineering **38**(7), 2428–2437.
- Zhang, M.-G., Cao, Y.-P., Li, G.-Y. and Feng, X.-Q. [2014], ‘Spherical indentation method for determining the constitutive parameters of hyperelastic soft materials’, Biomechanics and Modeling in Mechanobiology **13**(1), 1–11.
- Zhang, Q., Li, X. and Yang, Q. [2018], ‘Extracting the isotropic uniaxial stress-strain relationship of hyperelastic soft materials based on new nonlinear indentation strain and stress measure’, AIP Advances **8**(11), 115013.
- Zhang, Q. and Yang, Q.-S. [2017], ‘Effects of large deformation and material nonlinearity on spherical indentation of hyperelastic soft materials’, Mechanics Research Communications **84**, 55 – 59.

Appendix A

Overview of experimental protocols in literature

Table A.1 – Max stresses in TMJ disc finite element simulations.

Author	disc model	load case	max von Mises stress
Hattori-Hara et al. [2014]	Kelvin model	clenching	9.1 MPa
Hirose et al. [2006]	Kelvin model	clenching	0.92 MPa
Jaisson et al. [2012]	3. degree polynomial hyperelastic	chewing	13.22 MPa
Mori et al. [2010]	Kelvin model	clenching	6.18 MPa
del Palomar and Doblaré [2006]	fibre-reinforced porohyperelastic	lateral excursion	2.5 MPa, max principal stress
Savoldelli et al. [2012]	neo-Hookean	clenching	5.1 MPa

Table A.2 – Overview of tensile test conditions used in literature.

Group	test	sample shape	preload	loading	preconditioning	test condition	σ_{max}
Angelo et al. [2016]	tensile, elongation to failure	whole disc; ovine	-	strain until failure	0.5 mm/min	-	Young's modulus A-P 3.97 ± 0.73 MPa, M-L 9.39 ± 1.67 MPa; tensile strength, elongation at break; σ_{max} M-L: ≈ 14 MPa, A-P: ≈ 5 MPa
Beatty et al. [2001]	tensile, elongation to failure	bone shape from whole disc; porcine	-	0.5, 50, 500 mm/min; 0.002, 0.02, 0.2 strain/s	-	-	Apparent modulus M-L: ≈ 2 MPa, 4 MPa, 6 MPa; A-P: ≈ 25 MPa, 40 MPa, 80 MPa; ultimate strength A-P: ≈ 2 MPa, M-L: $\approx 28-38$ MPa
Detamore and Athanasiou [2003b]	tensile, incremental stress relaxation	stripes (3 M-L, 3 A-P); porcine	0.02N to straighten	11 increments at 6mm/min	5.5% strain, 15 cycles at 10 mm/min	37°C, immersion in PBS	peak stress, max A-P: 28 MPa, max: M-L 31 MPa
Matuska et al. [2016]	tensile, elongation to failure	porcine stripes (5 A-P); porcine	-	1% strain/s	cyclic at 5% strain like [Detamore and Athanasiou, 2003b]	room temperature, immersion in PBS	Young's modulus highest in IZ ≈ 150 MPa
Snider et al. [2008]	tensile, dynamic	stripes (3 M-L, 3 A-P); porcine	1g tare load	1% strain at 0.1-100 rad/s	-	room temperature, immersion in PBS	in average: storage modulus up to 3.5 MPa; loss modulus up to 0.35 MPa; loss tangent up to 0.17 MPa
Tanne et al. [1991]	tensile canine	stripes (medial, central, lateral) porcine	-	loading: 0.1 N/s, up to forces resulting in 3.5 MPa stresses	-	-	max Young's modulus max central region 101.1 MPa
Wright et al. [2016]	tensile incremental stress relaxation, (human)	stripes M-L, A-P	0.05 N	5/10/15/20/30% strain at 1% strain/s, 15/15/15/20/30 min relaxation time	10 cycles between 0-2% strain at 0.2% strain/s	37°C, immersion in PBS	max. Young's modulus 18.9 ± 8.5 MPa (A-P, central region, female), 15.6 ± 7.7 MPa (M-L posterior region, male)

Table A.3 – Literature overview cyclic compression test on TMJ discs.

Group	test	sample shape	preload	charge Hz	preconditioning	condition	σ_{max}
Fazaeli et al. [2016]	unconfined cyclic compression	whole disc (cylindrical indenter \varnothing 4mm)	0.02N $\sigma_{pre} \approx 0.0016MPa$	1 Hz; 20 cycles; 10% strain	3min cycles at 10% strain and 1 Hz; followed by 5min recovery	room temperature complete in PBS chamber	Instantaneous modulus 0.12 MPa-0.15 MPa; $\sigma_{max} = 1.8MPa$
Lumpkins and McFetridge [2009]	unconfined cyclic compression	cylindrical \varnothing 4mm	-	0.1/0.5/1/1.5/2 Hz; 15 cycles; 5/10/15% strain	initial set (0.1 Hz; 5% strain)	37°C complete in PBS	0.1Hz, 15% strain: $E_{int} = 3MPa$; $E_{SS} = 1.25MPa$; $\sigma_{max} = 0.2MPa$
Tanaka et al. [2003b]	unconfined cyclic compression	cylindrical \varnothing 6.9mm	-	0.1/0.5/1 Hz; 25 cycles; 5/10/15% strain	2min cycles at 0-15% strain followed by 4 min recovery	immersed in PBS at room temperature	0.1Hz, 15% strain: $E_{int} = 7MPa$; $E_{SS} = 2.5MPa$; for 0.5Hz at 10% strain $\sigma_{max} = 0.55MPa$

Table A.4 – Literature overview compression test on TMJ discs.

Group	test	com-	sample shape	preload	charge	preconditioning	condition	σ_{max}
Allen and Athanasiou [2005]	unconfined pression	com-	cylindrical \varnothing 3mm, divided in superior and inferior samples	$< 0.02N$	10,15,20,25,30 % strain	10 cycles at strain	$37 \pm 1.5^\circ C$ complete in PBS chamber	Instantaneous modulus 80 kPa-3870 kPa region and strain depended; Relaxation modulus 17 kPa-74 kPa region and strain depended
Allen and Athanasiou [2006]	unconfined pression; incremen- tal stress relaxation (5% strain/step in 4 steps)	com-	cylindrical \varnothing 3mm	0.02N	50% strain/s	10 cycles at strain	$37^\circ C$ complete in PBS (thermocou- ple, immersion coil and temperature controller in bath)	Instantaneous modu- lus 79 kPa-1924 kPa; Relaxation modulus 22 kPa-169 kPa
Barrientos et al. [2016]	compression		whole disc	0.005N	1% strain, 0.01-10 Hz	3 min, 1% sinusoidal strain	room temp./lubrification	storage modulus 36.85- 84.46 kPa, loss modu- lus 10.03-26.97 kPa; in- creasing with increas- ing frequency
Beek et al. [2001]	local compression		whole disc	-	20/40% max strain at 0.0,0.05,0.1 Hz	-	$37^\circ C$ complete in 0.9% NaCl chamber	2.0 MPa - 9.0 MPa
Commisso et al. [2016]	unconfined pression	com-	cylindrical \varnothing 5 mm	upper moved erage ($2.14 \pm 0.43mm$)	50/40/30% strain/s	20 cycles from 0-10% strain at 1 Hz	$37^\circ C$, complete, 0.9% saline (heater and thermostat in bath)	4.5 MPa
Calvo-Gallego et al. [2017]	compression/ relax- ation	relax-	cylindrical \varnothing 4mm	upper moved to av- erage thickness ($1.82 \pm 0.21mm$)	50% strain/s followed by 15 min holding time	20 cycles from 0-10% strain at 1 Hz	$37^\circ C$, complete, 0.9% saline (temperature controller in bath)	0.35 MPa
Fernandez et al. [2011]	unconfined pression	com-	cylindrical \varnothing 8 mm	500/1000/1500 g	relaxation: 10,15,20,25% strain; creep: 500 g load for 1200s; cyclic: 0.5/2 Hz for 1/5% strain	-	$37^\circ C$ immersed, 0.9% saline	relaxation modulus 150-300 kPa (region dependent); storage modulus 20-38 MPa
Fernández et al. [2013]	unconfined pression; relaxation and creep	com-	cylindrical \varnothing 4 mm	5 mN (0.005 N)	1% strain, 0.01-1.0 Hz, 1% sinusoidal strain	3 min 1% sinusoidal strain	room temperature	storage 40 kPa-60 kPa and loss moduli 10 kPa-15 kPa
Lamela et al. [2013]	cylindrical indenta- tion	indenta-	whole sam- ple (carti- lage)	5 mN (0.005 N)	0.01 Hz-10 Hz, 1% sinu- soidal strain	3 min 1% sinusoidal strain	room temperature	storage and loss moduli 0.1 MPa-0.4 MPa
Matuska et al. [2016]	cyclic compression		cylindrical \varnothing 4 mm	0.05 N to find con- tact	15 cycles at 5% strain	-	max compressive modulus in posterior region $\approx 300 kPa$ chamber at $37^\circ C$	relaxed modulus up to 30 MPa
Wright et al. [2016]	tension		band	0.05N	1% strain/second	10 cycles 0-2% strain at 0, 2%/s strain rate		

Appendix B

General finite element simulations

B.1 Details of finite element simulations

Table B.1 – Overview simulations thickness study, which were carried out using two different Young’s moduli (therefore two wallclock times).

case	ratio $\frac{t_0}{r}$	number of elements	wallclock time [s]	remarks
(1)	0.5	1600 (nodes: 1771)	29	length of element 0.05; displacement of indenter 0.35 mm
(2)	0.75	2400 (nodes: 2576)	128	length of element 0.05; displacement of indenter 0.5 mm
(3)	1	3200 (nodes: 3381)	62	length of element 0.05; displacement of indenter 0.5 mm
(4)	1.5	4800 (nodes: 4991)	91	length of element 0.05; displacement of indenter 0.5 mm
(5)	2	6400 (nodes: 6.601)	75	length of element 0.05
(6)	5	16000 (nodes: 16.261)	162	length of element 0.05
(7)	10	32000 (nodes: 32.361)	291	length of element 0.05
(8)	20	64000 (nodes: 64.561)	623	length of element 0.05
(9)	30	96000 (nodes: 96.761)	1078	length of element 0.05
(10)	40	128000 (nodes: 128961)	1433	length of element 0.05
(11)	50	160000 (nodes: 161161)	2058	length of element 0.05
(12)	100	320000 (nodes: 322161)	3273	length of element 0.05

B.2 Stress derivation

The incompressible neo-Hookean energy strain function is:

$$\Psi = \frac{\mu_0}{2}(I_1 - 3), \quad (\text{B.1})$$

with $I_1 = \lambda_1^2 \lambda_2^2 \lambda_3^2$ the first invariant of the right Cauchy-Green deformation tensor, it becomes:

$$\Psi = \frac{\mu_0}{2}(\lambda_1^2 \lambda_2^2 \lambda_3^2 - 3). \quad (\text{B.2})$$

The Cauchy stress is defined as:

$$\sigma_{Cauchy} = \frac{\lambda_i}{\lambda_1 \lambda_2 \lambda_3} \frac{\partial \Psi}{\partial \lambda_i} \quad i = 1, 2, 3. \quad (\text{B.3})$$

In the case of incompressible materials $\lambda_1 \lambda_2 \lambda_3 = J = 1$, so the principal stresses are:

$$\sigma_{11}^{Cauchy} = \mu_0 \lambda_1^2, \quad (\text{B.4})$$

$$\sigma_{22}^{Cauchy} = \mu_0 \lambda_2^2, \quad (\text{B.5})$$

$$\sigma_{33}^{Cauchy} = \mu_0 \lambda_3^2. \quad (\text{B.6})$$

Regarding a uniaxial loading case ($\lambda_1 = \lambda$, $\lambda_2 = \lambda_3 = \sqrt{\frac{J}{\lambda}}$):

$$\sigma_{11} - \sigma_{33} = \mu_0 \lambda_1^2 - \mu \frac{1}{\lambda} \quad (\text{B.7})$$

$$\sigma_{11} - \sigma_{33} = \mu_0 \left(\lambda_1^2 - \frac{1}{\lambda} \right) \quad (\text{B.8})$$

and

$$\sigma_{22} - \sigma_{33} = 0. \quad (\text{B.9})$$

If no traction on the sides is assumed, $\sigma_{22} = \sigma_{33} = 0$ and Equation B.8 becomes:

$$\sigma_{11}^{Cauchy} = \mu_0 \left(\lambda^2 - \frac{1}{\lambda} \right). \quad (\text{B.10})$$

The corresponding nominal stress is:

$$\sigma_{nH}^n = \mu_0 \left(\lambda - \frac{1}{\lambda^2} \right). \quad (\text{B.11})$$

Appendix C

Complementary experimental results

C.1 Temporomandibular joint disc sample harvesting

As mentioned in Section 3.2.1, knife, scissors and scalpel were used to harvest discs as well as a saw to obtain the condyles. In the following, the steps obtaining TMJ disc samples are described.

Tissue around the temporomandibular joint was carefully removed. Then the jaw is carefully opened so that the superior part of the capsule can be reached and slowly be opened using a scalpel. In this way, the inferior part of the disc can be exposed and the skull and mandible can be separated. Finally, by cutting carefully around the disc and the surrounding tissue, the disc can be separated from the condyle.

In all, six of the harvested samples were used for local spherical compression, their date of harvest and testing are summarised in Table C.1.

Table C.1 – Overview sample origin for spherical compression tests.

sample no.	side	date of harvest	head no.	date of testing
1	left	18.04.2018	Head 2	28./29.11.2018
2	right	18.04.2018	Head 2	29./30.11.2018
3	left	18.04.2018	Head 3	05./06.12.2018
4	right	18.04.2018	Head 3	06./07.12.2018
5	left	25.04.2018	Head 1	12./13.12.2018
6	right	25.04.2018	Head 1	13./14.12.2018

Further seven samples have been used for additional experiments such as 3D scans, MRI acquisition and histology. Their date of harvest and testing are summarised in Table C.2.

Table C.2 – Overview sample origin for different experiments.

Test	side	date of harvest	head no.	date of testing
3D scan	left	30.03.2017	Head 1	01.09.2017
3D scan	left	07.02.2018	Head 2	16.02.2018
3D scan	right	07.02.2018	Head 2	16.02.2018
3D scan	left	07.02.2018	Head 3	16.02.2018
MRI	right	20.09.2017	Head 1	11./12.12.2017
histology	left	18.04.2018	Head 1	21.06.2018
histology	right	18.04.2018	Head 1	21.06.2018

C.2 3D printed condyles

The 3D scans of the condyles were also postprocessed. Scans of three left and three right condyles were combined to a single "average" .stl file using MeshLab (MeshLab, Visual Computing Lab - ISTI - CR; Version 1.3.2_64bit). These scans were printed using a 3D printer (Form 2, Formlabs, Somerville, Massachusetts, USA) with a resin (Standard Black, FLGPBL04, Formlabs) of a tensile modulus of 2.8 GPa (following ASTM D 638-10, datasheet formlabs). To verify if the 3D scan has the same dimension than the model, test cubes were printed and their dimensions after printing evaluated. As can be seen from Table C.3 a slight expansion was observed in all three directions. The 3D printed condyles served as support of the samples during different experiments.

Table C.3 – Dimensional data of printed testing cubes.

dimension [mm]	Cube 1 model	Cube 1 print	difference	Cube 2 model	Cube 2 print	difference
x	20	20.14	0.7 %	20	20.38	1.9 %
y	26.5	26.99	1.9 %	25	25.22	0.9 %
z	28.5	29.12	2.2 %	30	30.67	1.9 %

C.3 Magnetic resonance image acquisition

Table C.4 – Imaging parameters for sagittal, transverse and frontal plane acquisition (MSME - multi-slide multi-echo).

Image No	Type of Sequence	Echo Time T_E [ms]	Repetition Time T_R [ms]	Slice thickness [mm]	FOV [cm ²]	Matrix size	Space resolution [cm/pixel]	Acquisition time [min]	planes
20	MSME	5.2	2000	0.5	1.60x4.00	256x256	0.0063x0.0156	8	2D with bubble
55	MSME	6	2000	0.5	1.75x3.51	256x256	0.0068x0.0137	8	M-L central
56	MSME	6	2000	0.5	1.75x3.51	256x256	0.0068x0.0137	8	M-L
57	MSME	6	2000	0.5	1.75x3.51	256x256	0.0068x0.0137	8	M-L
58	MSME	6	2000	0.5	1.75x3.51	256x256	0.0068x0.0137	8	A-P central
59	MSME	6	2000	0.5	1.75x3.51	256x256	0.0068x0.0137	8	A-P
60	MSME	6	2000	0.5	1.75x3.51	256x256	0.0068x0.0137	8	A-P
61	MSME	8.5	2000	0.5	3.51x3.51	512x256	0.0137x0.0137	8	axial
63	MSME	8.5	2000	0.5	3.51x3.51	512x256	0.0137x0.0137	8	axial superior
64	MSME	8.5	2000	0.5	3.51x3.51	512x256	0.0137x0.0137	8	axial inferior

Table C.5 – Imaging parameters for 3D acquisition.

Image No	Type of Sequence	Echo Time T_E [ms]	Repetition Time T_R [ms]	FOV [mm ³]	Matrix size	Space resolution [cm/pixel]	Acquisition time [min]	planes
49	MSME	4.9	500	1.75x3.5x3.5	256x64x64	0.0068x0.0547x0.0547	34	3D fast
50	MSME	10	2000	1.75x3.5x3.5	256x128x128	0.0068x0.0273x0.0273	540 (9h)	3D
62	MSME	4.9	50	1.75x3.5x3.5	256x64x64	0.0068x0.0547x0.0547	34	3D fast repetition 49

C.4 Test machine restrictions

The displacement and displacement velocity of the compression tool were imposed through a protocol for the universal testing machine. However, analysis of the displacement - time curves (examples shown in Figures C.1, C.4, C.6) depict a deviation of the imposed loading frequency and the actual one conducted by the machine. Figure C.4 shows that for a loading frequency of 0.1 Hz one test cycle takes ≈ 10.5 s in contrast to theoretically imposed 10 s. For the highest loading frequency 1 Hz it can be observed that a test cycle takes 1.6 s compared to 1 s imposed (see Figure C.6).

The differences between the imposed and actual loading frequencies are consequences of the actuators movement, which is moving the compression tool up- and downwards. It appears that the actuator has a delay while changing direction which is around 0.6 s. This delay influences the experimental results in so far that the sample is given time to relax during the direction change. This effect can be observed mainly for medium and high loading frequencies. Figures C.5 and C.7 do not show a clear peak force as it is the case for a loading frequency of 0.01 Hz (see Figure C.2). Instead a plateau can be observed during which the measured force is declining. Compared to the decrease in force during the unloading phase, the decline during the plateau is low. In the example shown in Figure C.7 the decline in force is ≈ 0.08 N.

In order to minimise these troubles for future tests, a dynamic testing machine could be used. Furthermore, sinusoidal test cycles might reduce the time of direction change.

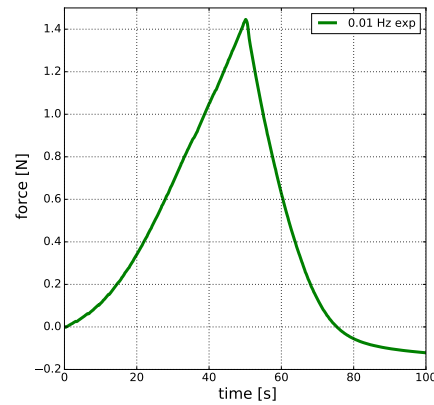
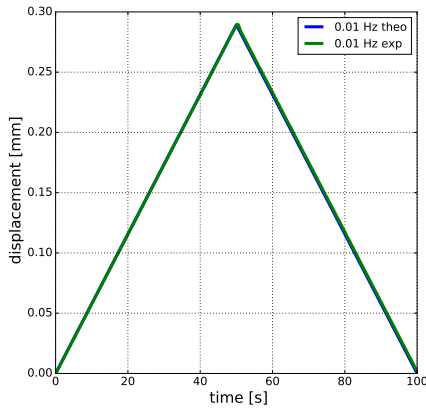


Figure C.1 – Machine's displacement - time curve at a frequency of 0.01 Hz. Figure C.2 – Machine's force - time curve at a frequency of 0.01 Hz.

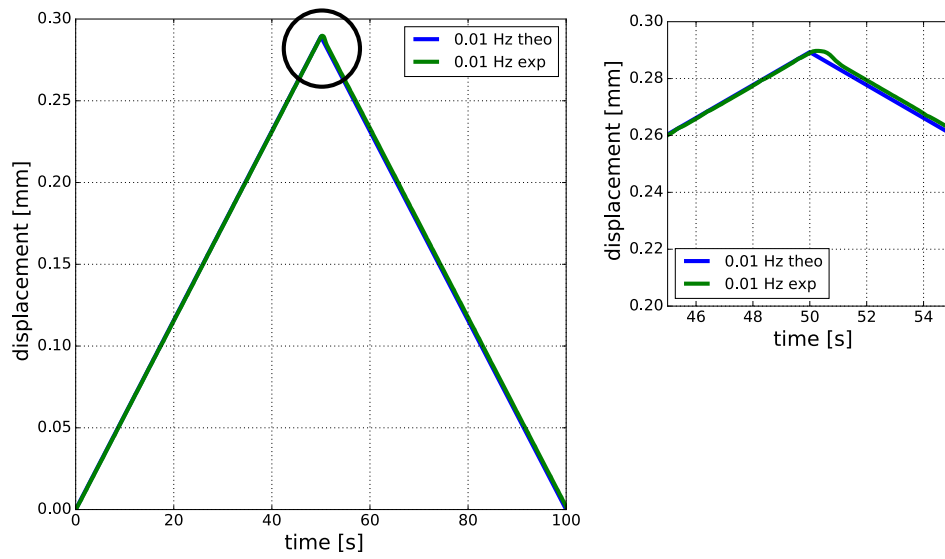


Figure C.3 – Machine's displacement - time curve at a frequency of 0.01 Hz, detailed view.

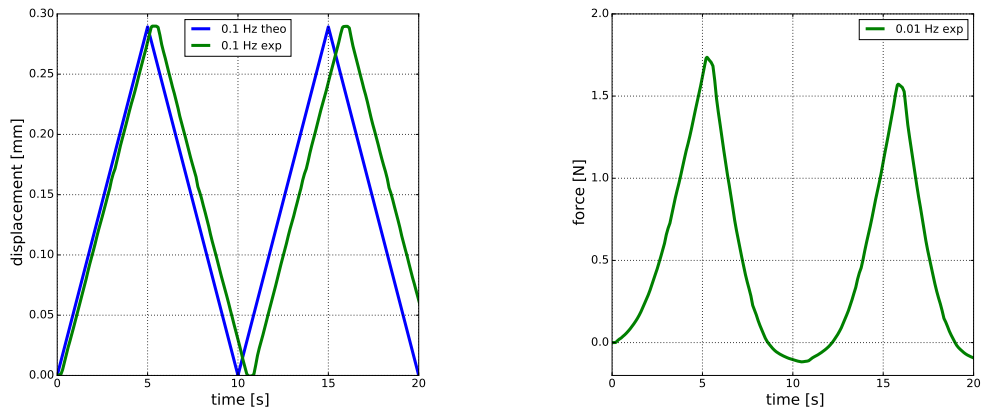


Figure C.4 – Machine's displacement - time curve at a frequency of 0.1 Hz. Figure C.5 – Machine's force - time curve at a frequency of 0.1 Hz.

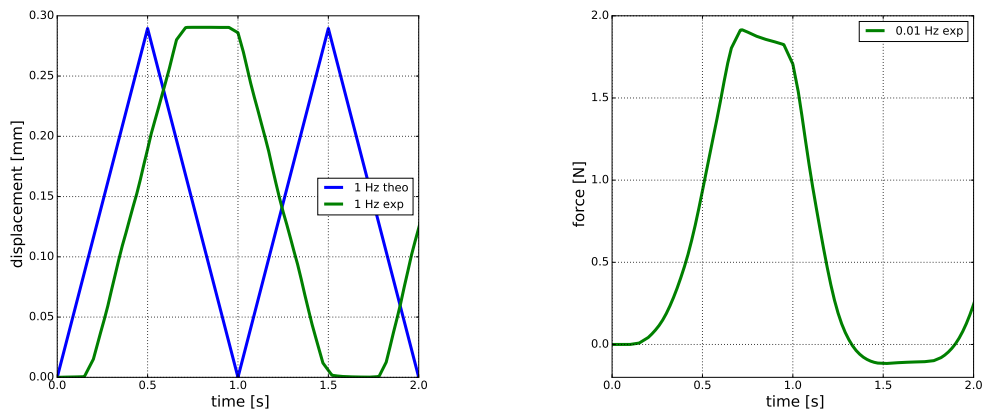


Figure C.6 – Machine's displacement - time curve at a frequency of 1 Hz. Figure C.7 – Machine's force - time curve at a frequency of 1 Hz.

C.5 Data base structure

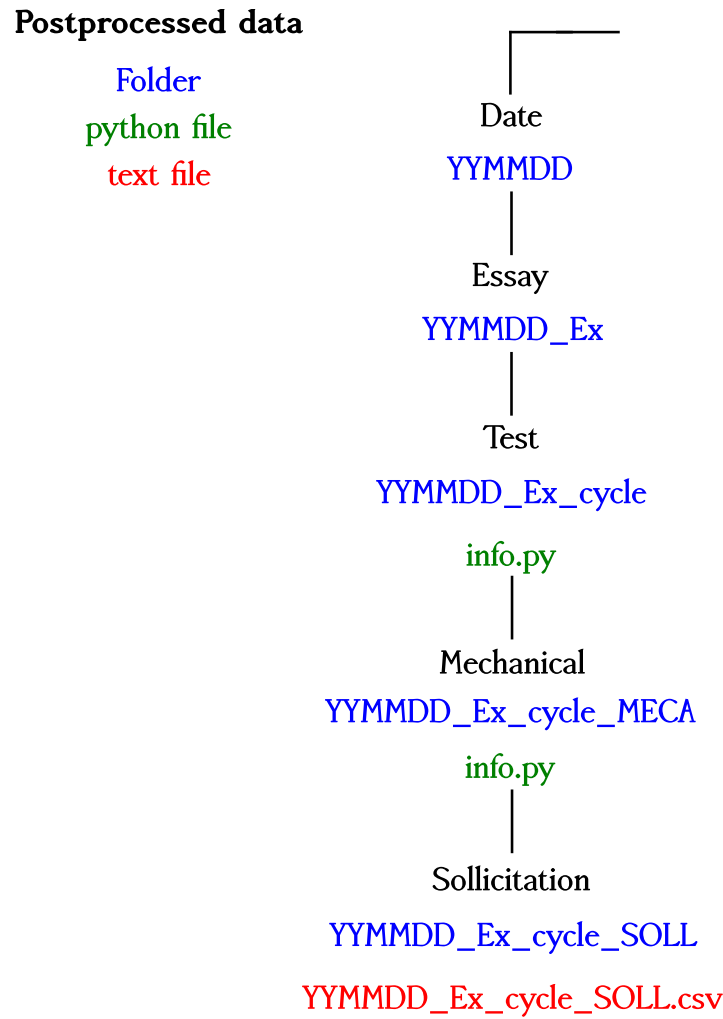


Figure C.8 – Data base structure of experimental data.

C.6 GOM

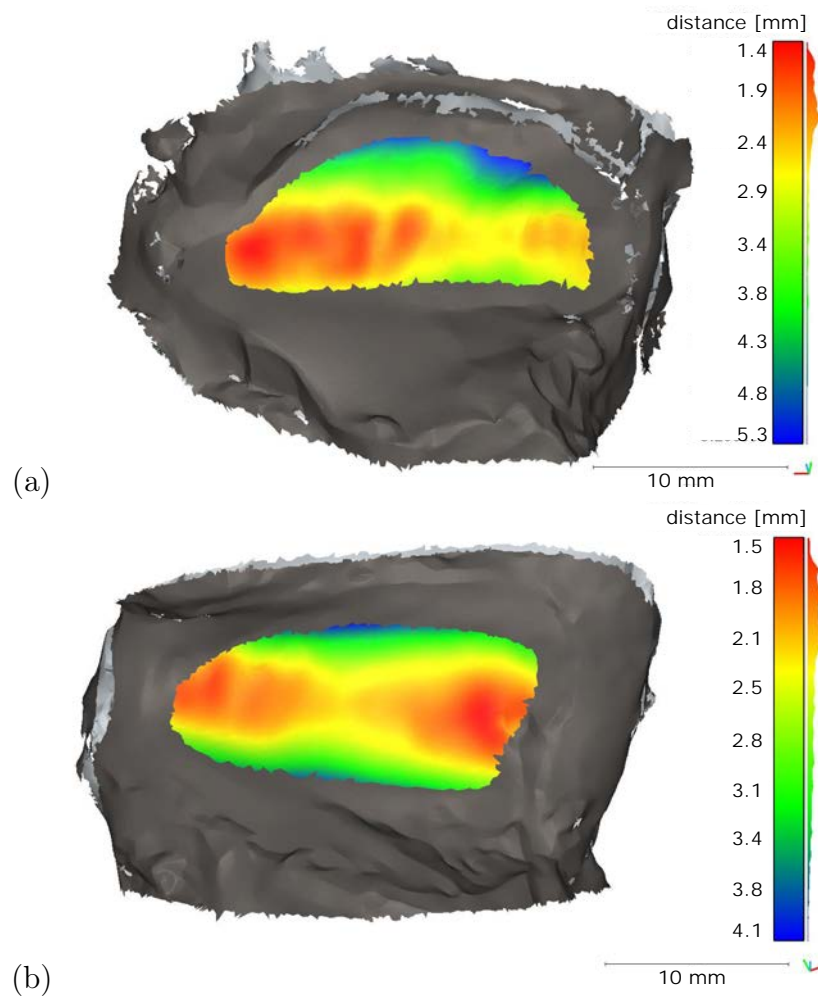


Figure C.9 – Thickness measurements of three samples using CloudCompare software; the average thicknesses (\pm STD) are the following; (a) 2.32 ± 0.56 mm, (b) 2.43 ± 0.58 mm. The grey areas were not included in the thickness measurement.

C.7 Experimental force-displacement curves

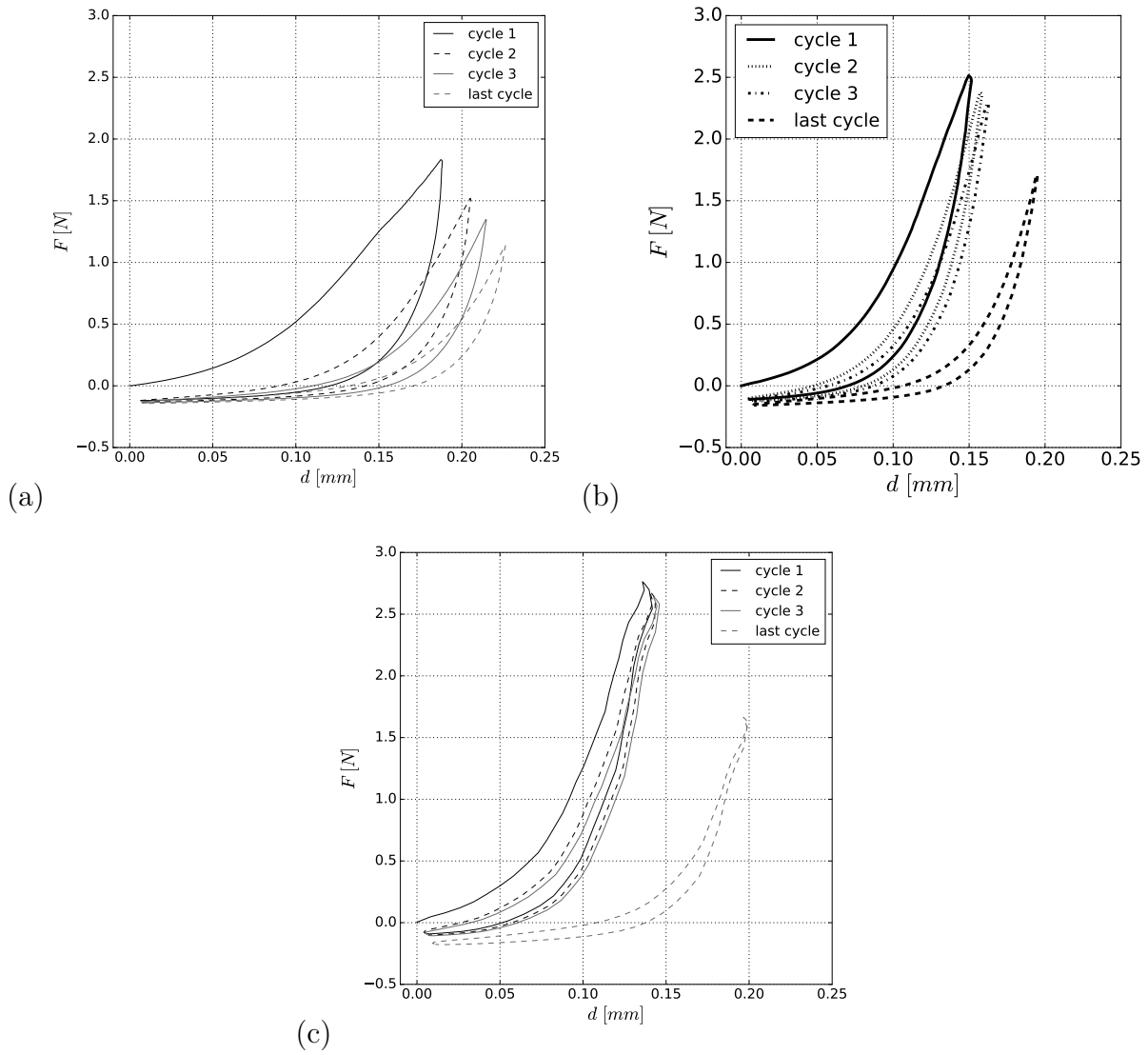


Figure C.10 – Experimental force - displacement curves using a compression tool of 3 mm radius testing the samples central site for different loading frequencies, (a) 0.01 Hz, (b) 0.1 Hz and (c) 1 Hz.

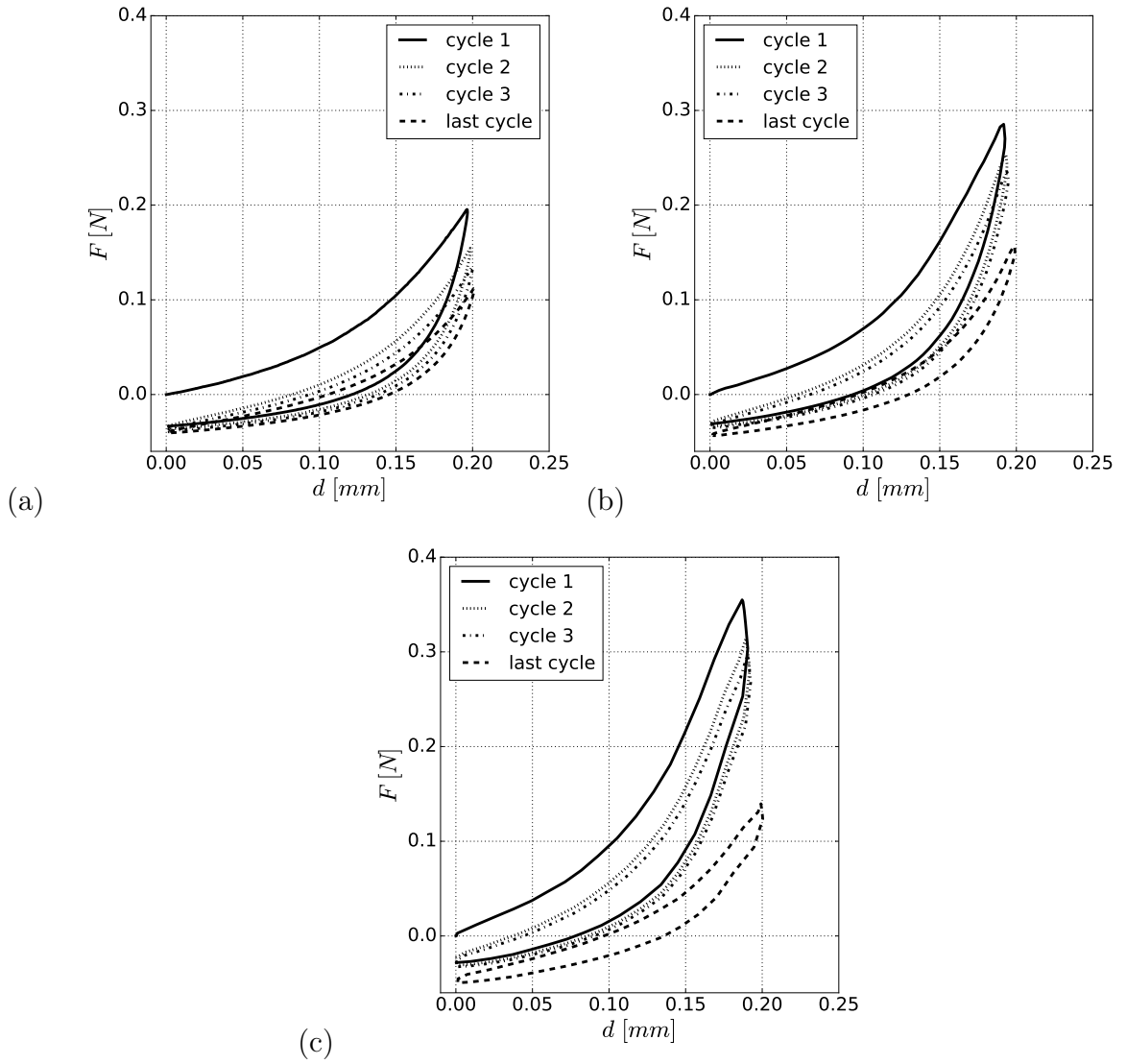


Figure C.11 – Experimental force - displacement curves using a compression tool of 1.75 mm radius testing the samples central site for different loading frequencies, (a) 0.01 Hz, (b) 0.1 Hz and (c) 1 Hz.

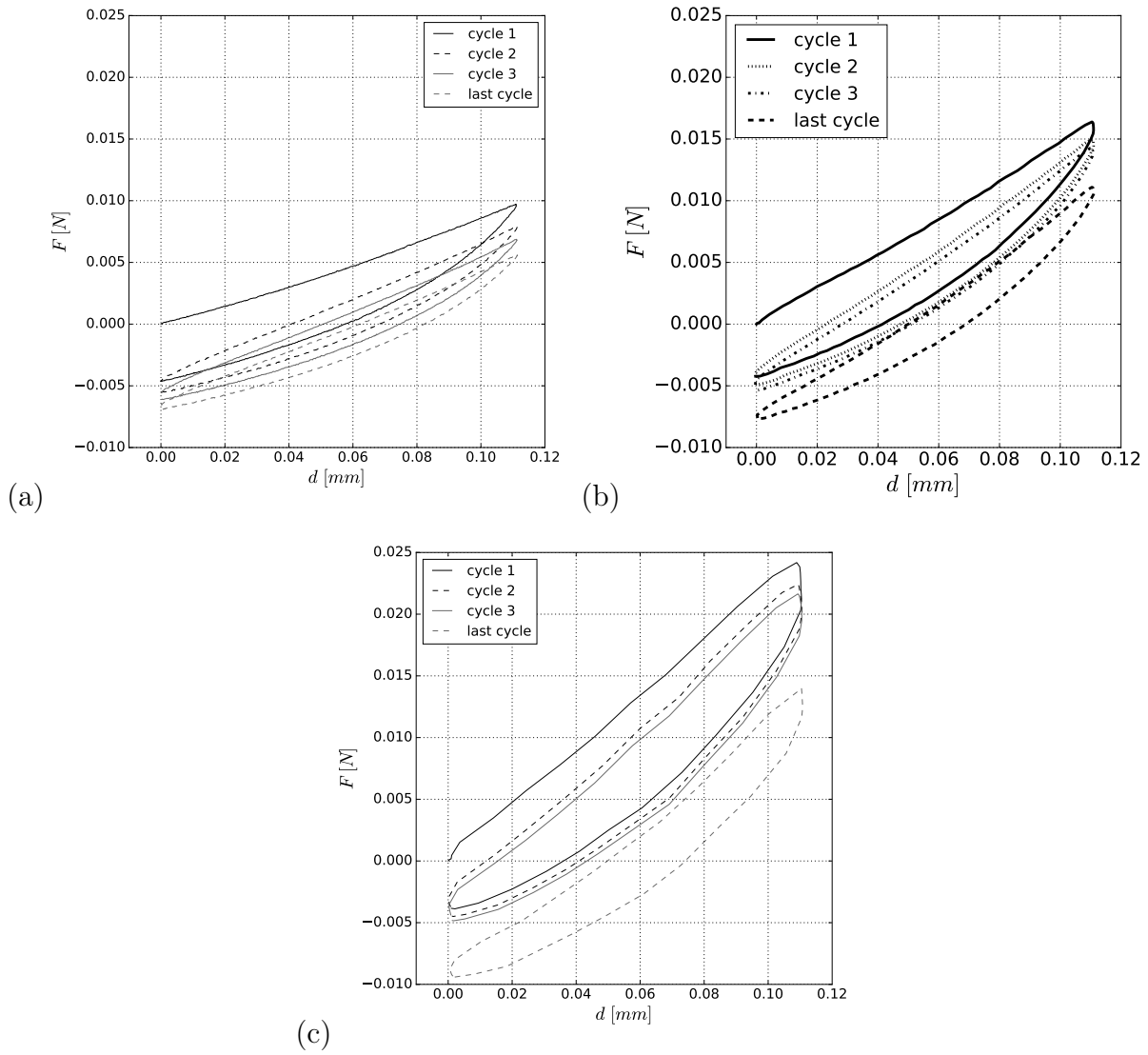


Figure C.12 – Experimental force - displacement curves using a compression tool of 0.875 mm radius testing the samples central site for different loading frequencies, (a) 0.01 Hz, (b) 0.1 Hz and (c) 1 Hz.

C.8 Average maximal forces per test cycle

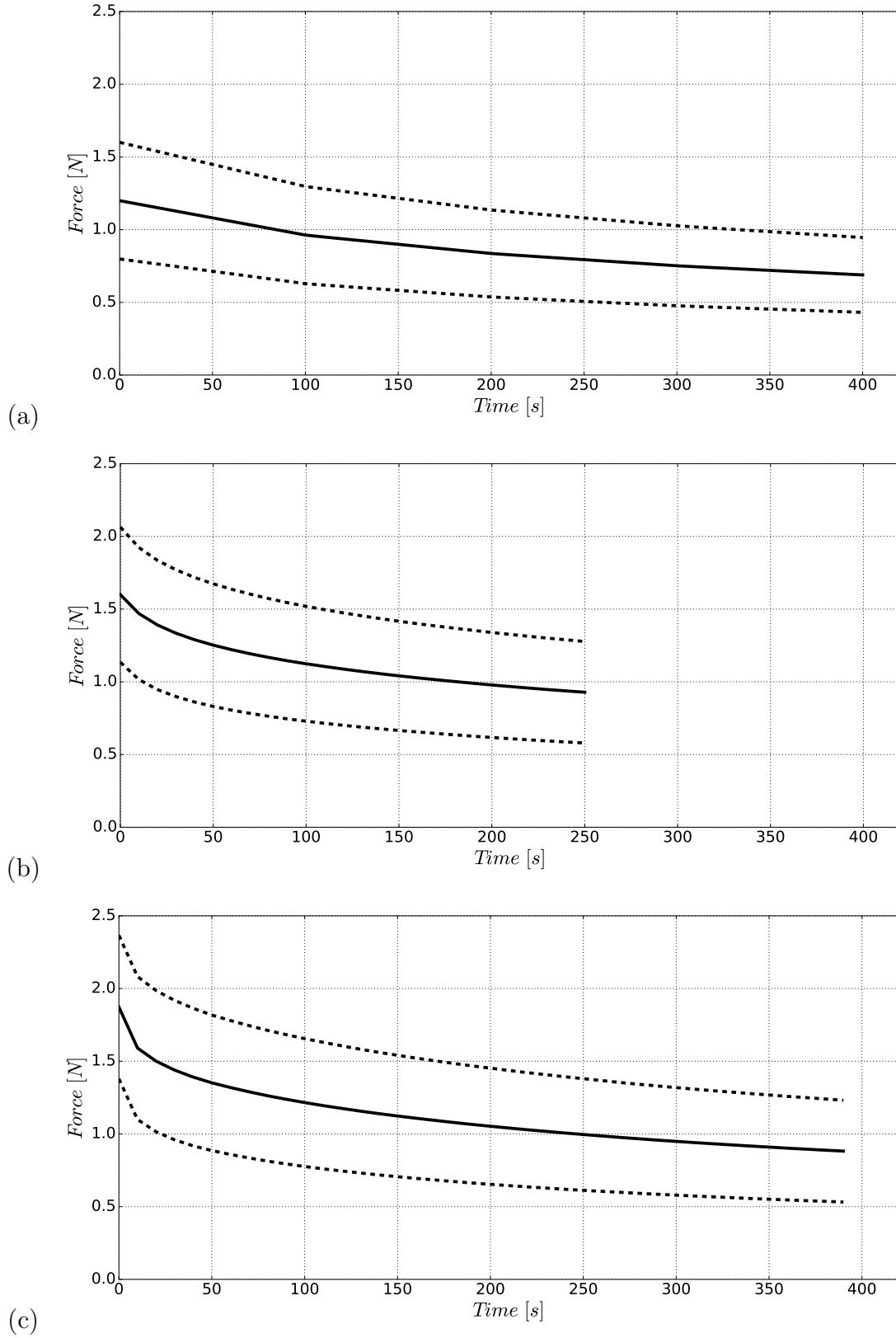


Figure C.13 – Average (—) and standard deviation (---) of maximal measured forces as function of experimental time using a compression tool of 3 mm radius for different loading frequencies, (a) 0.01 Hz, (b) 0.1 Hz and (c) 1 Hz, ($n=18$).

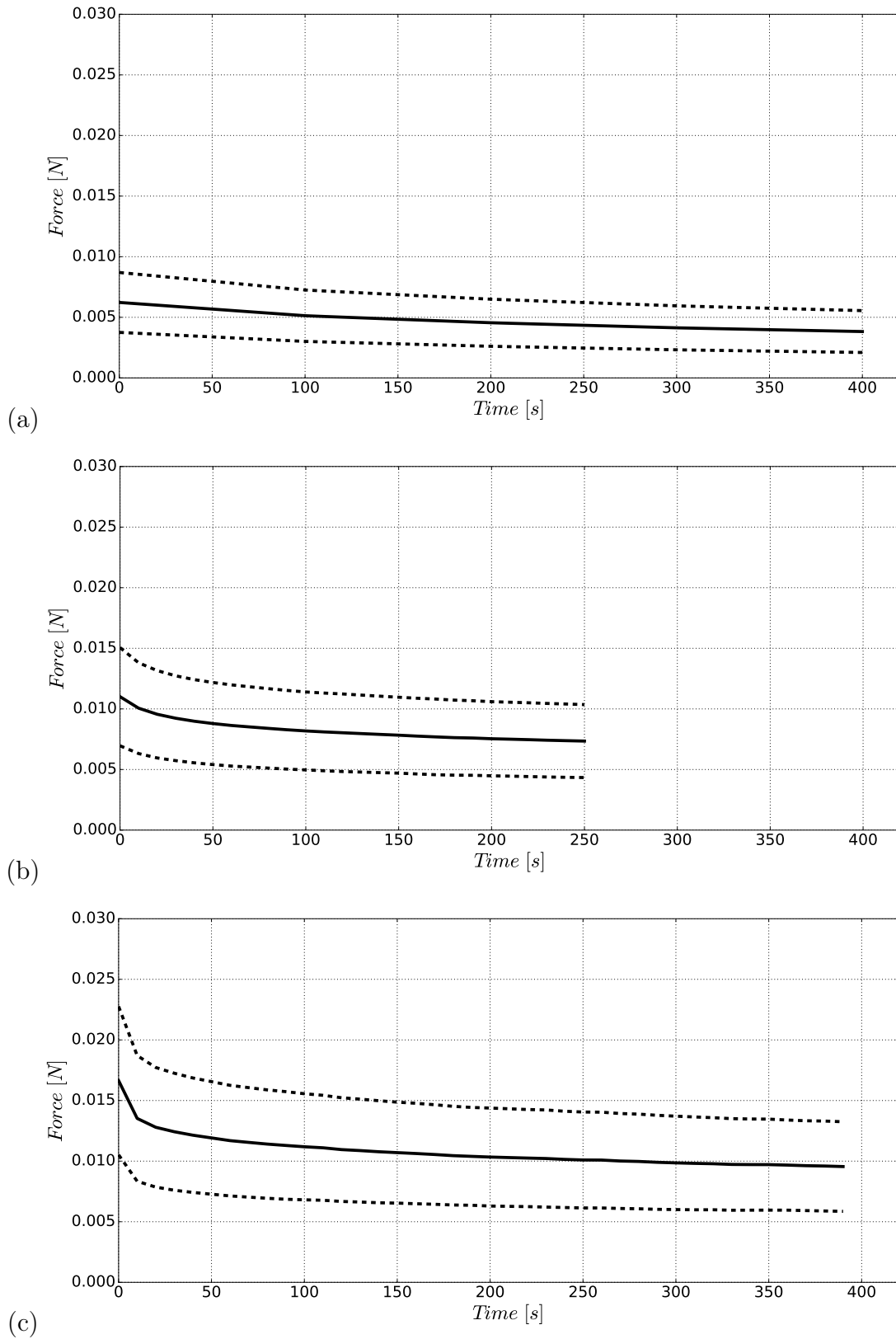


Figure C.14 – Average (–) and standard deviation (– –) of maximal measured forces as function of experimental time using a compression tool of 0.875 mm radius for different loading frequencies, (a) 0.01 Hz, (b) 0.1 Hz and (c) 1 Hz, (n=18).

C.9 Average hysteresis per test cycle

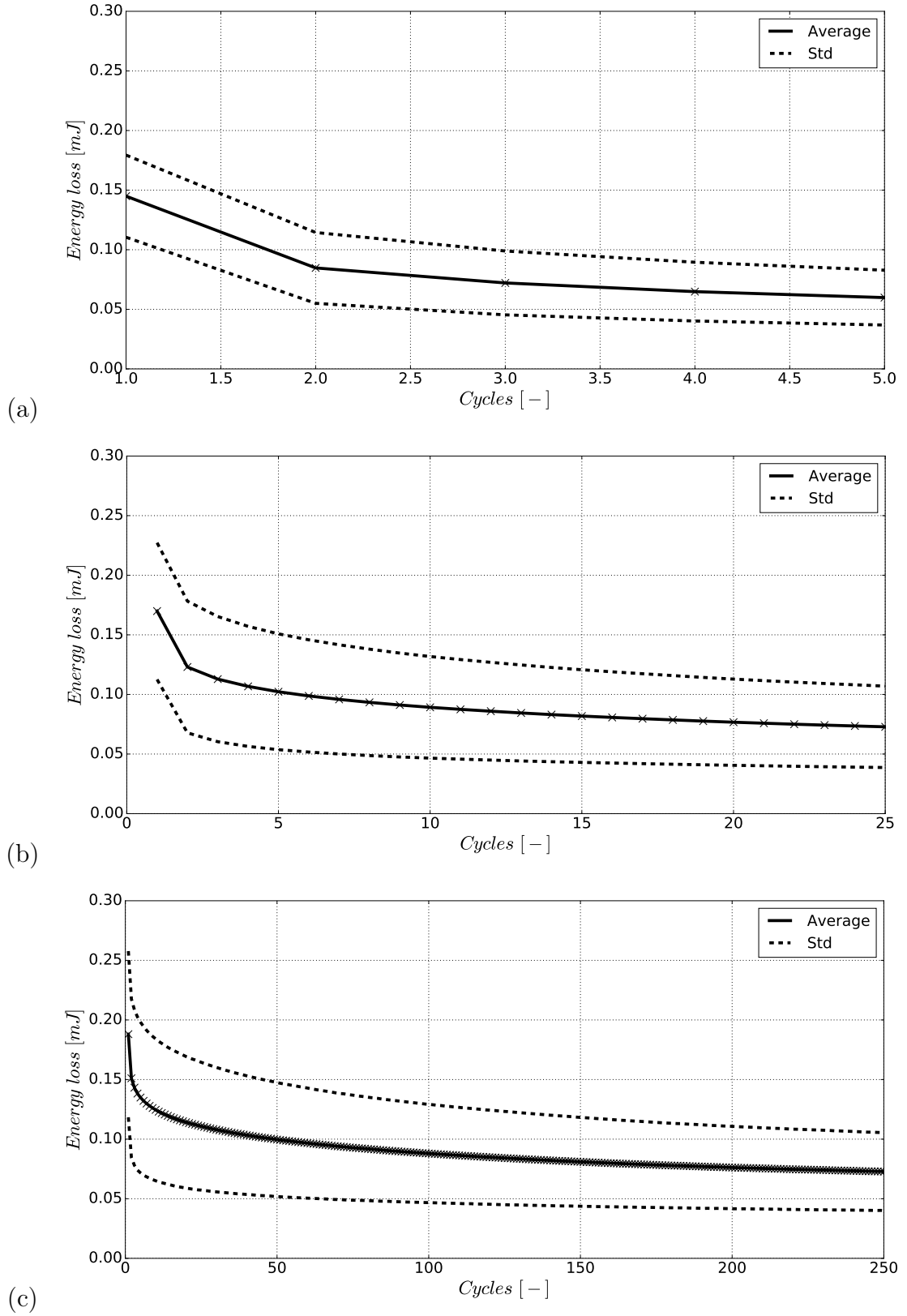


Figure C.15 – Average (—) (\pm standard deviation (---)) hysteresis for all spherical compression tests ($n=18$) using a sphere of radius 3 mm at frequencies (a) 0.01 Hz, (b) 0.1 Hz and (c) 1 Hz.

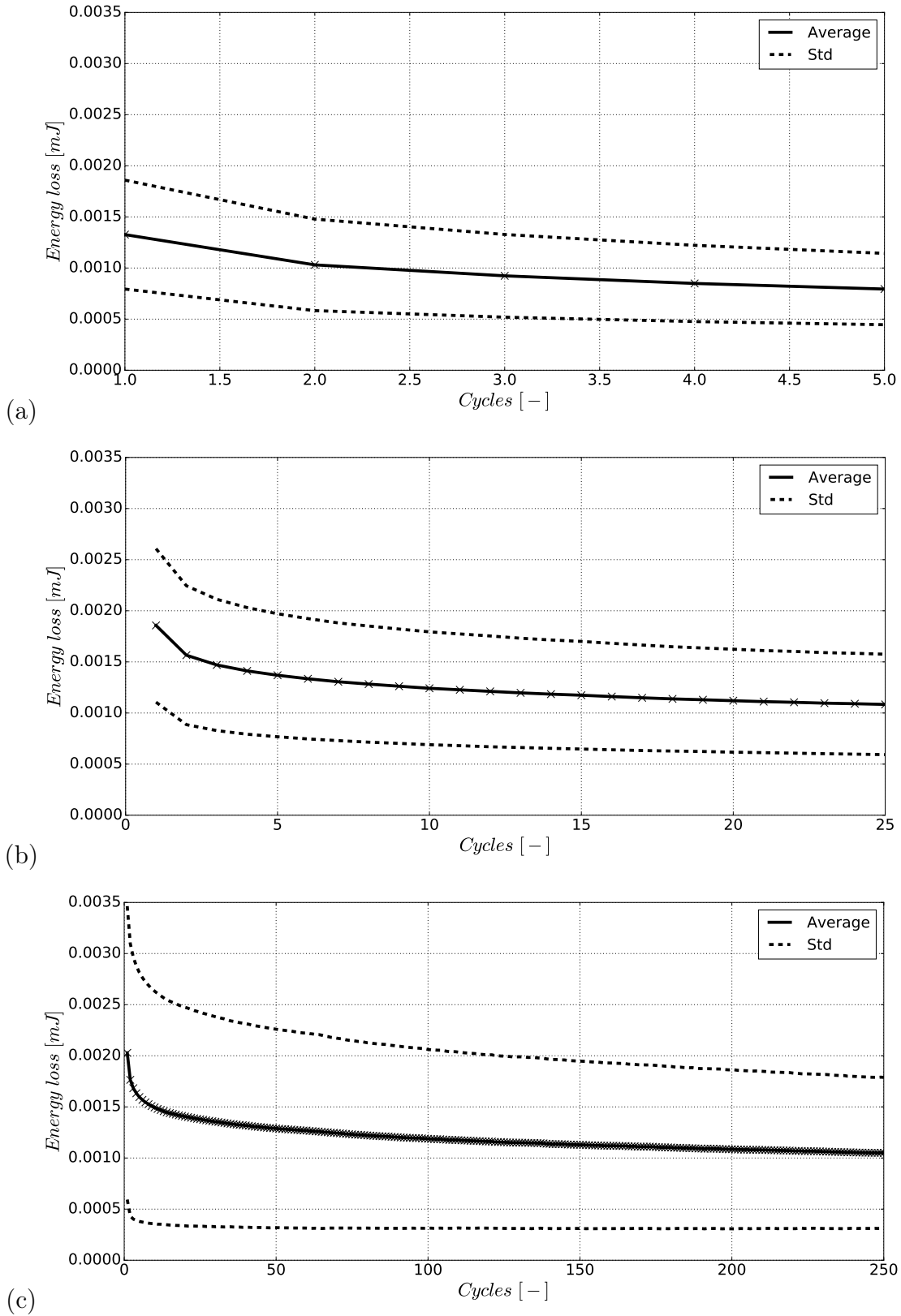


Figure C.16 – Average (–) (\pm standard deviation (– –)) hysteresis for all spherical compression tests ($n=18$) using a sphere of radius 0.875 mm at frequencies (a) 0.01 Hz, (b) 0.1 Hz and (c) 1 Hz.

C.10 Additional of results internal strain analysis

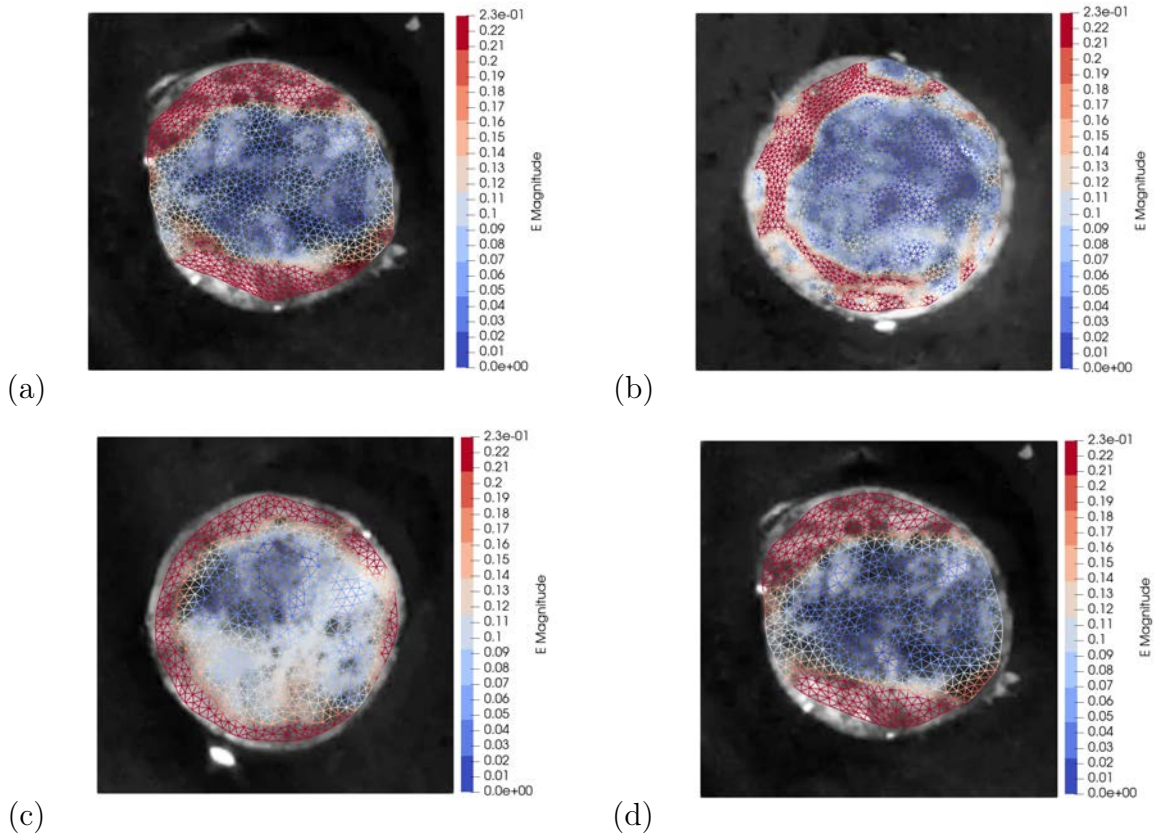


Figure C.17 – Strain field magnitude obtained on hole drilling specimen, (a) 181206, (b) 181207, (c) 181213 and (d) 181214.

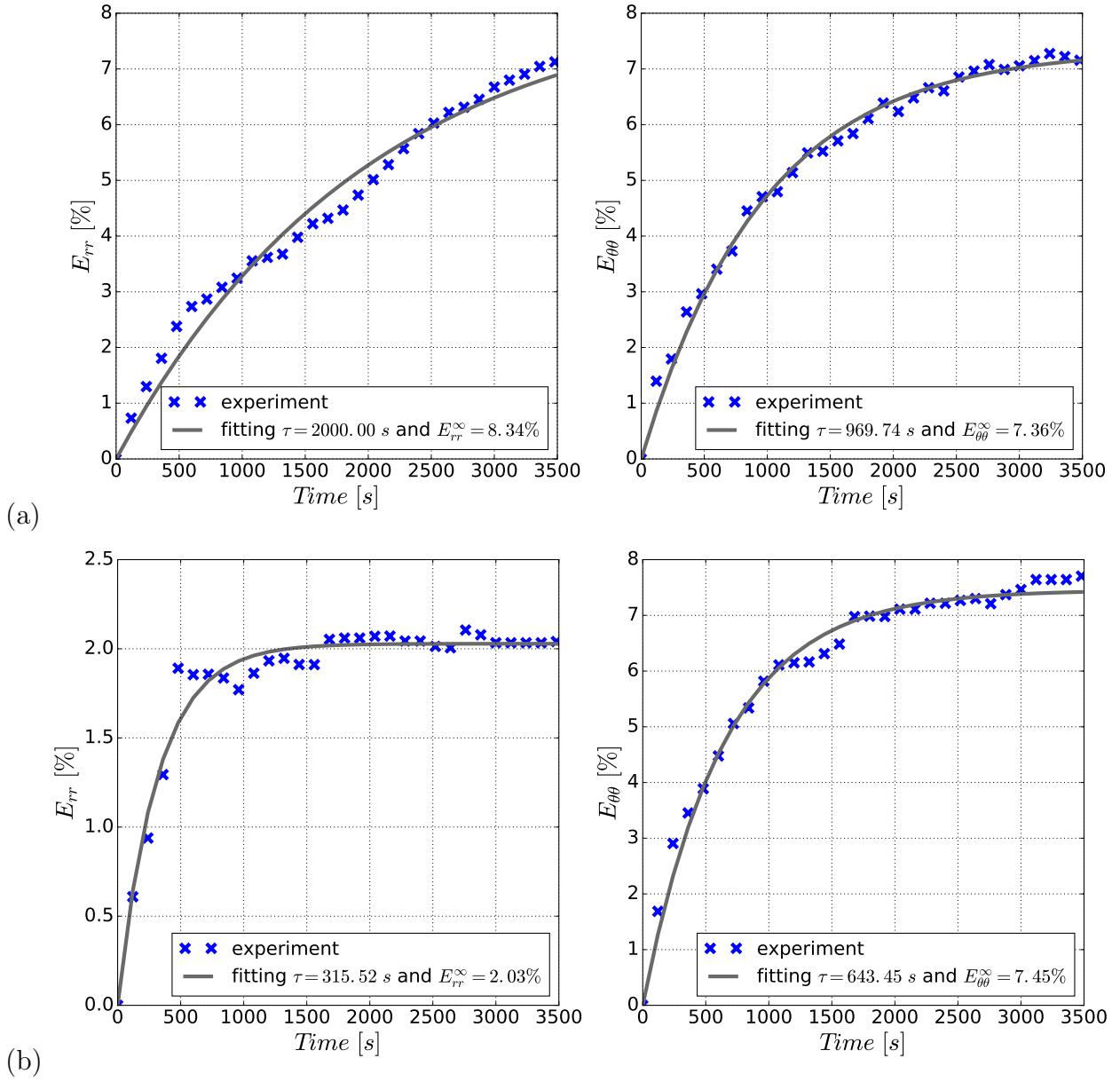


Figure C.18 – Radial and tangential average strain fields as function of time obtained on hole drilling specimen (a) 181206 and (b) 181207, with exponential fitting highlighting characteristic times τ and theoretical *in vivo* internal strains E^∞ .

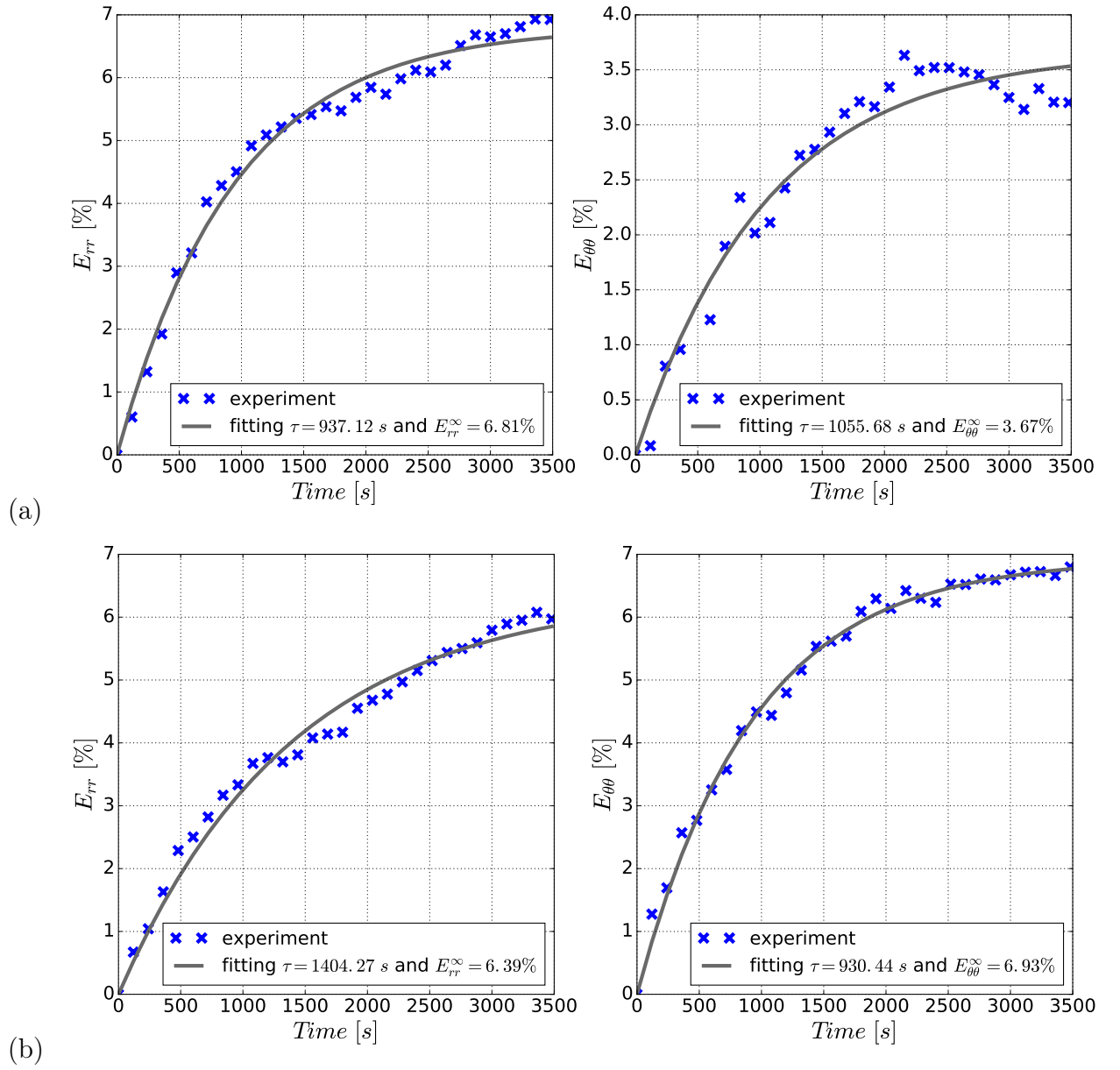


Figure C.19 – Radial and tangential average strain fields as function of time obtained on hole drilling specimen (a) 181213 and (b) 181214, with exponential fitting highlighting characteristic times τ and theoretical *in vivo* internal strains E^∞ .

Appendix D

Stress-strain curves

Table D.1 – Results for two-term Ogden fitting for local spherical compression tests on samples central site at 0.01 Hz using a compression tool of size 3 mm.

Essay	d_{max} [mm]	ϵ_{max}^*	μ_1 [MPa]	α_1	μ_2 [MPa]	α_2	R^2
181128 E4	0.94	0.27	$1.19e-3$	6.03	$2.08e-6$	89.10	0.995
181129 E11	0.88	0.26	$1.03e-2$	8.07	$1.02e-4$	59.96	0.999
181205 E1	0.76	0.25	$4.49e-3$	6.69	$2.53e-6$	103.19	0.991
181206 E11	0.72	0.24	$1.18e-2$	6.41	$8.37e-5$	77.77	0.994
181212 E1	0.92	0.27	$4.95e-3$	6.10	$1.67e-6$	91.82	0.990
181213 E11	0.92	0.27	$6.61e-3$	6.02	$2.70e-6$	87.76	0.994
average	0.86		$6.56e-3$	6.55	$3.24e-5$	84.9	
std	0.093		0.0039	0.788	$4.72e-5$	14.70	

Table D.2 – Results for two-term Ogden fitting for local spherical compression tests on samples lateral site at 0.01 Hz using a compression tool of size 3 mm.

Essay	d_{max} [mm]	ϵ_{max}^*	μ_1 [MPa]	α_1	μ_2 [MPa]	α_2	R^2
181128 E2	0.87	0.27	$7.46e-3$	5.93	$3.56e-6$	88.52	0.998
181129 E13	1.61	0.36	$1.25e-3$	4.41	$7.44e-7$	61.08	0.976
181205 E2	0.95	0.28	$9.05e-3$	5.04	$9.09e-6$	74.87	0.993
181206 E13	0.85	0.26	$8.61e-3$	5.34	$3.31e-6$	90.93	0.996
181212 E2	1.59	0.36	$1.45e-3$	4.75	$6.16e-7$	62.36	0.934
181213 E13	1.11	0.30	$3.37e-3$	5.56	$7.79e-7$	83.09	0.960
average	1.16		$5.20e-3$	5.17	$3.02e-6$	76.8	
std	0.350		0.0036	0.553	$3.26e-6$	12.93	

Table D.3 – Results for two-term Ogden fitting for local spherical compression tests on samples medial site at 0.01 Hz using a compression tool of size 3 mm.

Essay	d_{max} [mm]	ϵ_{max}^*	μ_1 [MPa]	α_1	μ_2 [MPa]	α_2	R^2
181128 E3	1.05	0.29	$2.77e-3$	5.71	$4.22e-6$	75.82	0.999
181129 E12	1.15	0.31	$4.96e-3$	5.00	$6.54e-5$	47.64	0.997
181205 E3	0.56	0.21	$1.36e-2$	5.62	$6.52e-5$	99.72	0.990
181206 E12	0.64	0.23	$1.54e-2$	6.17	$9.64e-5$	84.91	0.990
181212 E3	1.34	0.33	$1.78e-3$	5.59	$1.04e-6$	70.10	0.988
181213 E12	0.92	0.27	$4.70e-3$	6.21	$5.37e-6$	83.65	0.993
average	0.94		$7.20e-3$	5.72	$3.96e-5$	77.0	
std	0.300		0.0058	0.445	$4.11e-5$	17.516	

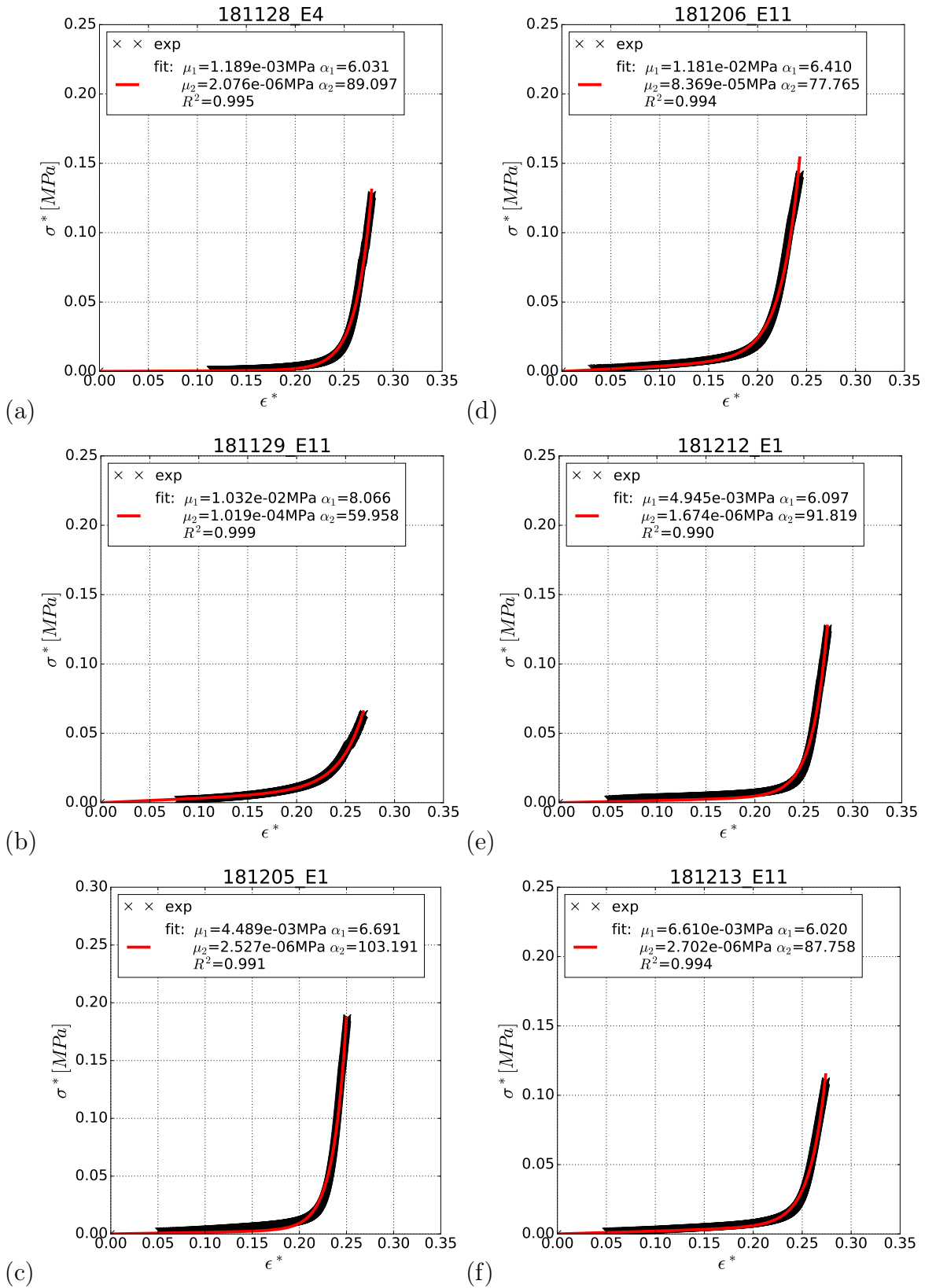


Figure D.1 – Representative stress-strain curves for local spherical compression test on the discs central site, using a compression tool of 3 mm radius at a frequency of 0.01 Hz and two-term Ogden model fitting.

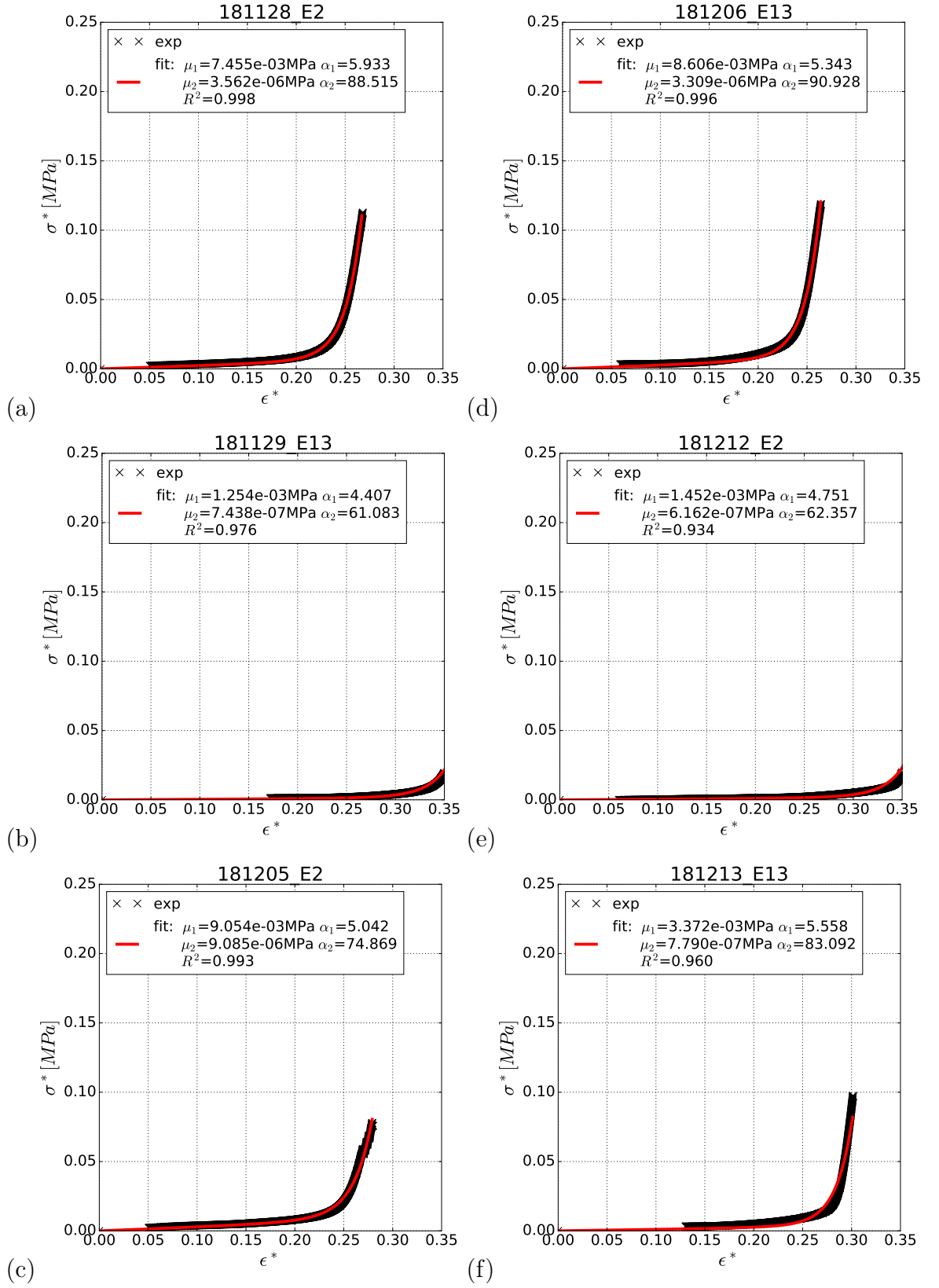


Figure D.2 – Representative stress-strain curves for local spherical compression test on the discs lateral site, using a compression tool of 3 mm radius at a frequency of 0.01 Hz and two-term Ogden model fitting.

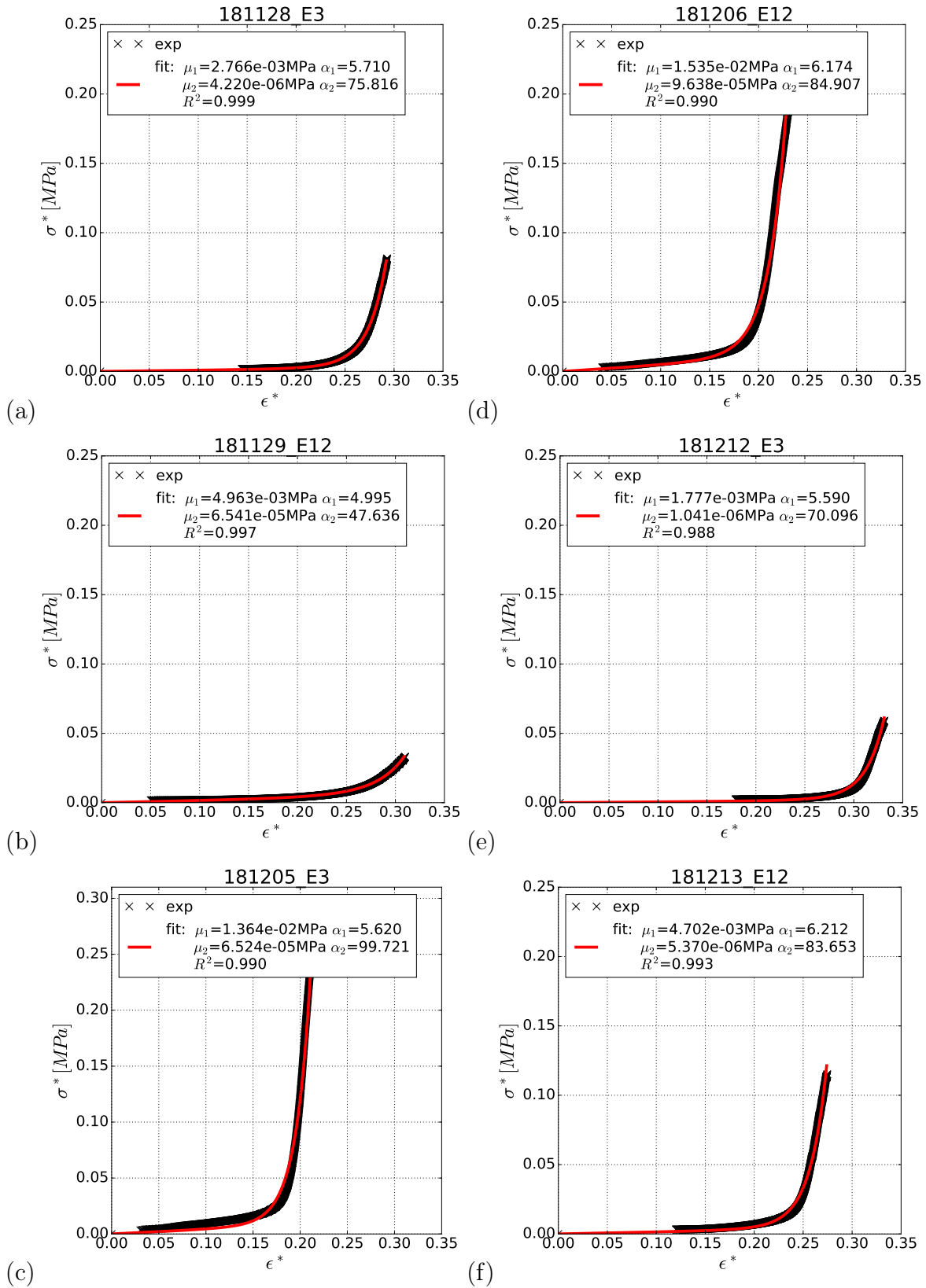


Figure D.3 – Representative stress-strain curves for local spherical compression test on the discs medial site, using a compression tool of 3 mm radius at a frequency of 0.01 Hz and two-term Ogden model fitting.

Table D.4 – Results for two-term Ogden fitting for local spherical compression tests on samples central site at 0.01 Hz using a compression tool of size 1.75 mm.

Essay	d_{max} [mm]	ϵ_{max}^*	μ_1 [MPa]	α_1	μ_2 [MPa]	α_2	R^2
181128 E14	0.70	0.29	$9.65e-3$	4.95	$1.75e-6$	80.97	0.997
181130 E1	0.77	0.30	$8.48e-3$	5.97	$8.08e-5$	45.29	0.999
181205 E11	0.82	0.31	$4.97e-3$	4.56	$3.66e-5$	51.85	0.984
181207 E1	0.63	0.27	$1.46e-2$	4.48	$4.65e-5$	59.52	0.999
181212 E10	0.99	0.34	$5.97e-3$	3.27	$8.65e-7$	60.17	0.990
181214 E1	0.86	0.32	$7.78e-3$	3.40	$7.01e-6$	55.53	0.998
average	0.795		$8.58e-3$	4.44	$2.89e-5$	58.9	
std	0.126		0.0034	1.01	$3.18e-5$	12.13	

Table D.5 – Results for two-term Ogden fitting for local spherical compression tests on samples medial site at 0.01 Hz using a compression tool of size 1.75 mm.

Essay	d_{max} [mm]	ϵ_{max}^*	μ_1 [MPa]	α_1	μ_2 [MPa]	α_2	R^2
181128 E13	0.59	0.25	$1.47e-2$	11.23	$1.34e-4$	59.66	0.999
181130 E2	0.70	0.27	$1.09e-2$	5.81	$8.07e-5$	54.12	0.999
181205 E13	0.80	0.29	$8.47e-3$	4.67	$6.88e-7$	82.71	0.991
181207 E2	0.56	0.25	$1.70e-2$	5.94	$6.98e-5$	71.20	0.999
181212 E12	0.98	0.32	$5.52e-3$	3.97	$6.39e-7$	68.82	0.994
181214 E2	1.06	0.33	$5.12e-3$	3.28	$5.27e-7$	64.31	0.996
average	0.78		$1.03e-2$	5.82	$4.77e-5$	66.8	-
std	0.205		0.0049	2.85	$5.60e-5$	9.95	-

Table D.6 – Results for two-term Ogden fitting for local spherical compression tests on samples lateral site at 0.01 Hz using a compression tool of size 1.75 mm.

Essay	d_{max} [mm]	ϵ_{max}^*	μ_1 [MPa]	α_1	μ_2 [MPa]	α_2	R^2
181128 E12	1.1	0.34	$3.67e-3$	3.66	$2.30e-6$	56.11	0.999
181130 E3	1.28	0.37	$2.08e-3$	4.28	$4.71e-6$	45.49	0.999
181205 E12	0.87	0.30	$8.34e-3$	3.17	$1.21e-6$	68.98	0.998
181207 E3	0.76	0.28	$1.16e-2$	4.57	$1.80e-6$	72.92	0.992
181212 E11	1.1	0.34	$5.30e-3$	3.44	$7.76e-7$	57.64	0.993
181214 E3	1.08	0.34	$5.09e-3$	3.17	$4.77e-7$	64.54	0.988
average	1.03		$6.01e-3$	3.72	$1.88e-6$	60.9	-
std	0.186		0.0034	0.587	$1.54e-6$	9.94	-

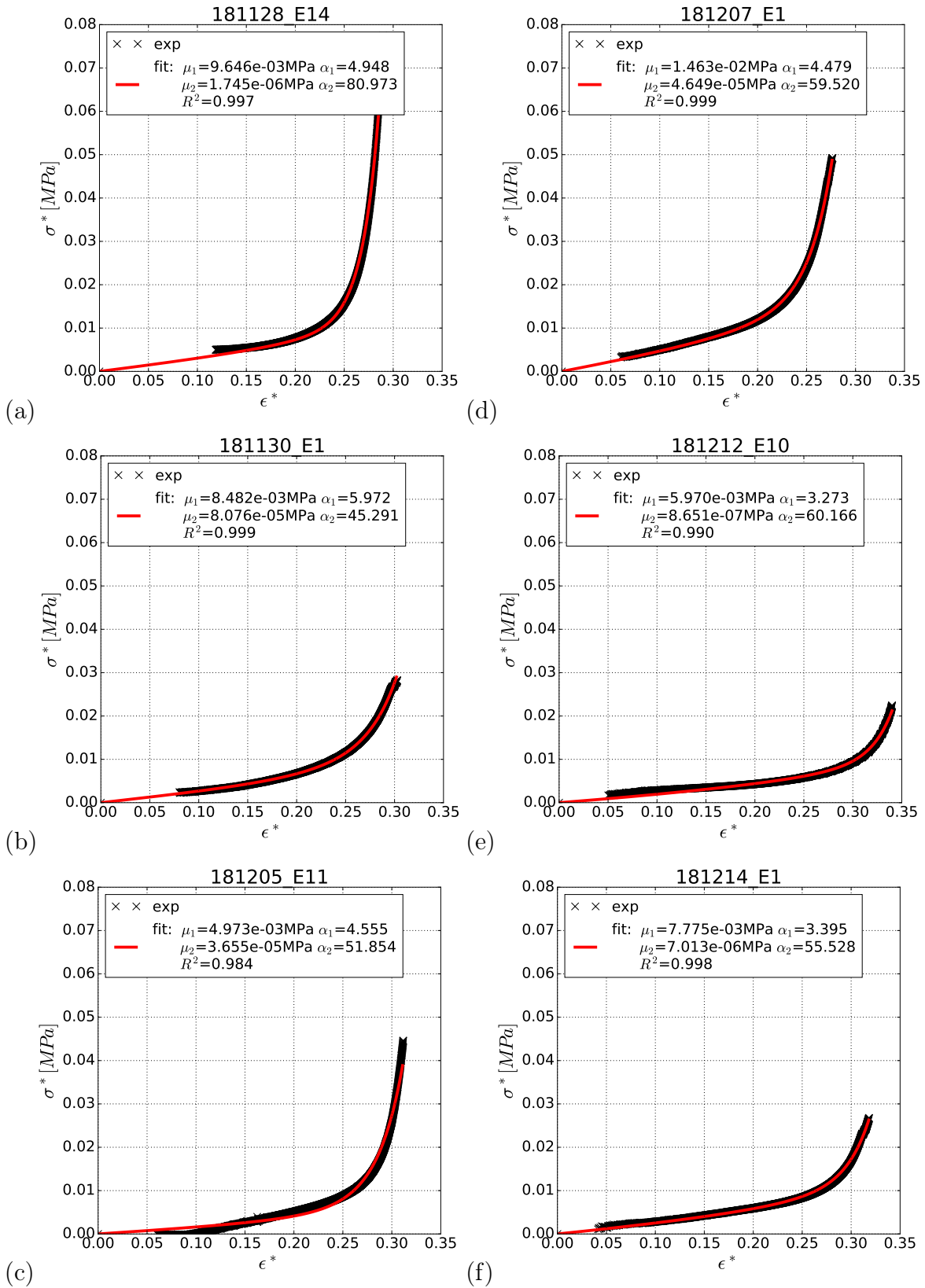


Figure D.4 – Representative stress-strain curves for local spherical compression test on the discs central site, using a compression tool of 1.75 mm radius at a frequency of 0.01 Hz and two-term Ogden model fitting.

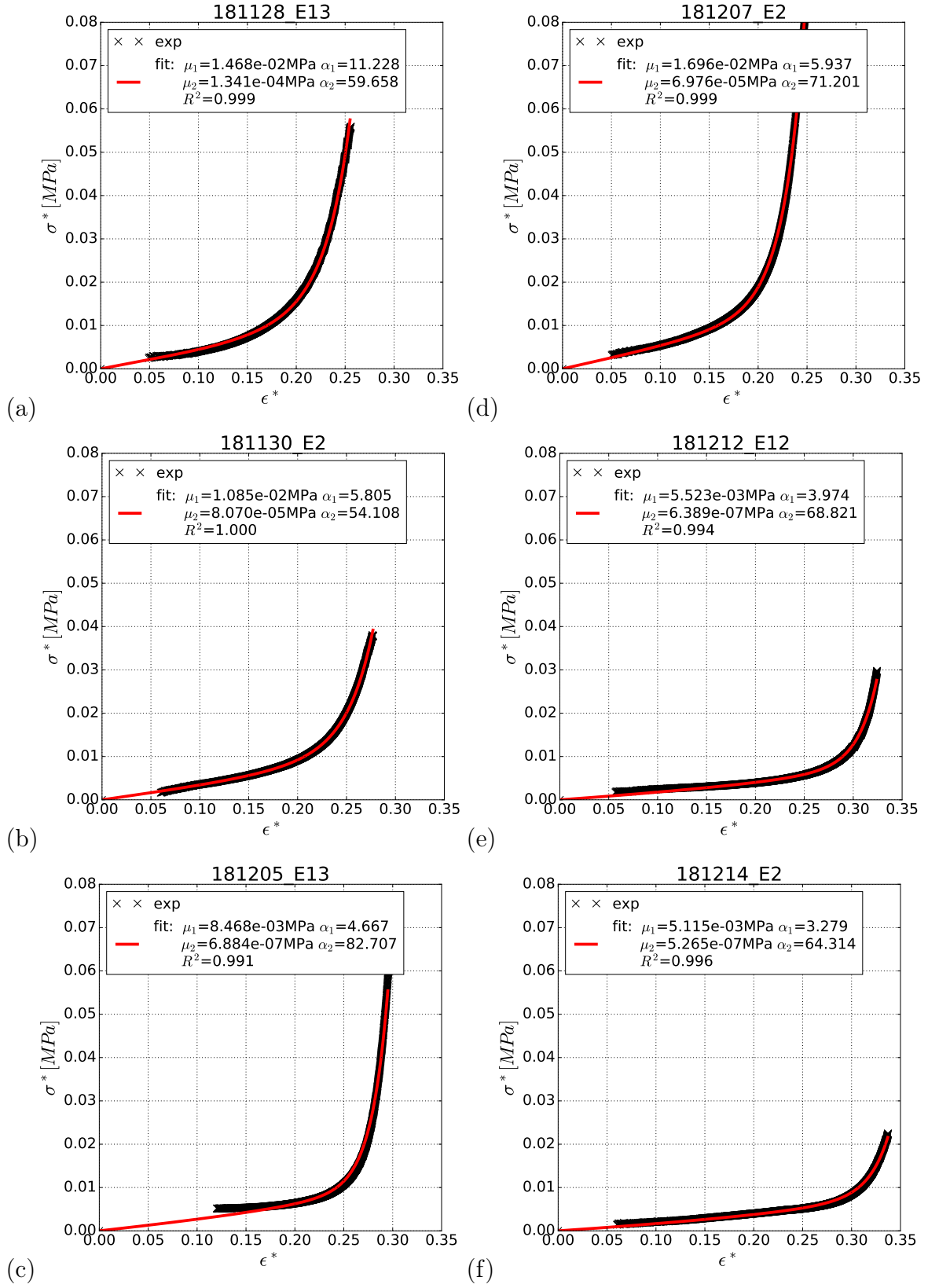


Figure D.5 – Representative stress-strain curves for local spherical compression test on the discs medial site, using a compression tool of 1.75 mm radius at a frequency of 0.01 Hz and two-term Ogden model fitting.

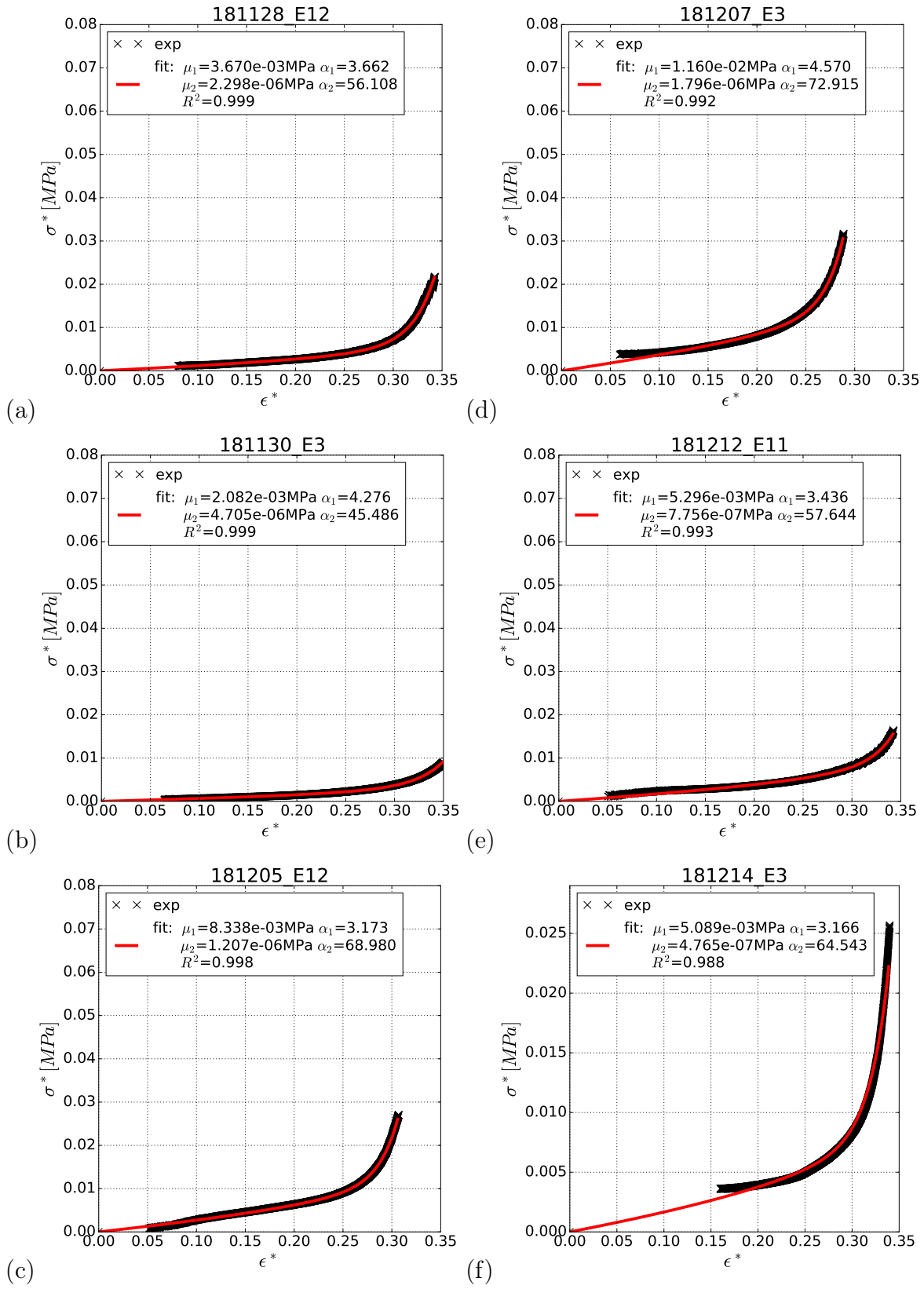


Figure D.6 – Representative stress-strain curves for local spherical compression test on the discs lateral site, using a compression tool of 1.75 mm radius at a frequency of 0.01 Hz and two-term Ogden model fitting.

Table D.7 – Results for two-term Ogden fitting for local spherical compression tests on samples central site at 0.01 Hz using a compression tool of size 0.875 mm.

Essay	d_{max} [mm]	ϵ_{max}^*	μ_1 [MPa]	α_1	μ_2 [MPa]	α_2	R^2
181129 E1	0.45	0.30	$8.85e-3$	4.44	$3.82e-6$	50.53	0.999
181130 E11	0.45	0.30	$5.35e-3$	13.15	$8.11e-5$	13.16	0.980
181206 E1	0.35	0.27	$1.41e-2$	9.74	$8.22e-5$	16.33	0.998
181207 E11	0.39	0.28	$1.34e-2$	3.49	$6.64e-5$	3.49	0.973
181213 E1	0.45	0.30	$9.05e-3$	3.12	$6.32e-5$	3.12	0.988
181214 E10	0.47	0.31	$7.95e-3$	3.15	$7.07e-5$	3.15	0.969
average	0.43		$9.79e-3$	6.21	$6.09e-5$	16.0	-
std	0.05		0.00334	4.23	$3.02e-5$	20.72	-

Table D.8 – Results for two-term Ogden fitting for local spherical compression tests on samples medial site at 0.01 Hz using a compression tool of size 0.875 mm.

Essay	d_{max} [mm]	ϵ_{max}^*	μ_1 [MPa]	α_1	μ_2 [MPa]	α_2	R^2
181129 E4	0.55	0.31	$6.93e-3$	2.94	$6.66e-5$	2.94	0.951
181130 E12	0.38	0.26	$1.31e-2$	4.60	$8.67e-6$	57.89	0.999
181206 E3	0.36	0.26	$1.6e-2$	3.95	$7.21e-5$	3.95	0.975
181207 E12	0.35	0.25	$1.76e-2$	4.88	$5.00e-7$	83.87	0.978
181213 E3	0.38	0.26	$1.48e-2$	3.81	$6.47e-5$	3.81	0.960
181214 E11	0.45	0.28	$9.56e-3$	3.64	$6.79e-5$	3.64	0.983
average	0.41		$1.30e-2$	3.98	$4.67e-5$	26.6	-
std	0.08		0.0041	0.715	$3.29e-5$	36.82	-

Table D.9 – Results for two-term Ogden fitting for local spherical compression tests on samples lateral site at 0.01 Hz using a compression tool of size 0.875 mm.

Essay	d_{max} [mm]	ϵ_{max}^*	μ_1 [MPa]	α_1	μ_2 [MPa]	α_2	R^2
181129 E2	1.13	0.42	$1.97e-3$	1.94	$6.45e-5$	1.94	0.894
181130 E13	0.79	0.36	$2.84e-3$	4.35	$6.42e-5$	4.36	0.984
181206 E2	0.36	0.25	$1.71e-2$	3.95	$7.58e-5$	3.95	0.980
181207 E13	0.46	0.28	$1.03e-2$	3.31	$6.55e-5$	3.31	0.973
181213 E2	0.53	0.30	$7.18e-3$	3.12	$6.79e-5$	3.12	0.899
181214 E12	0.47	0.28	$8.86e-3$	3.30	$5.55e-5$	3.30	0.971
average	0.62		$8.04e-3$	3.33	$6.56e-5$	3.33	-
std	0.29		0.0055	0.825	$6.55e-6$	0.827	-

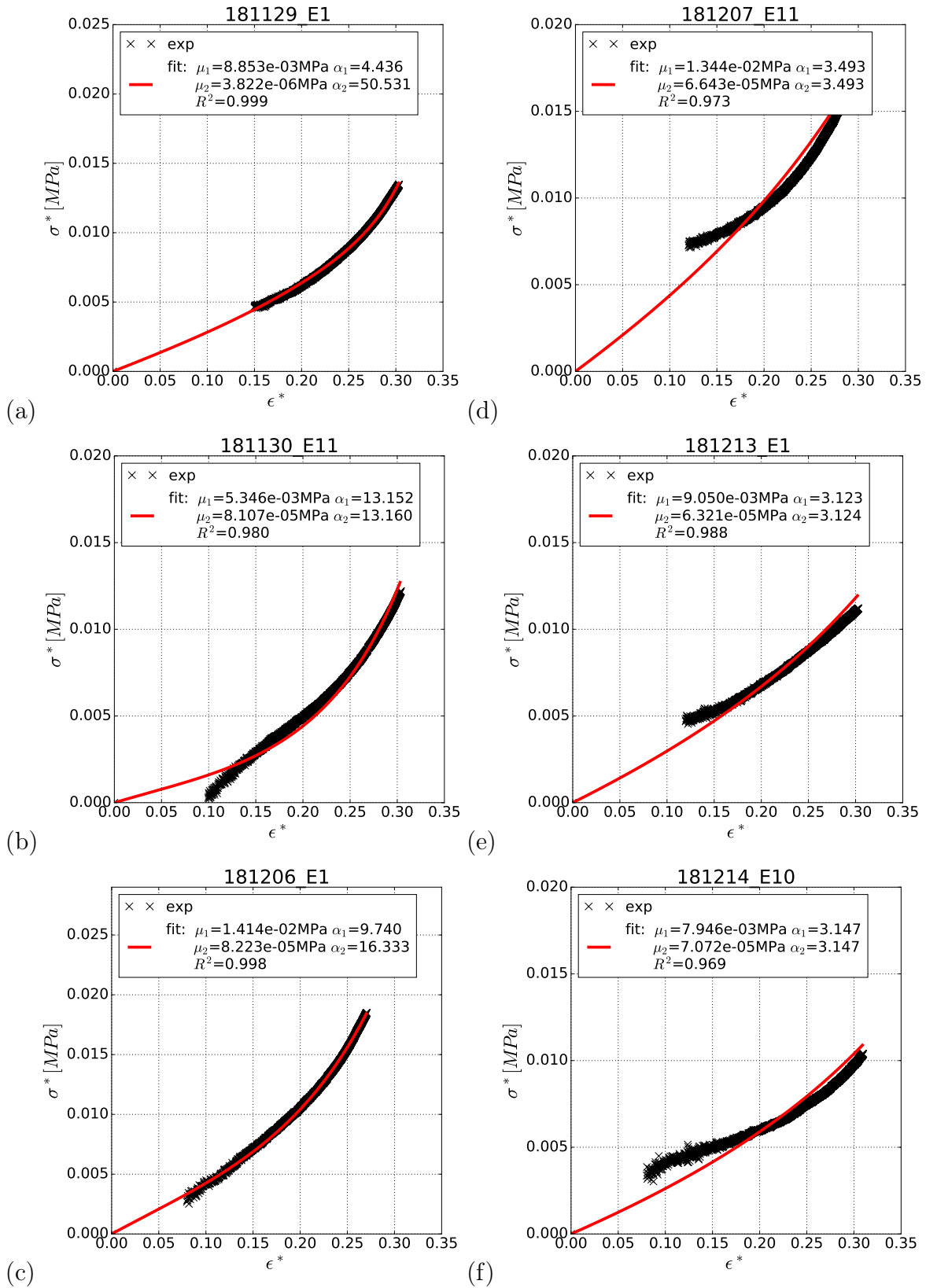


Figure D.7 – Representative stress-strain curves for local spherical compression test on the discs central site, using a compression tool of 0.875 mm radius at a frequency of 0.01 Hz and two-term Ogden model fitting.

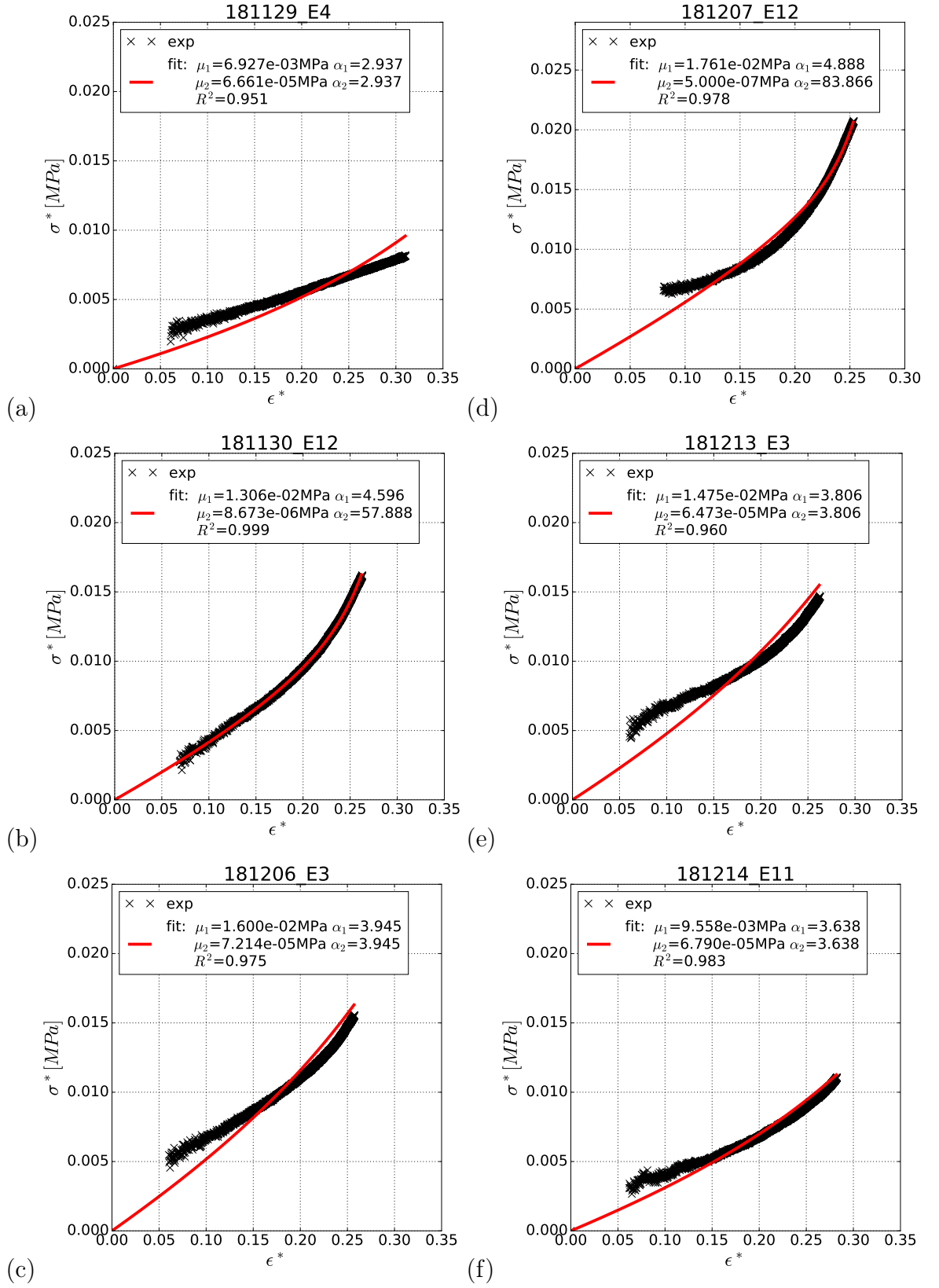


Figure D.8 – Representative stress-strain curves for local spherical compression test on the discs medial site, using a compression tool of 0.875 mm radius at a frequency of 0.01 Hz and two-term Ogden model fitting.

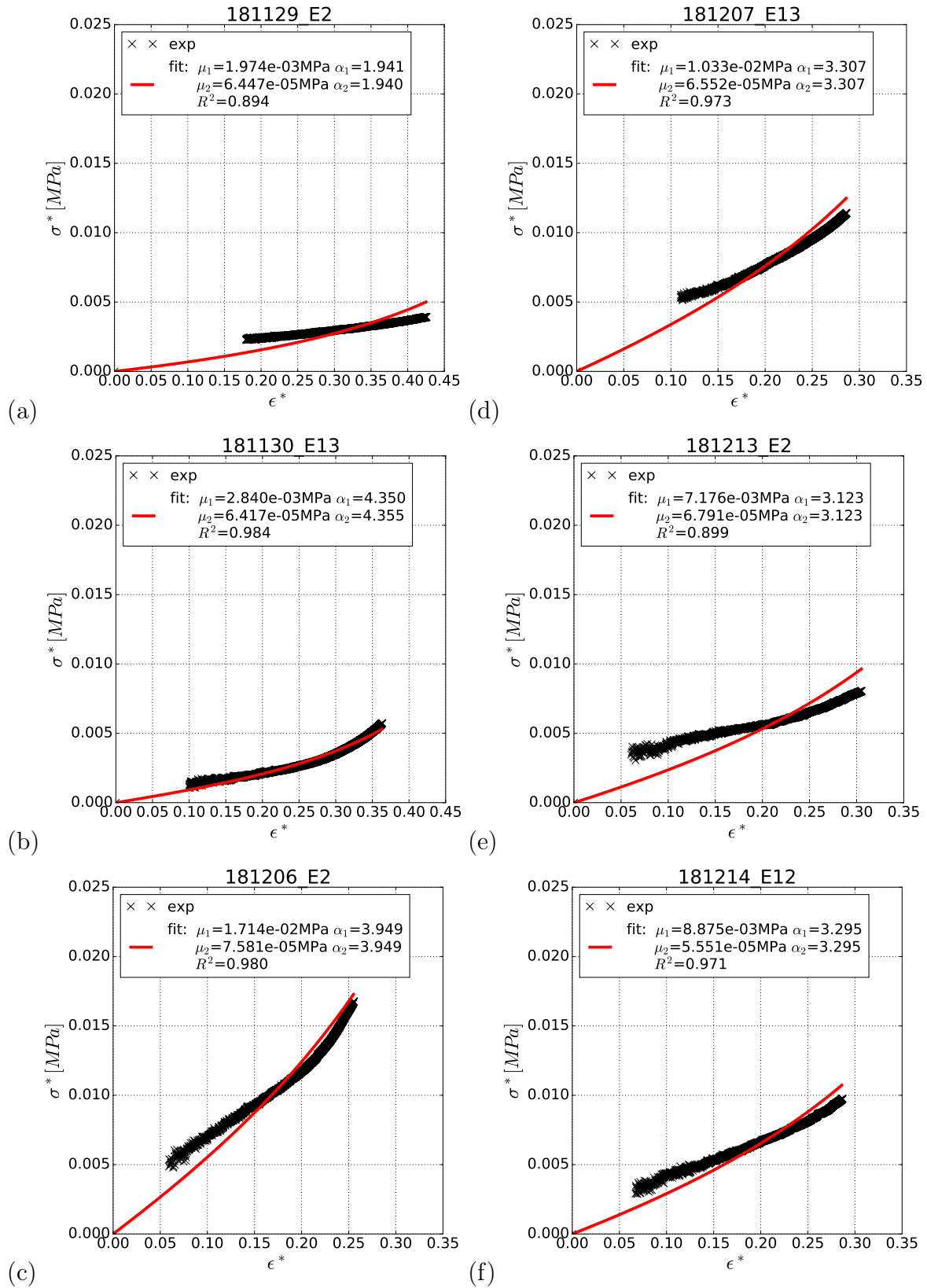


Figure D.9 – Representative stress-strain curves for local spherical compression test on the discs lateral site, using a compression tool of 0.875 mm radius at a frequency of 0.01 Hz and two-term Ogden model fitting.

Experimental and numerical analysis of the temporomandibular joint disc behaviour.

Abstract: The temporomandibular joint disc is a fibrocartilage that provides congruency of the bony structures of the temporomandibular joint (TMJ). It is a crucial element of the TMJ and several TMJ pathologies are related to the disc. To better understand this soft tissue six porcine TMJ disc samples were tested in local spherical compression tests. The experimental setup included physiological conditions, provided by 3D printed condyles as sample holder, humid test environment using a testing chamber filled with physiological solution at a controlled temperature and different test velocities to cover the physiological range of joint activities. The experiments revealed the non-linear and viscous tissue behaviour leading to the creation of a database. The experimental setup allowed testing the disc samples in its integrity. This is a paramount condition since the TMJ disc is the site of internal strains, which has been shown through residual strain analysis. Furthermore, interpretation tools through simulation allowing defining constitutive laws suitable for the temporomandibular joint disc were developed. Therefore, theoretical analysis has been performed on thin layer spherical compression enriched by finite element analysis simulations. Resulting stress-strain curves led to constitutive parameters feeding three dimensional finite element models of spherical compression tests on the TMJ disc. In conclusion, this work provides data and tools leading to large perspectives regarding simulation of the temporomandibular joint that can be used to predict its behaviour for given conditions.

Keywords: biomechanics; soft-tissue; TMJ disc; spherical compression; internal strain analysis; finite element method.

Étude expérimentale et modélisation du comportement du disque de l'articulation temporo-mandibulaire.

Résumé : Le disque de l'articulation temporo-mandibulaire est un fibrocartilage qui assure la congruence des structures osseuses de l'articulation temporo-mandibulaire (ATM). C'est un élément crucial de l'ATM et plusieurs pathologies sont liées au disque. Pour mieux comprendre ce tissu mou, six échantillons de disque porcin ont été testés en compression sphérique locale. Le banc de mesure a permis de reproduire les conditions physiologiques, grâce à des condyles imprimés en 3D servant de porte-échantillons, ainsi qu'un environnement d'essai humide à travers une chambre d'essai remplie d'une solution physiologique contrôlée en température et différentes vitesses de chargement pour couvrir la gamme physiologique d'activités de l'articulation. Les essais ont révélé le comportement non-linéaire et visqueux du tissu et les résultats ont permis de constituer une riche base de données. Le banc de mesure a permis de tester les échantillons dans leur intégralité. Cette condition est primordial car le disque de l'articulation temporo-mandibulaire est le site de contraintes internes, ce qui a pu être analysé grâce aux déformations résiduelles. De plus, des outils d'interprétation par simulation permettant de définir des lois de comportement adaptées au disque l'articulation temporo-mandibulaire ont été développés. Par conséquent, une analyse théorique a été effectuée sur la compression sphérique de couches fines enrichie par des simulations par éléments finis. Les courbes de contrainte-déformation résultantes ont conduit à des paramètres constitutifs alimentant des modèles éléments finis tridimensionnels d'essais de compression sphérique sur le disque ATM. En conclusion, ces travaux fournissent des données et des outils conduisant à de larges perspectives de simulation de l'articulation temporo-mandibulaire qui peuvent être utilisées pour prédire son comportement dans des conditions données.

Mots clés : biomechanique ; tissus mous ; disque ATM ; compression sphérique ; contraintes internes; méthode des éléments finis.